

**Status Report on the Small Secure Transportable Autonomous Reactor
(SSTAR)/Lead-Cooled Fast Reactor (LFR) and Supporting Research
and Development**

by

**James J. Sienicki, Anton Moiseyev, Won Sik Yang, David C. Wade, Anna
Nikiforova,¹ Pierre Hanania,² Ho Jin Ryu, Konrad P. Kulesza,³ and Sang Ji Kim**

**Nuclear Engineering Division
Argonne National Laboratory
9700 South Cass Avenue
Argonne, Illinois 60439**

**William G. Halsey, Craig F. Smith, Neil W. Brown, Ehud Greenspan,⁴ and
Magdalena de Caro**

**Lawrence Livermore National Laboratory
7000 East Avenue
Livermore, California 94550**

**Ning Li, Peter Hosemann, Jinsuo Zhang, and Huidan Yu
Los Alamos National Laboratory**

September 29, 2006

- 1. Massachusetts Institute of Technology**
- 2. Ecole des Mines de Paris**
- 3. Oregon State University**
- 4. University of California, Berkeley**

Disclaimer

This report was prepared as an account of work sponsored by an agency of the United States Government. Neither the United States Government nor any agency thereof, nor UChicago Argonne, LLC, nor any of their employees or officers, makes any warranty, express or implied, or assumes any legal liability or responsibility for the accuracy, completeness, or usefulness of any information, apparatus, product, or process disclosed, or represents that its use would not infringe privately owned rights. Reference herein to any specific commercial product, process, or service by trade name, trademark, manufacturer, or otherwise, does not necessarily constitute or imply its endorsement, recommendation, or favoring by the United States Government or any agency thereof. The views and opinions of document authors expressed herein do not necessarily state or reflect those of the United States Government or any agency thereof, Argonne National Laboratory, or UChicago Argonne, LLC.

Table of Contents

Abstract	10
1. Executive Summary	12
2. Argonne National Laboratory – SSTAR/LFR Development.....	20
2.1. Rationale for Fast Reactors for International Deployment	20
2.2. Status of SSTAR Development	26
2.2.1. SSTAR Configuration.....	26
2.2.2. SSTAR S-CO ₂ Brayton Cycle Improvements	41
2.2.3. SSTAR Reactor Autonomous Load Following Reactivity Feedback Coefficient Assessment.....	56
2.2.4. LFR Fuel Pin Design Computer Code Development	62
2.2.5. SSTAR Safety Design Approach.....	63
2.2.6. SSTAR Inherent Safety Features	63
2.2.7. SSTAR Passive Safety Systems.....	65
2.2.8. SSTAR Active Safety Systems	66
2.2.9. Role of SSTAR Inherent Safety Features and Passive and Active Safety Systems in Safety Design Approach.....	66
2.3. Estimate of Po-210 Production and Heat Source in Lead-Bismuth Eutectic Coolant.....	68
2.4. LFR Core Neutronics Benchmark	74
2.4.1. Introduction.....	74
2.4.2. Description of the Benchmark Problem.....	75
2.4.3. Analysis Methods.....	80
2.4.4. Benchmarking Results	83
2.4.5. Benchmarking Pre-Existing Russian Criticals Data Relevant to Lead-Cooled Reactors.....	99
2.4.6. Benchmarking Summary	101
2.5. Industrial Health and Safety Aspects of Lead and Lead Industrial Practice.	101
2.5.1. Introduction.....	101
2.5.2. Acronyms and Definitions	102
2.5.3. Health Effects of Lead	102
2.5.4. Emergency and First Aid Procedure Recommendations	104
2.5.5. Health Effects of Bismuth.....	104
2.5.6. Health Rules and Regulations for Lead	104
2.5.7. Lead Health Industrial Practice.....	111
2.5.8. Lead Industrial Accident Practice.....	113
2.5.9. Respirator Requirements of 29 CFR 1910.1025 (General Industry Lead Standard)	114
2.5.10. Respirator Requirements of 29 CFR 1926.62 (Construction Lead Standard)	115
2.5.11. Supplementary Exposure Limits.....	115
2.5.12. Partial List of Websites	116
2.6. Argonne National Laboratory International Collaborations	116
2.7. Argonne National Laboratory International Interactions.....	117
2.8. LFR Co-System Integration Manager Coordination.....	119

2.9.	ANL Conference Proceeding Publications and Reports	119
3.	Los Alamos National Laboratory – Lead Coolant Testing.....	121
3.1.	Introduction to Lead Coolant Testing	121
3.2.	Modeling System Corrosion Kinetics.....	121
3.3.	Sources and Categories of Test Results	122
3.4.	Results.....	124
3.5.	Analysis of DELTA Tested Al-Rich ODS Steels	127
3.6.	Additional Analysis of DELTA Tested Laser-Peened Specimens	130
3.7.	W- and Mo-Coated F/M Steels Tested in DELTA	132
3.7.1.	W-Coated EP823	132
3.7.2.	Mo-Coated EP823.....	133
3.7.3.	W-Coated HT-9	133
3.7.4.	Mo-Coated HT-9.....	134
3.7.5.	W-coated 9Cr	135
3.7.6.	Mo-Coated 9Cr	136
3.7.7.	W-Coated MA957.....	137
3.7.8.	Mo-Coated MA957	138
3.8.	Effects of Oxygen on Heat Transfer Due to Fouling.....	139
3.9.	Preparation of Materials for DELTA Testing	140
4.	Lawrence Livermore National Laboratory	141
4.1.	LFR System Design Support Activities.....	141
4.1.1.	General LFR Planning, Reporting, and Interface	141
4.1.2.	Generation IV System Support	141
4.2.	International Cooperation	142
4.2.1.	Generation IV International Forum (GIF) LFR SSC.....	142
4.2.2.	Heavy Metal-Cooled Reactor Technology Meeting	143
4.2.3.	Cooperation with ELSY.....	144
4.2.4.	Small Modular Fast Reactor Coordination with CRIEPI	144
4.3.	University Partnership: UC-Berkeley	144
4.4.	LLNL Materials Evaluations	145
4.4.1.	Material Modeling	145
4.4.2.	Laser Peening.....	155
4.4.3.	Thermal Treatment Experiments	157
4.4.4.	Residual Stress Measurements using the Slitting Method.....	159
4.4.5.	EDS in Samples Participating in Corrosion Tests	161
5.	Acknowledgements.....	163
6.	References.....	163

List of Figures

Figure 1. Illustration of Regional Fuel Cycle Center Architecture.....	22
Figure 2. SSTAR Modular Lead-Cooled Fast Reactor.....	28
Figure 3. SSTAR Flow Shroud, Flow Distributor Head, and Radial Reflector.....	29
Figure 4. SSTAR Reactor and In-Vessel Internals.	30
Figure 5. SSTAR Thermal Baffle to Protect the Reactor Vessel from Thermal Stresses Induced by Exposure to Heated Pb During Startup and Shutdown Cycles.	31
Figure 6. SSTAR Open-Lattice Core Configuration (All Fuel Pins Shown).	32
Figure 7. SSTAR Core and Radial Reflector (Left) and Uniform Distribution of Control Rods in Core Lattice (Right).....	34
Figure 8. SSTAR Control Rod, Control Rod Driveline, and Control Rod Driveline Guide Tube.	34
Figure 9. SSTAR Fuel Pins, Control Rod Guide Tubes, and Grid Spacers.....	35
Figure 10. SSTAR Grid Spacer Cell with Spring Clips.....	35
Figure 11. SSTAR Core, Radial Reflector, Control Rod Drivelines, and Control Rod Drives.....	36
Figure 12. Dense Packing of Control Rod Drives Above Upper Closure Head.....	37
Figure 13. SSTAR Upper Closure Head Region.	37
Figure 14. Possible Approach Involving Top Support of SSTAR Vessels from Ledge Inside Seismically-Isolated Reactor Building.....	38
Figure 15. Comparison of the Performance Maps for Axial and Centrifugal S-CO ₂ Compressors.....	45
Figure 16. SSTAR Turbine Bypass Control.	47
Figure 17. SSTAR Inventory Control.	49
Figure 18. Inventory Accumulation in Tank and Tank Pressure for Different Tank Total Volumes.	51
Figure 19. SSTAR Turbine Inlet Valve Control.	53
Figure 20. Combination of Inventory and Turbine Bypass Controls.....	54
Figure 21. SSTAR Temperatures During Load Following for BOC, POC, and EOC with Un-enhanced Radial Expansion Reactivity Feedback Coefficient.	58
Figure 22. SSTAR Temperatures During Load Following for BOC, POC, and EOC with Radial Expansion Reactivity Feedback Coefficient Enhanced by a Factor of Two.	59
Figure 23. SSTAR Temperatures During Load Following for BOC, POC, and EOC with Radial Expansion Reactivity Feedback Coefficient Enhanced by a Factor of Three.	60
Figure 24. Reactor Temperatures under Load Following by Means of Turbine Bypass Control for Un-enhanced (a) and Enhanced (b) Core Radial Expansion Reactivity Feedback Coefficients.	61
Figure 25. Neutron Capture Cross Section for 208Pb from ENDF/B-VI Compared with That for 209Bi.....	69
Figure 26. Neutron Capture Cross Sections for ²⁰⁹ Pb.	70
Figure 27. SSTAR Core Layout Nodalization for Evaluation of ²¹⁰ Po Production – The Core Incorporates Five Enrichment Zones and Two Independent Control Systems.	71

Figure 28. SSTAR ^{210}Po Specific Activity (Bq/(Kg Bi)) versus Time Following Reactor Startup for LBE Coolant and ^{209}Bi Capture Cross Sections from ENDF/B-VI and ENDF/B-V.	73
Figure 29. SSTAR ^{210}Po Total Decay Heat versus Time Following Reactor Startup for LBE Coolant and ^{209}Bi Capture Cross Sections from ENDF/B-VI and ENDF/B-V.	74
Figure 30. Core Configuration of 900 MWt RBEC-M Design.	76
Figure 31. R-Z Benchmark Model of RBEC-M Core.	76
Figure 32. k-effective versus Time for the 1800-Day Cycle.	84
Figure 33. Radial Power Profiles in the Core.	85
Figure 34. Axial Power Profiles in the Core at the Beginning of Cycle.	86
Figure 35. Axial Power Profiles in the Core at the End of Cycle.	86
Figure 36. Flux/Lethargy vs. Neutron Energy at the Beginning of Cycle.	87
Figure 37. Flux/Lethargy vs. Neutron Energy at the End of Cycle.	87
Figure 38. k-effective vs. Time for the 900-Day Cycle.	89
Figure 39. Radial Power Profiles in the Core.	90
Figure 40. Axial Power Profiles in the Core at the Beginning of Cycle.	91
Figure 41. Axial Power Profiles in the Core at the End of Cycle.	91
Figure 42. Flux/Lethargy vs. Neutron Energy at the Beginning of Cycle.	92
Figure 43. Flux/Lethargy vs. Neutron Energy at the End of Cycle.	92
Figure 44. Evolution of k-effective, DIF3D.	95
Figure 45. Evolution of k-effective, TWODANT.	95
Figure 46. Radial Power Profiles in the Core for Subcycle 1.	96
Figure 47. Flux/Lethargy vs. Neutron Energy at the Beginning of Cycle, Time=0 days.	98
Figure 48. Flux/Lethargy vs. Neutron Energy at the End of Cycle, Time=2100 days.	98
Figure 49. Example of Protection Against Inhalation.	112
Figure 50. Shoe Cleaning Machine.	113
Figure 51. Boot Washing Machine.	113
Figure 52. Framework of Modeling System Corrosion Kinetics in Closed Flowing Systems.	121
Figure 53. Part of the Reported Oxide Thickness Data for a Number of Steels Tested in Flowing LBE Loops in the Literature. Long-Term Corrosion Rates Cannot be Obtained from These Results Using the Previous Models.	126
Figure 54. Using the Kinetics Model Developed at LANL and Nonlinear Least Square Fitting, the Majority of the Test Results Can be Collapsed onto One Universal Curve. The Length and Time Scales in This Model Can be Used to Determine the Asymptotic Oxide Thickness and the Long-Term Corrosion Rate of an Individual Steel. There are Still Considerable Scatter and Uncertainties in the Prediction, Highlighting the Need for Longer-Term Tests.	127
Figure 55. (a) Shallow SDP and Deep SDP (Sputter Depth Profile) of PM2000 using XPS.	128
Figure 56. A Comparison Between the Measured Amount of O_2 in the Oxide Layer and a Calculation Based on the Stoichiometric Amount of O_2 in Cr_2O_3 , Fe_2O_3 , Al_2O_3 and Y_2O_3	129
Figure 57. (a) Cross Section of the 14YWT Sample after Exposure to LBE for 600 h at 535 °C. (b) Grain Structure of the Same Material (TEM Image, Un-Exposed).	

	(c) Cross Section of the MA957 Sample after Exposure to LBE for 600 h at 535 °C. (d) Grain Structure of this Material (TEM Image, Un-Exposed). ...	130
Figure 58.	Figures 58a and 58b Present the SEM Image and the Corresponding WDX Line Scan of the As Received HT-9 Material after 600 h Exposure to LBE. Figures 58d and 58e Present the SEM Image and the Corresponding WDX Line Scan of the Laser Peened HT-9 Material after 600 h Exposure to LBE. At both SEM Images, the Nano Indents are Visible. The Area where the Nano Indents were Made (Results are Given in Figures 58c and 58f) are Marked in the SEM Images as Well as the Area where the Line Scans were Made.....	131
Figure 59.	W Coated EP823. a) 100x SEM Image. b) 2000x SEM Image Between Layer and Substrate. c) 2000x W Layer Surface Image. d) SEM/EDX Results Taken at Location b).	132
Figure 60.	Mo coated EP823. a) 500x SEM Image of the Mo/Substrate Interface. b) 2000x SEM Image of the Mo/Substrate Interface. c) 2000x SEM Image of the Mo/Substrate Interface at a Different Location. d) 5000x SEM/EDX Results of Location in Image b) Showing the Cr and O Enrichment in the Interface.	133
Figure 61.	W-Coated HT9. a) 100x SEM Image. b) 2000x SEM Image of the Interface Features Marked in a). c) LBE-Facing Surface of the W Coating. d) A Crack in W Coating. e) SEM/EDX Results of the Area in b).	134
Figure 62.	HT-9 Mo-Coated. a) 100x SEM Image. b) 2000x SEM Image of the Interface Features Marked in a). c) 2000x LBE-Facing Surface of the Mo Coating. d) SEM/EDX Results of the Area in b).	135
Figure 63.	W-Coated 9Cr. a) 100x SEM Image. b) 2000x SEM Image of the Interface. c) 2000x SEM Image of the LBE-Facing Side of the W Layer. d) 2000x SEM Image of the W Layer. Cracks are Visible. e) SEM/EDX Analysis of the Layer Substrate	136
Figure 64.	Mo-Coated 9Cr. a) 500x SEM Image. b) 5000x SEM Image of the Interface. c) 2000x SEM Image of the LBE-Facing Side of the Mo Layer. d) SEM/EDX Analysis of the Layer Substrate Interface.	137
Figure 65.	W-Coated MA957. a) 500x SEM Image. b) 2000x SEM Image the Interface is Shown. c) 2000 x SEM Image the W Surface is Shown. d) SEM/EDX Element Maps of the Interface Between the Coating and Substrate.....	138
Figure 66.	MA957 Mo-Coated. a) 2000x SEM Image of the Interface. b) 2000x SEM Images of the Mo Surface. c) SEM/EDX Line Scan Across the Mo Layer. Cr and O Enrichment Can be Seen.	139
Figure 67.	Fouling Factor versus Oxygen Concentration.....	140
Figure 68.	Fe-Cr Mixing Enthalpy a) Red Line from Ab-Initio Calculations b) Dotted Line from CALPHAD Database.	149
Figure 69.	CALPHAD Phase Diagram for Fe-Cr.	150
Figure 70.	New Phase Diagram (Solid Red Line) as Compared to the Standard Phase Diagram from CALPHAD (Black Dashed Curve).	151
Figure 71.	Formation Energy of <110> and <111> Self-Interstitial Atoms in Pure Fe.	152
Figure 72.	Formation Energy of <110> and <111> Self-Interstitial Atoms in Pure Cr.	153

Figure 73. $\langle 110 \rangle$ and $\langle 111 \rangle$ Self-Interstitial Formation Energy as a Function of Cr Concentration.....	154
Figure 74. Homogeneous Precipitation in a Fe-Cr Sample ($x_{Cr} \sim 20$ at %).	155
Figure 75. Shot Peening and Laser Peening Process (LP) Description. a) The Sample is Protected by an Ablative Layer and an Inertial Tamping Layer b) Laser Pulse Forms High Pressure Plasma on the Surface. The Shock Wave Travels Through the Depth and Plastically Deforms It in Its Wake. [34].	156
Figure 76. T91, HT-9, 316 L, and EP-823 Samples after Laser Peening.	157
Figure 77. Residual-Stress versus Depth for Laser Peened (LP).....	158
Figure 78. Cold-Work Measured in Terms of Full-Width-Half-Maximum (FWHM) for LaserPe ened (LP) and Un-Peened T91 Steel Samples with and without Thermal Treatment.....	159
Figure 79. Residual Stress Measurements for 3 mm Thick 316 L Coupons.	161
Figure 80. Micrographs for 316 L Samples: a) Peened and b) Unpeened. Corresponding EDS Maps for Oxygen, Iron, Chromium and Lead Content in the Sample.	162
Figure 81. HT-9 Micrographs: a) Non-Peened and b) Peened Ssamples.	162

List of Tables

Table 1. Summary of Nuclear Power Growth Scenarios.....	21
Table 2. Conditions and Dimensions for SSTAR.....	40
Table 3. Comparison of Axial and Centrifugal Compressors.....	43
Table 4. SSTAR Reactivity Feedback Coefficients.....	57
Table 5. Conditions for SSTAR Core Assumed for Analysis of ^{210}Po Production	72
Table 6. Temperatures of Physical Zones.....	77
Table 7. Nuclear Densities of Components of Physical Zones.....	78
Table 8. BOC k_{eff} Obtained from Different Codes	83
Table 9. k-effective for 900 MW RBEC, 1800 Days Cycle	83
Table 10. Region Powers and Power Peaking Factors, 1800-Day Cycle	84
Table 11. Volume Averaged Neutron Spectra in the Core, 1800-Day Cycle.....	88
Table 12. k-effective for 900 MW RBEC, 900-Day Cycle	89
Table 13. Region Powers and Power Peaking Factors, 900-Day Cycle	90
Table 14. Volume Averaged Neutron Spectra in the Core, 900-Day Cycle.....	93
Table 15. k-effective Evolution for 900 MW RBEC, 6 Cycles.....	94
Table 16. Region Powers and Power Peaking Factors, 6 Cycles.....	97
Table 17. Volume Averaged Neutron Spectra in the Core, 6 Cycles	99
Table 18. Criticality Comparison.....	100
Table 19. Theoretical/Experimental data for spectral indexes for BFS-77	100
Table 20. Control Rod Worth, BFS-77	101
Table 21. Reported Test Conditions and Durations for Steels in LBE and Pb.....	124
Table 22. Temperature Dependence of K_p , K_r , and x_f	125
Table 23. Partial List of Materials and Conditions to be Included in the Next DELTA Test.....	140
Table 24. T91 Test Matrix for X-ray Diffraction (XRD) Measurements	157
Table 25. Experiment Parameters for Residual Stress Coupons.....	160

Abstract

This report provides an update on development of a pre-conceptual design for the Small Secure Transportable Autonomous Reactor (SSTAR) Lead-Cooled Fast Reactor (LFR) plant concept and supporting research and development activities. SSTAR is a small, 20 MWe (45 MWt), natural circulation, fast reactor plant for international deployment concept incorporating proliferation resistance for deployment in non-fuel cycle states and developing nations, fissile self-sufficiency for efficient utilization of uranium resources, autonomous load following making it suitable for small or immature grid applications, and a high degree of passive safety further supporting deployment in developing nations. In FY 2006, improvements have been made at ANL to the pre-conceptual design of both the reactor system and the energy converter which incorporates a supercritical carbon dioxide Brayton cycle providing higher plant efficiency (44 %) and improved economic competitiveness. The supercritical CO₂ Brayton cycle technology is also applicable to Sodium-Cooled Fast Reactors providing the same benefits. One key accomplishment has been the development of a control strategy for automatic control of the supercritical CO₂ Brayton cycle in principle enabling autonomous load following over the full power range between nominal and essentially zero power. Under autonomous load following operation, the reactor core power adjusts itself to equal the heat removal from the reactor system to the power converter through the large reactivity feedback of the fast spectrum core without the need for motion of control rods, while the automatic control of the power converter matches the heat removal from the reactor to the grid load. The report includes early calculations for an international benchmarking problem for a LBE-cooled, nitride-fueled fast reactor core organized by the IAEA as part of a Coordinated Research Project on Small Reactors without Onsite Refueling; the calculations use the same neutronics computer codes and methodologies applied to SSTAR. Another section of the report details the SSTAR safety design approach which is based upon defense-in-depth providing multiple levels of protection against the release of radioactive materials and how the inherent safety features of the lead coolant, nitride fuel, fast neutron spectrum core, pool vessel configuration, natural circulation, and containment meet or exceed the requirements for each level of protection. The report also includes recent results of a systematic analysis by LANL of data on corrosion of candidate cladding and structural material alloys of interest to SSTAR by LBE and Pb coolants; the data were taken from a new database on corrosion by liquid metal coolants created at LANL. The analysis methodology that considers penetration of an oxidation front into the alloy and dissolution of the trailing edge of the oxide into the coolant enables the long-term corrosion rate to be extracted from shorter-term corrosion data thereby enabling an evaluation of alloy performance over long core lifetimes (e.g., 30 years) that has heretofore not been possible. A number of candidate alloy specimens with special treatments or coatings which might enhance corrosion resistance at the temperatures at which SSTAR would operate were analyzed following testing in the DELTA loop at LANL including steels that were treated by laser peening at LLNL; laser peening is an approach that alters the oxide-metal bonds which could potentially improve corrosion resistance. LLNL is also carrying out Multi-

Scale Modeling of the Fe-Cr system with the goal of assisting in the development of cladding and structural materials having greater resistance to irradiation.

1. Executive Summary

This report documents research and development carried out during FY 2006 directed at assessment of viability and development of a pre-conceptual design for the Small Secure Transportable Autonomous Reactor (SSTAR) Lead-Cooled Fast Reactor (LFR) concept. Development of SSTAR has been focused on a small, modular proliferation-resistant reactor for international deployment suitable for small grid applications. A 20 MWe (45 MWt) concept has been developed in previous fiscal years under ongoing LFR System Design and Evaluation at ANL and has been further refined and analyzed during FY 2006. SSTAR is a small, proliferation-resistant, fissile self-sufficient, autonomous load following, and passively safe exportable LFR for deployment at remote sites. Customers of SSTAR include: i) clients looking for energy security at small capital outlay; ii) cities in developing nations; and iii) deregulated independent power producers in developed nations. The SSTAR pre-conceptual design integrates three major features: natural circulation heat transport; lead (Pb) coolant; and transuranic nitride fuel. Conversion of the core thermal energy to electricity is accomplished using a supercritical carbon dioxide (S-CO₂) Brayton cycle energy converter providing higher plant efficiencies and lower balance of plant costs than the traditional Rankine steam cycle operating at the same reactor core outlet temperature. The SSTAR pre-conceptual design can be scaled up to 181 MWe (400 MWt) for a reactor plant (STAR-LM) providing efficient electricity supply for growing cities with optional production of desalinated water using a portion of the reject heat.

The interest in higher plant efficiencies has heretofore driven interest in operation of SSTAR at higher Pb temperatures. In particular, a peak cladding temperature of 650 °C has been used as a goal. At this temperature, a reactor core outlet temperature of 564 °C is achieved resulting in a Brayton cycle efficiency of 44.2 % and a net plant efficiency of 43.8 %. It has always been recognized that this would require the development of cladding and structural materials for long-term service in Pb coolant up to 650 °C peak cladding temperature with corrosion protection provided by active maintenance and control of the dissolved oxygen potential in the coolant giving rise to the formation of protective oxide layers on the steel cladding and structures.

This need for materials development has heretofore been consistent with the guidance of the Generation IV Nuclear Energy Systems Initiative that supported research and development on the viability of advanced reactor concepts for deployment in a 2025 to 2030 time frame. With the advent of the Global Nuclear Energy Partnership (GNEP) in 2006, the focus of LFR development is shifting towards the development of a near-term deployable LFR test demonstrator and a near-term deployable small LFR for international deployment. Both the test demonstrator and exportable small LFR would operate at lower temperatures enabling the use of existing materials such as T91 ferritic/martensitic (F/M) stainless steel that is already incorporated into the ASME codes or HT9 F/M stainless steel. These materials have been shown to have corrosion resistance to lead-bismuth eutectic with active oxygen control at temperatures below about 550 °C in experiments carried out in the DELTA loop at Los Alamos National

Laboratory (LANL) and elsewhere. The peak cladding temperature in the near-term deployable LFRs would therefore be no higher than about 550 °C. A significant portion of the work during FY 2006 has been carried out to support a transition to near-term deployable liquid metal reactors and also to support elements of the GNEP.

The LFR concept directly supports the nonproliferation aims and the reactors for international deployment element of GNEP. The fissile self-sufficient LFR with a conversion ratio of unity represents an alternative option for management of actinides whereby LFRs such as SSTAR securely store the actinides in an operating power reactor for 30 years and then return them to the supplier when the core is reprocessed at the end of its lifetime. The nonproliferation features of SSTAR which include restricted access to fuel and a 30-year core lifetime reduce the concerns about deploying SSTARs in non-fuel cycle states thereby supporting the nonproliferation goals of GNEP.

In this report, a preference has been given to the use of the terms, “reactor for international deployment,” and “exportable reactor,” rather than “small reactor,” in recognition that a major objective is viable deployment in non-fuel cycle states and developing nations of reactors that meet nonproliferation goals while enabling the sustainable growth of large amounts of nuclear power to meet projected demands for energy. Development of SSTAR has always been driven by the requirement to fill a perceived need for an exportable long core life fast reactor for international deployment.

The present report includes a review of the rationale for fast reactors for international deployment and the current status of efforts on small and medium size reactors which may be considered for international deployment. Here, the IAEA definitions of small and medium size have been adopted whereby small reactors have electrical powers between 0 and 300 MWe while medium size reactors cover the range, 300 to 700 MWe. The rationale is as follows. Meeting future worldwide projected energy demands during this century (e.g., 1000 to 2000 GWe by 2050) in a sustainable manner while maintaining CO₂ emissions at or below today’s level will require massive deployments of nuclear reactors in non-fuel cycle states as well as fuel cycle states. The projected energy demands of non-fuel cycle states will not be met solely through the deployment of Light Water Reactors (LWRs) in those states without using up the world’s resources of fissile material (e.g., known plus speculative virgin uranium resources = 15 million tonnes). Thus, there shall be a need to deploy fast reactors in non-fuel cycle states. For those deployments, it is expected that long core lifetime fast reactor converters which are fissile self-sufficient by creating as much fissile material as they consume shall be preferred to breeders that create more fissile material than they consume on the basis of meeting non-proliferation aims.

The report provides a description of the configuration and features of the SSTAR reactor. Three-dimensional computer aided design (CAD) drawings illustrating the current configuration of SSTAR are included in the report. The reactor vessel (12 meters height by 3.23 meters diameter) has a large height-to-diameter ratio reflecting the fact that SSTAR is a natural circulation reactor in which heat is removed from the core at all power levels up to and exceeding 100 % nominal power by natural circulation. The Pb

flows upward through the core which is an open-lattice of large-diameter (2.5 centimeter) fuel pins arranged on a triangular pitch. The core does not incorporate removable fuel assemblies as one means of restricting access to the fuel. Instead, the whole core is a single removable assembly with a long core lifetime of 30 years. The coolant volume fraction in the core is large reducing the frictional pressure drop and enhancing natural circulation. This feature is feasible with Pb coolant which has a relatively low absorption of neutrons compared with other liquid metals such as sodium. Each fuel pin incorporates a cylindrical cladding containing a layer of silicon-enhanced ferritic/martensitic steel for corrosion resistance on a substrate of ferritic/martensitic steel for irradiation stability. The cladding surrounds transuranic nitride fuel pellets and molten Pb as a bond between the pellets and cladding to minimize the thermal resistance of the pellet-cladding gap. The Pb coolant exiting the core flows upward through a chimney above the core formed by a cylindrical shroud. The coolant flows radially through flow openings near the top of the shroud and enters four modular Pb-to-CO₂ heat exchangers installed between the reactor vessel and cylindrical shroud. Inside each heat exchanger, the Pb flows downward over the exterior of tubes through which the CO₂ flows upwards. The Pb exits the heat exchangers and flows downward through an annular downcomer to enter flow openings in a flow distributor head beneath the core.

During FY 2006, the SSTAR plant pre-conceptual design has been refined with respect to both the reactor configuration and the S-CO₂ Brayton cycle energy converter. One way in which the pre-conceptual design of the reactor system has evolved has been identification of the need to incorporate a thermal baffle to protect the reactor vessel in the vicinity of the Pb free surface from the effects of thermal stresses resulting from exposure to Pb from the riser region above the core (nominally at the core outlet temperature) during thermal transients as occur during startup and shutdown. A thermal baffle has been incorporated into the pre-conceptual design. The baffle consists of a cylindrical barrel welded to the reactor vessel at an elevation below the tops of the shells of the Pb-to-CO₂ heat exchangers and extending upwards to nearly the bottom surface of the upper closure head. The annular space between the baffle and the reactor vessel inner surface remains filled with argon cover gas thermally insulating the reactor vessel from the Pb interior to the baffle. During shutdown and startup, the Pb temperature in the upper plenum varies between the nominal core outlet temperature of 564 °C and the core inlet temperature of 420 °C which is the nominal temperature at which the coolant is maintained during shutdown. Work was also carried out on optimally locating control rods and control rod guide tubes uniformly throughout the core and the feasibility of accommodating the control rod drivelines in the riser above the core and the drives in the available space above the upper closure head. The control rod guide tubes in the core are structures to which grid spacers are welded; the grid spacers hold and maintain spacing between the fuel pins located in the vicinity of each control rod guide tube.

The S-CO₂ Brayton cycle is a significant feature of SSTAR. It is also a technology that is applicable to sodium-cooled fast reactors to enhance the plant efficiency and improve the plant economic competitiveness. Significant improvements have been made to the pre-conceptual design for the SSTAR S-CO₂ Brayton cycle energy converter. The pre-conceptual design was originally developed with axial flow compressors and an axial

flow turbine based upon previous experience with axial flow steam turbines. The axial flow compressors have been replaced by centrifugal (radial flow) compressors that provide the benefits of a wider operating range, better stability during operation near the critical point, and a better capability to handle two-phase flow that might develop during certain accidents. The S-CO₂ Brayton cycle pre-conceptual design with centrifugal compressors was optimized and the cycle efficiency calculated. The efficiency is essentially the same or slightly better than with axial compressors. Significantly, fewer stages are required with centrifugal compressors. Fewer stages contributes to the wider operating range of the centrifugal compressors relative to axial compressors. Wider range here means principally a wider regime of flowrates between stall at the low end of flowrate and choking at the high end of flowrate. Significantly fewer stages also potentially contributes to a lower compressor cost for radial compressors relative to axial compressors. However, actual cost estimates for centrifugal and axial compressors need to be performed to investigate this point. Off-design performance maps calculated for the centrifugal compressors confirm the wider operating range relative to the previous axial pre-conceptual designs.

A control strategy was developed for the SSTAR S-CO₂ Brayton cycle whereby the cycle is automatically controlled such that the heat removal from the in-reactor Pb-to-CO₂ heat exchangers matches the generator load from the electrical grid. This strategy enables autonomous load following by the reactor whereby the core power adjusts itself due to inherent feedbacks such that the core power matches the heat removal from the Pb-to-CO₂ heat exchangers. It is not necessary for the reactor core power to be changed through the operation of control rods. The S-CO₂ Brayton cycle control strategy for SSTAR involves inventory control and turbine bypass control for grid loads between 35 and 100 % nominal and turbine bypass control between 0 and 35 % nominal load. In the inventory control approach, CO₂ is removed from the circuit in response to a decrease in load demand and added to the circuit in response to a load demand increase. Removing or adding CO₂ decreases or increases the CO₂ density decreasing or increasing the CO₂ mass flowrate, respectively. This has the effect of reducing or raising the rate of energy transport by the CO₂ while tending to maintain the CO₂ temperatures around the circuit which tends to maintain the cycle efficiency. Thus, inventory control is attractive as a means of maintaining high cycle efficiencies at reduced load demands. It requires the addition of inventory control tanks into which CO₂ is withdrawn from the cycle or returned to the cycle by means of opening and closing valves located in the high and low pressure portions of the cycle. In turbine bypass control, a portion of the CO₂ flow is made to bypass the high temperature recuperator, Pb-to-CO₂ heat exchangers, and the turbine by opening a valve connecting the high and low pressure CO₂ streams. This reduces the flow of heated CO₂ entering the Pb-to-CO₂ heat exchangers thereby reducing the rate of heat removal from the reactor. It also reduces the CO₂ flow entering the turbine reducing the work performed by the turbine and, hence, the power produced in the generator. In principle, the control strategy enables autonomous load following over this complete operating range. The incorporation of centrifugal compressors widens the range over which inventory control can be used.

The autonomous load following of the SSTAR core depends upon the values of the reactivity feedback coefficients for fuel Doppler, axial expansion, coolant density, and core radial expansion. It is the large feedback of the fast spectrum core with nitride fuel and lead coolant that enables autonomous load following. Reactivity feedback coefficients were calculated for the 30-year lifetime core during FY 2006. A steady state analysis of autonomous load following revealed that autonomous load following would not be feasible with the as-calculated coefficients because the coolant density coefficient is too large relative to the other three coefficients. This situation can be remedied by enhancing the radial expansion of the core by a factor of two or more; such an enhancement can be achieved by means of mechanical design. Thus, the need for such a mechanical design feature to enhance the core radial expansion was identified and enhancement of the core radial expansion reactivity feedback coefficient by a factor of two has been assumed in analyses. A simple example of a mechanical device that can enhance the core radial expansion feedback is the incorporation of grid spacers having a higher coefficient of thermal expansion than the mainly ferritic/martensitic cladding. The grid spacer material must be compatible with Pb at the core temperatures and have sufficient irradiation stability.

Development of a new transient fuel pin design computer code was initiated at Argonne National Laboratory (ANL) during FY 2006. The motivation for this new development was the realization that it may be feasible to reliably calculate the long-term wastage of cladding from analysis of shorter-term data on exposure of alloys to heavy liquid metal coolants based upon data analysis using modeling of the type carried out by Ning Li and his colleagues at LANL. Thus, the new ANL code integrates together time dependent fission gas release over the fuel pin height dependent upon the local peak fuel temperature and burnup, fission gas pressure dependent upon the cumulative gas release plus initial fill gas and temperature, local thermal creep of the cladding represented by the time to rupture as a function of the stress, the local thickness of unoxidized cladding remaining dependent upon the simultaneous penetration of an oxide layer into the cladding metal and dissolution of the oxide layer trailing surface by the heavy liquid metal coolant, and a cumulative damage fraction to evaluate the cladding creep damage and failure. Further development of the code will account for the fact that in the SSTAR core the locations of the fuel pins experiencing the peak power, temperature, and burnup migrate inward with time such that the time history of power and burnup must be input based upon neutronics analysis. It is envisioned that the code shall be used to determine the required initial cladding thickness that shall enable all of the fuel pins to survive the core lifetime at the calculated thermal hydraulic conditions. This new model shall be particularly useful to the development of concepts for a near-term deployable demonstration test reactor and a near-term exportable LFR during FY 2007.

The report presents the SSTAR safety design approach which is based upon the defense-in-depth principle of providing multiple levels of protection against the release of radioactive materials by means of: 1) design to achieve a high level of reliability such that specific accident initiators are eliminated or accident initiators are prevented from occurring; 2) provision of protection in the event of equipment failure or operating error; and 3) provision of additional protection of the public health and safety in an extremely

unlikely event that is not expected to occur during the lifetime of the plant or which was not foreseen at the time that the plant was designed and constructed. The inherent safety features of SSTAR take advantage of the key inherent properties of Pb coolant, transuranic nitride fuel, and a fast neutron spectrum core together with specific design options including a pool reactor vessel containing all major primary coolant system components and natural circulation heat transport. Important inherent properties of Pb coolant which provide and enhance safety are the high boiling temperature of about 1740 °C which is well above the temperatures at which stainless steels structures lose their strength and melt, the lack of chemical reaction of Pb with the CO₂ working fluid, the low absorption of neutrons by Pb, and the heavy Pb density that limits void growth and downward penetration following a heat exchanger tube rupture. Lead also does not react vigorously with water or air. Experiments carried out at the Forschungszentrum Karlsruhe have shown that iodine, cesium, and cesium-iodide (i.e., fission products with low melting and boiling points) are absorbed and immobilized by lead-bismuth eutectic at temperatures of 400 and 600 °C. Cesium forms inter-metallic compounds in LBE while iodine forms PbI₂.

Transuranic nitride fuel offers a number of potential benefits provided that it can be demonstrated to perform suitably well in steady state and transient irradiation tests and can be reliably manufactured to meet the performance requirements. Inherent favorable properties of the nitride fuel are the high thermal conductivity which when combined with bonding to the cladding by liquid Pb reduces the peak fuel temperatures during normal operation and accidents reducing stored energy in the fuel, the high transuranic nitride decomposition temperature estimated to exceed 1350 °C, compatibility with the cladding materials, low volumetric swelling per unit burnup, and low fission gas release per unit burnup.

The report discusses how the inherent safety features as well as passive and active safety systems of the SSTAR pre-conceptual design enable SSTAR to meet the objectives of the defense-in-depth approach.

Researchers in Italy currently involved in development of the European Lead-cooled System (ELSY) LFR for waste transmutation have previously calculated that if lead-bismuth eutectic (LBE) is used as the coolant, then the ²¹⁰Po isotope generated in the coolant as a result of neutron capture in ²⁰⁹Bi and ²⁰⁸Pb inside and in the vicinity of the core could contribute a significant heat source in the bulk of the coolant rivaling the decay heat power in the fuel from fission products. The use of LBE is an option for a near-term deployable demonstration test reactor or LFR for international deployment due to the lower melting temperature (125 °C) of LBE relative to Pb (327 °C). An investigation was carried out to estimate the ²¹⁰Po heat source that would exist in the coolant of a SSTAR utilizing LBE instead of Pb as the coolant. Existing neutronics results for an earlier 20-year lifetime 45 MWt core were used. It was found that the total heat source from ²¹⁰Po is estimated to be only 36 KW or less which is equivalent to only 0.08 % of the nominal 45 MWt core power. The heat source is dependent upon the coolant volume fraction in the core and the ratio of the activation coolant volume to the total coolant volume. The result is at odds with the results of the Italian researchers.

ANL is participating in an international neutronics benchmark analysis for a lead-cooled fast reactor, which is being performed under an International Atomic Energy Agency (IAEA) Coordinated Research Project (CRP) on “Small Reactors without On-site Refueling.” The main purpose of this benchmark analysis is to provide a forum to inter-compare the performance of different codes and nuclear data libraries used in designing fast reactors with lead-based coolants and mixed nitride fuels. The benchmark is based on the core of the RBEC-M reactor, which is a 900 MWt lead-bismuth cooled, mixed nitride-fueled fast reactor concept developed by the Russian Research Center Kurchatov Institute (RRC KI). Other participants in the benchmark include the Tokyo Institute of Technology, the RRC KI, OKB Gidropress, as well as Belgium and Indonesia. An initial set of calculations for the benchmarking analysis which consists of three problems was carried out at ANL using the same neutronics computer codes and methodologies that have been applied to SSTAR and other LFRs at ANL.

A review was undertaken of the health effects of lead and bismuth, U.S. regulations for protecting workers from lead hazards, as well as examples of industrial and construction practice for working with lead. U.S. regulations for protecting workers from lead hazards, or analogous regulations in other nations, have not impeded the charging, startup, operation, or modification of any LBE or lead experiment loops or facilities. Additional regulations to protect against the effects of radioactivity with lead or lead-bismuth coolant were not addressed. The initial results of the review demonstrate that regulations and procedures for protecting industrial and construction workers from the health hazards of lead are well established and routinely implemented. The review has not identified any regulations that would be expected to significantly impact the initial startup, operation, or decommissioning and decontamination of a LFR.

A database on corrosion of alloys by liquid metal coolants was constructed at Los Alamos National Laboratory (LANL) and a systematic analysis was initiated of reported corrosion test data from around the world using a new oxidation and corrosion kinetics model developed at LANL. This work was also supported by the Advanced Fuel Cycle Initiative (AFCI). The evolution of the thickness of the oxidized alloy layer is assumed to follow a simple model involving penetration of an oxidation front into the metal limited by parabolic kinetics and simultaneous dissolution of the trailing edge of the oxide layer by the heavy liquid metal coolant limited by linear kinetics. By fitting data to the nonlinear solution for the oxide layer thickness versus time, values can be extracted for the parabolic and linear rate constants. In particular, the linear rate constant for dissolution of the oxide layer provides the long-term corrosion rate of the alloy. Thus, by systematically applying the model solution to shorter-term corrosion data, it is possible to extract the long-term corrosion rate. Rate constants were obtained for twenty-four different alloys, each at a constant temperature. In this manner, it was found that the long-term corrosion rate for HT9 ferritic/martensitic (F/M) stainless steel at 550 °C is large, probably precluding its usage over long lifetimes such as 30 years at this temperature. In contrast, the silicon-enhanced Russian F/M steel, EP-823, has a long-term corrosion rate at 470 °C that is smaller by nearly two orders of magnitude.

Analysis was carried out of a number of alloy specimens with special treatments or coatings for the purpose of investigating possible approaches to enhancing corrosion resistance and that were exposed to flowing LBE in the DELTA loop at LANL. These included Al-rich oxide dispersion-strengthened steels; laser-peened (at LLNL) HT9, T91, EP-823, and 316L; and W- and Mo-coated F/M steels. Materials were prepared for future testing in the DELTA loop during FY 2007. The new specimens shall be partially coated with Al_2O_3 which is resistant to heavy liquid metal such that one can directly measure the extent of corrosion instead of the oxide thickness.

Lawrence Livermore National Laboratory (LLNL) has maintained continuing contact with the European Union European Lead-cooled System (ELSY) program to develop a LFR for transmutation of waste. It is planned to carry out design of an ELSY concept in sufficient detail during the next two years such that cost estimates can be independently carried out by two commercial companies. Based upon the results of the cost estimates, a decision to proceed with further development and construction may be made in 2008. LLNL also has an ongoing cooperation with the Japan Central Research Institute of the Electric Power Industry (CRIEPI) and continues to monitor the proposal for Toshiba to provide a 4S small modular sodium-cooled fast reactor to the town of Galena, Alaska, as a demonstration of a long lifetime core fast reactor for use in remote areas.

A highlight of the LLNL material work has been investigation of the application of laser peening technology and preparation of laser peened samples for testing in the DELTA loop at LANL. The laser peening process generates a state of compressive stress near the surface that alters metal-oxide bonds at the surface and may thereby affect the corrosion rate. Samples of HT9, T91, and EP-823 F/M steels and 316L austenitic stainless steel were laser peened and measurements were carried out to determine residual stress levels. Samples were then exposed to flowing LBE in the DELTA loop.

LLNL has also been carrying out Multi-Scale Modeling of Materials (MMM) focusing on the Fe-Cr system. LLNL has unique tools for studying point defect interaction using the full potential of LLNL's massively parallel super-computing resources. Use is made of atomistic information as input to the meso-scale, and to couple the meso-scale Dislocation Dynamics methodology to Quasi-continuum and other multi-scale methods to produce an "Integrated Modeling Platform" that connects to polycrystal plasticity studies. This work is at the forefront of research in the mechanical properties field. A goal of this work is to assist in the development of materials having greater resistance to irradiation. The MMM approach may provide insights that lead to a better understanding of the variables that control the processes of material degradation under irradiation. If these variables can be identified, then perhaps the degradation processes can be reduced resulting in materials with improved performance under irradiation.

2. Argonne National Laboratory – SSTAR/LFR Development

2.1. Rationale for Fast Reactors for International Deployment

Development of SSTAR has always been driven by the capability to fill a perceived need for a fast reactor for international deployment. It is therefore useful to begin by reviewing the rationale for exportable fast reactors and the current status of efforts on small reactors which may be considered for export.

Fast Reactors Shall Need to be Deployed Outside of Fuel Cycle States if Projected Energy Demands Are to be Met

At the 2006 ANS Meeting in Reno, Vic Reis presented a slide stating two simultaneous goals for GNEP: 1) Lots of Nuclear Power (1000 ~ 2000 GW by 2050); and 2) Reduced Proliferation Risk. Large increases in nuclear generation capacity are currently envisioned to help meet future projected worldwide energy demands. The present U.S. policy is focused upon domestic deployment of large-scale light water reactors (LWRs) and sodium-cooled fast spectrum Advanced Burner Reactors (ABRs) working in a symbiotic relationship that burns existing fissile material while destroying the actinides that are generated. Other major nuclear nations are carrying out the development and deployment of Sodium-Cooled Fast Reactor (SFR) breeders as witness the planning for SFR breeder deployments in France, Japan, China, India, and Russia. However, global nuclear deployments of this level will be insufficient to stem increasing greenhouse gas emissions as developing nations massively increase in both population and in energy use per capita. If nuclear were to contribute significantly to greenhouse gas mitigation, growth in the range of 16000 GWe or more by 2050 would be required to reduce CO₂ emissions to one-half the current level by 2100 (Table 1). Under this level of growth, fissile mass becomes a limiting factor and fast reactors of moderate to high conversion ratio must attain a significant market share. This introduces an institutional challenge – how to simultaneously meet energy needs while avoiding exacerbating proliferation hazards. An architecture based on centralized fuel cycle operations sited at a few locations worldwide (including co-sited high performance Sodium-Cooled Fast Reactors dedicated to fissile production) supporting fleets of long refueling interval reactors at distributed customer sites has been proposed to solve this energy security/nonproliferation dilemma [1 and 2]. Both the Global Nuclear Energy Partnership (GNEP) and Regional Fuel Cycle Center architectures currently under study incorporate the features of this institutional structure.

Table 1. Summary of Nuclear Power Growth Scenarios

Goal	Nuclear Market Share by 2100, %	Nuclear Power by 2100, TWt	100-year Growth Rate, % per year
Maintain Market Share*	6**	3.18 (~ factor of 3 increase)	1.2
Cap Fossil at Current Absolute Level	75	39.8 (~ factor of 40 increase)	3.68
Reduce Fossil to ½ Current Absolute Level by Manufacture H ₂ at $\eta = 0.5$ for 2/3 of Primary Market	144	76.3 (~ factor of 75 increase)	4.34

*Assumes world primary energy growth at 1.2 % per year from 16 TWt to 53 TWt over a 100-year period (53 TWt would support 10 Billion people at 4 tonnes of oil equivalent per capita)

**Current nuclear market share is ~ 6 % of the total primary energy of 16 TWt.

The Regional Fuel Cycle Center architecture (Figure 1) involves centralized regional fuel cycle centers with facilities for enrichment, recycle, fabrication, and waste management co-sited with large breeder reactors sized to take advantage of economy-of-scale. The regional fuel cycle centers provide services to distributed power plants at customer sites. The distributed power plants may include a variety of reactor types determined by market forces: light water reactors (LWRs) and high temperature gas reactors (i.e., thermal spectrum reactors) and Secure Transportable Autonomous Reactors (STARs) (fast spectrum converter reactors) of small to medium power rating and long refueling interval. Breeder reactors are sited only at regional fuel cycle centers.

LWRs are proven technology and are available in the near term; they are an inevitable component of the evolving mix of reactor designs. Their initial ore requirement per GWt deployed is small but their lifetime consumption of ore is considerable. Distributed STARs are designed for the international deployment market. They are “right sized” for initially small but fast growing electric grids. They provide energy security by virtue of a long (15- to 30-year) refueling interval for nations which don’t want the expense of an indigenous fuel cycle and waste repository infrastructure and will accept the guarantees of service from a regional fuel cycle center. Because of the long refueling interval, shipping of fuel is carried out infrequently in large (15- to 30-year core cassette) discrete batches simplifying item accountancy. STARs require a very large initial fissile working inventory but their one-time initial loading of fissile is actually less than a LWR’s lifetime consumption of ²³⁵U for the same energy delivery. Most significantly, once loaded, they are fissile self-sufficient having a conversion ratio (CR) ~ 1.0. STARs

provide an alternative approach to actinide management in which actinides are “stored” in long core lifetime operating power reactors instead of being transmuted in ABRs.

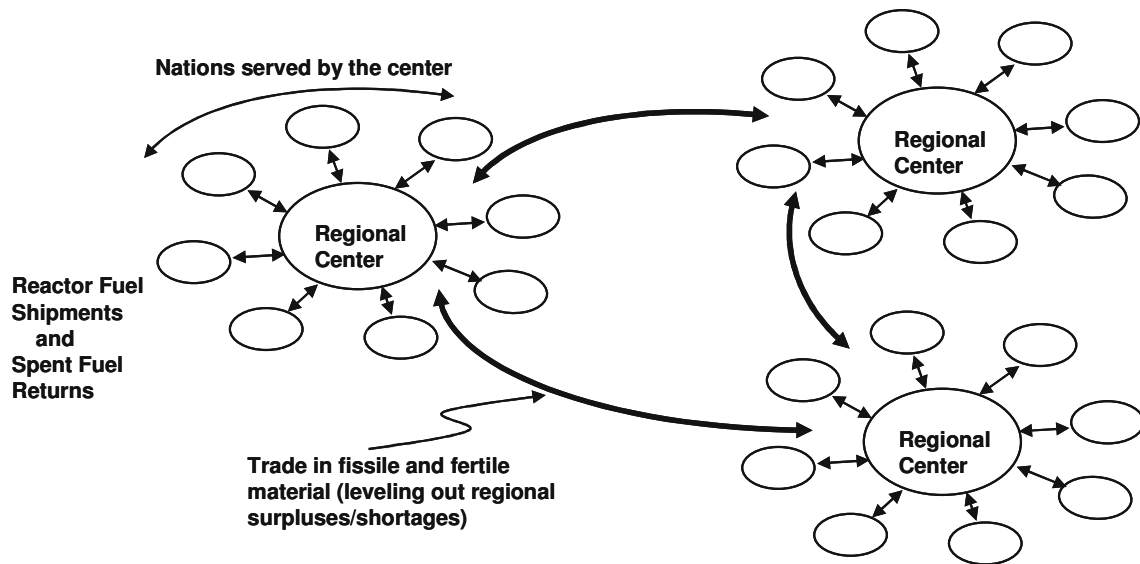


Figure 1. Illustration of Regional Fuel Cycle Center Architecture.

France provides a good indication of what future fast reactor options could end up looking like if alternative fast reactors for international deployment are not developed. The French are planning to replace their current fleet of LWRs with a fleet of European Pressurized Reactor (EPR) passively safe 1600 MWe large-scale PWRs which shall, in turn, be gradually replaced by large-scale SFR breeders initially operating at the same time. Deployment of EPRs has started and a new SFR to be developed by CEA is planned to begin operation in 2020. Thus, large-size SFRs may be the only fast reactor products available for export. The Japanese (JAEA) are similarly developing the 1500 MWe large-scale Japan Sodium Fast Reactor (JSFR). Such reactors could raise proliferation concerns if they were to be offered for export to non-fuel cycle states. If a goal is to avoid the deployment of large-scale SFRs in non-fuel cycle states but fast reactor deployments in such states are unavoidable if the world’s fissile resources are not to be consumed in LWRs or other thermal spectrum reactors, then development of suitable proliferation-resistant, alternative exportable fast reactors is essential.

Some Vendors Are Preparing for the Development of a Global Market for Exportable Small and Medium Size Reactors – “Right Sized” for Developing Nation Markets and Supported by Fuel Cycle and Management Services from the Supplier

The IAEA defines small reactors as reactors with power levels between 0 and 300 MWe while medium size reactors have power levels between 300 and 700 MWe.

- PBMR (Pty.) Ltd. (Eskom and its partners) are positioned to respond to any near-term market need for small exportable reactors with their PBMR. The first PBMR is on track with pouring of concrete scheduled to begin in 2007. However, the PBMR is not a fast reactor and could not be operated as a converter.
- Toshiba and CRIEPI have assessed the development of a potentially enormous market for exportable small reactors with a long refueling interval. They have developed their 4S small sodium-cooled fast reactor for this market. They are hoping to jump start development and deployment of 4S beginning with a 4S for the town of Galena on the Yukon River in Alaska. The Galena 4S reactor project is proceeding ahead; pre-application meetings with the U.S. NRC are in progress.
- Rosatom recently made a decision to proceed down a path of accelerated development of the SVBR-75/100 (**Lead-Bismuth Fast Reactor** with power level between **75** and **100** MWe depending upon the Rankine steam cycle conditions), transportable, 7- to 10-year refueling interval lead-bismuth eutectic-cooled fast reactor based on the oxide-fueled Alfa submarine reactor technology. If funded aggressively, this could lead to beginning construction of a SVBR-75/100 two years from now and initial operation in 2013. Available information indicates that the current level of funding is very limited.
- Development of the European Lead-cooled System (ELSY) 600 MWe Pb-cooled fast reactor for waste transmutation began in September 2006. The ELSY project is being funded at a total of 7.16 Million Euros for three years of which 2.95 Million Euros is from the European Commission and the remainder from Italy. The first two years of the project are focused upon demonstrating technical feasibility of a Lead-Cooled Fast Reactor (LFR) design that is less costly than Sodium-Cooled Fast Reactors and possibly even less costly than LWRs. If successful in achieving cost competitiveness relative to SFRs, the project shall consider a test demonstrator and continuing development of ELSY may be heavily funded by industry and commercial investors similar to PBMR. Although it shall likely be significantly smaller in power level, ELSY may be viewed as the non-French European fast reactor reply to the new SFR being developed in France by CEA.
- The Russians are building a KLT-40S barge-mounted PWR at Severodvinsk. The KLT-40S was developed by OKBM in Nizhny Novgorod, the Russian Research Center “Kurchatov Institute,” and CKB “Aisberg” based upon icebreaker reactor technology. The KLT-40S was developed from an existing icebreaker propulsion reactor but with the addition of new passive systems. Each barge houses two KLT-40S reactors plus fuel storage. Two reactors provide up to 70 MWe total of electrical power; each reactor has a thermal power of 150 MWt. The fuel

type is uranium metal with zirconium cladding; the U enrichment is limited to 18 %. The Russians are now developing a new class of icebreakers using KLT-40Ss for propulsion. A license for the KLT-40S NPP to be constructed at Severodvinsk has been granted by Gosatomnadzor (the Russian regulatory body). Construction is expected to begin in 2006. Part of the purpose of the first KLT-40S NPP is to “prove” the reactor design and operation. The Russians are also considering constructing another KLT-40S NPP for a town located on the shore of the “Northern Icy Ocean” but this is only under consideration. The KLT-40S is a modular design in that the core is located in one reactor vessel while the steam generators and main coolant pumps are located in separate vessels connected with short nozzles without long pipelines. A noncondensable gas pressurizer is connected to the reactor vessel via a pipeline. A flow restrictor with a 25 mm diameter limits the coolant loss rate, in the event of a pipeline break. The KLT-40S is a thermal reactor and could not be operated in a converter mode.

- The International Reactor Innovative and Secure (IRIS) is being developed by an international consortium including Westinghouse. However, IRIS is a PWR and could not be operated as a converter.

What Are Some Desirable Features of Exportable Fast Reactors?

- Proliferation resistance is clearly the major priority and is reflected in the first few features:
- Restricted access to fuel.
- Long core life further restricting access by reducing or eliminating the need for refueling.
- Restricted potential to be misused in a breeding mode.
- Fuel form that is unattractive in the safeguards sense.
- Conversion ratio of unity to self-generate as much fissile material as it consumes.
- Small power level to match the smaller demand of towns or sites that are off-grid or on immature local grids.
- Low enough cost to be economically competitive with alternative energy sources available to developing nation customers such as diesel generators in remote locations.
- Readily transported and assembled from transportable modules.
- Simple to operate and highly reliable reducing plant operating staff requirements.

- High reliability and passive safety reducing the number of accident initiators and need for safety systems as well as reducing the size of the exclusion zone.

Example of SSTAR Lead-Cooled Fast Reactor (LFR) – Accomplishment of Generation IV R&D

- The Small Secure Transportable Autonomous Reactor (SSTAR) LFR was developed under the Generation IV Nuclear Energy Systems Initiative as an modular fast reactor for international deployment concept at the low power end of the spectrum at 19.7 MWe (45 MWt). As such, it could meet the electricity requirements of a town with a population of about 25000. It can be scaled-up to 181 MWe (400 MWt) for highly efficient electricity production for a city of about 225000. Some key features of SSTAR are:
- Pb coolant and transuranic nitride fuel with which a conversion ratio of unity can be achieved but which cannot support as large a breeding ratio or short doubling time as Na coolant making the Pb system less attractive for clandestine or other use in a breeding mode;
- Pb coolant which allows simplification of the reactor system through elimination of the intermediate coolant circuit; eliminates the potential for vigorous interactions of the coolant with the CO₂ working fluid, water, or air, enables the coolant volume fraction to be enlarged due to the low neutron absorption by Pb reducing the core pressure drop such that natural circulation heat transport is possible at power levels exceeding 100 % nominal eliminating the need for main coolant pumps – All of these features enhance plant reliability and simplify plant operation;
- Thirty-year lifetime compact open-lattice core which is a single cassette without removable individual fuel assemblies enhancing proliferation resistance – the entire core is replaced as a whole cassette after the 30-year life at which time refueling equipment is temporarily brought onsite, the core cassette is replaced, the used cassette is installed in a shipping cask for transport to a secure fuel cycle support center in a fuel cycle state, and the refueling equipment is removed;
- Transuranic fuel which is reprocessed and fabricated with incomplete fission product removal rendering the fuel self-protective in a safeguards sense;
- Average (peak) discharge burnup of 81 (131) MWd/Kg of Heavy Metal;
- Burnup reactivity swing < 1 \$ reducing the requirement for excess reactivity and the amount of reactivity insertion accompanying the unintended withdrawal of one or more control rods thereby enhancing passive safety;
- Autonomous load following due to the strong reactivity feedbacks of the fast spectrum core simplifying operator workload and requirements;
- Small shippable reactor vessel (12 m height by 3.2 m diameter);

- Enhanced passive safety due to the inherent safety features of the Pb coolant with its high 1740 °C boiling temperature, nitride fuel with its high decomposition temperature (estimated > 1350 °C), and a fast spectrum core together with passive safety design features including a pool reactor vessel (surrounded by a guard vessel) containing all major primary coolant system components and natural circulation heat transport – For traditional postulated accidents, the core and in-vessel heat exchangers remain covered by single-phase Pb coolant and natural circulation heat transport removes the core power which is removed from the reactor system either by the normal heat removal path through the in-vessel heat exchangers or by means of an emergency decay heat removal system;
- Plant efficiency = 43.8 % with 564/420 °C core outlet/inlet temperatures and an advanced supercritical carbon dioxide Brayton cycle power converter; and
- Cost of energy generation < 5.5 cents/KWhr.

2.2. Status of SSTAR Development

2.2.1. SSTAR Configuration

The Small Secure Transportable Autonomous Reactor (SSTAR) is a 20 MWe (45 MWt) exportable, small, proliferation-resistant, fissile self-sufficient, autonomous load following, and passively safe lead-cooled fast reactor (LFR) concept for deployment at remote sites. Potential customers for SSTAR include: clients looking for energy security at small capital outlay; cities in developing nations; and deregulated power producers in developed nations. SSTAR makes extensive use of inherent safety features; most notably, natural circulation heat transport, Pb coolant, and transuranic nitride fuel. The SSTAR nuclear power plant incorporates a supercritical carbon dioxide (S-CO₂) Brayton cycle power converter for higher plant efficiency and lower balance of plant costs. The efficiency of the S-CO₂ Brayton cycle increases as the reactor core outlet temperature increases; an efficiency of about 44 % can be attained for a turbine inlet temperature of about 550 °C. To take advantage of the economic benefits of such a high plant efficiency, there has been interest in operating at higher Pb coolant temperatures. In particular, a peak cladding inner surface temperature of 650 °C has been an objective.

SSTAR is currently at a pre-conceptual level of development. Research and development has been carried out establishing the technical viability of the SSTAR/LFR concept. Engineering design for manufacturing of components and systems has not been carried out. A probabilistic risk assessment has not been performed. Accident analyses of a set of design basis and beyond design basis accidents have not yet been carried out.

SSTAR is scalable to a higher power level of 181 MWe (400 MWt); this is the STAR-LM (Secure Transportable Autonomous Reactor with Liquid Metal) concept. STAR-LM is a scaled-up version of SSTAR for high efficiency electric power production with optional production of desalinated water using a portion of the reject heat. The STAR-LM reactor vessel size (16.9 m height by 5.5 m diameter) is assumed to be limited in

height by a rail shipment length limitation of 18.9 m. The power level of 400 MWt approaches the maximum value at which heat transport can be accomplished through single-phase natural circulation given the reactor vessel height limitation. The scaled-up version can alternately be used for hydrogen and oxygen generation using a Ca-Br thermochemical (“water cracking”) cycle, if cladding and structural materials for operation with Pb up to about 800 °C can be developed; this high temperature version is named STAR-H2.

Figure 2 illustrates SSTAR which is a pool-type reactor. The lead coolant is contained inside a reactor vessel surrounded by a guard vessel. Lead is chosen as the coolant rather than lead-bismuth eutectic (LBE) to reduce the amount of alpha-emitting ^{210}Po isotope formed in the coolant by two to three orders of magnitude relative to LBE, and to eliminate dependency upon bismuth which might be a limited resource.

The Pb coolant flows through a perforated flow distributor head located beneath the core; this structure provides an essentially uniform pressure boundary condition at the inlet to the core. The Pb flows upward through the core and a chimney above the core formed by a cylindrical shroud (Figures 3 and 4). SSTAR is a natural circulation reactor such that the vessel has a height-to-diameter ratio large enough to facilitate natural circulation heat removal at all power levels up to and exceeding 100 % nominal. The coolant flows through flow openings near the top of the shroud and enters four modular Pb-to- CO_2 heat exchangers located in the annulus between the reactor vessel and the cylindrical shroud. Inside each heat exchanger, the Pb flows downwards over the exterior of tubes through which the CO_2 flows upwards. The CO_2 enters each heat exchanger through a top entry nozzle which delivers the CO_2 to a lower plenum region in which the CO_2 enters each of the vertical tubes. The CO_2 is collected in an upper plenum and exits the heat exchanger through two smaller diameter top entry nozzles. The Pb exits the heat exchangers and flows downward through the annular downcomer to enter the flow openings in the flow distributor head beneath the core.

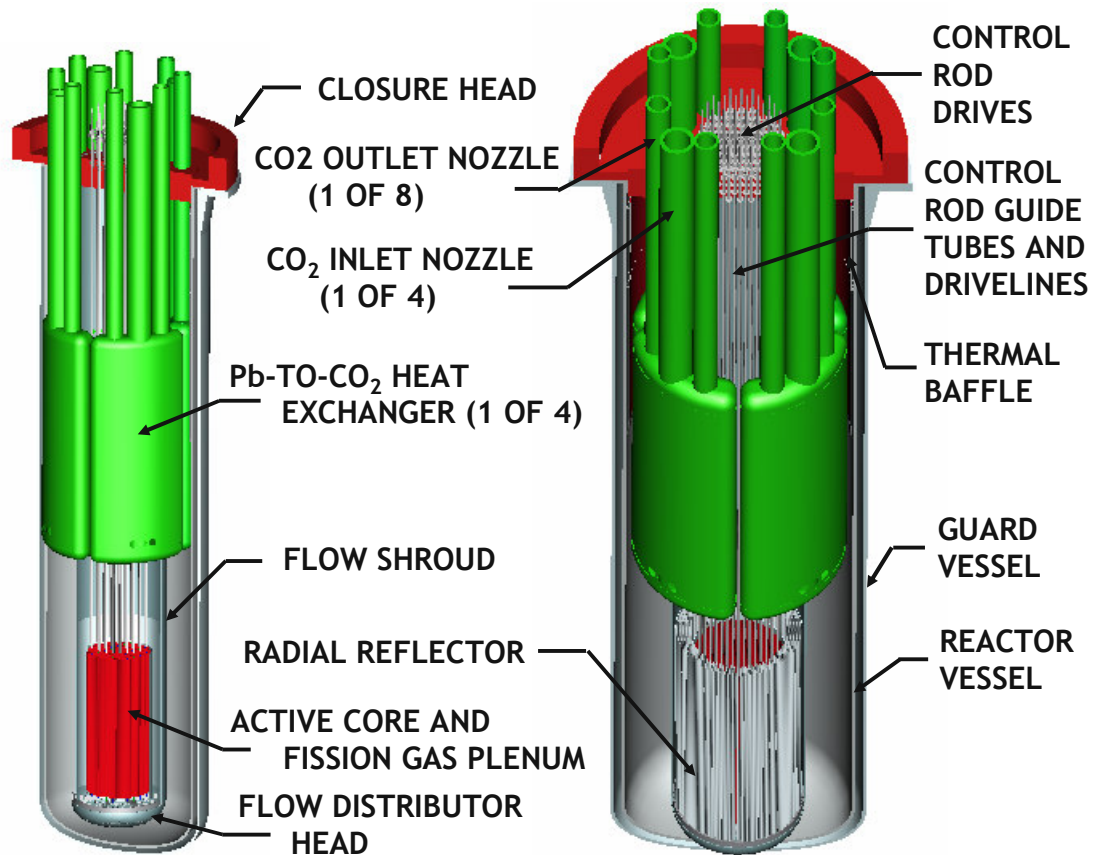


Figure 2. SSTAR Modular Lead-Cooled Fast Reactor.

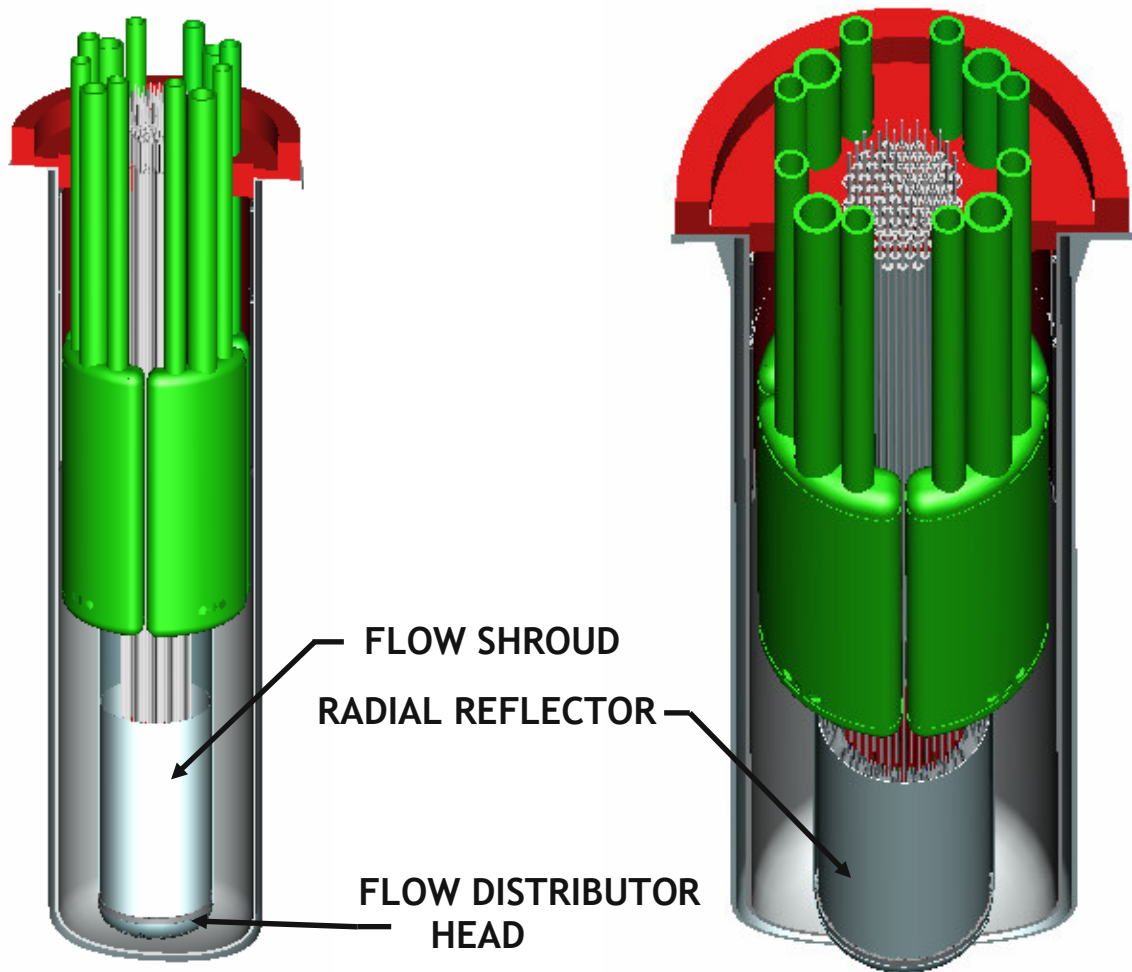


Figure 3. SSTAR Flow Shroud, Flow Distributor Head, and Radial Reflector.

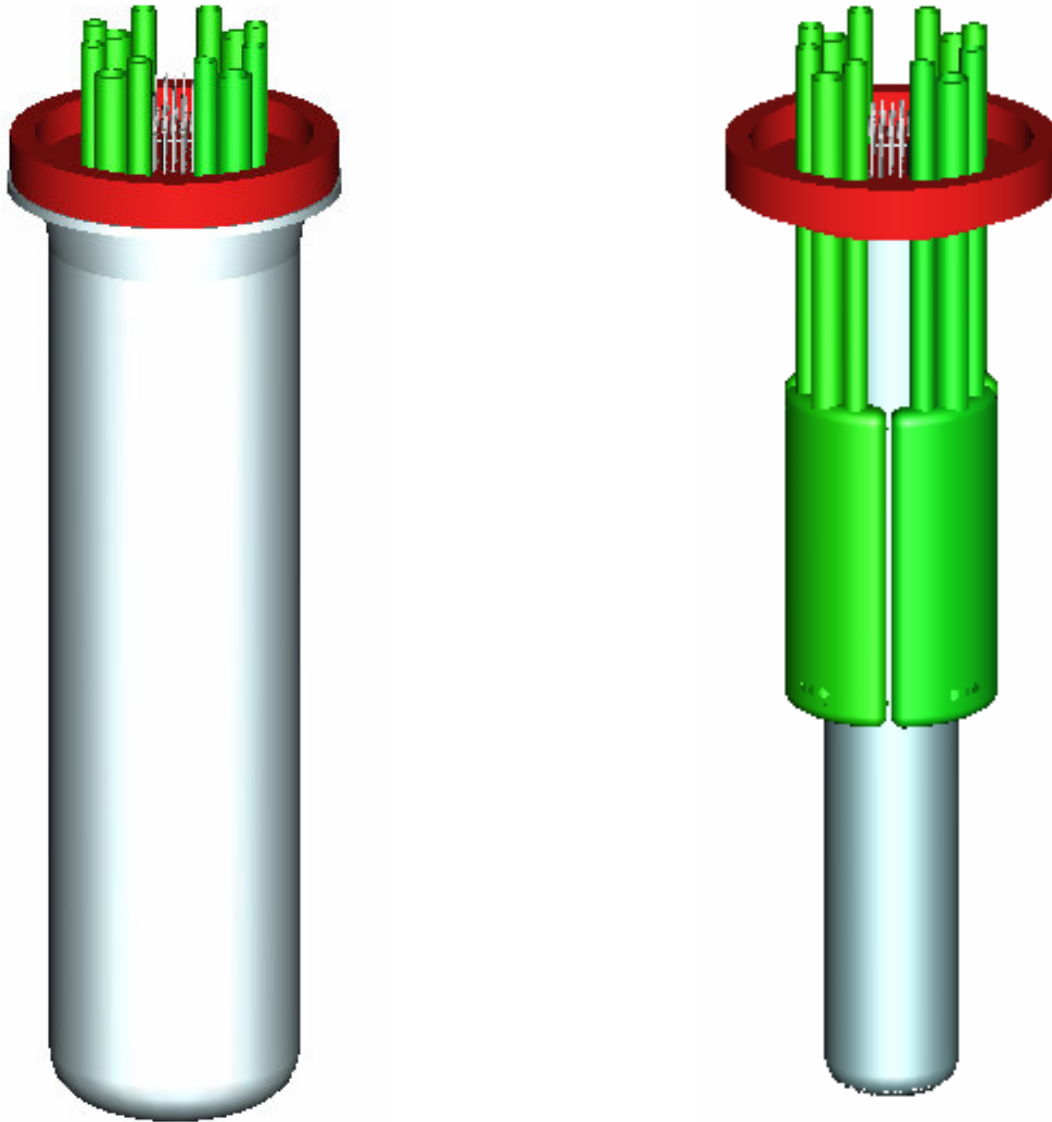


Figure 4. SSTAR Reactor and In-Vessel Internals.

A thermal baffle is provided in the vicinity of the Pb free surface. As shown in Figure 5, the baffle consists of a cylindrical shell welded to the reactor vessel at the bottom of the baffle below the tops of the Pb-to-CO₂ heat exchanger shells. The baffle continues up to slightly below the bottom surface of the upper closure head. The annular space between the baffle and the reactor vessel inner surface remains filled with argon cover gas thermally insulating the reactor vessel from the Pb interior to the baffle. The insulating effect of the baffle is necessary to protect the vessel from thermal stresses that would otherwise result from exposure to the heated Pb coolant during startup and shutdown transients. During shutdown and startup, the Pb temperature in the upper plenum varies between the nominal core outlet temperature of 564 °C and the core inlet temperature of 420 °C which is the nominal temperature at which the coolant is maintained during

shutdown. Horizontal plates containing hole perforations are provided to maintain spacing between the baffle and the reactor vessel.

SSTAR does not incorporate an intermediate heat transport circuit. This is a simplification possible with Pb coolant which is calculated not to react chemically with the working fluid below about 250 °C (i.e., well below the 327 °C Pb melting temperature). A passive pressure relief system is provided on the reactor system to vent CO₂ from the reactor, in the event of a heat exchanger tube rupture.

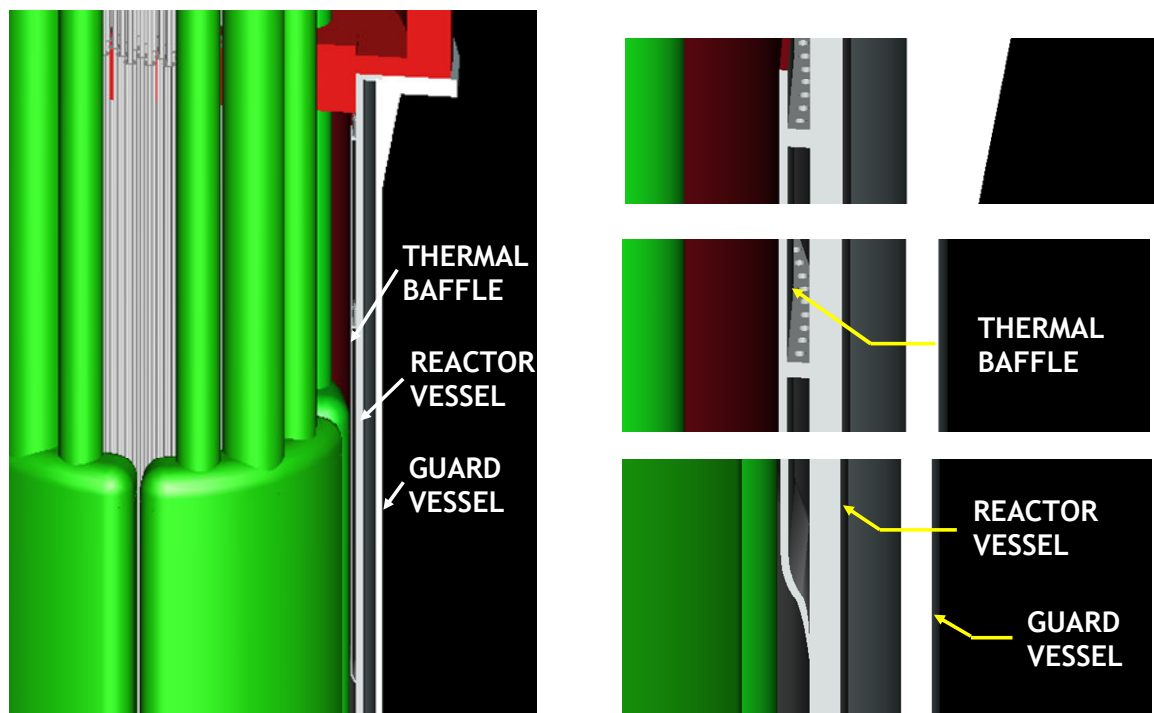


Figure 5. SSTAR Thermal Baffle to Protect the Reactor Vessel from Thermal Stresses Induced by Exposure to Heated Pb During Startup and Shutdown Cycles.

Figure 6 shows the 30-year lifetime core configuration. The core has an open lattice configuration of large diameter (2.5 centimeter) fuel pins arranged on a triangular pitch. This eliminates potential flow blockage accidents since crossflow paths are always available for cooling. The fuel consists of pellets of transuranic nitride fuel. Existing ferritic/martensitic (F/M) steels such as T91 or HT9 have been shown to have corrosion resistance to lead-bismuth eutectic with active oxygen control at temperatures below ~ 550 °C [3]. Active maintenance and control of the dissolved oxygen potential in lead-bismuth eutectic (LBE) and Pb coolants is a well established technique for providing corrosion protection for steel by maintaining the dissolved oxygen concentration within a proper window such that protective oxide layers (Fe₃O₄ below ~ 570 °C) form on the cladding and steel structures but solid PbO does not precipitate in the coolant [3].

Operation of SSTAR at peak cladding temperatures as high as 650 °C will require the development and testing of new materials for service in Pb up to 650 °C. A promising approach for cladding may be weldment of a surface layer of Si-enhanced steel upon F/M steel to form a layered billet which is co-extruded [4]. The Si-enhanced steel layer provides improved corrosion resistance but has poor irradiation stability. The F/M substrate provides structural strength and irradiation stability. Alternatively, the peak cladding and coolant temperatures could be reduced but at the expense of a penalty in plant efficiency. The fuel pellets are bonded to the cladding by molten Pb to reduce the temperature difference between the pellet outer surface and cladding inner surface.

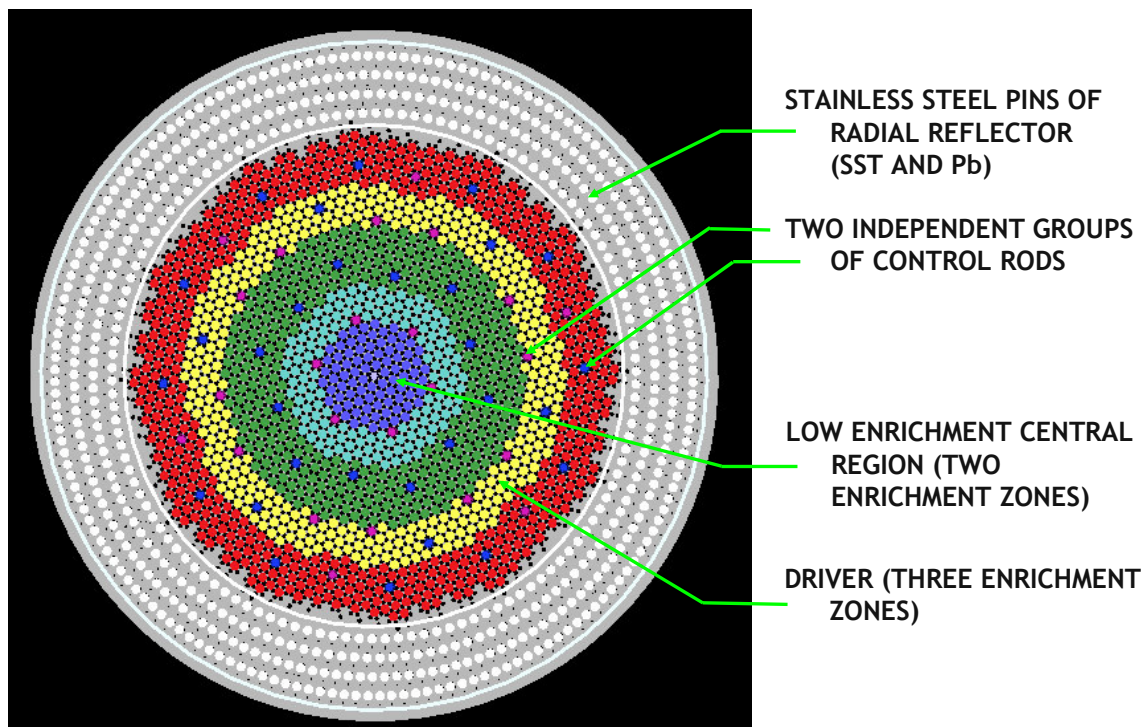


Figure 6. SSTAR Open-Lattice Core Configuration (All Fuel Pins Shown).

The active core diameter of 1.22 m is selected to minimize the burnup reactivity swing over the 30-year core lifetime. The power level of 45 MWt is conservatively chosen to limit the peak fluence on the cladding to 4×10^{23} neutrons/cm²; this is the maximum exposure time for which HT9 cladding has been irradiated. The core has three enrichment zones to reduce the power peaking and two central low enrichment zones which further reduce the burnup reactivity swing. The core has strong reactivity feedback coefficients which enable autonomous load following whereby the reactor power adjusts itself to the heat removal from the reactor as a result of the reactivity feedbacks. Because heat transport is accomplished by natural circulation, the primary coolant flowrate and system temperatures also adjust themselves to transport the heat from the core.

Figure 7 further shows the core and surrounding radial reflector. The core does not consist of individual removable fuel assemblies but is a single cassette/assembly. The fuel pins are permanently attached by welding or other means to a core support plate at the bottom of the core. This limits access to either fuel or neutrons. Normally, refuelling equipment is not present on the site. Refueling equipment including a crawler crane is brought onsite only following the 30-year lifetime. The upper closure head for the guard and reactor vessels is removed (note: one closure head is used for both the guard vessel and the reactor vessel), the spent core is removed from the vessel, the core is placed inside of a shipping cask, and transported to a fuel cycle support center located in a fuel cycle state. A fresh core is installed in the reactor vessel, and the refuelling equipment is removed from the site.

Two sets of control rods are provided for independence and redundancy of scram. Small adjustments of the control rods are carried out to compensate for small changes in the burnup reactivity swing. The control rod locations have been uniformly distributed throughout the core as shown in Figures 6 and 7. Primary control rods are shown colored magenta and secondary control rods blue in Figure 6. Each control rod moves inside of the control rod guide tube occupying a position in the triangular lattice (Figure 8). Spacing between fuel pins is maintained by two levels of grid spacers (Figures 9 and 10). Each grid spacer is welded to a control rod guide tube; the grid spacer holds the surrounding fuel pins by means of spring clips allowing for thermal expansion of the fuel pins relative to the control rod guide tube. The active core is surrounded by a radial reflector which is an annular “box” containing stainless steel rods and Pb having approximately equal volume proportions. Stainless steel is needed to shield the reactor vessel from neutron fluxes. There is a small Pb flow through the reflector to remove the small power deposition taking place there.

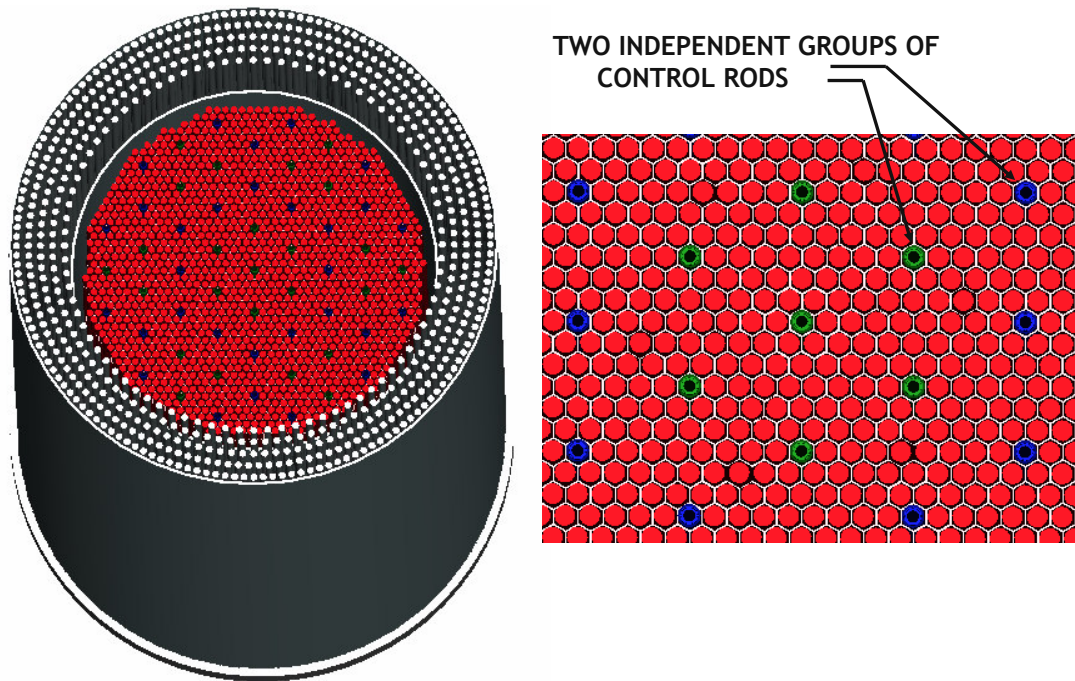


Figure 7. SSTAR Core and Radial Reflector (Left) and Uniform Distribution of Control Rods in Core Lattice (Right).

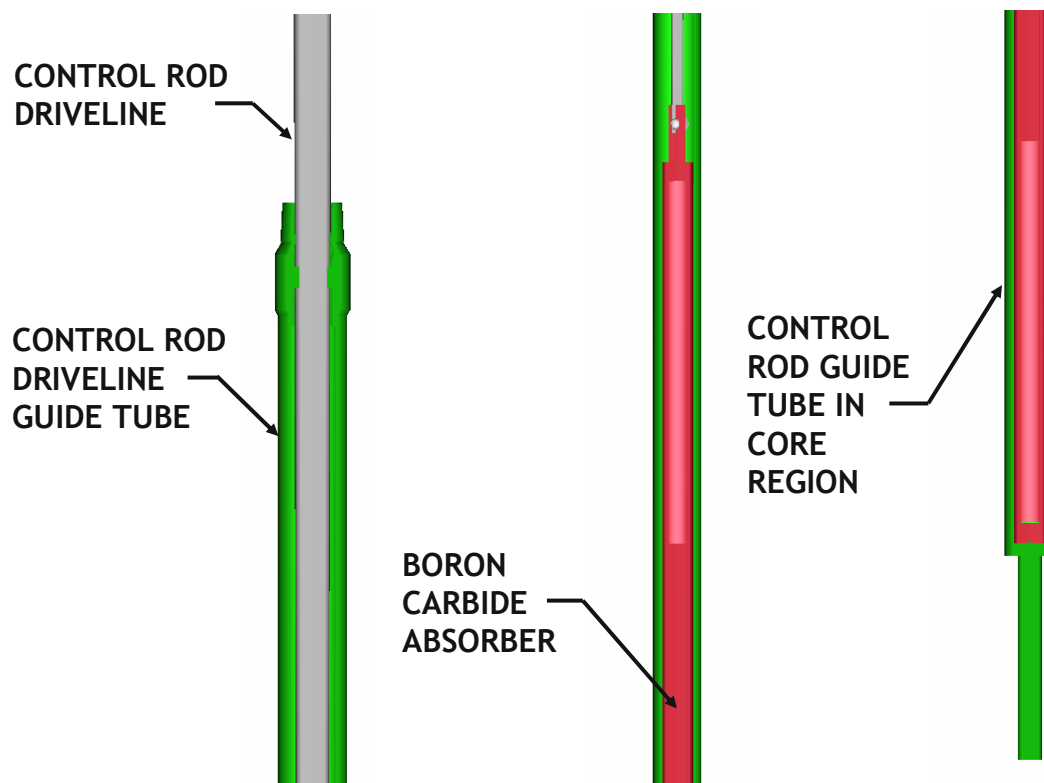


Figure 8. SSTAR Control Rod, Control Rod Driveline, and Control Rod Driveline Guide Tube.

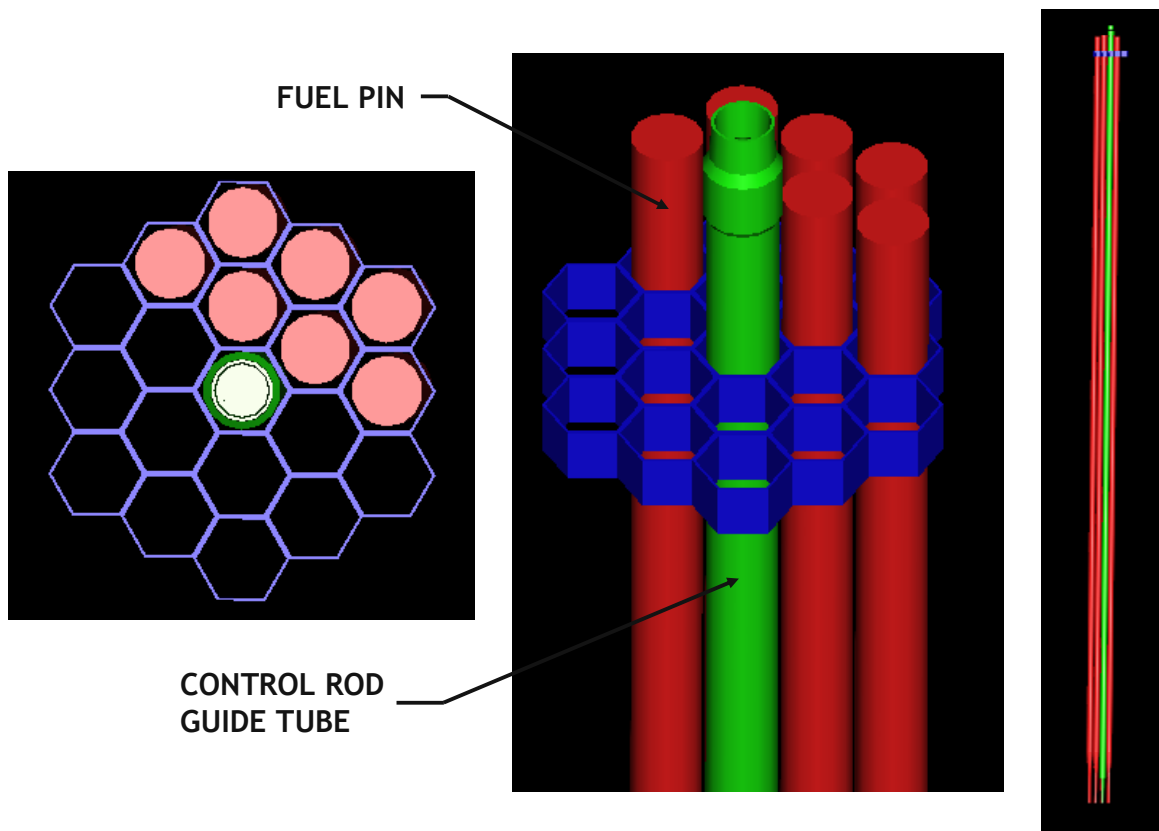


Figure 9. SSTAR Fuel Pins, Control Rod Guide Tubes, and Grid Spacers.

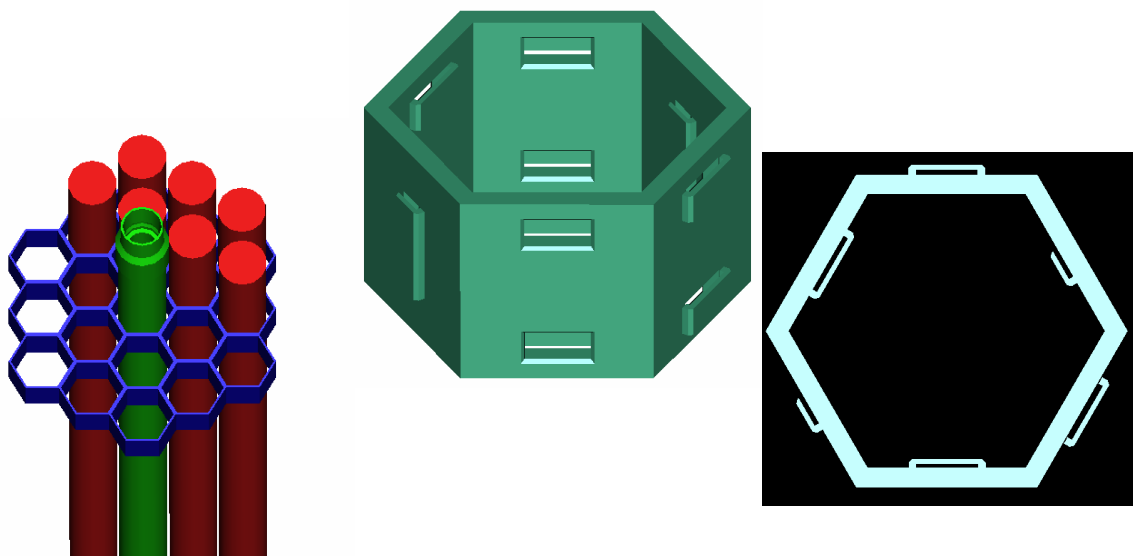


Figure 10. SSTAR Grid Spacer Cell with Spring Clips.

Figure 11 shows the SSTAR core, radial reflector, control rod drivelines, and control rod drives; the drives are located above the upper head. For a realistically sized drive, the uniform distribution of control rods throughout the core lattice results in a dense packing of the control rod drives above the upper closure head as illustrated in Figure 12. This dense packing is a consequence of providing a separate drive for each individual control rod. An alternative approach would involve clustering rods together with each cluster moved by means of a single drive; this approach would decrease the number of drives. Figure 13 provides a view of the upper closure head region.

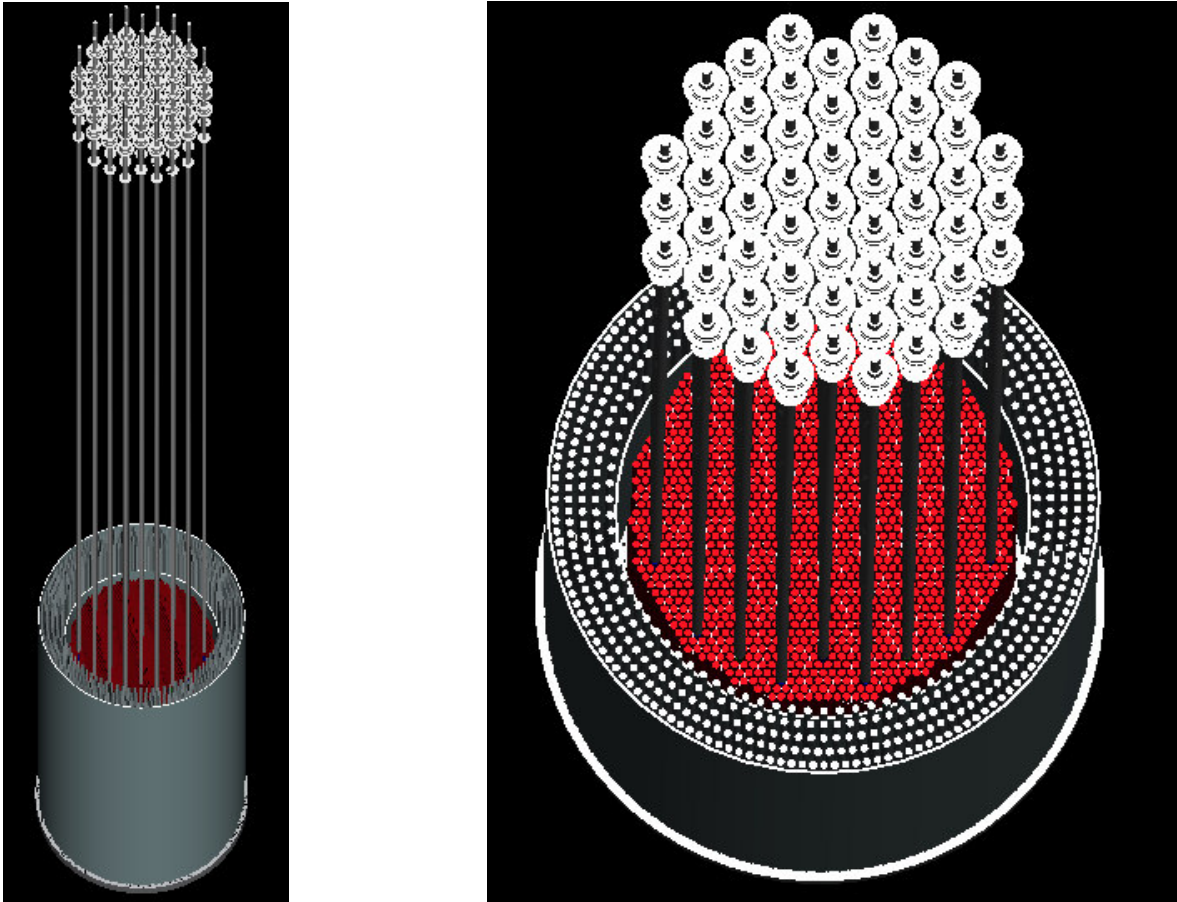


Figure 11. SSTAR Core, Radial Reflector, Control Rod Drivelines, and Control Rod Drives.

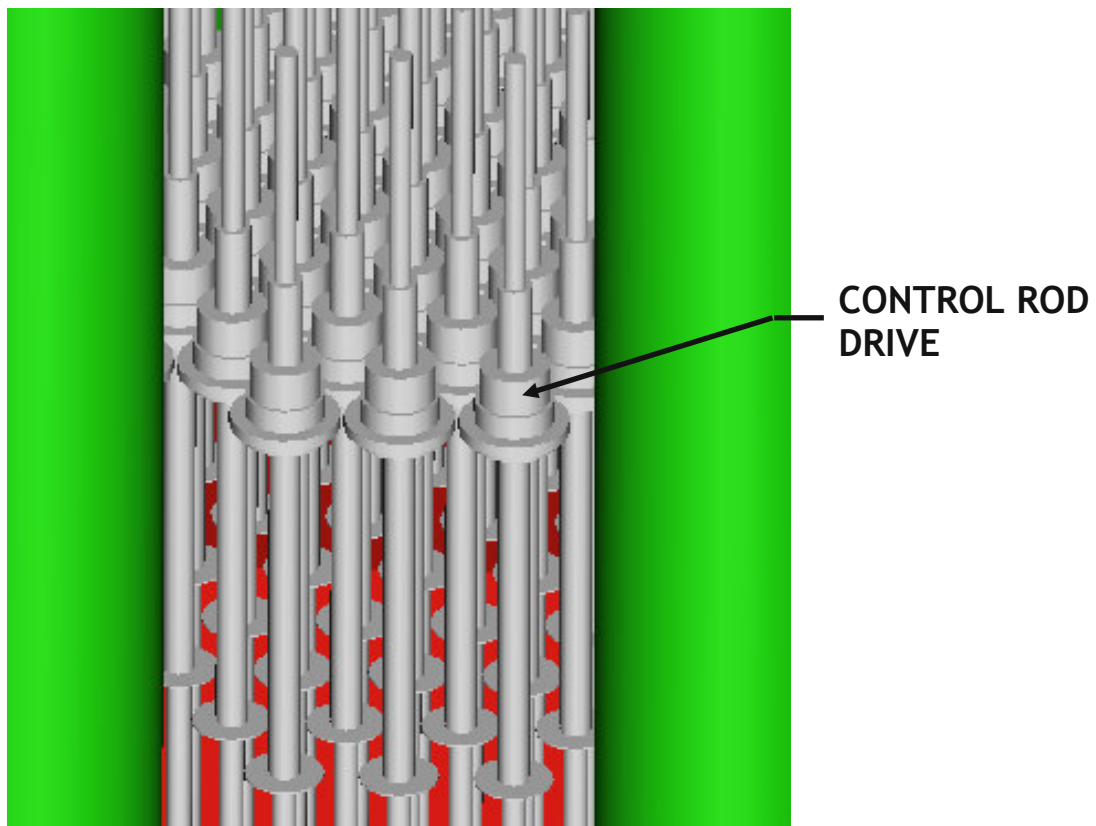


Figure 12. Dense Packing of Control Rod Drives Above Upper Closure Head.

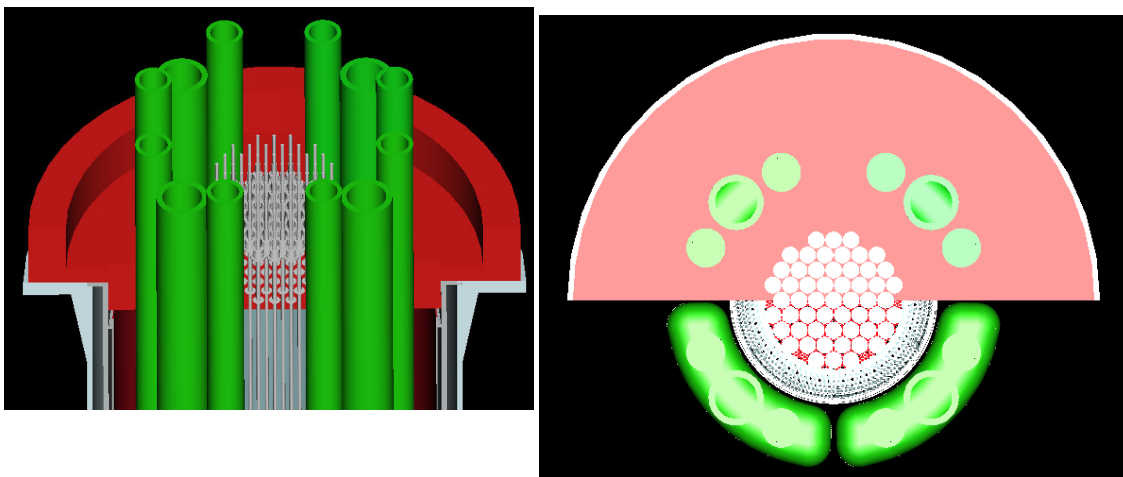


Figure 13. SSTAR Upper Closure Head Region.

SSTAR incorporates a Reactor Vessel Auxiliary Cooling System (RVACS) for decay heat removal should the normal heat removal path involving the Pb-to-CO₂ heat exchangers be unavailable. The RVACS involves heat removal from the outside of the guard vessel due to natural circulation of air which is always in effect. The RVACS is a safety grade system. To provide for greater reliability of emergency heat removal beyond that corresponding to the single RVACS system, it is planned to also incorporate multiple safety grade Direct Reactor Auxiliary Cooling System (DRACS) heat exchangers into the reactor vessel.

Figure 14 illustrates a possible approach in which the reactor system is supported from above from a ledge inside a seismically-isolated reactor building. In this particular illustration, the RVACS is dispensed with altogether and emergency heat removal is to be provided solely by a DRACS.

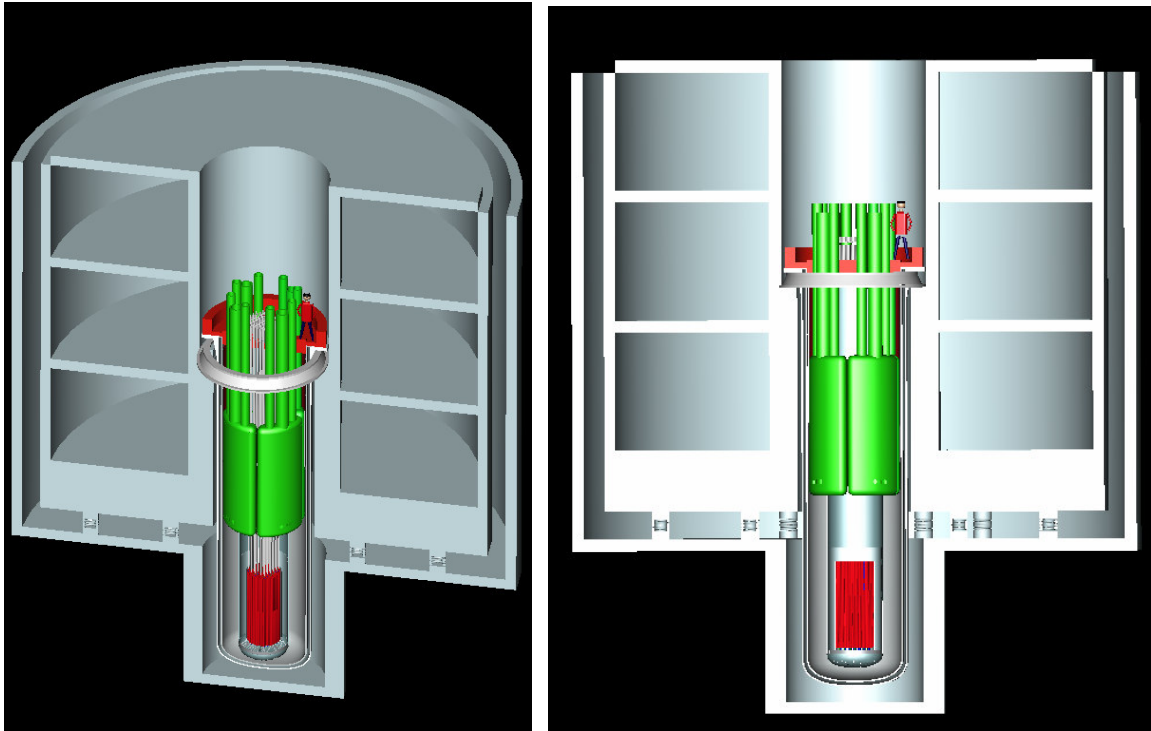


Figure 14. Possible Approach Involving Top Support of SSTAR Vessels from Ledge Inside Seismically-Isolated Reactor Building.

Conditions, dimensions, and other parameters for SSTAR are included in Table 2. Notable achievements of SSTAR development include:

- Pb coolant;
- 30-year core lifetime;
- Average (peak) discharge burnup of 81 (131) MWd/Kg of Heavy Metal;
- Burnup reactivity swing < 1 \$;
- Peak cladding temperature = 650 °C;
- Core outlet/inlet temperatures = 564/420 °C;
- Peak transuranic nitride fuel temperature = 882 °C;
- Small shippable reactor vessel (12 m height by 3.23 m diameter)
- Autonomous load following;
- Supercritical CO₂ Brayton cycle energy conversion efficiency = 44.2 %;
- Plant efficiency = 43.8 %;
- Cost of energy generation < 5.5 cents/KWhr (55 \$/MWhr).

Table 2. Conditions and Dimensions for SSTAR

LFR	SSTAR (Small Secure Transportable Autonomous Reactor)
Power, MWe (MWt)	19.7 (45)
Client – Assume 4.0 tonnes of Oil Equivalent per Capita per year = 167 GJ per Capita per year = 5.3 KWt-year per Capita per year of which ~ 1/3 is used for electricity	Electricity for a Town of ~ 25400
Coolant	Pb
Fuel	Transuranic Nitride (TRUN) Enriched to N ¹⁵
Enrichment, %	1.7/3.5/17.2/19.0/20.7 TRU/HM, 5 Radial Zones
Core Lifetime, years	30
Core Inlet/Outlet Temperatures, °C	420 / 564
Coolant Flow Rate, Kg/s	2150
Power Density, W/cm ³	42
Average (Peak) Discharge Burnup, MWd/Kg HM	81 (131)
Peak Fuel Temperature, °C	882
Cladding	Si-Enhanced Ferritic/Martensitic Stainless Steel
Peak Cladding Temperature, °C	650
Fuel/Coolant Volume Fractions	0.45 / 0.35
Core Lifetime, years	30
Fuel Pin Diameter, cm	2.50
Fuel Pin Triangular Pitch-to-Diameter Ratio	1.185
Active Core Dimensions Height/Diameter, m	0.976 / 1.22
Core Hydraulic Diameter, cm	1.371
Pb-to-CO ₂ HXs Type	Shell-and-Tube
Number of Pb-to-CO ₂ HXs	4
HX Tube Length, m	4.0

HX Tube Inner/Outer Diameters, cm	1.0 / 1.4
Number of Tubes (all HXs)	10,688
HX Tube Pitch-to-Diameter Ratio	1.255
HX Pb Hydraulic Diameter, cm	1.030
HX-Core Thermal Centers Separation Height, m	6.80
Reactor Vessel Dimensions Height/Diameter, m	12.0 / 3.23
Reactor Vessel Thickness, cm	5.08
Gap Between Reactor Vessel and Guard Vessel, cm	12.7
Gap Filling Material	Air
Guard Vessel Thickness, cm	5.08
Air Channel Thickness, cm	15
Air Ambient Temperature, °C	36
Working Fluid	Supercritical CO ₂
CO ₂ Turbine Inlet Temperature, °C	550
Minimum CO ₂ Temperature in Cycle, °C	31.25
Max/Min CO ₂ Pressures in Cycle, MPa	20 / 7.4
CO ₂ Flow Rate, Kg/s	245
Net Generator Output, MWe	19.7
Supercritical CO ₂ Brayton Cycle Efficiency, %	44.2
Net Plant Efficiency, %	43.8

2.2.2. SSTAR S-CO₂ Brayton Cycle Improvements

The pre-conceptual design of the S-CO₂ Brayton cycle energy converter for SSTAR was originally developed with axial flow compressors and an axial flow turbine based upon previous experience with axial flow steam turbines. However, a review of the earlier S-CO₂ Brayton cycle development by Barber Nichols Incorporated [5] indicated that

centrifugal (radial flow) compressors may have several advantages compared to axial flow compressors including a wider operating range and better handling of two-phase flow that might develop during certain accidents. Wider operating range means mainly a larger regime between a minimal flowrate at which stall occurs and a maximum flowrate limited by choking. Centrifugal compressors also exhibit better scalability than axial compressors which may facilitate meaningful testing at a smaller scale of a centrifugal compressor operating with CO₂ under prototypical conditions than is possible with an axial flow compressor. The disadvantage of radial turbomachinery has historically been lower efficiency. However, in the S-CO₂ Brayton cycle, the compressor work is significantly smaller than the turbine work such that the cycle efficiency is less sensitive to the compressor efficiencies than to the turbine efficiency. Therefore, lower centrifugal compressor efficiencies might not significantly penalize the cycle efficiency. On the other hand, operating range is a lesser concern for the turbine but the efficiency of the turbine is very important for the cycle efficiency. For these reasons, it was decided to develop a centrifugal compressor model and investigate the effect of the compressor type on the system behavior. A centrifugal turbine model has also been developed but it is not applied to the current S-CO₂ cycle design; however it is needed for testing and comparison of S-CO₂ Brayton cycle modeling against the results of small scale, recuperated, closed gas Brayton cycle tests incorporating a centrifugal turbine.

Centrifugal compressor models have been developed and have been applied to the S-CO₂ Brayton cycle for SSTAR. The models have been implemented in the steady state design code as well as steady state autonomous load following code. Incorporation of the centrifugal compressor models into the Plant Dynamics Computer Code is currently in progress.

Steady-State Cycle Analysis

The centrifugal compressor design model was implemented into the S-CO₂ Brayton cycle design code and used to calculate the efficiency of the centrifugal S-CO₂ compressors in comparison with axial compressors, and to investigate the effects of compressor design on cycle performance. It should be noticed here that the centrifugal compressor designs have not yet been optimized for this application.¹ For example, the effect of the number of stages on the compressor and cycle efficiencies has not yet been determined. Rather, the simplest design which provides a reasonable efficiency has been adopted for the analysis and for comparison with the axial design.

Table 3 shows the main design parameters and efficiencies of the axial and centrifugal compressors. The turbine data is also presented for comparison.

¹ A detailed centrifugal compressor design optimization for the S-CO₂ Brayton cycle has been carried out for a sodium-cooled fast reactor under a different project.

Table 3. Comparison of Axial and Centrifugal Compressors

Component	Turbine	Compressor No. 1		Compressor No. 2	
Type	Axial	Axial	Centrifugal	Axial	Centrifugal
Number of stages	5	8	1	9	2
Efficiency, Total-to-static, %	92.0	88.0	88.1	86.8	88.7
Max. diameter, ¹ m	0.34	0.21	0.59	0.28	0.60
Length ² (stages), m	0.48	0.22	0.10	0.18	0.18
Length (with diffuser), m	1.80	1.68	n/a	1.82	n/a
Min. hub diameter, cm	19.4	17.4	9.8	26.2	10.6
Min. blade height, cm	3.4	1.1	0.7	0.5	0.6
Max. blade height, cm	7.5	1.7	2.8	1.1	3.1
Cycle efficiency, ³ %		44.11	44.15		

It follows from Table 3 that centrifugal compressors achieve the same or even slightly better performance with significantly fewer stages. The only possible disadvantage of the centrifugal compressor designs might be the relatively larger radial dimensions (which could complicate mounting them on the same shaft with the turbine and generator). The resulting cycle efficiencies for the axial and centrifugal designs are very close.

Off-Design Performance Analysis

The performance of the centrifugal and axial compressors at off-design conditions was compared using the steady-state load following code. The investigation of the cycle behavior under various control actions was carried out in the same way as reported in Reference [6]. Even though the systems investigated in [6] and here are very similar (both cycles are designed for LFRs with similar temperatures and efficiencies), the power levels of the LFR plants are different resulting in different designs for the compressors and turbines. Therefore, the results could not be compared directly, but major trends in the behavior of the different systems should be the same.

Compressor Performance Maps

¹ Without casing and volute/collector.

² Estimated.

³ Cycle efficiency is shown for the two compressors having similar designs (either both axial or both centrifugal).

Figure 15 compares the performance maps (pressure ratio and efficiency versus flow rate) for the design inlet conditions. Figure 15 confirms the expected increased operating range of the centrifugal compressors, which is expected to improve the operating range of the cycle control mechanisms. Also, the efficiency curve is more flat for the centrifugal compressors meaning that good performance should be maintained over a wider range of flow rate variations. However, Figure 15 also demonstrates that centrifugal compressors could not achieve same pressure ratios as axial compressors could. This may affect the cycle performance under conditions where the compressor pressure ratio tends to increase (such as during turbine throttle control).

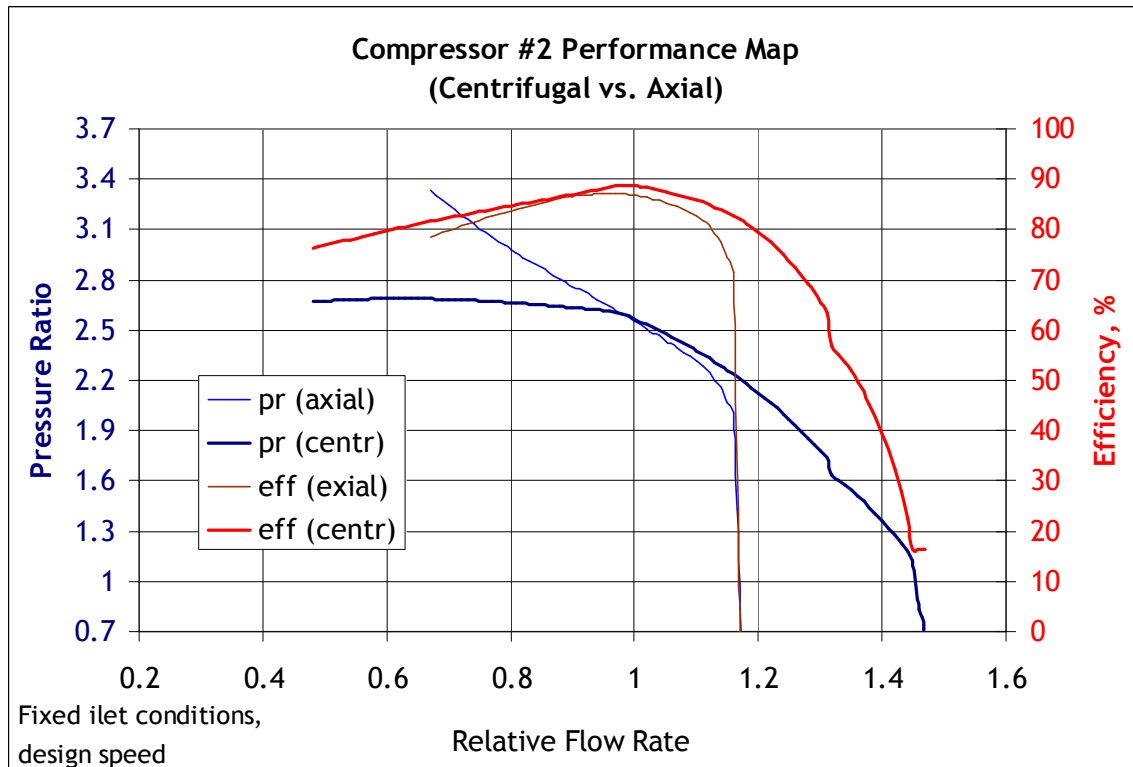
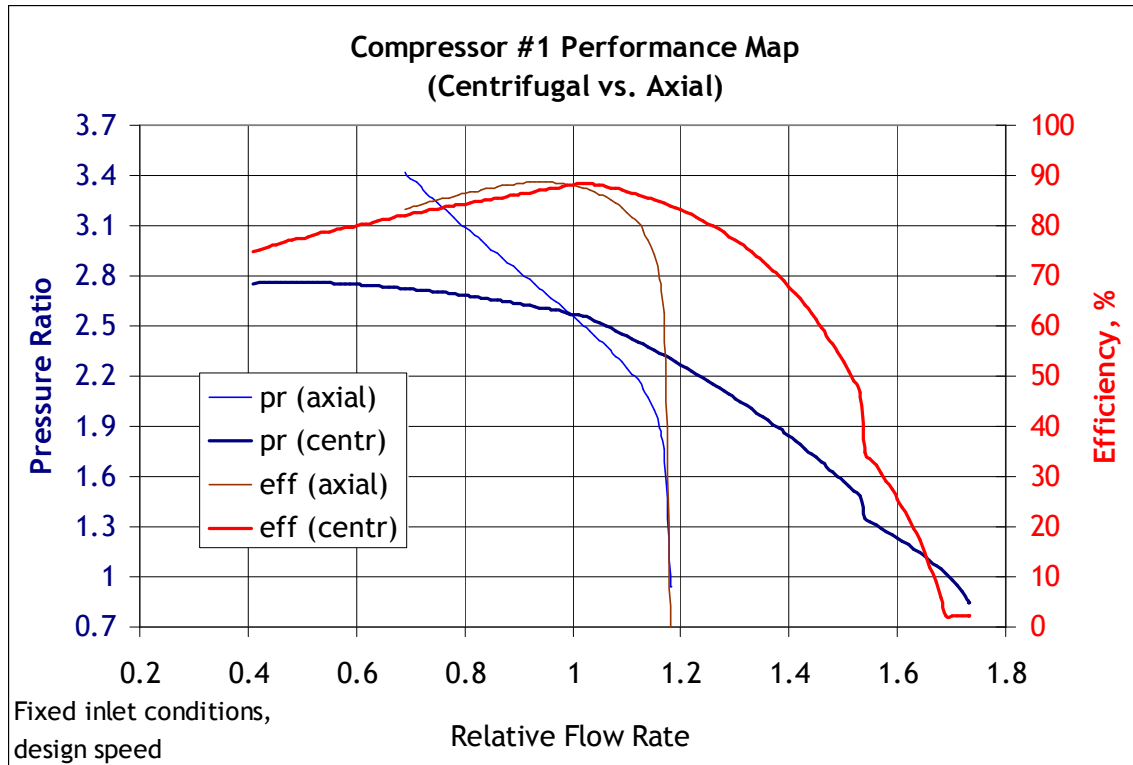


Figure 15. Comparison of the Performance Maps for Axial and Centrifugal S-CO₂ Compressors.

Turbine Bypass Control

In this control scheme, part of the flow is allowed to bypass the high temperature recuperator (HTR), in-reactor heat exchangers (IRHXs), and turbine. As a result, the turbine work is reduced as is the generator load. Calculations of the system response with centrifugal compressors (Figure 16) show that this control mechanism is capable of controlling the system from 100 % load all the way down to 0% load. However, since the compressor pressure ratios are decreasing under this control approach, according to Figure 15, the flow rate through the centrifugal compressors is higher than what it would be for axial compressors (for the same pressure ratio). As a result, the flow rate through the turbine (and, therefore, the IRHXs) is decreasing less in the case of centrifugal compressors compared to axial compressors. As a result, the autonomous reactor control does not change the reactor power significantly. Therefore, the excess of the heat produced in the reactor is going to the cooler such that the heat removal requirement in the cooler is increasing demanding a significant increase in the water flow rate and water pumping power. Figure 16 shows a significant increase in the cooling water pumping power requirement as the percentage of flow bypassing the HTR, IRHXs and turbine rises, which might not be feasible unless a separate high-power pump is reserved in the system. (Pumping power for the larger 400 MWt STAR-LM LFR plant with axial compressors remained approximately flat over the whole range of control action).

As a result, although centrifugal compressors have a wider operating range, their flatter pressure ratio curves result in the need for a greater cooler water side pumping power.

Inventory Control

Under inventory control, some mass of CO₂ is removed from the S-CO₂ Brayton cycle by means of opening valves in the high pressure portion of the cycle allowing the CO₂ to flow into inventory control tanks. As a result, the system pressures and flow rate decrease reducing the turbine work and generator output. In a system with centrifugal compressors (Figure 17), a load reduction down to about 20 % nominal can be achieved without reaching the limits on compressor operating range.

However, the real limitation in this control scheme is the pressure inside of the inventory tank. As CO₂ inventory is removed from the S-CO₂ cycle and added to the inventory tank, the system pressures decrease while the tank pressure increases. At the same time, in order for the control to operate (without additional compressors), the tank pressure should remain below the pressure in the high pressure portion of the S-CO₂ cycle. Figure 18 shows the increase in tank pressure due to mass accumulation for various tank volumes (the HTR total volume is given for comparison). Inventory control with a tank(s) of total volume about the same as that of the HTR is capable of controlling the system from about 35 % up to 100 % load. The previous lower limit for the STAR-LM system with axial compressors was 50 % load.

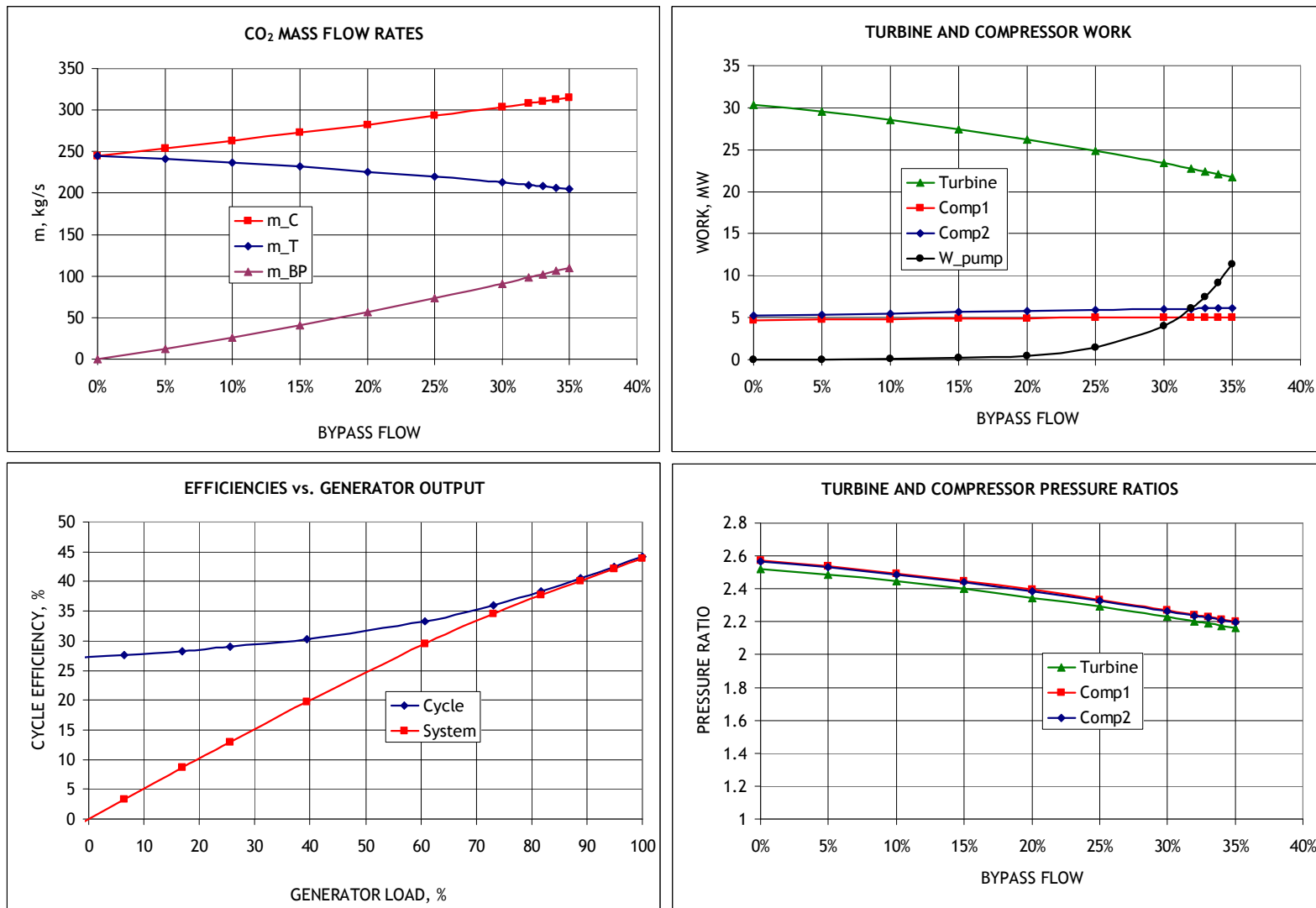


Figure 16. SSTAR Turbine Bypass Control.

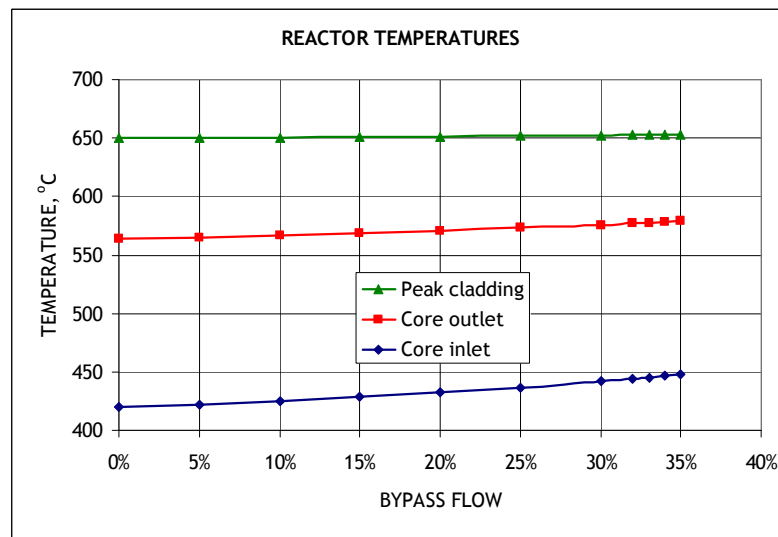
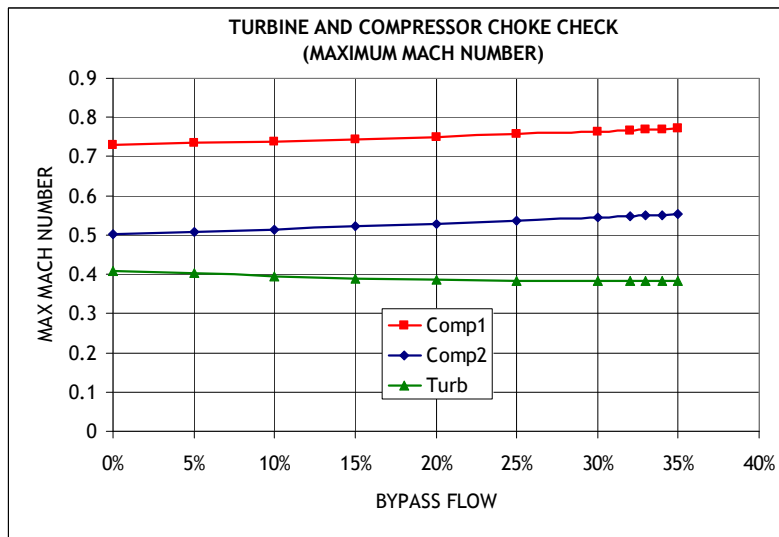
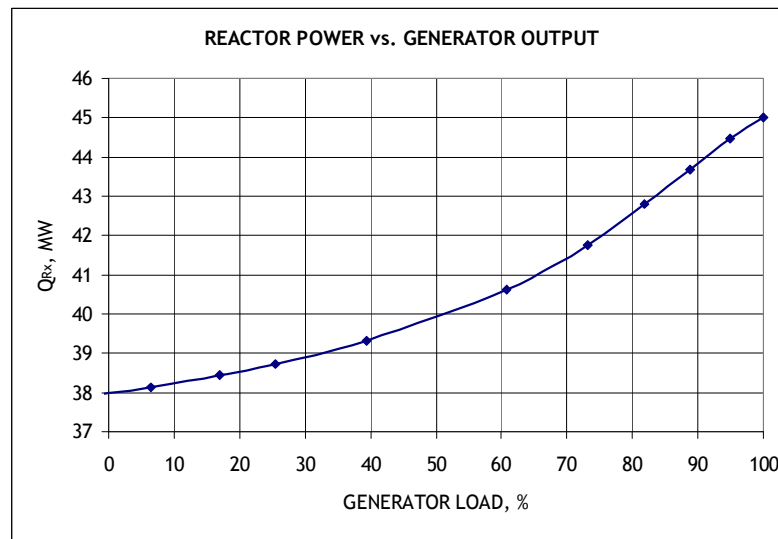
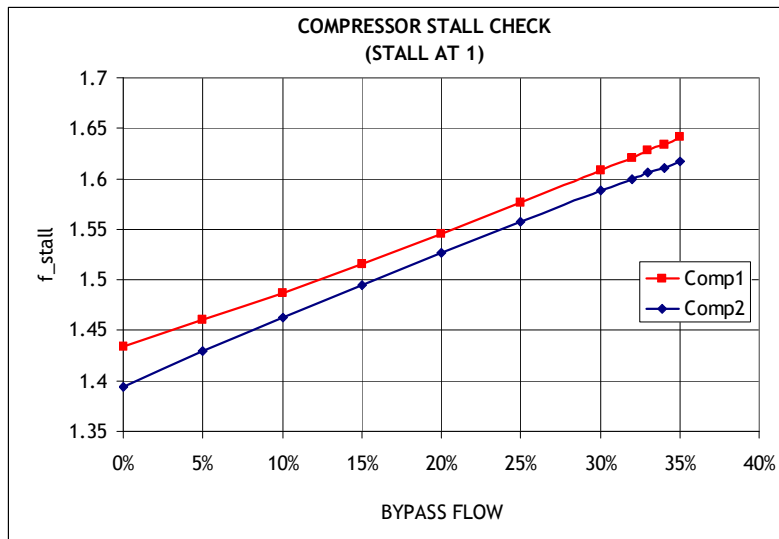


Figure 16 (Continued). SSTAR Turbine Bypass Control.

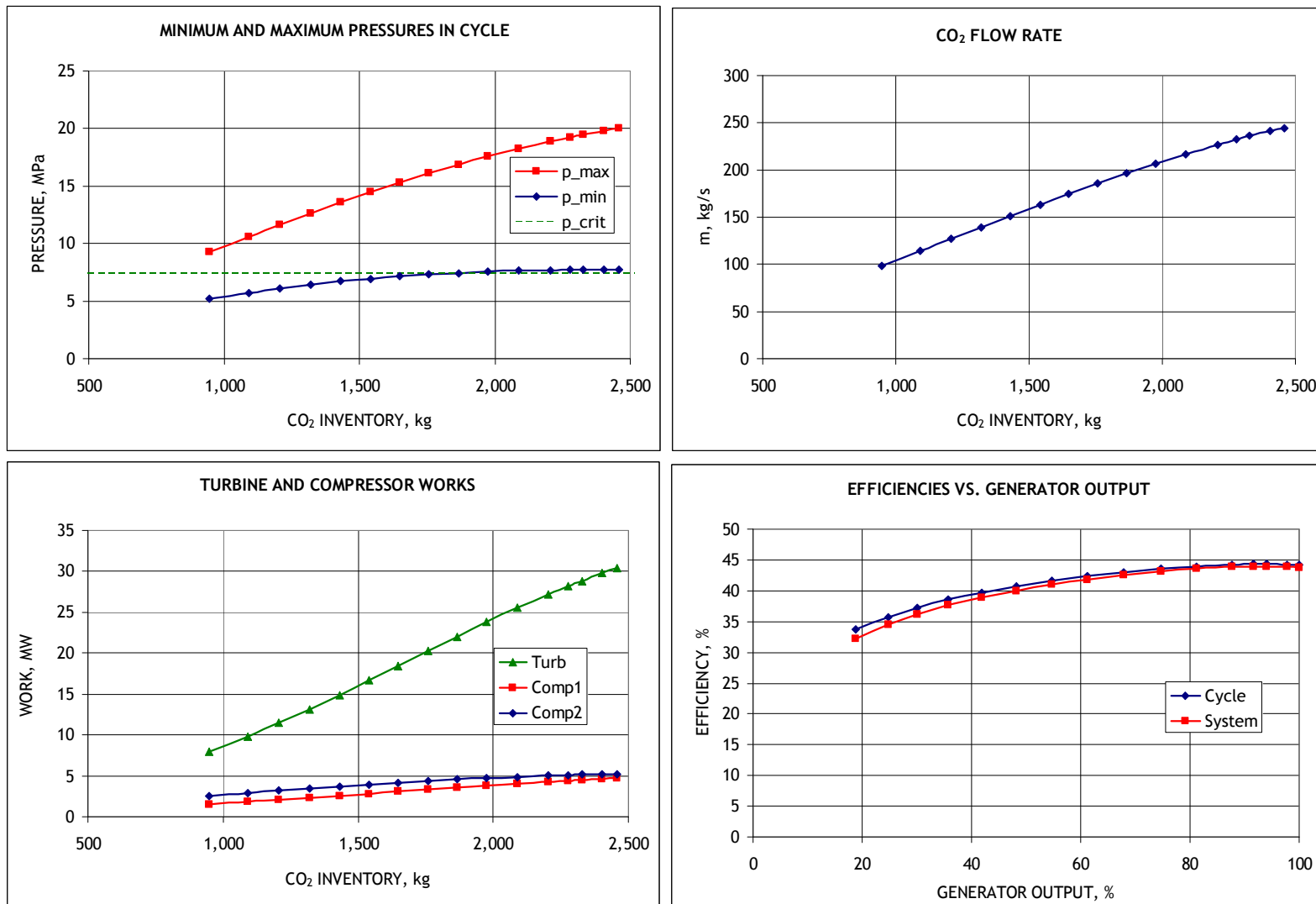


Figure 17. SSTAR Inventory Control.

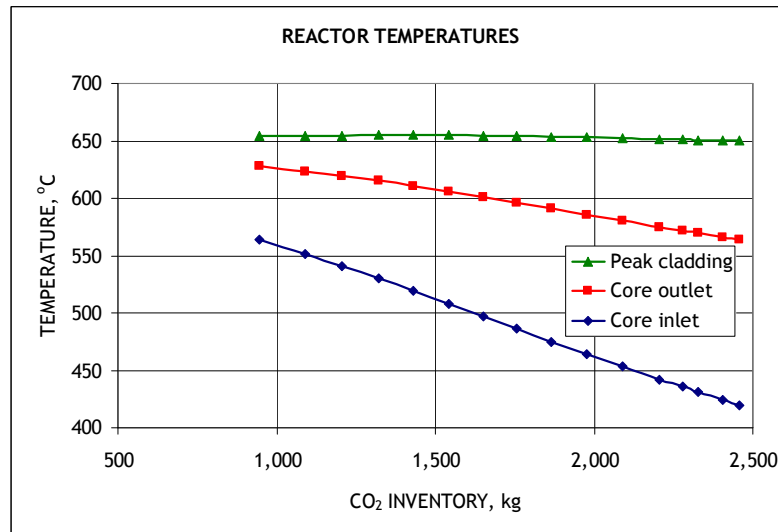
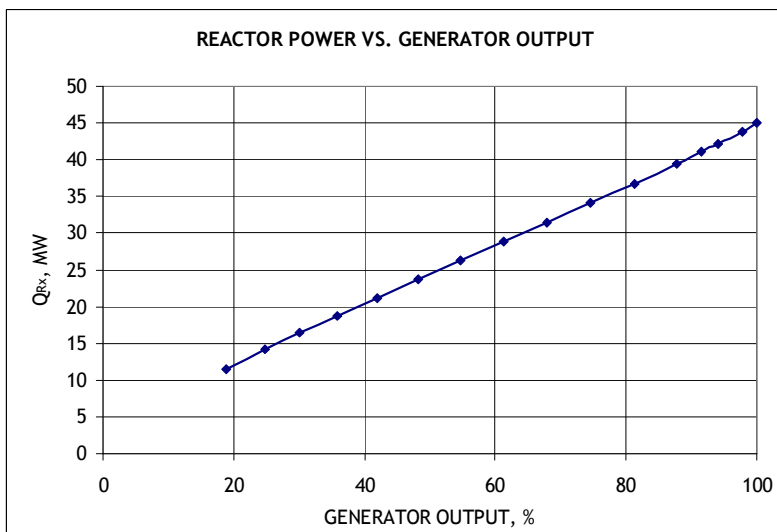
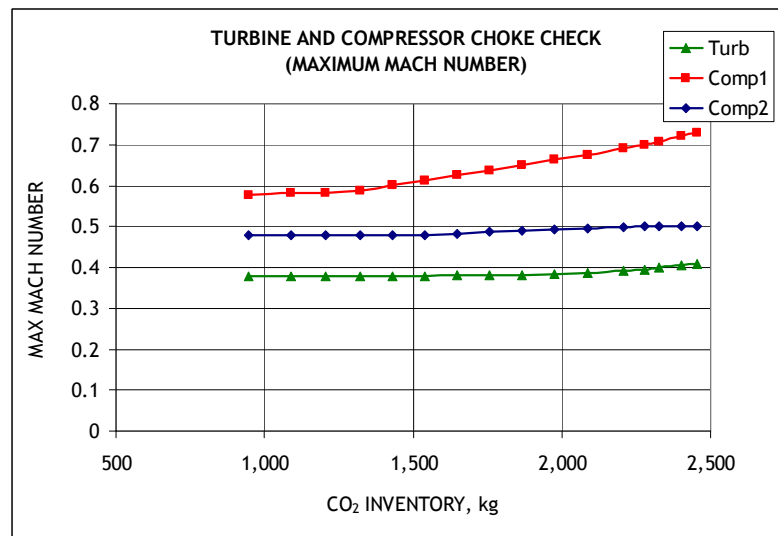
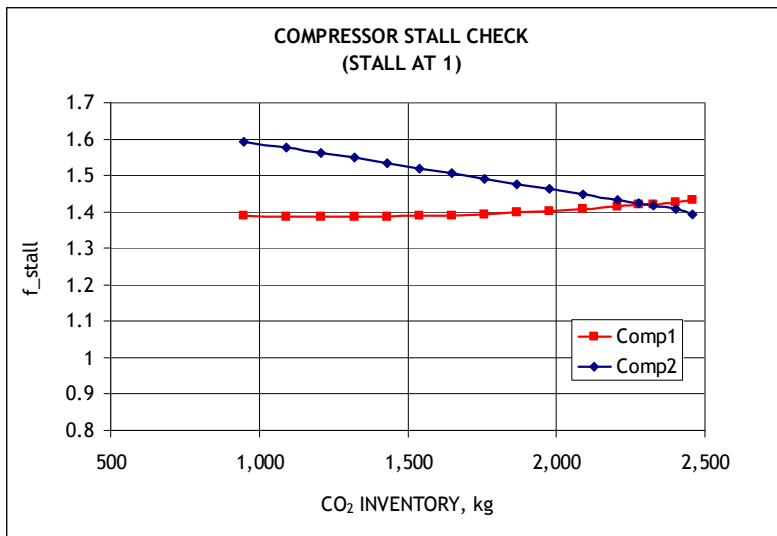


Figure 17 (Continued). SSTAR Inventory Control.

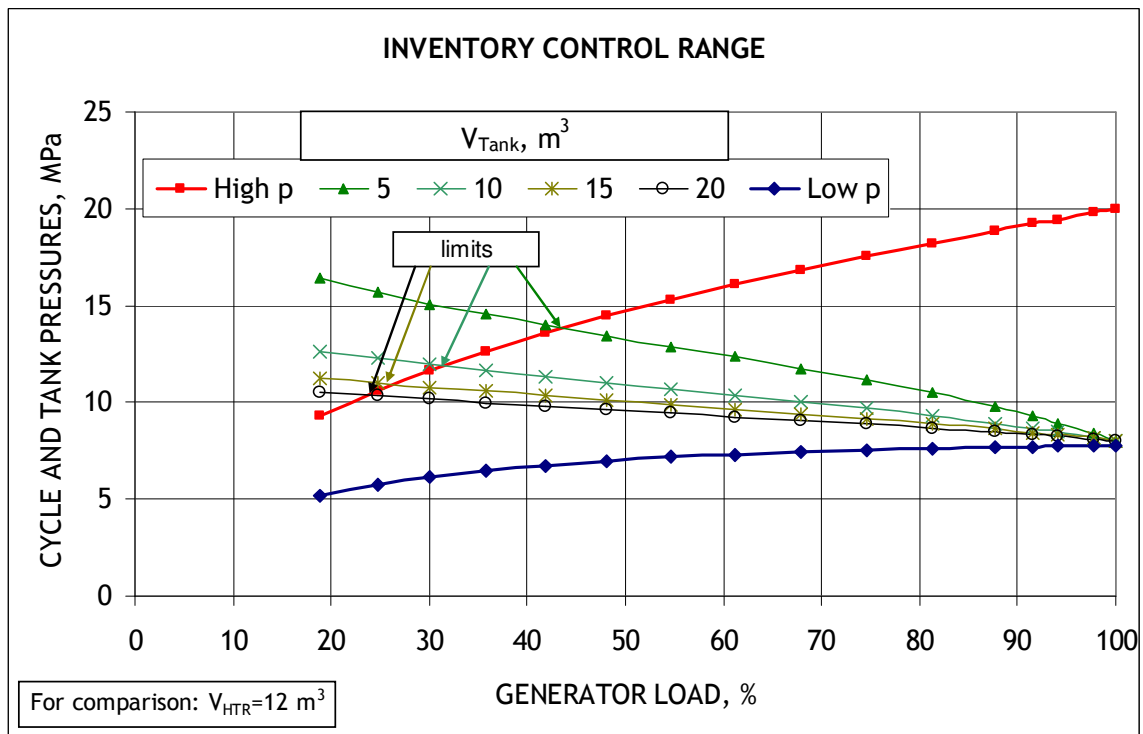
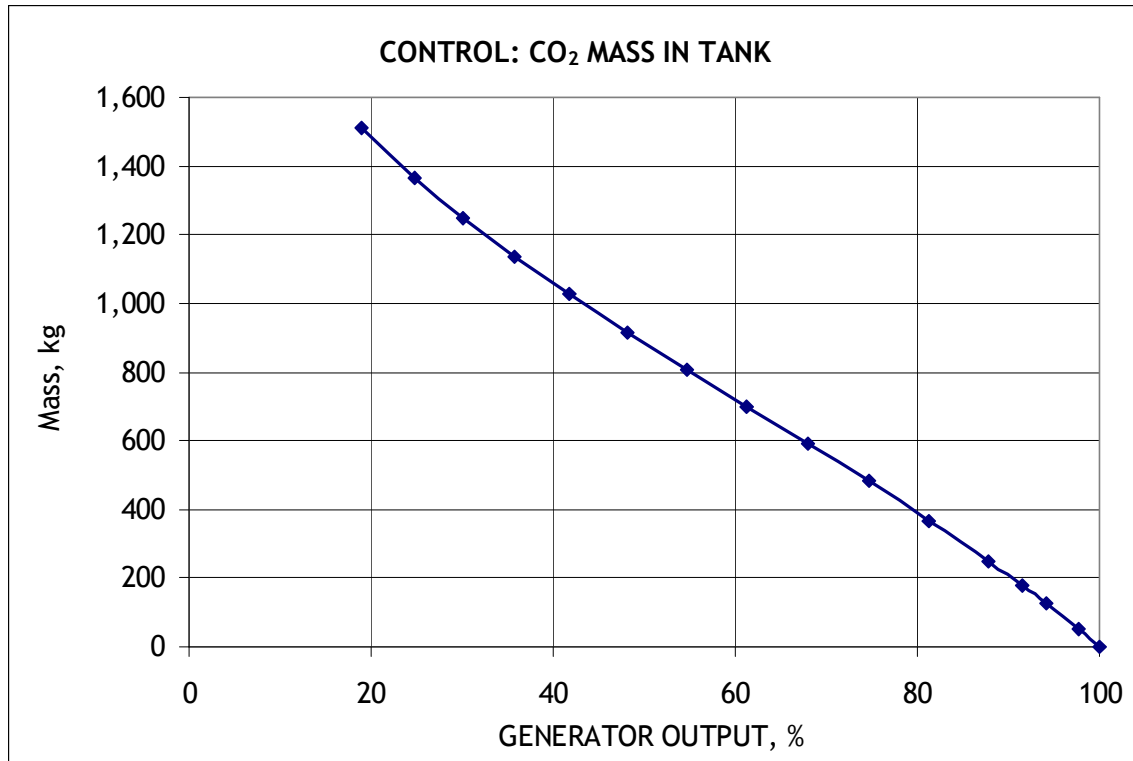


Figure 18. Inventory Accumulation in Tank and Tank Pressure for Different Tank Total Volumes.

Turbine Inlet Valve Control

Under this control mechanism, the pressure ratio in the turbine is reduced by introducing a pressure drop before the turbine by means of a throttle valve. As a result, the turbine pressure ratio decreases, while the compressor pressure ratio increases (Figure 19). Since centrifugal compressors can achieve a significantly lower pressure ratio before stall compared to axial designs (Figure 15), compressor stall is predicted earlier at approximately 50 % load. This can be seen from the plot of the stall parameter in Figure 18. Stall corresponds to a value of the stall parameter equal to unity. The stall parameter for Compressor No. 2, f_{stall} , approaches unity at a turbine inlet valve pressure drop of about 5 MPa at which the generator load demand is about 50 % nominal. The STAR-LM system with axial compressors reached about 35 % load before the onset of a compressor stall.

Summary of Load Following Analysis for SSTAR

The increased operating range of the centrifugal compressors helps widen the effective range of the control mechanisms in terms of staying away from compressor stall or choking conditions. However, the flatter pressure ratio curves for centrifugal compressors introduces new limitations on the control ranges. Overall, the ranges of the control mechanisms for the S-CO₂ Brayton cycle with centrifugal compressors are close to those calculated previously for the cycle with axial compressors. In particular, a combination of control mechanisms is still required to effectively control the S-CO₂ Brayton cycle with centrifugal compressors over the entire operating range.

Inventory control combined with turbine bypass control is recommended for higher loads of 35 to 100 % nominal. Calculations show that the SSTAR plant could be controlled between 35 and 0 % load by means of turbine bypass control. Figure 20 shows the results of the control calculations for the entire range of load.¹ Inventory control together with turbine bypass control are followed by turbine bypass control below 35 % load. Since the calculations assume no active reactor control power by the motion of control rods, autonomous reactor control is demonstrated for the SSTAR reactor with a S-CO₂ Brayton cycle power converter over the entire range of grid load demand.

¹ The solution becomes harder to converge for very low loads. For this reason, no solution is obtained for loads below about 7 % in Figure 20. However, no physical reasons were found which might limit the load to 7 %. Thus, it is believed that the control strategy can be applied from 100 % nominal load all the way down to 0 % load.

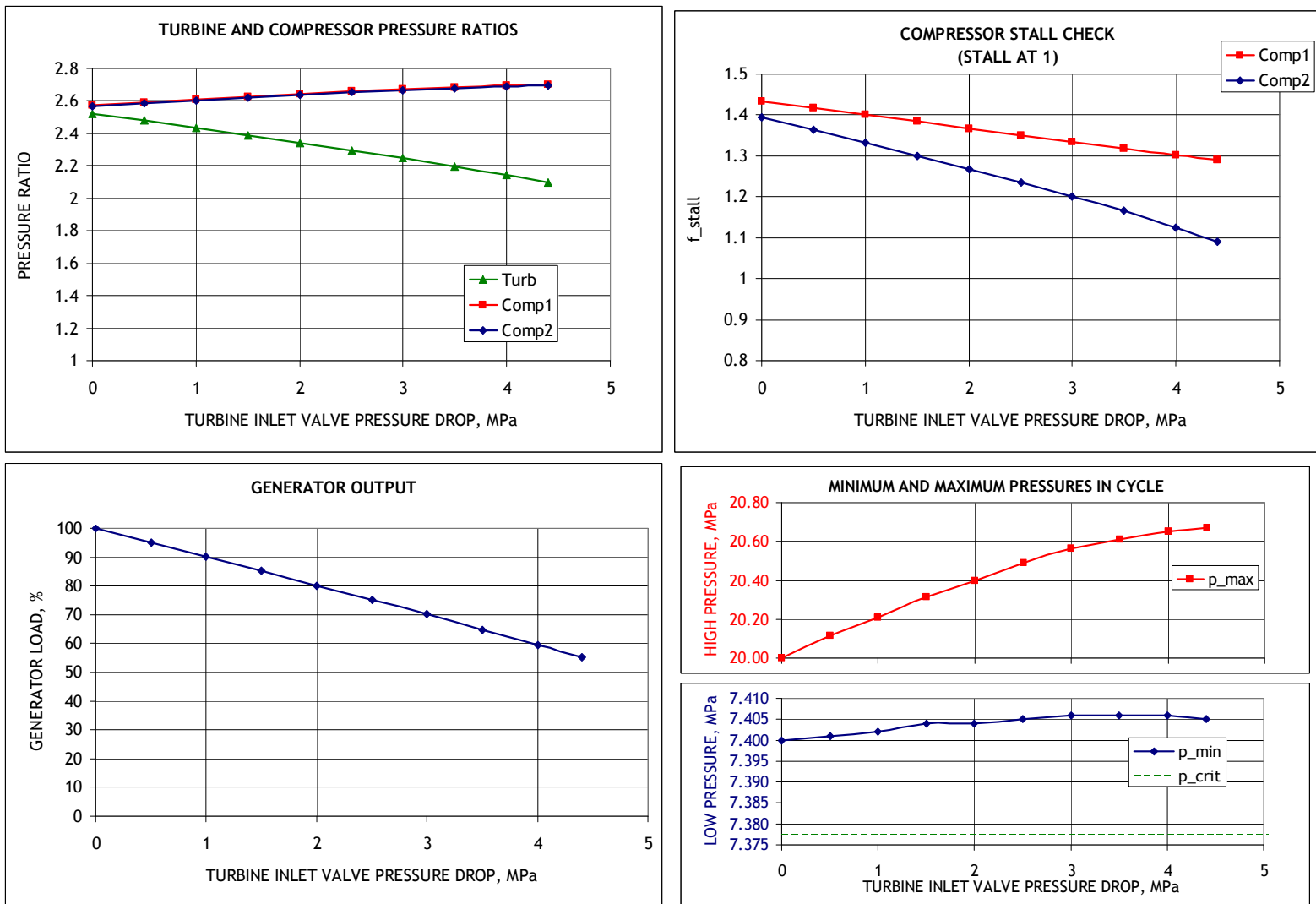


Figure 19. SSTAR Turbine Inlet Valve Control.

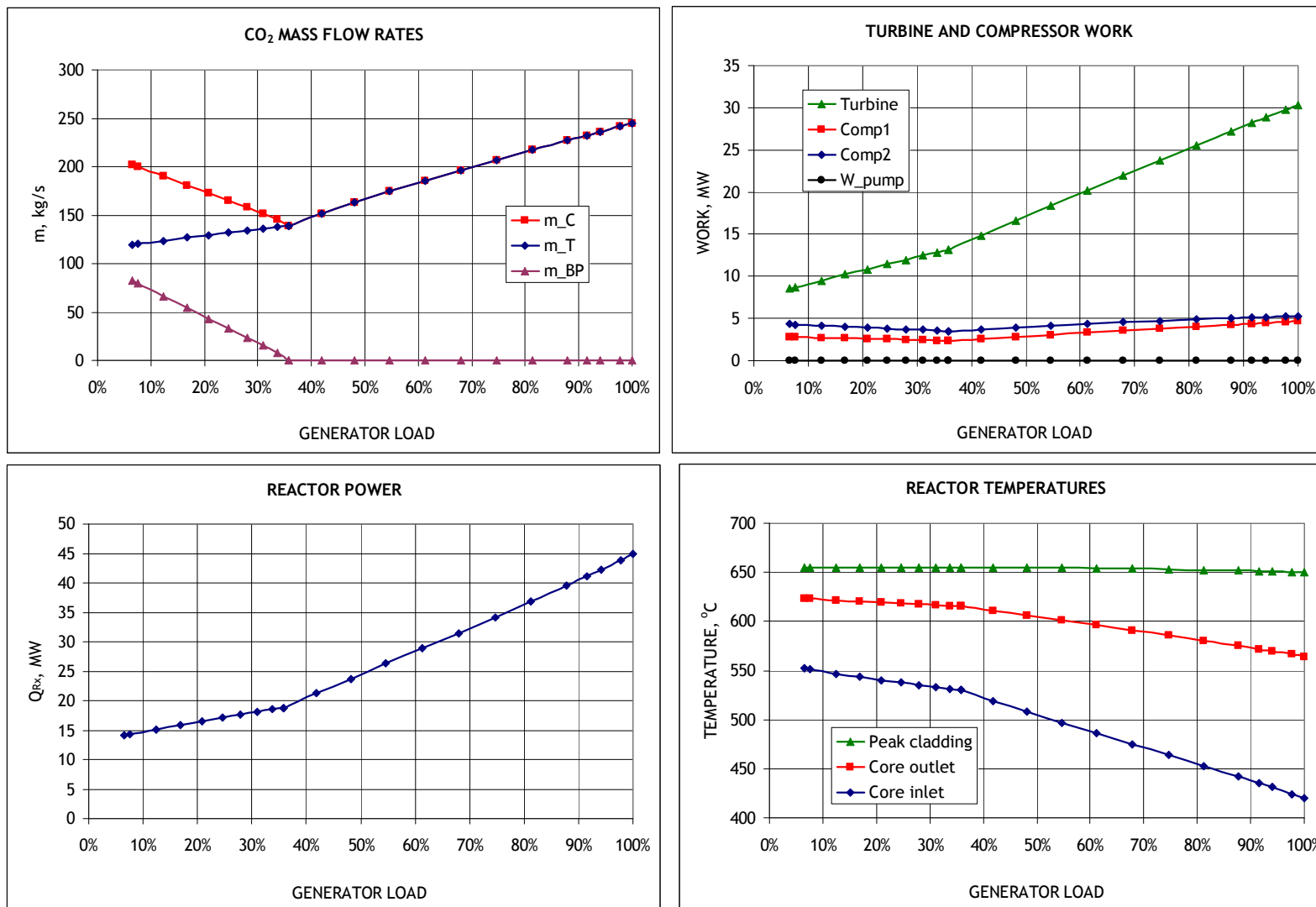


Figure 20. Combination of Inventory and Turbine Bypass Controls.

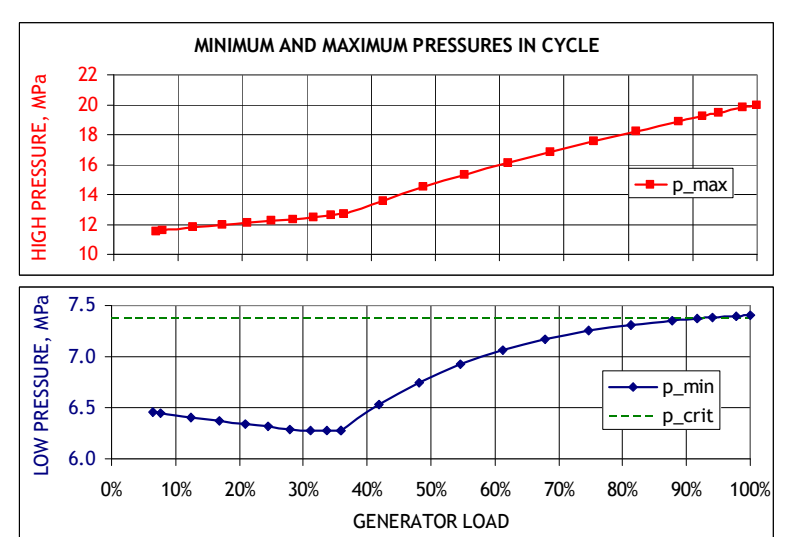
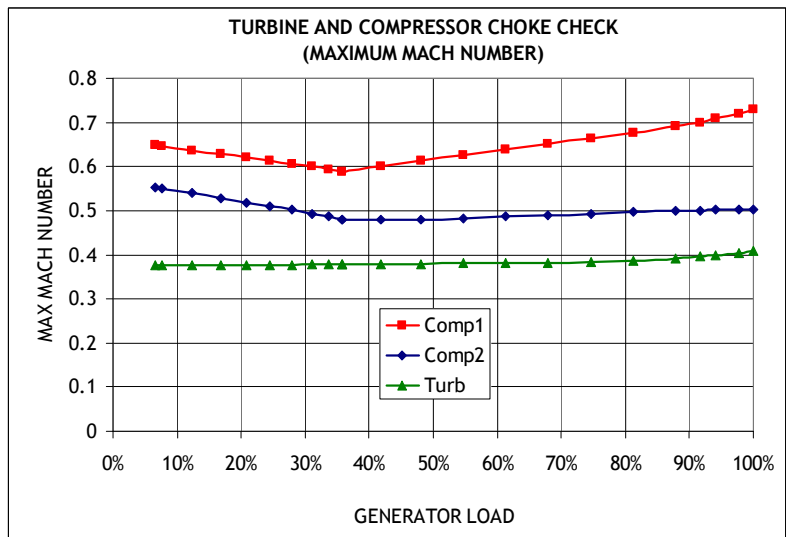
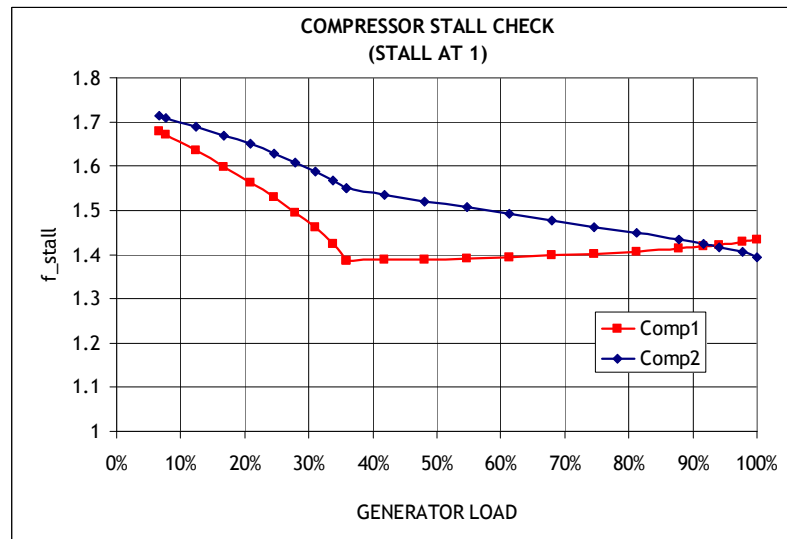
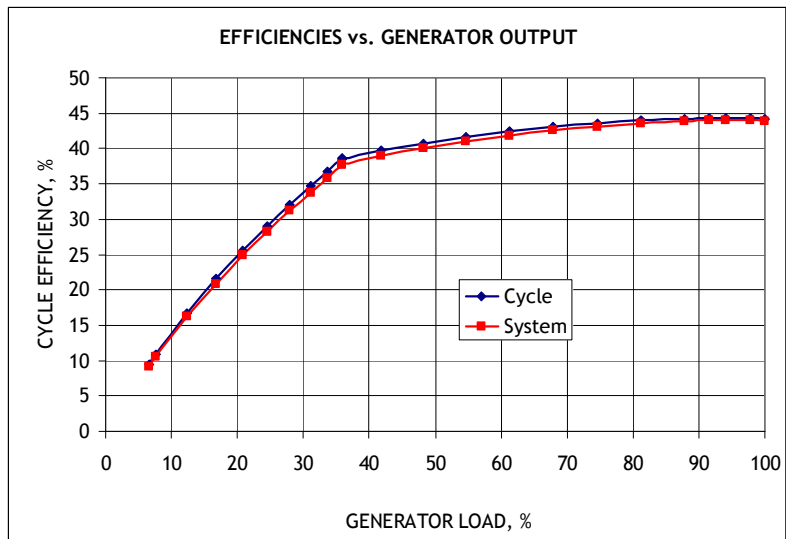


Figure 20 (Continued). Combination of Inventory and Turbine Bypass Controls.

2.2.3. SSTAR Reactor Autonomous Load Following Reactivity Feedback Coefficient Assessment

Reactivity feedback coefficients for the 30-year lifetime SSTAR core were calculated by Sang Ji Kim. The reactor system temperatures attained as the reactor power adjusts itself to autonomously follow changes in heat removal from the reactor system are dependent upon the values of the reactivity feedback coefficients. To estimate the effects of the reactivity coefficients on the reactor behavior (temperatures and coolant flow rate) under autonomous load following, a quasi-static load following analysis was carried out for SSTAR. The calculations show how the reactor system temperatures vary when the reactor power changes. In transitioning from one steady state to another steady state, the change in the total reactivity is zero; that is, the temperatures are such that the incremental reactivity contributions from fuel Doppler, axial expansion, core radial expansion, and coolant density are compensating to produce a zero net change in the total reactivity. In the analysis, it is assumed that there is no external reactivity insertion such as from the insertion or withdrawal of control rods. The coolant flow rate is recalculated for each power level consistent with natural circulation heat removal of the core power.

Table 4 shows the reactivity coefficients calculated for the current SSTAR 30-year lifetime core configuration for beginning of cycle (BOC), peak of cycle (POC), and end of cycle (EOC). Figures 21 through 23 show the temperature response of the reactor for the calculated values of the reactivity feedback coefficients (Figure 21) and for the calculated core radial expansion coefficient enhanced by factors of two (Figure 22) and three (Figure 23). Enhancement of the core radial expansion feedback may be achieved through core mechanical design features. A simple example of a mechanical device that can enhance the core radial expansion feedback is the incorporation of grid spacers having a higher coefficient of thermal expansion than the mainly ferritic/martensitic cladding. The grid spacer material must be compatible with Pb at the core temperatures and have sufficient irradiation stability.

It follows from Figures 21 through 23 that autonomous load follow would not work for the calculated reactivity feedback coefficients, since achieving lower power levels would require temperatures that are too high. Enhancement of the core radial expansion reactivity feedback coefficient by a factor of two would be sufficient to keep the peak cladding temperature at approximately the nominal steady state limit of 650 °C during reductions in power from 100 % nominal. However, the coolant core outlet temperature would increase in this case. If it were desired to hold the core outlet temperature at approximately the nominal steady state value, then the radial expansion reactivity feedback coefficient should be increased by a factor of three, as shown in Figure 23. Figure 24 shows an example of how the enhancement of the radial expansion coefficient by a factor of two affects the reactor temperatures under autonomous load following; the temperatures are shown for the case of turbine bypass control for the POC reactivity feedback coefficients.

For the load following calculations involving control of the S-CO₂ Brayton cycle plant discussed in the previous section, the radial expansion reactivity feedback coefficient was enhanced by a factor of two compared to the value reported in Table 4.

Table 4. SSTAR Reactivity Feedback Coefficients

Coefficient	Value, cents/°C		
	BOC	POC	EOC
Coolant density	0.196	0.304	0.301
Radial expansion	-0.15	-0.15	-0.15
Axial expansion	-0.08	-0.07	-0.07
Fuel Doppler	-0.08	-0.08	-0.08

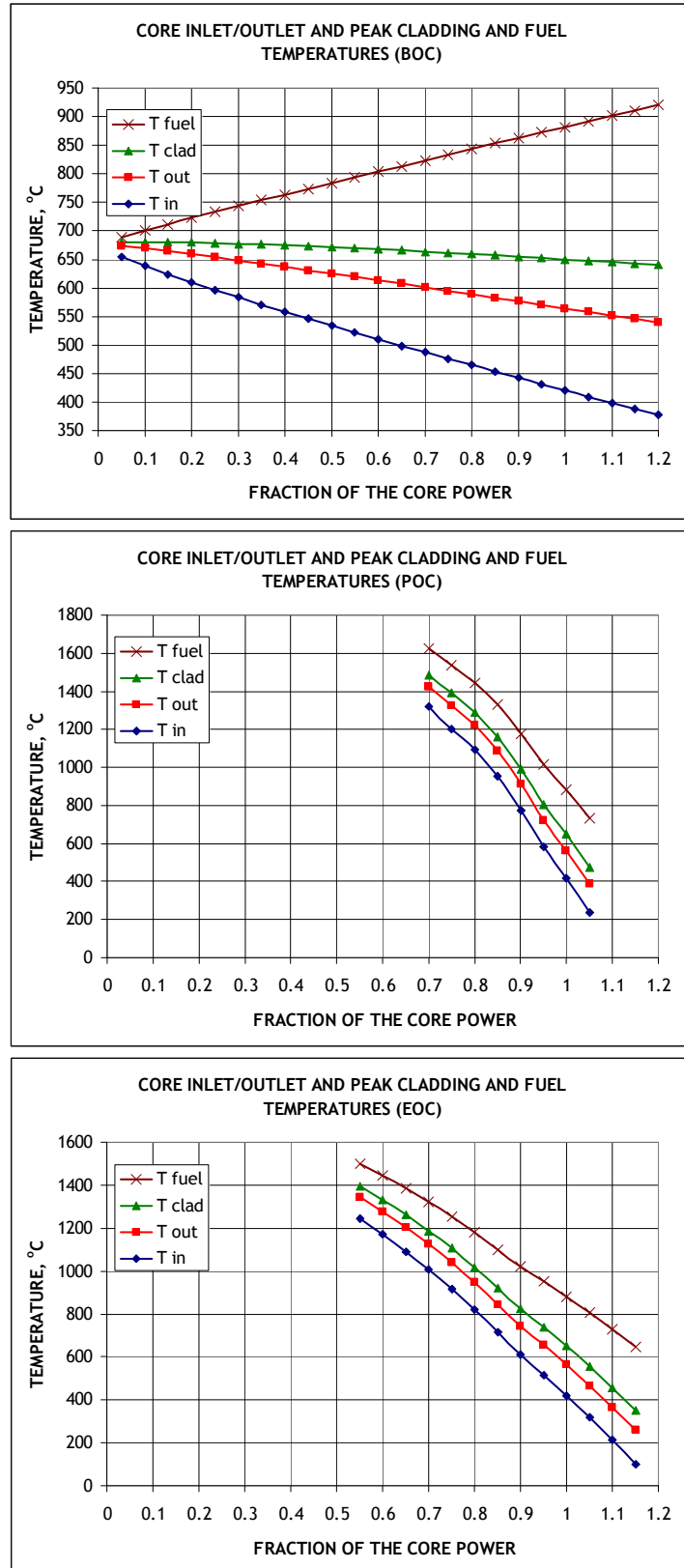


Figure 21. SSTAR Temperatures During Load Following for BOC, POC, and EOC with Un-enhanced Radial Expansion Reactivity Feedback Coefficient.

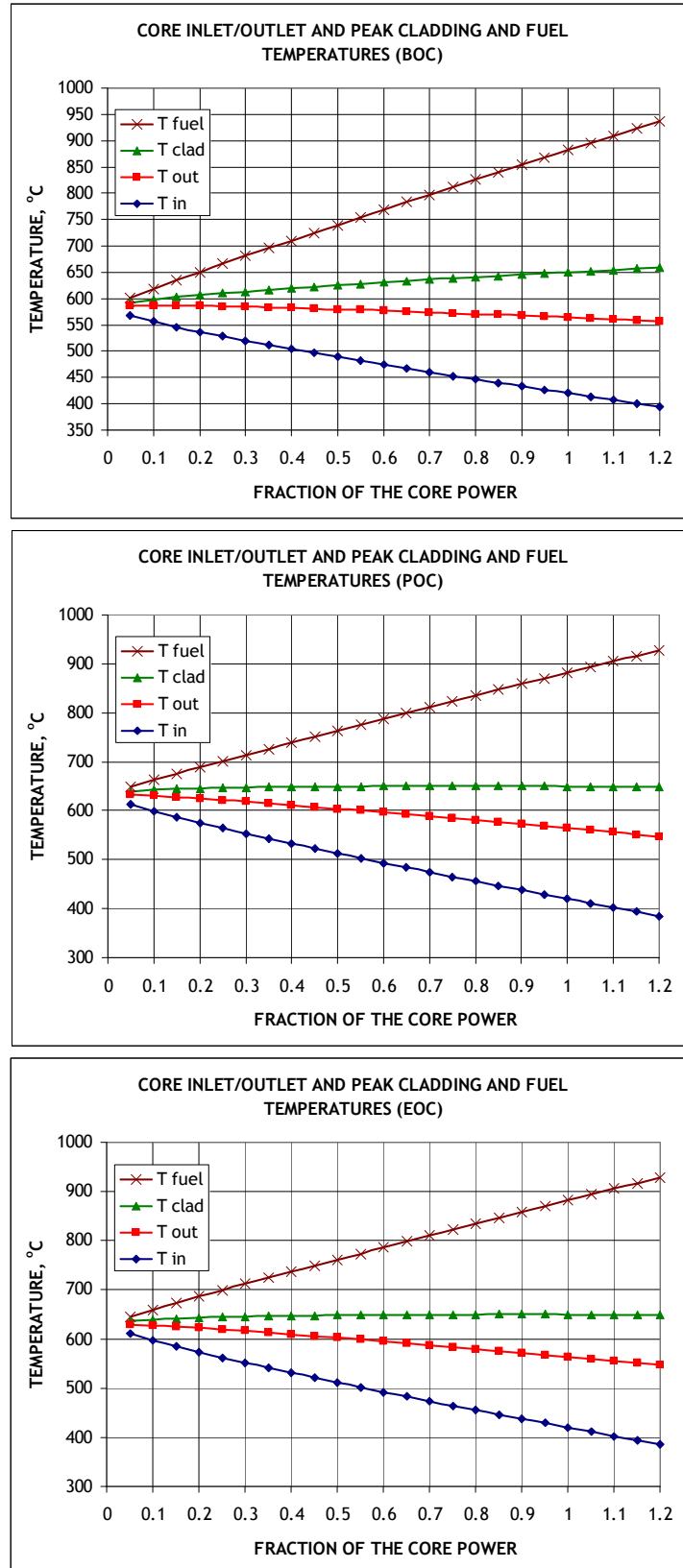


Figure 22. SSTAR Temperatures During Load Following for BOC, POC, and EOC with Radial Expansion Reactivity Feedback Coefficient Enhanced by a Factor of Two.

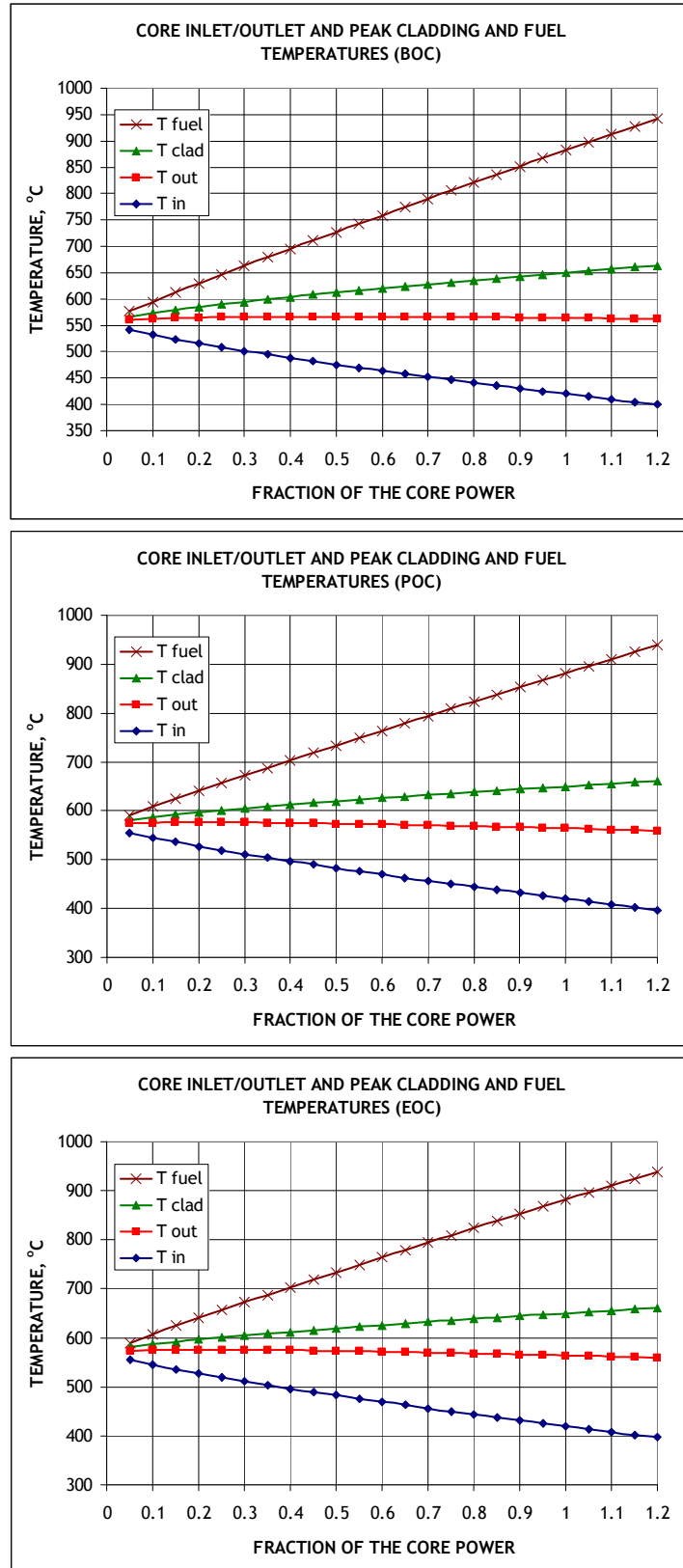
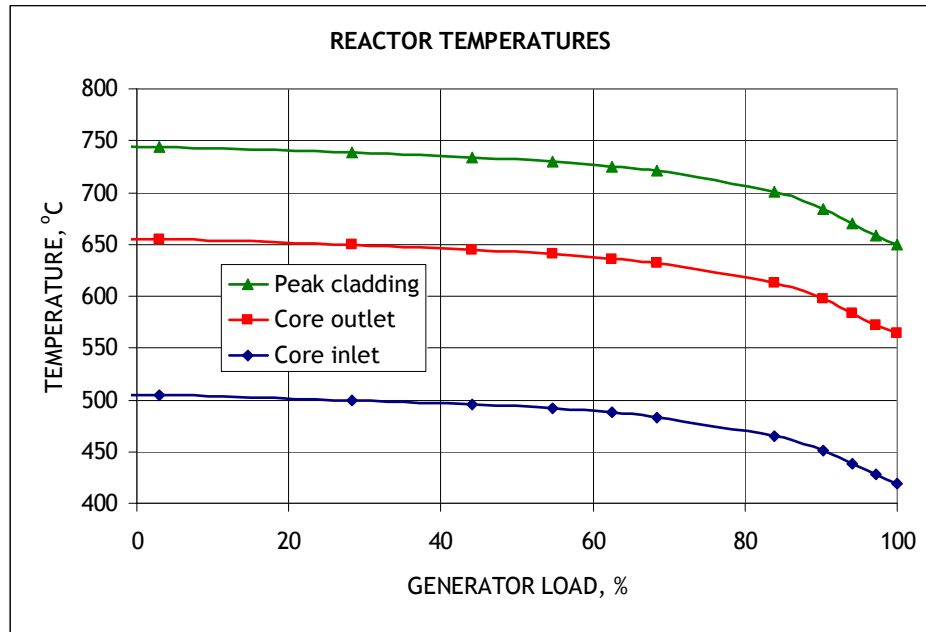
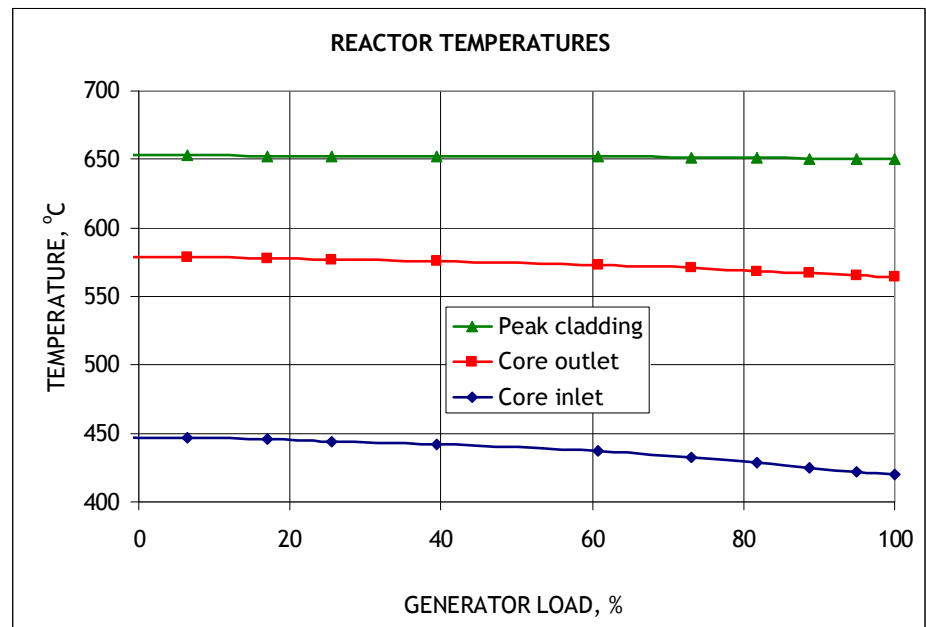


Figure 23. SSTAR Temperatures During Load Following for BOC, POC, and EOC with Radial Expansion Reactivity Feedback Coefficient Enhanced by a Factor of Three.



a)



b)

Figure 24. Reactor Temperatures under Load Following by Means of Turbine Bypass Control for Un-enhanced (a) and Enhanced (b) Core Radial Expansion Reactivity Feedback Coefficients.

2.2.4. LFR Fuel Pin Design Computer Code Development

Development of a new fuel pin design computer code was initiated at ANL. The motivation for this new development was the realization that it may be feasible to reliably calculate the long-term wastage of cladding due to corrosion using modeling of the type carried out by Ning Li and his colleagues based upon Tedmon's equation and reported in Section 3. At least in principle, one can calculate the diminishing effective thickness of cladding remaining and providing mechanical strength as a function of time, given the cladding temperature and the conditions of the flowing heavy liquid metal coolant adjacent to the cladding. The remaining thickness of cladding loses its strength over time mainly due to thermal creep. The creep loading is the result of the hoop stress loading from the pressure exerted by the fission gas released from the fuel and collected within the free volume of the fission gas plenum and porosity in the fuel. The hoop stress and fission gas pressure loadings generally increase with time due to the cumulative effects of gas release. In general, one is interested in the fuel pin inside the core that undergoes the most severe creep damage and, therefore, would be the first to fail if subjected to continuing loadings. Thus, one is led to investigate the "hottest channel" in the core and the fuel pin having the highest burnup of the fuel. For a LFR such as SSTAR, the situation is not straightforward because the locations of the peak power and peak burnup migrate radially across the core with time. In particular, at the beginning of cycle (BOC), the fuel pins having the peak power, burnup, and cladding temperature are located at radii roughly midway between the core centerline and edge. As time goes by, the location of the peak power/burnup moves inward towards the centerline such that different pins temporarily become the pins having the highest temperatures and burnup. Thus, one must calculate the time history of the fission gas loading, creep, and corrosion for a number of fuel pins at different radial locations in the core, in order to determine which fuel pin cladding undergo the greatest extent of damage. This means that power and burnup profiles across the core are needed as functions of time throughout the core lifetime.

The new time dependent fuel pin design computer code is focused on nitride fuel, ferritic/martensitic (F/M), silicon-enhanced F/M, or oxide dispersion-strengthened (ODS) steel, and oxidation-induced corrosion by oxygen-containing lead-bismuth eutectic (LBE) or Pb. An initial version of the transient computer code has been developed that integrates together time dependent fission gas release over the fuel pin height dependent upon the local peak fuel temperature and burnup, fission gas pressure dependent upon the cumulative gas release plus initial fill gas and temperature, local thermal creep of the cladding as represented by a law providing the time to rupture as a function of the stress, the local thickness of unoxidized cladding remaining dependent upon the simultaneous penetration of an oxide layer into the cladding metal and dissolution of the oxide layer trailing surface by the heavy liquid metal coolant. Input to the code includes the time dependent power and burnup rate at a number of radial locations in the core. The extent of cladding creep damage and failure are evaluated in terms of a cumulative damage fraction in the initial code version. Time to failure versus stress laws were identified or developed for HT9 and T91 F/M steels and implemented into the code. Time dependent power and burnup rate was obtained from a REBUS-3 calculation for the 30-year SSTAR core for a number of locations and number of time throughout the core lifetime. In a later

version, time dependent creep strain of the cladding shall also be calculated with a failure criterion based upon attainment of a specified total strain.

It is envisioned that the fuel pin design computer code shall be used to determine the required initial cladding thickness that shall enable all of the fuel pins to survive the core lifetime at the calculated thermal hydraulic conditions. As the cladding thickness is increased, the core neutronics is affected because of the need of additional steel in the core and less coolant. The thermal hydraulic design is affected because the coolant volume fraction is decreased reducing the effectiveness of natural circulation heat removal. It was planned to apply the fuel pin design computer code to the 30-year lifetime core with F/M steel cladding consisting of HT9 or T91. However, the coefficients for Tedmon's equation presented in Section 3 indicate that at temperatures of 550 °C or greater the corrosion of cladding would erode 3 or 4 mm of cladding or more. Thus, it was decided to incorporate cladding of Si-enhanced F/M stainless steel (e.g., like the Russian EP-823) for which the oxide layer dissolution rates are expected to be significantly lower. Unfortunately, the coefficients for EP-823 are provided only at 470 °C in Section 3.

In FY 2007, the focus shall be on development of LFR test demonstrator and exportable fast reactor concepts operating at lower temperatures with T91 codified material or HT9. The fuel pin design model shall be used to determine the required thickness of cladding for short exposures (e.g., three or four year target).

2.2.5. SSTAR Safety Design Approach

The SSTAR safety design approach is based upon the defense-in-depth principle of providing multiple levels of protection against the release of radioactive materials by means of: 1) design to achieve a high level of reliability such that specific traditional accident initiators are eliminated or accident initiators are prevented from occurring; 2) provision of protection in the event of equipment failure or operating error; and 3) provision of additional protection of the public health and safety in an extremely unlikely event that is not expected to occur during the lifetime of the plant or which was not foreseen at the time that the plant was designed and constructed. The inherent safety features of SSTAR take advantage of the key inherent properties of Pb coolant, transuranic nitride fuel, and a fast neutron spectrum core together with specific design options including a pool reactor vessel containing all major primary coolant system components and natural circulation heat transport.

2.2.6. SSTAR Inherent Safety Features

The Pb primary coolant has a high boiling temperature of about 1740 °C which is well above the temperatures at which the stainless steel structures lose their strength and melt. The Pb is therefore a low pressure coolant and does not flash should a leak develop in the primary coolant system boundary. All major primary system components including the core and Pb-to-CO₂ heat exchangers are contained inside of the reactor vessel which is surrounded by a guard vessel. The coolant level inside of the reactor vessel is such that in

the event of a reactor vessel leak the faulted level of coolant contained by the guard vessel always exceeds the Pb entrances to the Pb-to-CO₂ heat exchangers. The lack of coolant flashing or boiling due to the high Pb boiling temperature combined with the pool system configuration and guard vessel preclude the loss of primary coolant. It also assures that heat removal from the core and heat transfer to the in-vessel heat exchangers or the vessel wall for heat removal by the RVACS continues by means of natural circulation of single-phase primary Pb coolant.

The Pb coolant is calculated not to react chemically with the working fluid above about 250 °C which is well below the Pb melting temperature of 327 °C. In particular, there is no formation of combustible gas or exothermic energy release. Lead does not react vigorously with either water or air. Compatibility of Pb and the working fluid makes it possible to eliminate the need for an intermediate cooling circuit enhancing plant reliability.

Experiments carried out at the Forschungszentrum Karlsruhe have shown that iodine, cesium, and cesium-iodide (i.e., fission products with low melting and boiling points) are absorbed and immobilized by lead-bismuth eutectic at temperatures of 400 and 600 °C. Cesium forms inter-metallic compounds in LBE while iodine forms PbI₂.

Lead has a low absorption of neutrons. This permits the core to be opened up by increasing the coolant volume fraction without a significant reactivity penalty. Increasing the coolant volume fraction increases the hydraulic diameter for coolant flow through the core reducing the core frictional pressure drop. As a result, natural circulation is more effective and can transport a greater core power. It is possible to design LFRs in which natural circulation is effective at power levels exceeding 100 % nominal eliminating the need for main coolant pumps. Eliminating main coolant pumps eliminates loss-of-flow accident initiators. The open lattice core configuration with wide openings for crossflow eliminates flow blockage accident initiators in which the coolant flow entering at the bottom of the core is postulated to be locally blocked.

The high heavy liquid metal coolant density ($\rho_{\text{Pb}} = 10400 \text{ Kg/m}^3$) limits void growth and downward penetration following postulated in-vessel heat exchanger tube rupture such that void is not transported to the core but instead rises benignly to the lead free surface through a deliberate escape channel between the in-vessel heat exchangers and the vessel wall.

Transuranic nitride fuel offers a number of potential benefits provided that it can be demonstrated to perform suitably well in steady state and transient irradiation tests and can be reliably manufactured to meet the performance requirements. The transuranic nitride fuel has a high thermal conductivity which when combined with bonding of the fuel pellets to the cladding by means of liquid Pb between the pellets and cladding reduces the peak fuel temperatures during normal operation and accidents. This reduces the stored energy in the fuel and decreases the positive reactivity contribution resulting from cooldown of the fuel as the fuel and coolant temperatures equilibrate during accidents as the core power decreases.

Transuranic nitride fuel has a high decomposition temperature estimated to exceed 1350 °C such that the fuel maintains its integrity at temperatures above which the stainless steel structural materials lose their strength or melt.

Nitride fuel is expected to be compatible with both the Pb bond and ferritic/martensitic stainless steel cladding.

Nitride fuel has a high atom density making it possible to reduce the volume which must be occupied by fuel further enabling increase of the coolant volume fraction without loss of the ability to achieve a core internal conversion ratio of unity and a low burnup reactivity swing which in turn reduces the effects of rod withdrawal accident initiators.

Nitride fuel has a low volumetric swelling per unit burnup making it possible to reduce the size of the gap between fuel pellets and cladding filled by the Pb bond further facilitating increase of the coolant volume fraction.

Nitride fuel has a low fission gas release per unit volume. This reduces the thermal creep of the cladding resulting from the hoop stress loading due to internal pressurization of the fuel pin by released fission gas.

The fast neutron spectrum core with Pb coolant and transuranic nitride fuel has strong reactivity feedbacks which provide significant negative reactivity upon heatup or equilibration of system temperatures. The strong reactivity feedback reduces the core power to match the heat removal from the reactor system inherently shutting down the reactor, in the event that the two shutdown systems fail to scram the reactor.

The strong reactivity feedback of the fast neutron spectrum core with Pb coolant and transuranic nitride fuel enable autonomous load following whereby the core power adjusts itself through inherent mechanisms to match the heat removal from the reactor system without operation of control rods thereby simplifying operation and eliminating potential operator errors.

The low burnup reactivity swing of the 30-year lifetime fast neutron spectrum core decreases the excess reactivity requirements reducing the amount of reactivity insertion accompanying the unintended withdrawal of one or more control rods.

2.2.7. SSTAR Passive Safety Systems

SSTAR currently incorporates a single safety grade emergency heat removal system which is the Reactor Vessel Auxiliary Cooling System (RVACS). The RVACS cools the exterior of the guard vessel by natural circulation of air which is always in effect. Because the RVACS represents only a single safety grade system, it would be required to have a high reliability with respect to seismic events or sabotage. For example, a seismic event could result in blockage of air flow channels. At particular sites, flooding or dust storms might be factors. It is planned to add multiple safety grade passive Direct Reactor

Auxiliary Cooling System (DRACS) heat exchangers inside of the reactor vessel to provide for independent and redundant means of emergency heat removal.

A safety grade passive pressure relief system protects the primary coolant system from overpressurization enabling CO₂ to escape from the primary coolant system, in the event of heat exchanger tube rupture.

2.2.8. SSTAR Active Safety Systems

SSTAR incorporates two independent and redundant safety grade active shutdown systems. The core layout in Figure 6 shows the primary and secondary control rod locations; primary rods are colored magenta and secondary rods blue.

2.2.9. Role of SSTAR Inherent Safety Features and Passive and Active Safety Systems in Safety Design Approach

Level 1: Design to Achieve a High Level of Reliability such that Specific Traditional Accident Initiators are Eliminated or Accident Initiators are Prevented from Occurring

The inherent safety features of Pb coolant, nitride fuel, and a fast spectrum core together with natural circulation heat transport and the pool vessel configuration reduce the probability of failures through the elimination of reliance upon components, systems, or operators that would otherwise need to be considered as sources of failure. Specific traditional postulated accidents such as loss-of-flow or local flow blockage are eliminated.

The cladding and structures are protected from significant corrosion by the Pb coolant by control of the dissolved oxygen potential in the coolant within a suitable regime that avoids the formation of lead oxide while allowing protective Fe₃O₄ solid oxide layers to initially form upon structures at lower temperatures. The systems for monitoring the dissolved oxygen potential and maintaining the oxygen level in the desired regime shall be designed to have a high reliability such that the probability of failure of the systems in modes that could threaten the long-term integrity of the cladding or other structures, or result in the formation of solid debris that might locally block flow channels is sufficiently low.

Level 2: Provision of Protection in the Event of Equipment Failure or Operating Error

Due to the inherent safety features and passive safety design options of SSTAR, the expectation is that anticipated operational occurrences will not escalate into accidents. Although specific traditional postulated accidents such as loss-of-flow or local flow blockage are eliminated, other traditional postulated accidents such as reactivity insertion due to withdrawal of one or more control rods, loss-of-normal heat sink, heat exchanger tube rupture, loss-of-load, or station blackout remain. Due to the inherent safety features

of SSTAR, the core and heat exchangers remain covered by the molten Pb coolant and natural circulation heat transport removes the core power which is removed from the reactor system either by the normal heat removal paths or by the RVACS. The system fuel and coolant temperatures remain within acceptable values well below the temperatures at which the structures begin to lose their strength or at which failure of the cladding could occur. There is no need for reliance upon active systems or operator actions to provide for cooling of the core or heat removal from the reactor system.

Traditionally, escalation into a more serious event requires the occurrence of additional failures following the onset of the accident initiator. For liquid metal-cooled fast reactors, an example of an additional failure in addition to the accident initiator has been the assumption of failure to scram the reactor by the primary and secondary shutdown systems. For SSTAR, it is not necessary for either of the two independent and redundant shutdown systems to operate or for operators to take action to insert control rods; the inherent feedbacks of the fast spectrum core with Pb coolant and nitride fuel cause the power level to decrease such that the core power matches the heat removal from the reactor system. The reactor core self regulates the power level to match the heat removal through either the normal heat removal path involving the in-vessel Pb-to-CO₂ heat exchangers or the emergency heat removal path through the RVACS. If one or more in-vessel Pb-to-CO₂ heat exchanger tubes were to fail, the passive pressure relief system would release CO₂ from the reactor system protecting the reactor vessel and upper closure head from overpressurization. If the reactor vessel were to fail in addition to the accident initiator, the guard vessel would retain the primary Pb coolant such that the core and in-vessel heat exchangers still remain covered by single-phase Pb primary coolant. If the normal heat removal path or shutdown heat removal path were to fail, then the RVACS would remove the power generated in the core and transported to the reactor vessel by natural circulation of the Pb coolant. As discussed above, multiple DRACS heat exchangers shall also be incorporated into the reactor vessel to enhance the reliability of emergency heat removal beyond that provided by the RVACS. Therefore, it is not expected that a second failure would result in escalation into a more serious event in terms of release or transport of radioactivity from the fuel pins.

Level 3: Provision of Additional Protection of the Public Health and Safety in an Extremely Unlikely Event that is not Expected to Occur during the Lifetime of the Plant or which was Not Foreseen at the Time that the Plant was Designed and Constructed

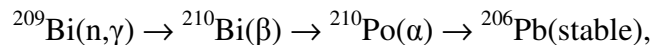
SSTAR incorporates a guard vessel surrounding the reactor vessel and an upper closure head which covers both the guard and reactor vessels. A hermetic seal is established between the upper closure head and the guard vessel. Thus, the guard vessel and upper closure head perform the function of a containment vessel surrounding the reactor vessel in retaining radioactivity as long as overpressurization of the guard vessel and upper closure head system does not occur. A containment structure is provided above the upper closure head. In the event of rupture of one or more Pb-to-CO₂ heat exchanger tubes, the pressure relief system would vent CO₂ into the volume of the containment structure.

It is an objective of SSTAR development to achieve an exclusion zone within the site boundary and to preclude the need for offsite emergency planning, in view of the small size of the reactor, the low pressure primary coolant, the capability of the fuel and coolant to retain fission products, the relative inertness of the primary coolant, as well as the lack of chemical reactivity of the primary coolant and working fluid which are expected to result in a low probability for radioactive material release. Thus, it is envisioned that the exclusion and emergency planning zones surrounding a SSTAR reactor may at the least be reduced in size relative to light water reactor designs having a similar power level.

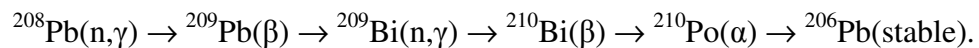
2.3. Estimate of Po-210 Production and Heat Source in Lead-Bismuth Eutectic Coolant

SSTAR utilizes Pb instead of lead-bismuth eutectic (LBE) as the primary coolant for two reasons. The first is reduction of the activity from the formation of ^{210}Po (Polonium-210) isotope by two to three orders of magnitude in going from LBE containing 55 wt % bismuth to Pb coolant which contains bismuth only as an impurity. The second is to eliminate dependence upon bismuth which may be a limited resource. The ^{210}Po is an alpha emitter and mainly represents a health hazard should it be released as during postulated accidents, refueling operations, replacement of in-vessel components, or leakages (e.g., from the active system for controlling the coolant dissolved oxygen potential or from the coolant purification system). The presence of ^{210}Po in the coolant also represents a distributed heat source. Recent investigations carried out in Italy of the amount of ^{210}Po that might be present in LBE coolant have identified the isotope as a potentially significant source of heat within the bulk coolant. This conclusion is not consistent with earlier estimates of ^{210}Po activity and heat source carried out at ANL. It was decided to take another look at ^{210}Po production and to make a new estimate of the potential heat source. The present analysis assumes a SSTAR reactor system that uses LBE instead of Pb coolant and makes use of neutron fluxes calculated for a previously investigated Pb-cooled SSTAR core.

The main ^{210}Po production chains in LBE and lead coolants are, respectively,



and



Lead coolant used in a LFR need not be pure Pb but could contain some Bi together with other impurities. Specific decay half-lives and energies are

β -decay of ^{210}Bi

Half-life: 5.013 days

Decay energy: 5.037 MeV,

β -decay of ^{209}Pb

Half-life: 3.253 hours

Decay energy: 0.644 MeV,

α -decay of ^{210}Po

Half-life: 138.376 days

Decay energy: 5.407 MeV.

The underlying reason for the much lower ^{210}Po activity in Pb relative to LBE is the much smaller neutron capture cross section in ^{208}Pb compared with ^{209}Bi , as shown in

Figure 25 which compares the cross sections from ENDF/B-VI. The capture cross sections in different nuclear data libraries differ significantly from each other. This is illustrated in Figure 26. A one-group cross section based on ENDF/B-VI is only 57 % of that based on the ENDF/B-V data. In view of the discrepancies between the nuclear data libraries, a re-evaluation of the Pb and Bi cross sections might be necessary for a more accurate evaluation of the activation of lead alloy coolants.

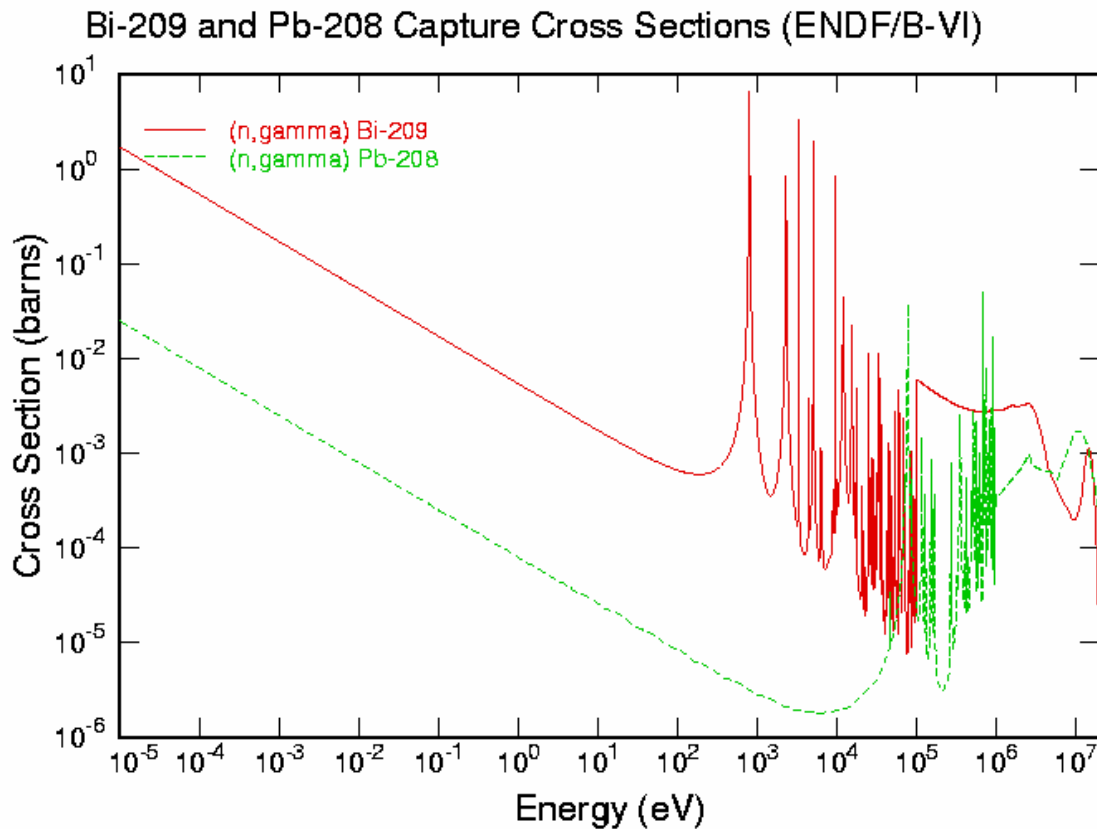


Figure 25. Neutron Capture Cross Section for ^{208}Pb from ENDF/B-VI Compared with That for ^{209}Bi .

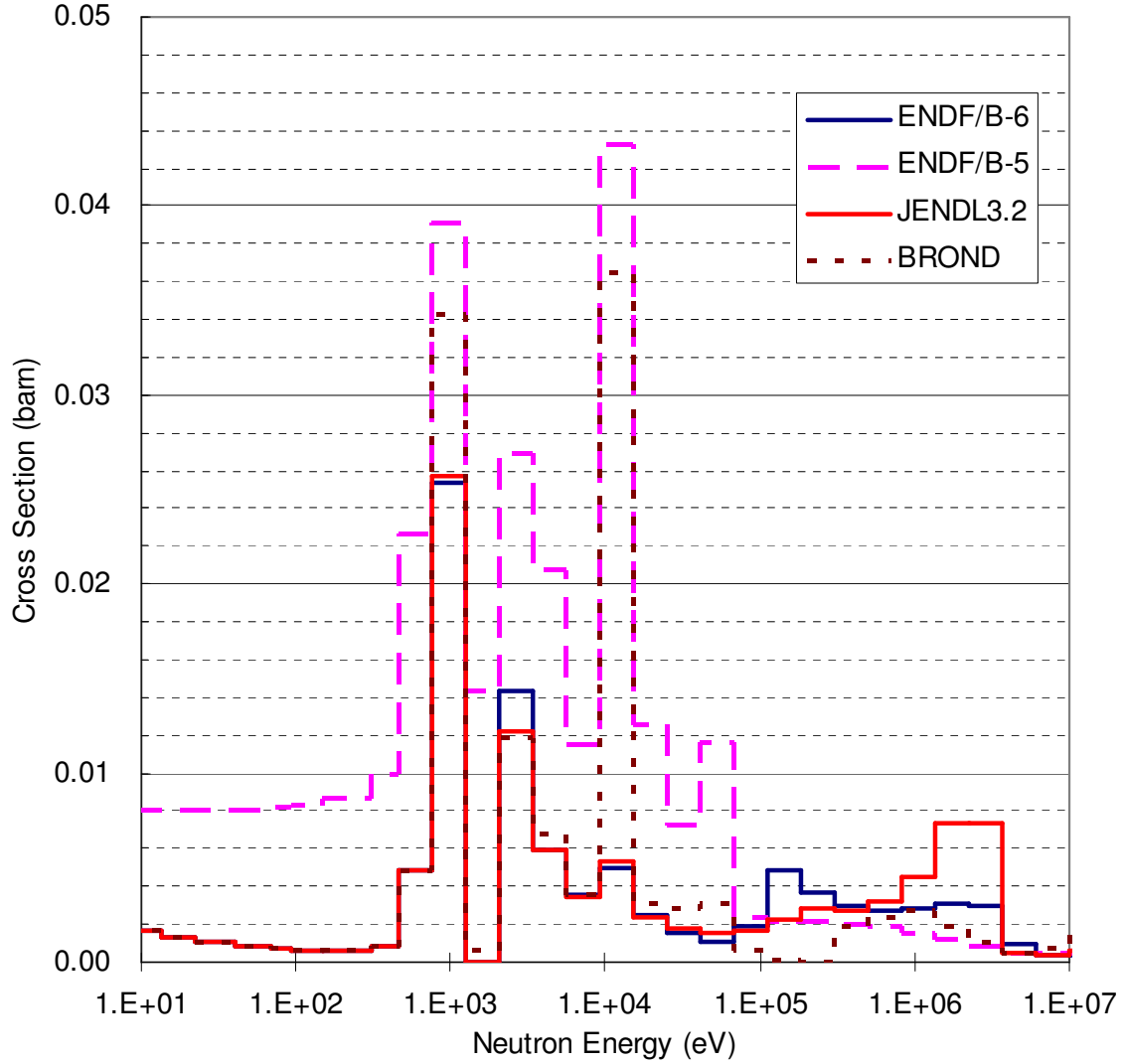


Figure 26. Neutron Capture Cross Sections for ^{209}Bi .

The average activity per unit volume in the coolant can be calculated from the equations,

$$\frac{d}{dt} \bar{N}_{Po} = \bar{N}_{Bi} \bar{\sigma}_{Bi} \bar{\phi} \frac{V_a}{V_t} - \lambda_{Po} \bar{N}_{Po}$$

$$\bar{\alpha}_{Po} = \lambda_{Po} \bar{N}_{Po} = \bar{N}_{Bi} \bar{\sigma}_{Bi} \bar{\phi} \frac{V_a}{V_t} (1 - e^{-\lambda_{Po} t})$$

where t = time, \bar{N} = average number of atoms per unit volume, $\bar{\sigma}$ = average one-group capture cross section, $\bar{\phi}$ = core-average one-group neutron flux, V_a = activation volume, V_t = total coolant volume, and λ = decay constant. The subscripts Po and Bi, respectively, denote ^{210}Po and ^{209}Bi . The total ^{210}Po activity and heat source in the primary coolant are given by

$$\alpha_{Po} = \bar{\alpha}_{Po} V_t = \bar{N}_{Bi} \bar{\sigma}_{Bi} \bar{\phi} V_a (1 - e^{-\lambda_{Po} t}) = \frac{\bar{N}_{Bi}}{\bar{N}_F} \frac{\bar{\sigma}_{Bi}}{\kappa \sigma_f} \frac{V_a}{V_c} P (1 - e^{-\lambda_{Po} t})$$

$$H_{Po} = E_\gamma \alpha_{Po} = \frac{\bar{N}_{Bi}}{\bar{N}_F} \frac{E_\gamma \bar{\sigma}_{Bi}}{\kappa \sigma_f} \frac{V_a}{V_c} P (1 - e^{-\lambda_{Po} t})$$

where P = total reactor power, E_γ = decay energy, $\kappa \sigma_f$ = energy release per fission times average one-group fission cross section, and N_F = average fuel atomic density.

The number density of ^{210}Po atoms and the ^{210}Po activity per unit volume are proportional to the ratio of the volume in which ^{209}Bi and ^{208}Pb are activated to the total coolant volume reflecting the fact that activation takes place only in the core region plus the volume immediately surrounding the core where the neutron flux level is significant. The size of the activation volume in the equations represents the effects of shielding by steel structures and the coolant itself in decreasing the local neutron flux outside of the core. The total activity and heat source are proportional to the rated core power. Thus, the total ^{210}Po activity and heat source are mainly determined by the ratio of the activation and total coolant volumes, the total core power, and the coolant-to-fuel volume ratio.

The neutron flux was obtained from previous calculations for a SSTAR 20-year lifetime 45 MWt core pre-conceptual design. Figure 27 shows the core layout assumed in the neutronics nodalization; major design and performance conditions are provided in Table 5.

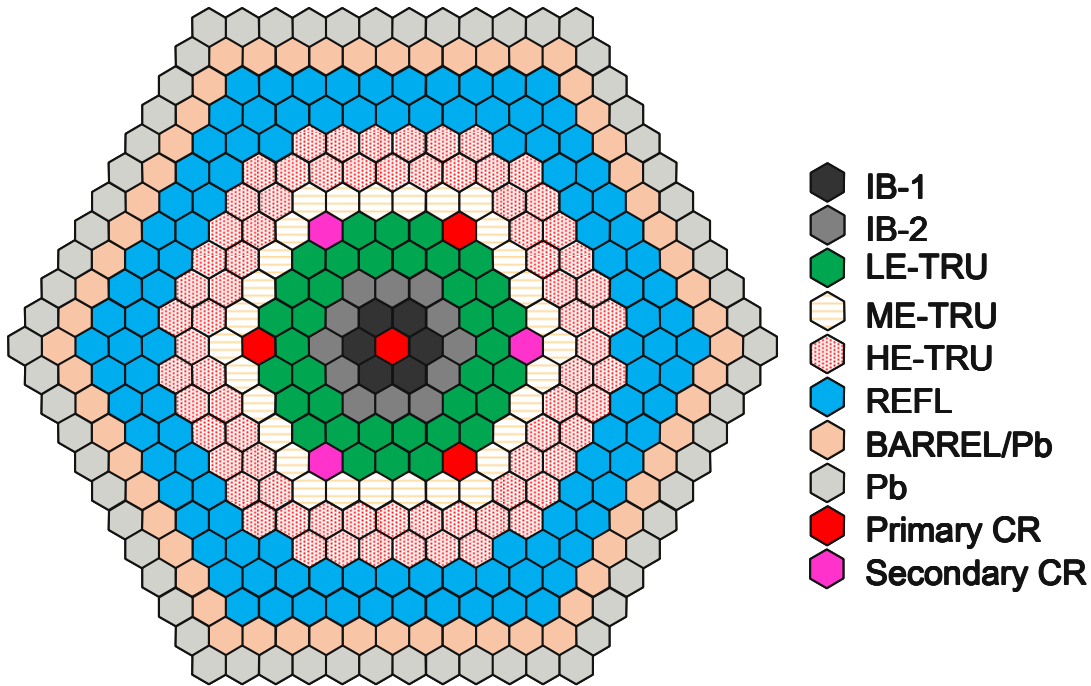


Figure 27. SSTAR Core Layout Nodalization for Evaluation of ^{210}Po Production – The Core Incorporates Five Enrichment Zones and Two Independent Control Systems.

Table 5. Conditions for SSTAR Core Assumed for Analysis of ^{210}Po Production

Core Power, MWt	45
Core Lifetime, years	20
Fuel Type	U-TRU-N
TRU Feed Cooling Time, years	25
Fuel Volume Fraction	0.55
Fuel Pin Diameter, cm	2.5
Fuel Pin Pitch-to-Diameter Ratio	1.121
^{10}B a/o in B_4C Control Rods	19.9
TRU Feed, Kg	750
Depleted U Feed, Kg	3671
Total Heavy Metal Feed, Kg	4421
Discharged Pu, Kg	632
Discharged MA, Kg	100
Discharged U, Kg	3348
Average Power Density, KW/L	72
Peak Power Density, KW/L	120
Specific Power, KW/Kg HM	10
Average Discharge Burnup, MWd/Kg HM	73
Peak Discharge Burnup, MWd/Kg HM	122
Peak Fast Fluence, n/cm^2	3.7×10^{23}
Maximum Burnup Reactivity Swing, $\% \Delta\rho$	0.32

The total ^{210}Po activity and heat source were estimated for SSTAR assuming LBE coolant. For the assumed core design, the core averaged neutron flux is $5.4 \times 10^{14} \text{ n}/(\text{cm}^2\text{-s})$. The core averaged one-group neutron capture cross section for ^{209}Bi is 3.02 mb when ENDF/B-VI is used and 5.28 mb for ENDF/B-V. The active core volume is 0.652 m^3 of which a fraction, 0.278, is occupied by the coolant. Thus, the coolant volume in the active core is 0.181 m^3 . The total primary coolant volume is taken to be 64.8 m^3 . The assumed coolant activation volume is estimated as 0.897 m^3 which is 4.95 times the coolant volume inside the active core. The ratio of activation to total coolant volume is equal to 0.0138.

Figures 28 and 29 provide the calculated ^{210}Po specific activity (Becquerel per Kilogram of bismuth) and the total heat source for SSTAR versus the time following startup of the reactor. The calculated total heat source rises to 36 KW when the larger capture cross section from ENDF/B-V is assumed. This is 0.08 % of the nominal 45 MWt core power. Thus, the heat source in the coolant from ^{210}Po is calculated to be small.

In summary, an estimate of the ^{210}Po specific activity and total heat source for SSTAR provides a heating rate in the coolant of only 36 KW which represents only 0.08 % of the

nominal core power. In comparing the heat source as a fraction of nominal power with calculations for other systems, it is necessary to consider the differences in the ratio of the coolant activation volume which is sensitive to the coolant volume fraction in the core and the ratio of the activation volume to the total coolant volume. The current estimate is a rough estimate because the size of the total activation volume is estimated only approximately. A more accurate evaluation would require a detailed in-vessel shielding analysis.

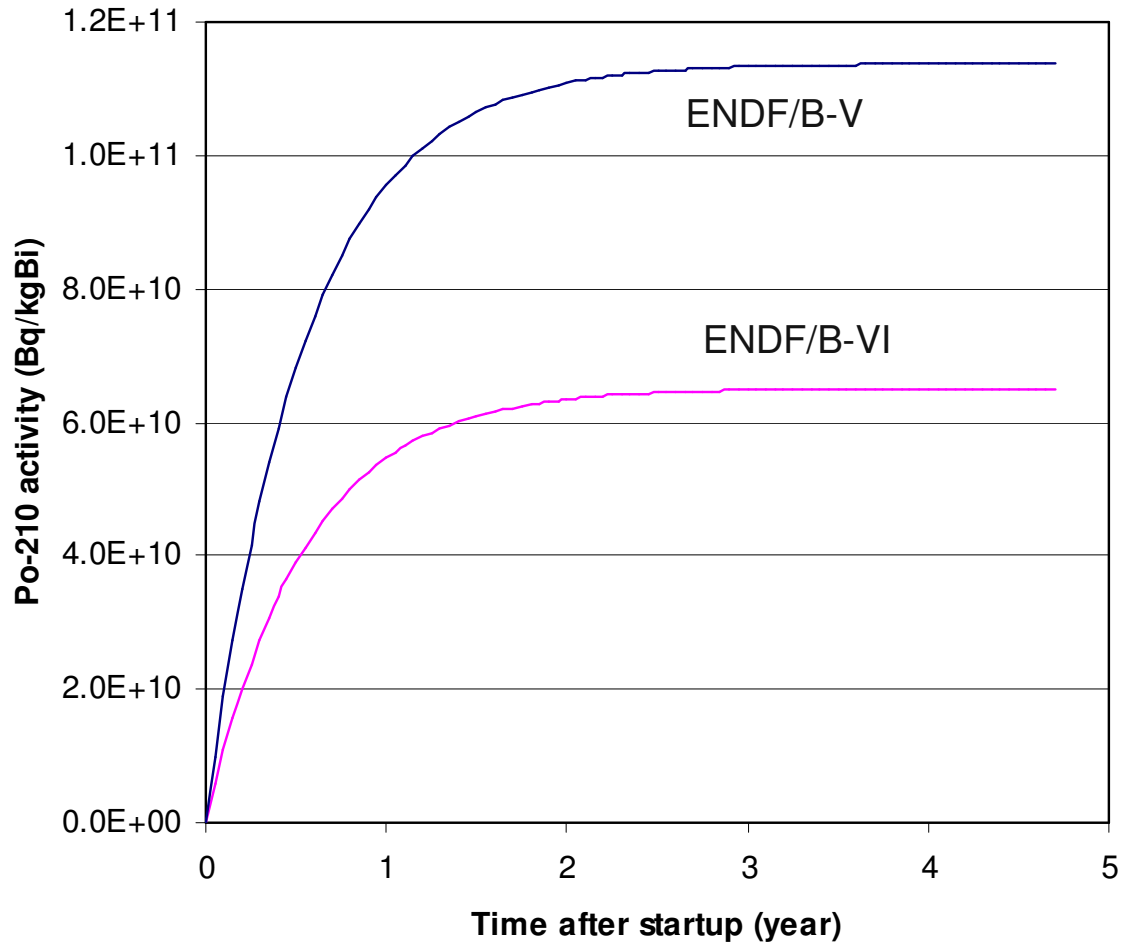


Figure 28. SSTAR ^{210}Po Specific Activity (Bq/(Kg Bi)) versus Time Following Reactor Startup for LBE Coolant and ^{209}Bi Capture Cross Sections from ENDF/B-VI and ENDF/B-V.

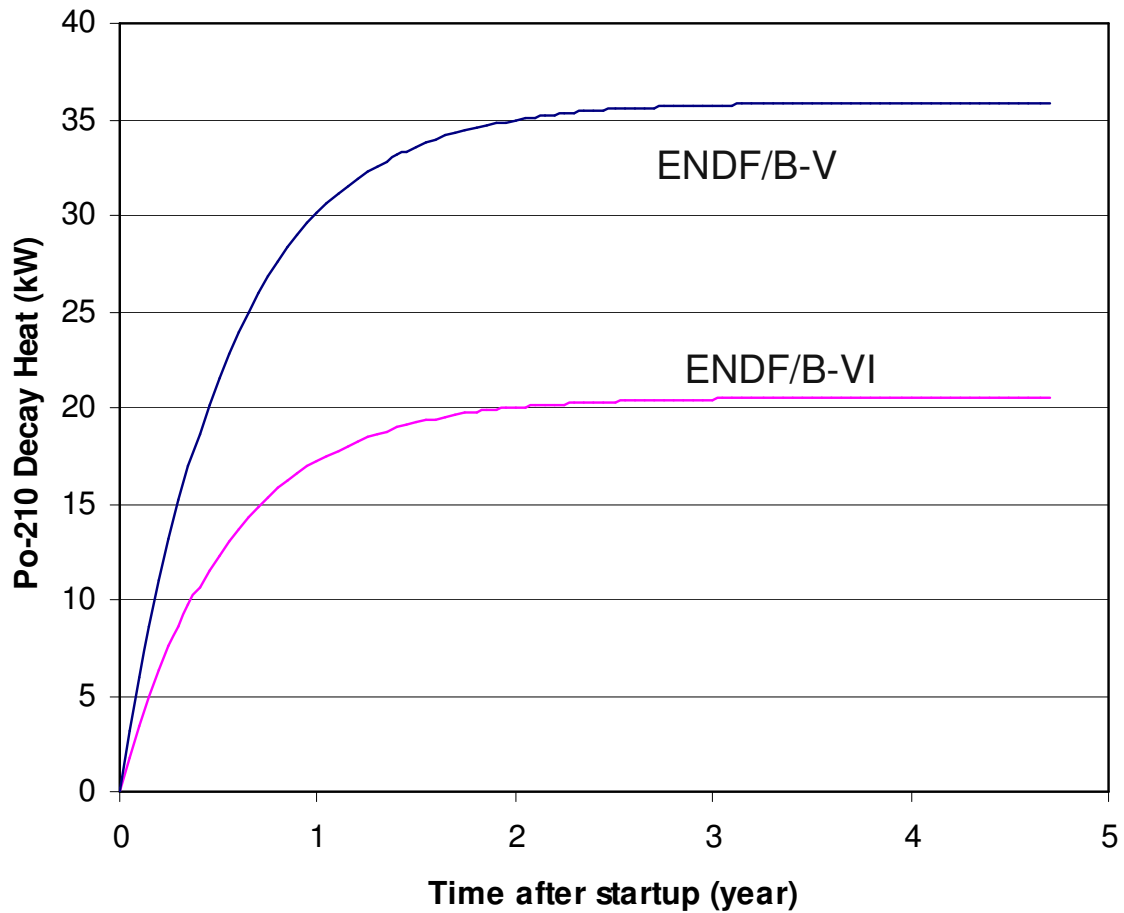


Figure 29. SSTAR ^{210}Po Total Decay Heat versus Time Following Reactor Startup for LBE Coolant and ^{209}Bi Capture Cross Sections from ENDF/B-VI and ENDF/B-V.

2.4. LFR Core Neutronics Benchmark

2.4.1. Introduction

Argonne National Laboratory (ANL) is participating in an international neutronics benchmark analysis for a LFR which is being performed under an International Atomic Energy Agency (IAEA) Coordinated Research Project (CRP) on “Small Reactors without On-site Refueling.” The main purpose of this benchmark analysis is to provide a forum to inter-compare the performance of different computer codes and nuclear data libraries used in designing fast reactors with lead-based coolants and mixed nitride fuels.

This benchmark exercise provides an opportunity to: 1) identify the main effects to be taken into account in modeling of neutron physics in the fast reactor core with mixed nitride fuels and lead-based coolants; 2) compare the different approaches for core modeling, burnup calculations, reactivity effect estimation, etc.; 3) estimate the computational uncertainties related to uncertainties in nuclear data and methodological errors; and 4) find the gaps in available test data and formulate the recommendations for additional experiments.

The benchmark problem was prepared based on the RBEC-M core, which is a 900 MWt lead-bismuth cooled fast reactor concept developed by the Russian Research Center, “Kurchatov Institute” (RRC KI). In this reactor concept, the fuel cycle is closed for plutonium and minor actinides except for curium and subsequent minor actinides. The cycle length is 300 effective full power days (EFPD) and the fuel resides in the core for six cycles. The spent fuel is reprocessed and curium isotopes and higher minor actinides are removed in addition to fission products. The reprocessed fuel is replenished with depleted uranium and returned to the core in two years. However, the initial phase of this benchmark exercise is focused on open fuel cycle analyses for specified fuel management schemes and fissile feeds.

In the following sections, the specifications of benchmark problems are described and the analysis results obtained with ANL suite of fast reactor analysis codes are presented.

2.4.2. Description of the Benchmark Problem

The IAEA benchmark problem was derived from the 900 MWt RBEC-M reactor design, having the core configuration shown in Figure 30. For the benchmark analysis, a R-Z model shown in Figure 31 was provided. Three homogenized core zones with different compositions were specified; the three core zones have the same enrichment but different fuel volume fractions. Mixed uranium-plutonium nitride fuel, $(U_{0.863}+Pu_{0.137})N$, is used, which is composed of reactor-grade plutonium recovered from typical light water reactor spent fuel and depleted uranium with 0.1 wt. % U-235. The core zones are surrounded by lateral (radial) and axial blankets. The blanket composition is depleted uranium nitride. The cladding and structural materials are ferritic/martensitic stainless steel, EP-823 (12 % Cr-Si), and the coolant material is lead-bismuth eutectic.

As shown in Figure 31, fifteen homogenized physical zones were specified in the benchmark problem. For each homogenized zone, nuclide densities and component-wise temperatures were provided. Tables 5 and 6 present the specified temperatures (in K) and nuclide densities (in 1/barn·cm) of all fifteen physical zones, respectively.

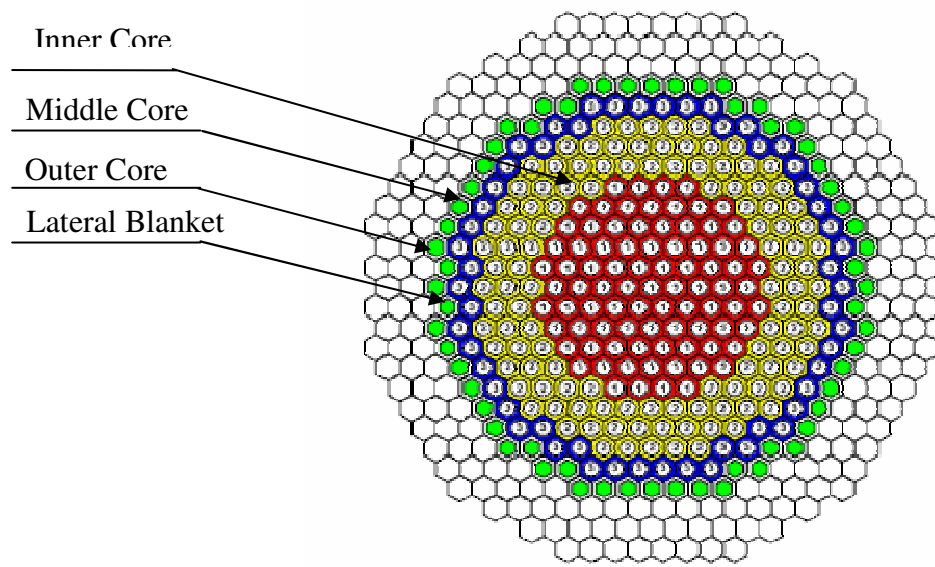


Figure 30. Core Configuration of 900 MWt RBEC-M Design.

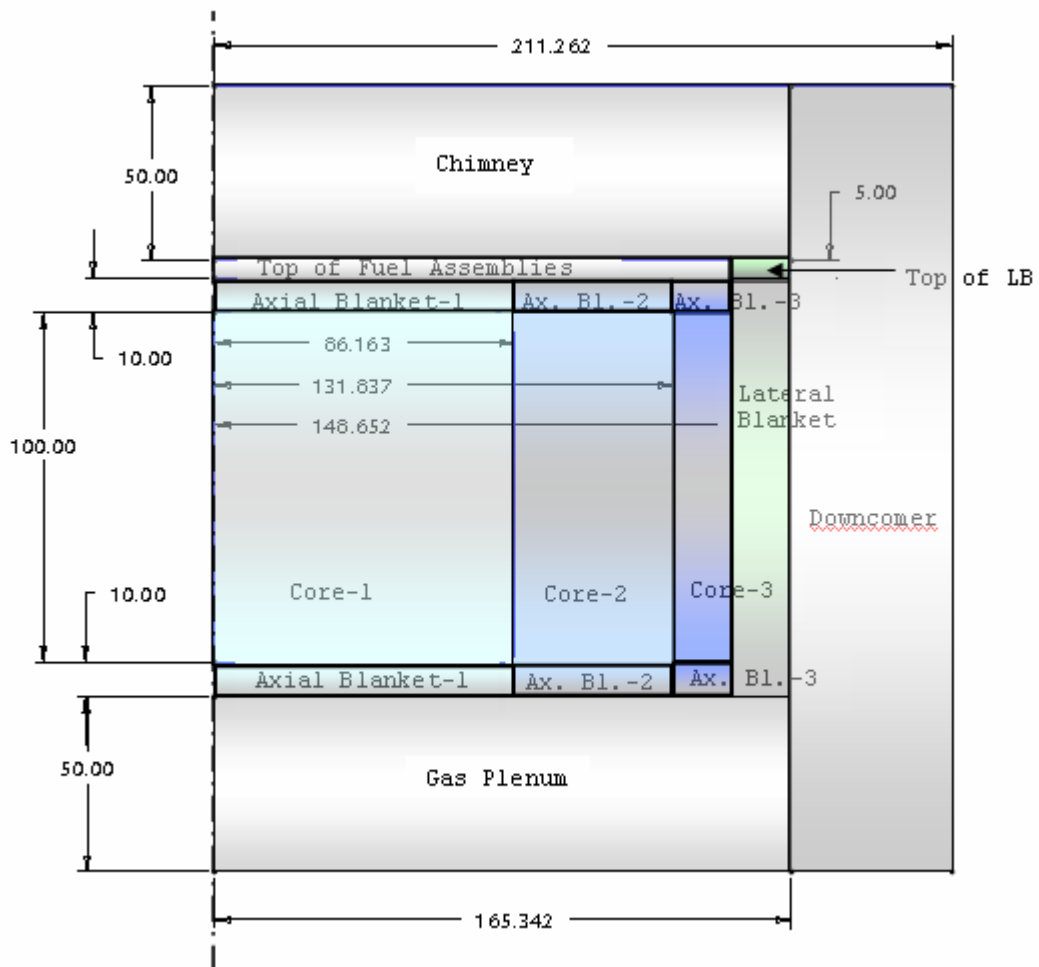


Figure 31. R-Z Benchmark Model of RBEC-M Core.

Table 6. Temperatures of Physical Zones			
Physical zone	Temperatures (K)		
	Fuel	Steel	Coolant
Core-1	1200	800	700
Core-2	1100	800	700
Core-3	1000	800	700
Axial blanket of core-1	900/700*	800/600*	800/600*
Axial blanket of core-2	900/700*	800/600*	800/600*
Axial blanket of core-3	900/700*	800/600*	800/600*
Lateral blanket	700	600	600
Top of fuel assemblies		800	800
Gas plenum		600	600
Top of assemblies of lateral blanket		600	600
Downcomer		700	700
Chimney		800	800

*Temperatures in top and bottom axial blankets.

Table 7. Nuclear Densities of Components of Physical Zones						
	Core 1	Core 2	Core 3	Axial Blanket	Axial Blanket	Axial Blanket
TRU Feed						
Pu238	1.33524E-05	1.58166E-05	2.18910E-05			
Pu239	6.07226E-04	7.19290E-04	9.95539E-04			
Pu240	2.43311E-04	2.88214E-04	3.98905E-04			
Pu241	8.31945E-05	9.85480E-05	1.36396E-04			
Pu242	4.92603E-05	5.83513E-05	8.07615E-05			
Am241	8.08633E-06	9.57866E-06	1.32574E-05			
Uranium Feed						
U235	6.42536E-06	7.61116E-06	1.05343E-05	7.47095E-06	8.84971E-06	1.22485E-05
U238	6.35962E-03	7.53328E-03	1.04265E-02	7.36921E-03	8.72919E-03	1.20817E-02
N Content						
N-14	4.96797E-04	5.88481E-04	8.14492E-04	4.97216E-04	5.88976E-04	8.15178E-04
N-15	6.87368E-03	8.14221E-03	1.12693E-03	6.87947E-03	8.14907E-03	1.12788E-02
Coolant						
Bi209	1.04654E-02	9.59466E-03	7.46809E-03	1.04654E-02	9.59466E-03	7.46809E-03
Pb206	2.06859E-03	1.89648E-03	1.47615E-03	2.06859E-03	1.89648E-03	1.47615E-03
Pb207	1.89696E-03	1.73913E-03	1.35367E-03	1.89696E-03	1.73913E-03	1.35367E-03
Pb208	4.49772E-03	4.12351E-03	3.20957E-03	4.49772E-03	4.12351E-03	3.20957E-03
Structure						
C	7.25829E-05	7.75886E-05	8.69743E-05	7.25829E-05	7.75886E-05	8.69743E-05
Si	2.23105E-04	2.38491E-04	2.67341E-04	2.23105E-04	2.38490E-04	2.97341E-04
V	3.74360E-05	4.00178E-05	4.48587E-05	3.74360E-05	4.00178E-05	4.48587E-05
Cr	1.15270E-03	1.23220E-03	1.38125E-03	1.15270E-03	1.23220E-03	1.38125E-03
Mn	6.44665E-05	6.89124E-05	7.72486E-05	6.44665E-05	6.89124E-05	7.72486E-05
Fe	8.22862E-03	8.79611E-03	9.86016E-03	8.22862E-03	8.79611E-03	9.86016E-03
Ni	6.03452E-05	6.45069E-05	7.23102E-05	6.03452E-05	6.45069E-05	7.23102E-05
Nb	1.75942E-05	1.88076E-05	2.10827E-05	1.75942E-05	1.88076E-05	2.10827E-05
Mo	4.25946E-05	4.55322E-05	5.10401E-05	4.25946E-05	4.55322E-05	5.10401E-05
W	1.92638E-05	2.05924E-05	2.30834E-05	1.92638E-05	2.05924E-05	2.30834E-05

Table 7. Nuclear Densities of Components of Physical Zones (cont.)						
	Lateral Blanket	Top of Fuel Assemblies	Gas Plenum	Top of LB Assemblies	Downcomer	Chimney
Uranium Feed						
U235	1.05171E-05					
U238	1.03738E-02					
N Content						
N-14	6.99943E-04					
N-15	9.68440E-03					
Coolant						
Bi209	9.46070E-03	9.52768E-03	9.52768E-03	9.46070E-03	1.50701E-02	1.66609E-02
Pb206	1.87001E-03	1.88324E-03	1.88324E-03	1.87001E-03	2.97877E-03	3.29320E-03
Pb207	1.71485E-03	1.72699E-03	1.72699E-03	1.71485E-03	2.73162E-03	3.01995E-03
Pb208	4.06593E-03	4.09472E-03	4.09472E-03	4.06593E-03	6.47671E-03	7.16036E-03
Structure						
C	5.88172E-05	7.75886E-05	2.22000E-04	5.88172E-05	6.25714E-05	3.12857E-06
Si	1.80792E-04	2.38491E-04	2.38491E-04	1.80792E-04	1.92332E-04	9.61659E-06
V	3.03361E-05	4.00178E-05	4.00178E-05	3.03361E-05	3.22724E-05	1.61362E-06
Cr	9.34084E-04	1.23220E-03	1.23220E-03	9.34084E-04	9.93706E-04	4.96853E-05
Mn	5.22401E-05	6.89124E-05	6.89124E-05	5.22401E-05	5.55745E-05	2.77873E-06
Fe	6.66802E-03	8.79611E-03	8.79611E-03	6.66802E-03	7.09364E-03	3.54682E-04
Ni	4.89004E-05	6.45069E-05	6.45069E-05	4.89004E-05	5.20217E-05	2.60109E-06
Nb	1.42574E-05	1.88076E-05	1.88076E-05	1.42574E-05	1.51674E-05	7.58370E-07
Mo	3.45163E-05	4.55322E-05	4.55322E-05	3.45163E-05	3.67195E-05	1.83598E-06
W	1.56104E-05	2.05924E-05	2.05924E-05	1.56104E-05	1.66068E-05	8.30338E-07

Three different fuel cycle problems were specified in the benchmark problem. The first and second ones are single cycle problems to deplete the specified fuels for 1800 and 900 effective full-power days (EFPD), respectively. The third one is a six-cycle problem to deplete the specified fuels for 300 EFPD and perform partial refueling at the end of each cycle. It is assumed that at each refueling operation, one sixth of core and blanket compositions are replaced with fresh compositions. The shutdown time for refueling is 60 days. For each of these problems, the following parameters are asked to be provided:

1. *Effective multiplication factor;*
2. *Axial and radial power profiles in the core;*
3. *Power peaking factors in the core zones;*
4. *Volume averaged neutron spectra in the core zone; and*
5. *k-infinity in the core central zone.*

2.4.3. Analysis Methods

The ANL suite of fast reactor analysis codes [7-10] was used to analyze the benchmark problems. Fuel cycle analyses were performed with the DIF3D/REBUS-3 code system. The multi-group cross sections were generated for each homogenized zone using the MC²-2 code based on the ENDF/B-V.2 data. The flux calculations were mainly performed with the discrete ordinate transport code TWODANT. For comparison purposes, additional diffusion theory calculations and Monte Carlo simulations were also performed for selected cases. In this section, the key elements of the computational methods are described.

Multi-group Cross Section Generation

For each of 15 homogenized physical zones, 33-group cross sections were generated for specified composition and component-wise temperatures using the MC²-2 code. The ENDF/B-V.2 data was used for all isotopes. For the three core zones, the critical buckling was determined using the consistent P1 approximation and the corresponding spectrum was used for group collapsing. For other compositions, the collapsing spectrum was determined by solving a fixed source problem by using the leakage spectrum from an adjacent zone as the external source. For example, the leakage spectra from core zones were used for blanket cross section generation, and blanket leakage spectra were used for fission gas plenum, chimney, and downcomer.

For resolved resonance integral calculation, the narrow resonance approximation was used, and the Doppler broadening, interference scattering, and the effects of overlap with neighboring resolved resonances were taken into account. It is noteworthy that an additional option is available to use the hyper-fine group integral transport calculation with RABANL, in which the Doppler width is divided into a few hyper-fine groups. In the preparation of MC²-2 library, wide and extremely weak resonances are pre-processed and represented by the ultra-fine-group (2082 groups) energy structure of MC²-2. The

other resonances are modeled by their resonance parameters, and their self-shielding effects are explicitly evaluated in the MC²-2 calculation.

The unresolved resonance integral calculation was performed with a narrow resonance approximation, and interference scattering, the effects of overlap with resonances in other spin sequences, and the effects of self-overlap with resonances of the same spin sequences were taken into account. The resolved and unresolved energy range used is specified by the ENDF data and is unique for each nuclide. The (n,2n) reaction was treated as a source term in the ultra-fine-group spectrum calculation. For the secondary energy distribution, tabulated function, evaporation spectrum and discrete levels were used. The discrete ultra-fine-group (n,2n) scattering source was approximately treated by neglecting the energy-angle correlation.

Flux Calculation

The flux distributions were mainly computed using the TWODANT transport theory code. An R-Z computational model was employed in these calculations with ~ 2.0 cm mesh size and vacuum boundary condition. For comparison, the finite difference diffusion theory option of the DIF3D was also used. It is noted that the DIF3D code is a collection of modules that provide various solution options for eigenvalue and fixed source problems: variational nodal transport (VARIANT), nodal diffusion theory, and finite difference diffusion theory options. These deterministic calculations were carried out using the same 33-group cross sections generated as aforementioned. In addition, a Monte Carlo calculation was performed for the core configuration at the beginning of life using the MCNP4C code. The MCNP calculation was performed with ENDF/B-V cross sections (.50c extension in MCNP libraries) for a consistent comparison with deterministic calculations.

Fuel Cycle Analysis

The fuel cycle analyses were performed using the REBUS-3 code, which was developed for fast reactor depletion and fuel cycle analysis. The REBUS-3 code contains unique features not generally found in three-dimensional burnup codes. These include the ability to perform equilibrium cycle calculation in addition to the common non-equilibrium calculation. A general external cycle capability is also provided by the code for modeling of the post-irradiation cooling, reprocessing, and fabrication stages of the fuel cycle. The radioactive decay is taken into account for specified time delays between various processes. The equilibrium cycle analysis assumes a fixed periodic fuel management scheme, but the non-equilibrium (or explicit cycle-by-cycle) option permits modeling reactor operation under a specified periodic or non-periodic fuel management scheme. Four types of search procedures may be carried out in order to satisfy user-supplied constraints during fuel cycle calculations: (1) adjustment of the fresh fuel enrichment to achieve a specified multiplication constant at a specified point during the burn cycle, (2) adjustment of the reactor burn cycle time to achieve a specified discharge burnup, (3) adjustment of the control poison density to maintain a specified value of the multiplication constant throughout the reactor burn cycle, and (4) adjustment of the

reactor burn cycle time to achieve a specified value of the eigenvalue at the end of the burn step.

Non-equilibrium cycle analyses were performed for the benchmark problems. As a preliminary analysis, each of core and blanket zones was represented as a single depletion zone. In the later analysis, each zone will be represented by at least five axial depletion zones. The employed burnup interval was 100, 200, and 300 days for the first, second, and third problems, respectively. However, the region density iteration was performed with a relative convergence criterion of 0.001. That is, the depletion calculation for each region was performed with the average of the beginning and end of time interval fluxes. The end of time interval flux was iteratively computed by iteration on the final nuclide densities. The depletion calculations were performed using burnup chains for nuclides ranging from U-234 to Cm-246. Capture, (n,2n), and fission reactions were considered for all actinide isotopes included in the burn chains. In the capture and (n,2n) reactions, short-lived intermediate products were neglected. As a result, the products of capture reactions of U-238, Np-238, Pu-242, and Am-243 were represented by Pu-239, Pu-239, Am-243, and Cm-244, respectively. The capture reaction of Am-241 was modeled to yield Cm-242, Am-242m, and Pu-242 with yield fractions of 0.66, 0.20, and 0.14, respectively. The products of (n,2n) reactions of Pu-238 and Am-241 were respectively represented by N-237 and Pu-240. The (n,2n) reaction of Am-243 was assumed to yield Am-242m, Pu-242, and Cm-242 with yield fractions of 0.5, 0.086, and 0.414, respectively. Cm-242 was assumed to yield Am-241 in 99% of its (n,2n) reactions and Np-237 in 1%. It was assumed that 37.4% of (n,2n) reactions of Np-237 yield U-236 and the remaining 62.6% yield a fictitious dummy isotope. The end products of Cm-246 capture and U-234 (n,2n) reactions were represented by a fictitious dummy isotope.

Important α and β decays of actinide isotopes were also considered. Specifically, α decay was considered for all actinide isotopes except for Np-238 and Pu-241. The β^- decays of Np-238, Pu-241, Am-242m and the β^+ decay of Am-242m were also included in the burn chains. The employed decay constants for the β^- , β^+ , and α decays of Am-242m were 1.189E-10, 2.487E-11, and 7.225E-13, respectively. The fission products were modeled with five lumped rare earth elements and five lumped fission products. The 33-group cross sections of these lumped elements were generated by weighting the 33-group cross sections of 180 fission products with fission yields of U-235, U-238, Pu-239, Pu-240, and Pu-241, respectively. Three dummy isotopes were also used to represent the other end products not included in the chains. For full reactor depletion calculations, the lumped fission products of U-234, U-235, and U-236 were represent by those of U-235, while the fission products of U-237, U-238, Np237, Np238, and Pu238 were represented by those of U-238. The fission products of Pu-241 and higher actinides were represented by those of Pu-241.

2.4.4. Benchmarking Results

Criticality at the Beginning of Life

Before performing the fuel cycle analysis, the performance of deterministic methods were examined by comparing the multiplication factors predicted with the deterministic codes with that obtained with MCNP4C simulation. Table 8 compares the multiplication factors at the beginning of life calculated with DIF3D, TWODANT and MCNP4. As can be seen, the results of three codes are in good agreement with each other. These results indicate that the 33-group cross sections generated as described in the previous section are acceptable. TWODANT yielded a higher multiplication factor than DIF3D, which is expected given that the diffusion theory generally overestimates the neutron leakage. Compared to the MCNP4C solution, the DIF3D resulted in a better solution than TWODANT. It is however considered to be due to error cancellation. To identify the exact reason, further analyses need to be performed.

Table 8. BOC k_{eff} Obtained from Different Codes	
Code	k_{eff} value
DIF3D	0.99715
TWODANT	0.99851
MCNP4C (.50c)	0.99761

Single Cycle Analysis for 1800 Effective Full Power Days

Table 9 and Figure 32 show the evolution of the multiplication factors obtained with TWODANT transport theory and DIF3D finite difference diffusion theory calculations. The depletion calculations were performed with 10 subintervals (200 days). As expected, the diffusion theory solution resulted in consistently lower multiplication factor due to higher estimated leakage.

Table 9. k-effective for 900 MW RBEC, 1800 Days Cycle		
Time (days)	k-effective, REBUS-3	
	DIF3D	TWODANT
0	0.99715	0.99851
200	1.00252	1.00385
400	1.00730	1.00862
600	1.01151	1.01284
800	1.01517	1.01651
1000	1.01829	1.01967
1200	1.02093	1.02235
1400	1.02311	1.02457
1600	1.02487	1.02637
1800	1.02624	1.02779

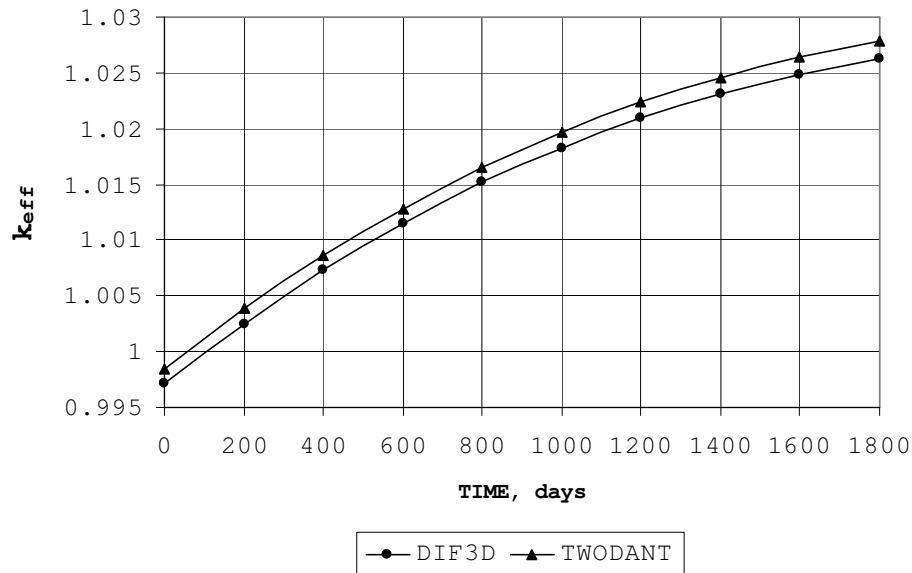


Figure 32. k-effective versus Time for the 1800-Day Cycle.

Figure 33 depicts radial power density profiles in the core for the beginning and end of cycle. Two planes were chosen to illustrate the power density distribution: at the core midplane and near the top (45 cm from the core midplane.) Spatial variations of the power distribution can be observed. As can be seen in Figure 33, power peaking appears at the boundaries between zones of different fuel loading.

Table 10 compares power densities and power peaking factors of different core regions.

Table 10. Region Powers and Power Peaking Factors, 1800-Day Cycle					
	ZONE NAME	POWER (WATTS)	POWER DENSITY (WATTS/CC)	PEAK DENSITY (WATTS/CC)	PEAK TO AVG. POWER DENSITY
BEGINNING OF CYCLE	CORE-1	3.33E+08	1.43E+02	1.90E+02	1.33E+00
	CORE-2	3.97E+08	1.27E+02	1.95E+02	1.53E+00
	CORE-3	1.48E+08	1.00E+02	1.58E+02	1.58E+00
END OF CYCLE	CORE-1	3.25E+08	1.39E+02	1.86E+02	1.34E+00
	CORE-2	3.68E+08	1.18E+02	1.78E+02	1.52E+00
	CORE-3	1.37E+08	9.27E+01	1.41E+02	1.52E+00

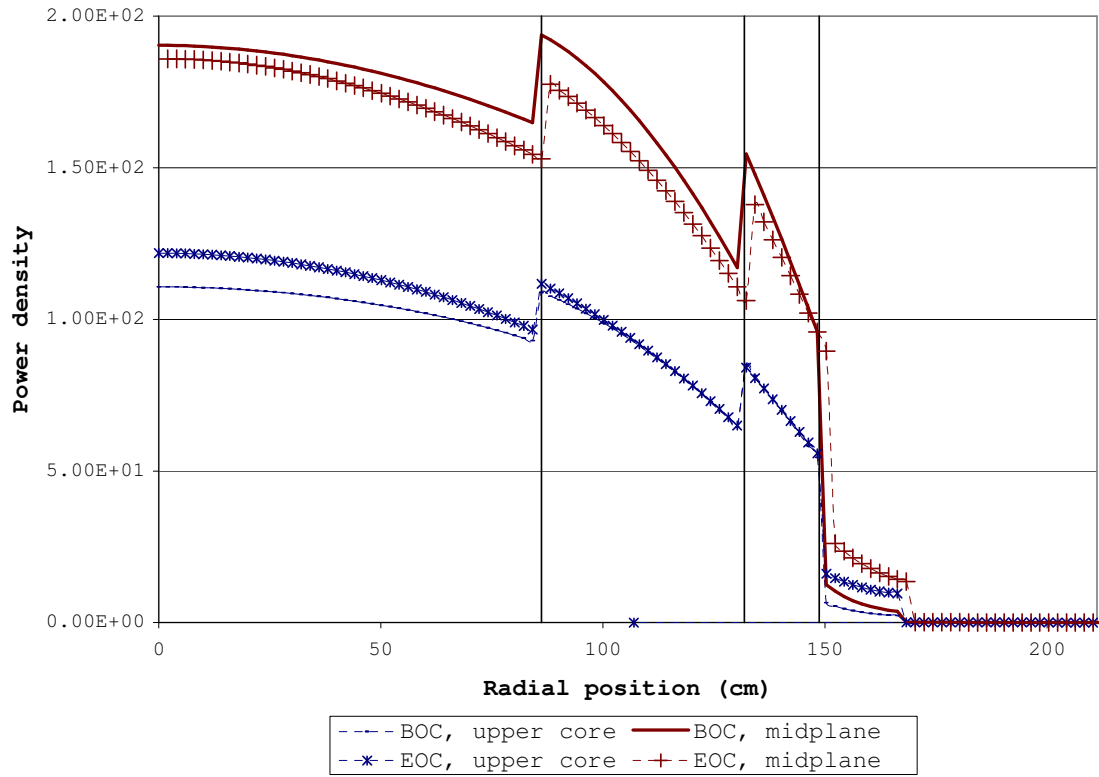


Figure 33. Radial Power Profiles in the Core.

Figures 34 and 35 illustrate axial power profiles in the core. The axial power distributions were determined at the center of each core zone.

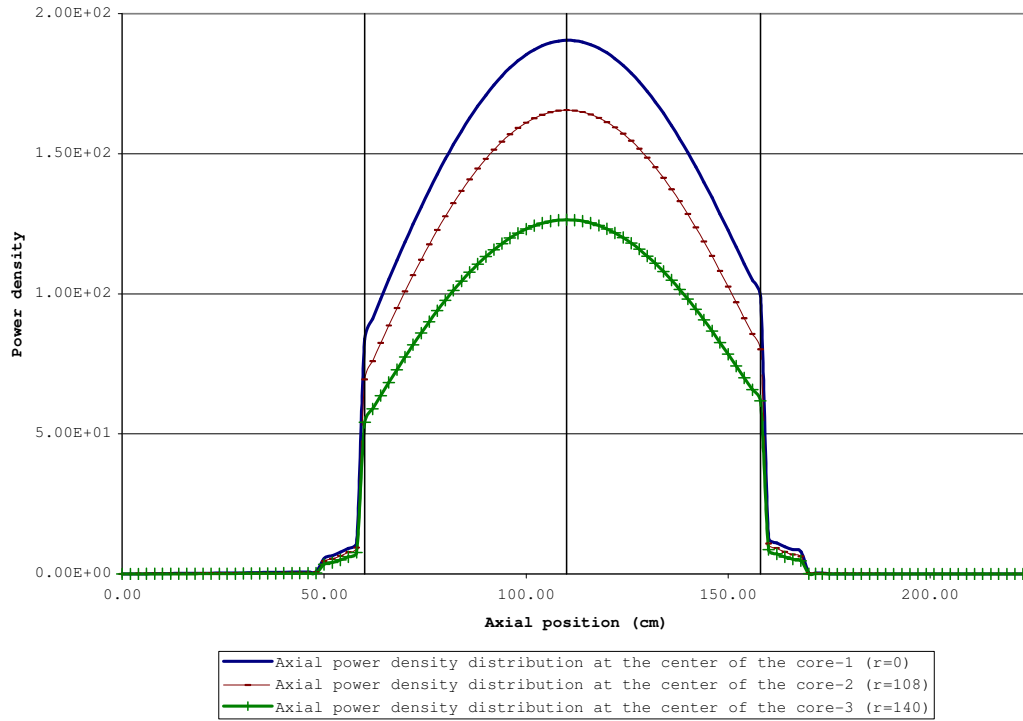


Figure 34. Axial Power Profiles in the Core at the Beginning of Cycle.

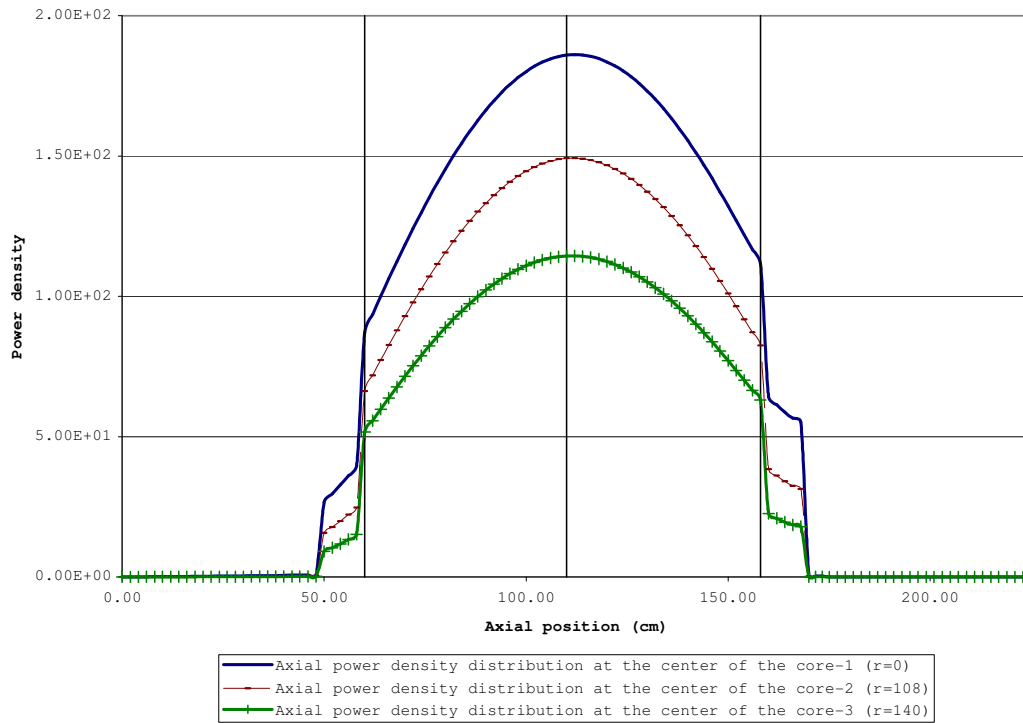


Figure 35. Axial Power Profiles in the Core at the End of Cycle.

Volume Averaged Neutron Spectra in the Core Zones

Volume averaged neutron flux per unit lethargy in the core zones was obtained at BOC and EOC. Figures 36 and 37 illustrate a histogram of the ratio of flux-to-lethargy versus neutron energy. Table 11 provides flux values for each energy group.

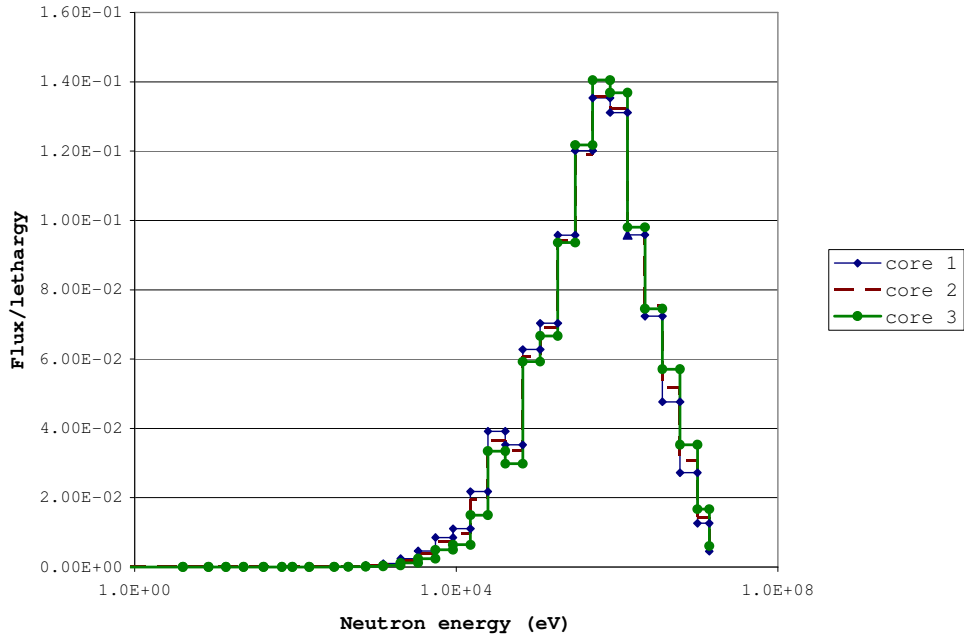


Figure 36. Flux/Lethargy vs. Neutron Energy at the Beginning of Cycle.

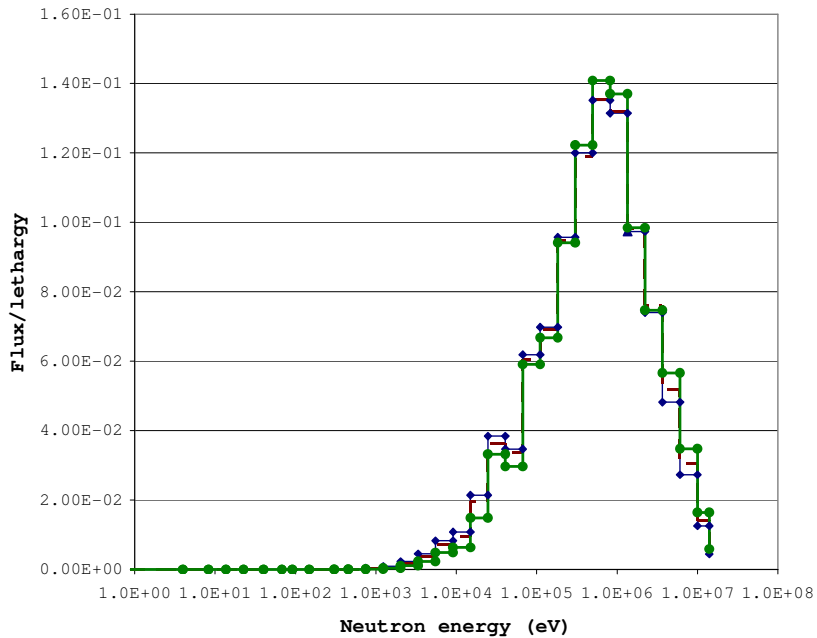


Figure 37. Flux/Lethargy vs. Neutron Energy at the End of Cycle.

Table 11. Volume Averaged Neutron Spectra in the Core, 1800-Day Cycle						
energy	BOC			EOC		
	1	2	3	1	2	3
1.41E+07	2.16E+11	1.88E+11	1.31E+11	2.06E+11	1.70E+11	1.20E+11
1.00E+07	3.82E+12	3.32E+12	2.28E+12	3.70E+12	3.04E+12	2.12E+12
6.07E+06	1.84E+13	1.59E+13	1.08E+13	1.79E+13	1.46E+13	1.00E+13
3.68E+06	5.01E+13	4.17E+13	2.71E+13	4.90E+13	3.85E+13	2.54E+13
2.23E+06	1.03E+14	8.22E+13	4.79E+13	1.02E+14	7.66E+13	4.53E+13
1.35E+06	1.72E+14	1.35E+14	7.96E+13	1.69E+14	1.25E+14	7.54E+13
8.21E+05	2.85E+14	2.20E+14	1.34E+14	2.76E+14	2.03E+14	1.27E+14
4.98E+05	3.45E+14	2.64E+14	1.61E+14	3.33E+14	2.44E+14	1.53E+14
3.02E+05	3.51E+14	2.66E+14	1.60E+14	3.39E+14	2.46E+14	1.52E+14
1.83E+05	3.15E+14	2.37E+14	1.39E+14	3.05E+14	2.20E+14	1.32E+14
1.11E+05	2.58E+14	1.94E+14	1.10E+14	2.48E+14	1.79E+14	1.04E+14
6.74E+04	2.54E+14	1.87E+14	1.08E+14	2.42E+14	1.73E+14	1.02E+14
4.09E+04	1.56E+14	1.14E+14	5.94E+13	1.48E+14	1.05E+14	5.58E+13
2.48E+04	1.87E+14	1.33E+14	7.23E+13	1.78E+14	1.23E+14	6.78E+13
1.50E+04	1.12E+14	7.72E+13	3.49E+13	1.07E+14	7.14E+13	3.27E+13
9.12E+03	6.12E+13	4.08E+13	1.60E+13	5.81E+13	3.77E+13	1.50E+13
5.53E+03	5.04E+13	3.27E+13	1.32E+13	4.77E+13	3.02E+13	1.23E+13
3.36E+03	2.92E+13	1.83E+13	6.71E+12	2.74E+13	1.68E+13	6.17E+12
2.04E+03	1.60E+13	9.60E+12	3.44E+12	1.49E+13	8.76E+12	3.10E+12
1.23E+03	6.67E+12	3.86E+12	1.29E+12	6.14E+12	3.49E+12	1.14E+12
7.49E+02	3.24E+12	1.86E+12	6.65E+11	2.85E+12	1.62E+12	5.48E+11
4.54E+02	9.22E+11	5.15E+11	2.08E+11	7.82E+11	4.37E+11	1.63E+11
3.04E+02	5.47E+11	2.99E+11	1.68E+11	4.09E+11	2.28E+11	1.11E+11
1.49E+02	8.03E+10	4.33E+10	4.29E+10	4.76E+10	2.72E+10	2.37E+10
9.17E+01	1.90E+10	1.05E+10	1.48E+10	7.85E+09	4.82E+09	6.06E+09
6.79E+01	1.39E+10	7.98E+09	1.47E+10	3.74E+09	2.54E+09	4.46E+09
4.02E+01	4.85E+09	2.88E+09	5.78E+09	1.36E+09	9.67E+08	1.85E+09
2.26E+01	8.80E+08	5.22E+08	7.10E+08	2.65E+08	1.85E+08	2.32E+08
1.37E+01	7.75E+08	4.54E+08	6.92E+08	6.79E+07	5.36E+07	7.06E+07
8.32E+00	1.87E+08	1.09E+08	1.36E+08	2.40E+07	1.79E+07	1.72E+07
3.99E+00	8.70E+08	5.79E+08	1.42E+09	2.36E+07	3.90E+07	1.61E+08
5.41E-01	4.55E+07	2.84E+07	6.20E+07	1.30E+06	1.40E+06	3.94E+06
4.14E-01	7.12E+07	4.26E+07	5.60E+07	3.53E+05	3.54E+05	6.45E+05

Problem 2: Fuel Cycle Consists of 900 Effective Full Power Days

Effective Multiplication Factor

The multiplication factor was obtained at 10 different times (every 100 days.) Throughout the cycle, k_{eff} appears to be linear, but it is actually a part of the “1800-day” cycle and, therefore, is parabolic.

Table 12. k-effective for 900 MW RBEC, 900-Day Cycle		
Time (days)	k-effective, REBUS-3	
	DIF3D	TWODANT
0	0.99715	0.99851
100	0.99991	1.00125
200	1.00252	1.00385
300	1.00498	1.00630
400	1.00730	1.00862
500	1.00948	1.01080
600	1.01151	1.01284
700	1.01340	1.01474
800	1.01516	1.01651
900	1.01679	1.01815

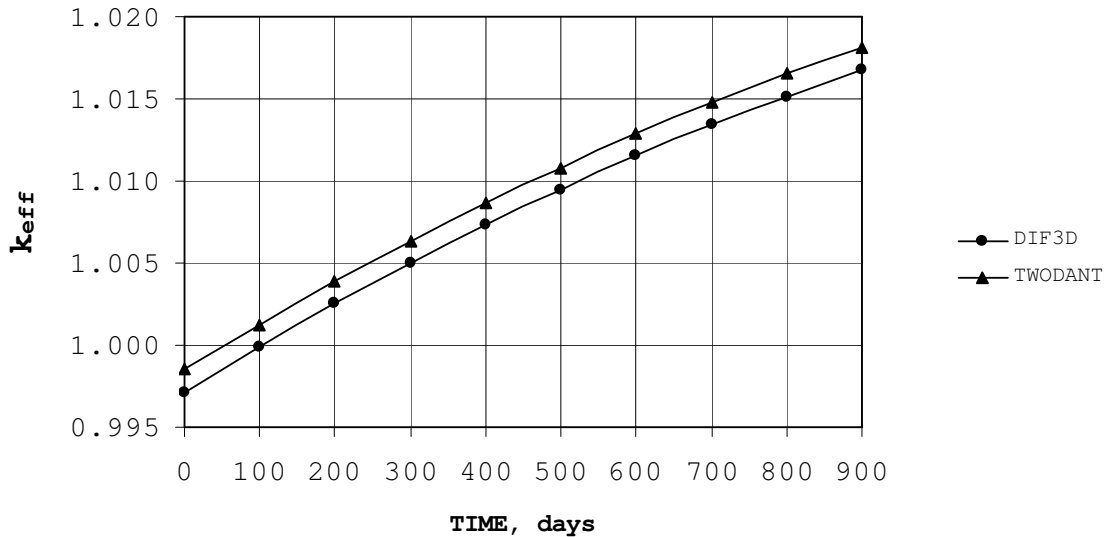


Figure 38. k-effective vs. Time for the 900-Day Cycle.

Axial and Radial Power Profiles in the Core

Figure 39 depicts radial power density profiles in the core for the beginning and end of cycle. Two planes were chosen to illustrate power density distribution: at the core midplane and near the top (45 cm from the core midplane.)

Table 13. Region Powers and Power Peaking Factors, 900-Day Cycle					
	ZONE NAME	POWER (WATTS)	POWER DENSITY (WATTS/CC)	PEAK DENSITY (WATTS/CC)	PEAK TO AVG. POWER DENSITY
BEGINNING OF CYCLE	CORE-1	3.33E+08	1.43E+02	1.90E+02	1.33E+00
	CORE-2	3.97E+08	1.27E+02	1.94E+02	1.53E+00
	CORE-3	1.48E+08	1.00E+02	1.58E+02	1.58E+00
END OF CYCLE	CORE-1	3.35E+08	1.44E+02	1.94E+02	1.35E+00
	CORE-2	3.78E+08	1.21E+02	1.86E+02	1.54E+00
	CORE-3	1.39E+08	9.40E+01	1.45E+02	1.55E+00

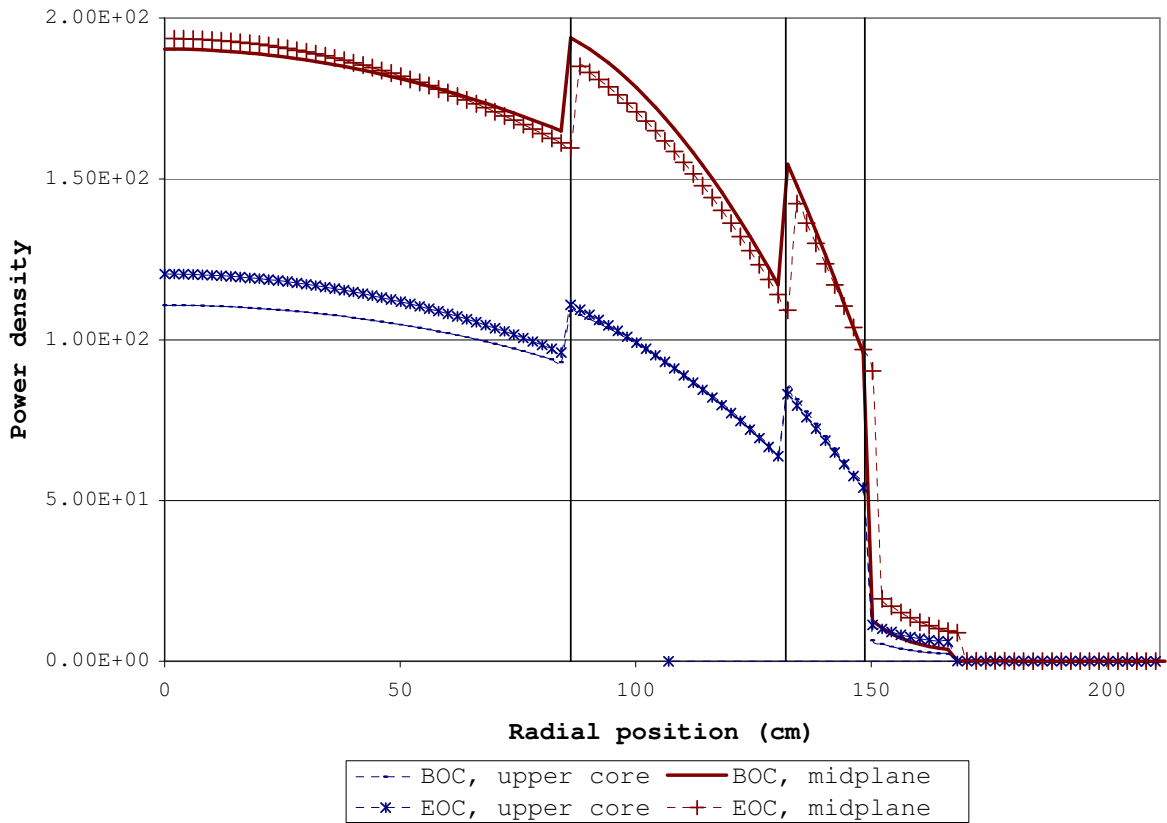


Figure 39. Radial Power Profiles in the Core.

Figures 40 and 41 illustrate axial power profiles in the core. The axial power distributions were determined at the center of each core zone.

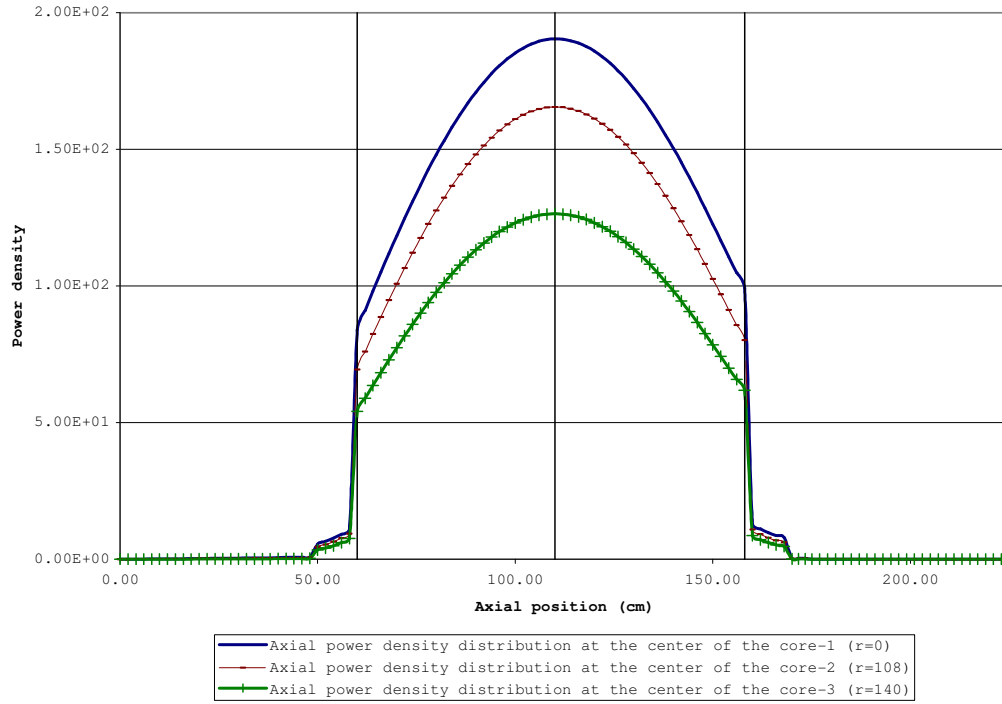


Figure 40. Axial Power Profiles in the Core at the Beginning of Cycle.

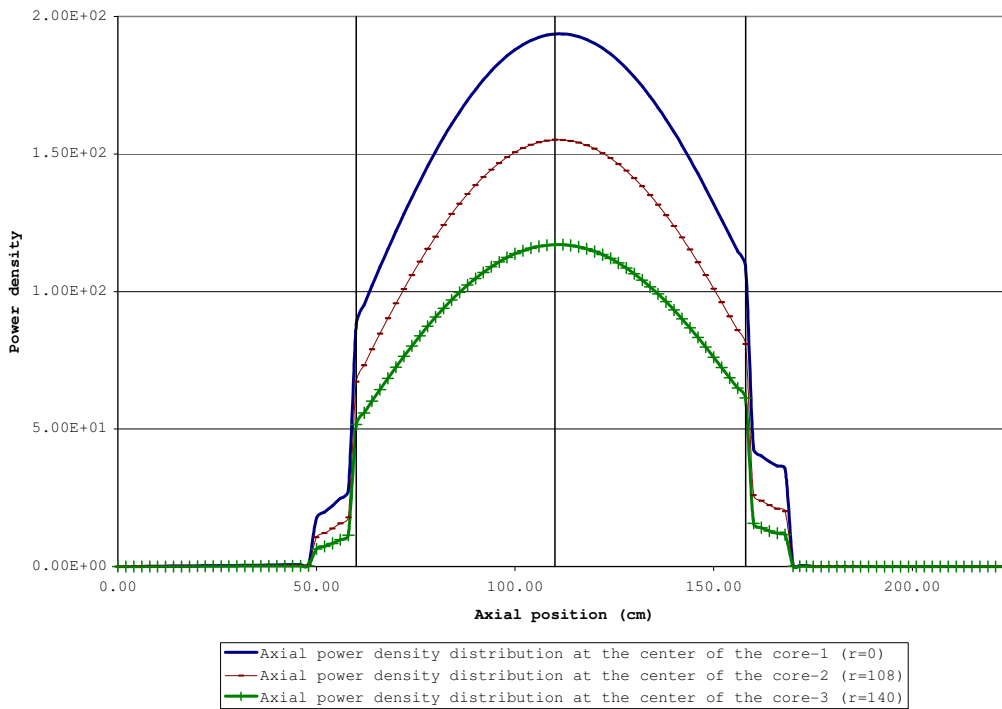


Figure 41. Axial Power Profiles in the Core at the End of Cycle.

Volume Averaged Neutron Spectra in the Core Zones

Volume averaged neutron flux per unit lethargy in the core zones was obtained at BOC and EOC. Figures 42 and 43 illustrate a histogram of the ratio of flux to lethargy versus neutron energy. Table 14 provides flux values for each energy group.

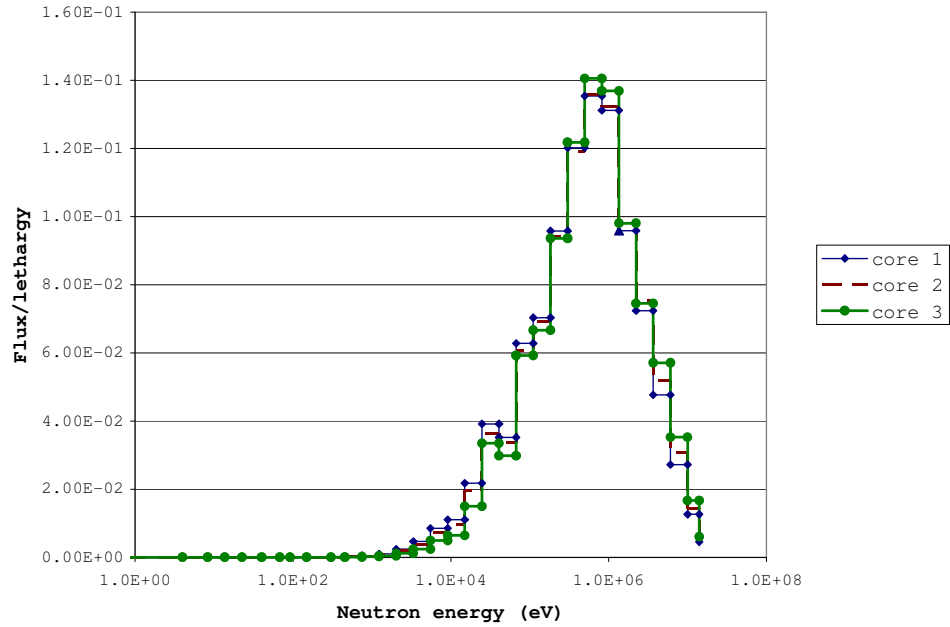


Figure 42. Flux/Lethargy vs. Neutron Energy at the Beginning of Cycle.

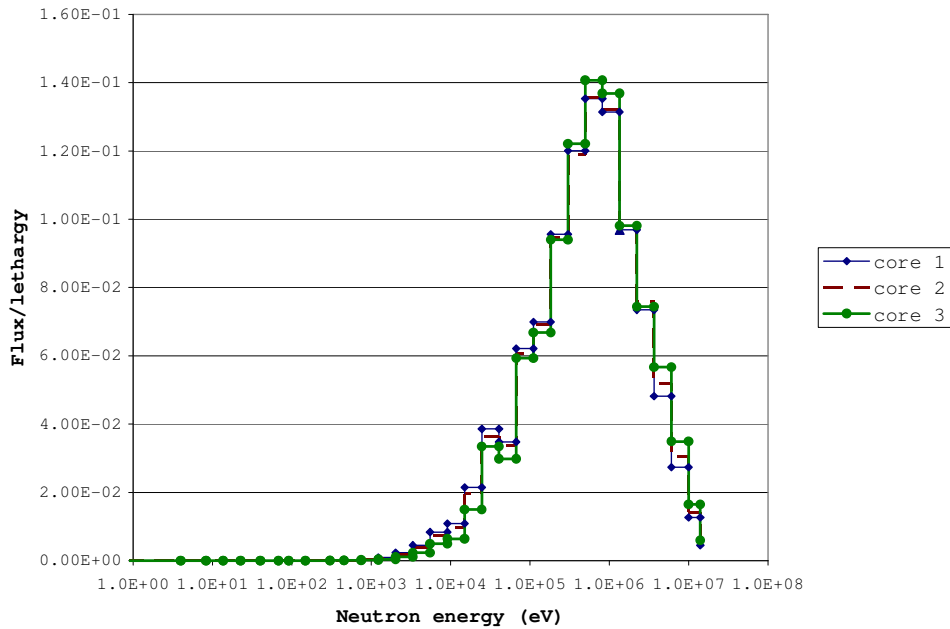


Figure 43. Flux/Lethargy vs. Neutron Energy at the End of Cycle.

Table 14. Volume Averaged Neutron Spectra in the Core, 900-Day Cycle						
Energy (eV)	BOC			EOC		
	Core 1	Core 2	Core 3	Core 1	Core 2	Core 3
1.41E+07	2.1584E+11	1.88E+11	1.31E+11	2.13E+11	1.75E+11	1.22E+11
1.00E+07	3.8242E+12	3.32E+12	2.28E+12	3.81E+12	3.13E+12	2.14E+12
6.07E+06	1.8403E+13	1.59E+13	1.08E+13	1.84E+13	1.50E+13	1.01E+13
3.68E+06	5.0082E+13	4.17E+13	2.71E+13	5.03E+13	3.95E+13	2.55E+13
2.23E+06	1.0302E+14	8.22E+13	4.79E+13	1.04E+14	7.82E+13	4.53E+13
1.35E+06	1.7237E+14	1.35E+14	7.96E+13	1.73E+14	1.28E+14	7.54E+13
8.21E+05	2.8480E+14	2.20E+14	1.34E+14	2.84E+14	2.08E+14	1.27E+14
4.98E+05	3.4453E+14	2.64E+14	1.61E+14	3.42E+14	2.50E+14	1.53E+14
3.02E+05	3.5078E+14	2.66E+14	1.60E+14	3.48E+14	2.52E+14	1.53E+14
1.83E+05	3.1530E+14	2.37E+14	1.39E+14	3.13E+14	2.26E+14	1.32E+14
1.11E+05	2.5780E+14	1.94E+14	1.10E+14	2.55E+14	1.84E+14	1.05E+14
6.74E+04	2.5359E+14	1.87E+14	1.08E+14	2.49E+14	1.77E+14	1.02E+14
4.09E+04	1.5551E+14	1.14E+14	5.94E+13	1.53E+14	1.08E+14	5.63E+13
2.48E+04	1.8729E+14	1.33E+14	7.23E+13	1.83E+14	1.26E+14	6.85E+13
1.50E+04	1.1231E+14	7.72E+13	3.49E+13	1.10E+14	7.32E+13	3.31E+13
9.12E+03	6.1175E+13	4.08E+13	1.60E+13	5.98E+13	3.87E+13	1.52E+13
5.53E+03	5.0412E+13	3.27E+13	1.32E+13	4.91E+13	3.10E+13	1.25E+13
3.36E+03	2.9159E+13	1.83E+13	6.71E+12	2.83E+13	1.73E+13	6.30E+12
2.04E+03	1.6014E+13	9.60E+12	3.44E+12	1.54E+13	9.03E+12	3.19E+12
1.23E+03	6.6742E+12	3.86E+12	1.29E+12	6.37E+12	3.61E+12	1.18E+12
7.49E+02	3.2363E+12	1.86E+12	6.65E+11	3.01E+12	1.70E+12	5.88E+11
4.54E+02	9.2239E+11	5.15E+11	2.08E+11	8.38E+11	4.65E+11	1.79E+11
3.04E+02	5.4687E+11	2.99E+11	1.68E+11	4.60E+11	2.54E+11	1.31E+11
1.49E+02	8.0318E+10	4.33E+10	4.29E+10	5.87E+10	3.28E+10	3.05E+10
9.17E+01	1.9035E+10	1.05E+10	1.48E+10	1.10E+10	6.56E+09	8.83E+09
6.79E+01	1.3949E+10	7.98E+09	1.47E+10	6.15E+09	4.00E+09	7.38E+09
4.02E+01	4.8520E+09	2.88E+09	5.78E+09	2.23E+09	1.50E+09	2.99E+09
2.26E+01	8.7954E+08	5.22E+08	7.10E+08	4.16E+08	2.78E+08	3.70E+08
1.37E+01	7.7468E+08	4.54E+08	6.92E+08	1.52E+08	1.15E+08	1.72E+08
8.32E+00	1.8664E+08	1.09E+08	1.36E+08	4.58E+07	3.29E+07	3.72E+07
3.99E+00	8.7011E+08	5.79E+08	1.42E+09	1.53E+08	1.69E+08	5.50E+08
5.41E-01	4.5486E+07	2.84E+07	6.20E+07	5.73E+06	5.48E+06	1.53E+07
4.14E-01	7.1190E+07	4.26E+07	5.60E+07	1.73E+06	1.80E+06	3.66E+06

Problem 3: Fuel Cycle Consists of Six Partial Fuel Cycles of 300 Effective Full Power Days Each

Effective Multiplication Factor

Table 15 and Figures 44 and 45 provide the effective multiplication factor evolution with time.

Table 15. k-effective Evolution for 900 MW RBEC, 6 Cycles		
Time (days)	k-effective, REBUS-3	
	DIF3D	TWODANT
0	0.99715	0.99851
300	1.00499	1.00631
360	1.00317	1.00449
660	1.01002	1.01134
720	1.00740	1.00872
1020	1.01344	1.01478
1080	1.01027	1.01160
1380	1.01567	1.01704
1440	1.01213	1.01349
1740	1.01705	1.01844
1800	1.01328	1.01466
2100	1.01783	1.01925

As can be observed from Figures 44 and 45, the effective multiplication factor is increasing during the 300-day irradiation period. The core is then “removed” and cooled. Thus, the decrease in reactivity occurs. With time, the time change in reactivity becomes smaller for the irradiation period and larger for the cooling time until it reaches a steady state where no more absolute change in the effective multiplication factor takes place.

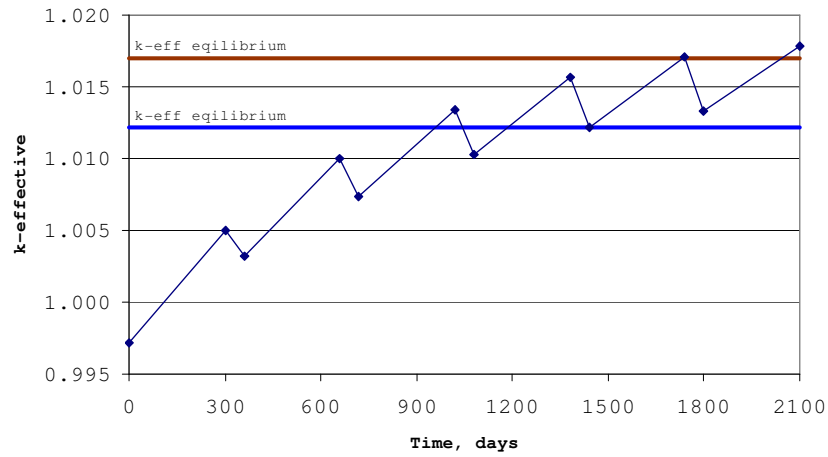


Figure 44. Evolution of k-effective, DIF3D.

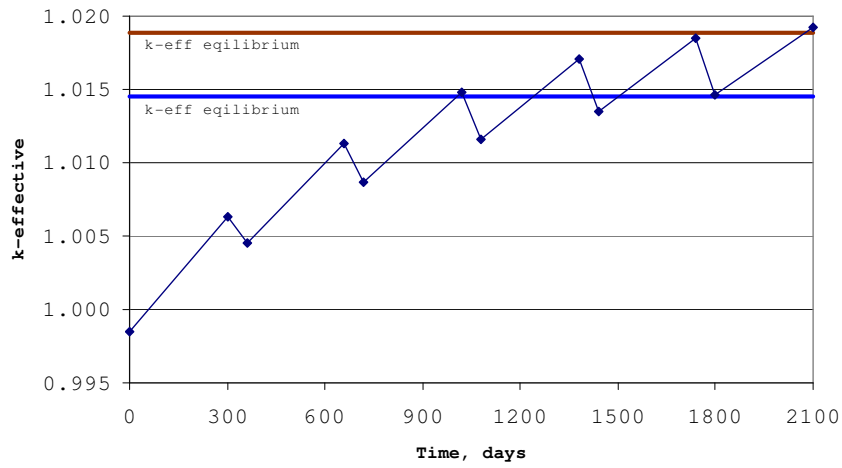


Figure 45. Evolution of k-effective, TWODANT.

Axial and Radial Power Profiles in the Core

Figure 46 depicts radial power density profiles in the core for the beginning and end of cycle. Two planes were chosen to illustrate the power density distribution: at the core midplane and near the top (45 cm from the core midplane.)

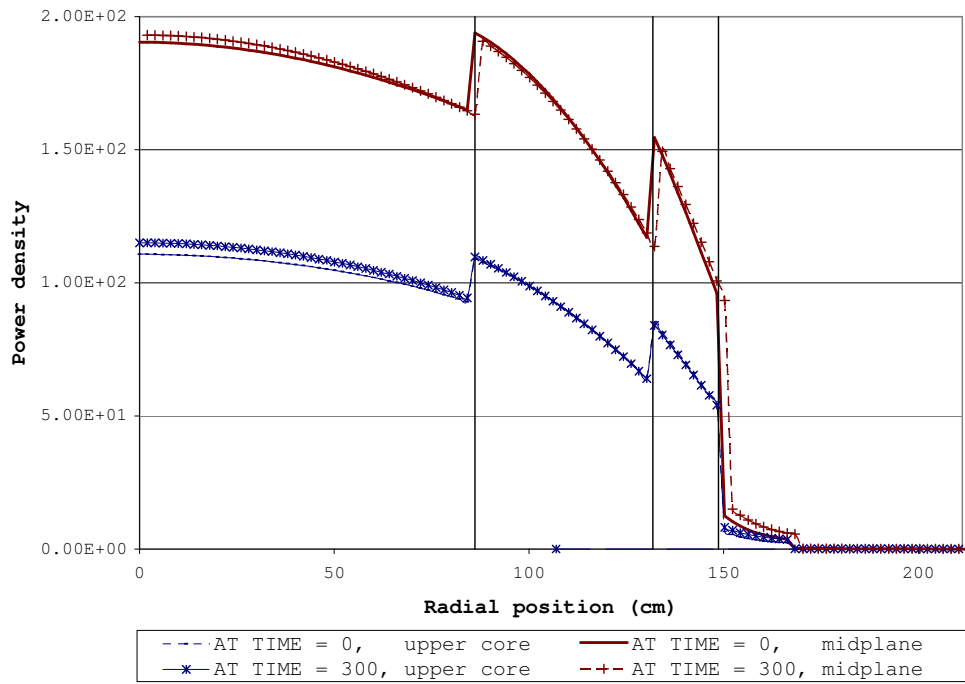


Figure 46. Radial Power Profiles in the Core for Subcycle 1.

Table 16. Region Powers and Power Peaking Factors, 6 Cycles					
TIME DAYS	ZONE NAME	POWER (WATTS)	POWER DENSITY (WATTS/CC)	PEAK DENSITY (WATTS/CC)(2)	PEAK TO AVG. POWER DENSITY
0	CORE-1	3.32878E+08	1.42723E+02	1.90442E+02	1.33435E+00
	CORE-2	3.97209E+08	1.26982E+02	1.94525E+02	1.53191E+00
	CORE-3	1.48398E+08	1.00153E+02	1.57904E+02	1.57662E+00
300	CORE-1	3.35270E+08	1.43748E+02	1.93038E+02	1.34289E+00
	CORE-2	3.89478E+08	1.24511E+02	1.91513E+02	1.53813E+00
	CORE-3	1.44271E+08	9.73679E+01	1.52553E+02	1.56677E+00
360	CORE-1	3.34861E+08	1.43573E+02	1.92603E+02	1.34150E+00
	CORE-2	3.90750E+08	1.24917E+02	1.92005E+02	1.53706E+00
	CORE-3	1.44957E+08	9.78307E+01	1.53439E+02	1.56841E+00
660	CORE-1	3.35826E+08	1.43987E+02	1.93897E+02	1.34663E+00
	CORE-2	3.84167E+08	1.22813E+02	1.89139E+02	1.54006E+00
	CORE-3	1.41727E+08	9.56514E+01	1.49086E+02	1.55864E+00
720	CORE-1	3.35358E+08	1.43786E+02	1.93352E+02	1.34472E+00
	CORE-2	3.86298E+08	1.23494E+02	1.90025E+02	1.53873E+00
	CORE-3	1.42815E+08	9.63855E+01	1.50519E+02	1.56164E+00
1020	CORE-1	3.35240E+08	1.43736E+02	1.93688E+02	1.34753E+00
	CORE-2	3.80538E+08	1.21653E+02	1.87252E+02	1.53923E+00
	CORE-3	1.40249E+08	9.46534E+01	1.46887E+02	1.55184E+00
1080	CORE-1	3.34894E+08	1.43587E+02	1.93184E+02	1.34541E+00
	CORE-2	3.83256E+08	1.22522E+02	1.88451E+02	1.53810E+00
	CORE-3	1.41569E+08	9.55445E+01	1.48665E+02	1.55598E+00
1380	CORE-1	3.33986E+08	1.43198E+02	1.92840E+02	1.34667E+00
	CORE-2	3.78077E+08	1.20866E+02	1.85741E+02	1.53675E+00
	CORE-3	1.39484E+08	9.41372E+01	1.45549E+02	1.54613E+00
1440	CORE-1	3.33863E+08	1.43145E+02	1.92489E+02	1.34471E+00
	CORE-2	3.81195E+08	1.21863E+02	1.87189E+02	1.53606E+00
	CORE-3	1.40926E+08	9.51103E+01	1.47538E+02	1.55123E+00
1740	CORE-1	3.32391E+08	1.42514E+02	1.91645E+02	1.34475E+00
	CORE-2	3.76422E+08	1.20337E+02	1.84537E+02	1.53351E+00
	CORE-3	1.39187E+08	9.39368E+01	1.44788E+02	1.54134E+00
1800	CORE-1	3.32541E+08	1.42579E+02	1.91501E+02	1.34313E+00
	CORE-2	3.79812E+08	1.21421E+02	1.86171E+02	1.53327E+00
	CORE-3	1.40678E+08	9.49429E+01	1.46899E+02	1.54723E+00
2100	CORE-1	3.30673E+08	1.41777E+02	1.90309E+02	1.34231E+00
	CORE-2	3.75317E+08	1.19984E+02	1.83561E+02	1.52988E+00
	CORE-3	1.39186E+08	9.39362E+01	1.44408E+02	1.53730E+00

Volume Averaged Neutron Spectra in the Core Zones

Volume averaged neutron flux per unit lethargy in the core zones was obtained at BOC and EOC. Figures 47 and 48 illustrate a histogram of the ratio of flux to lethargy versus neutron energy. Table 17 provides flux values for each energy group for all six cycles.

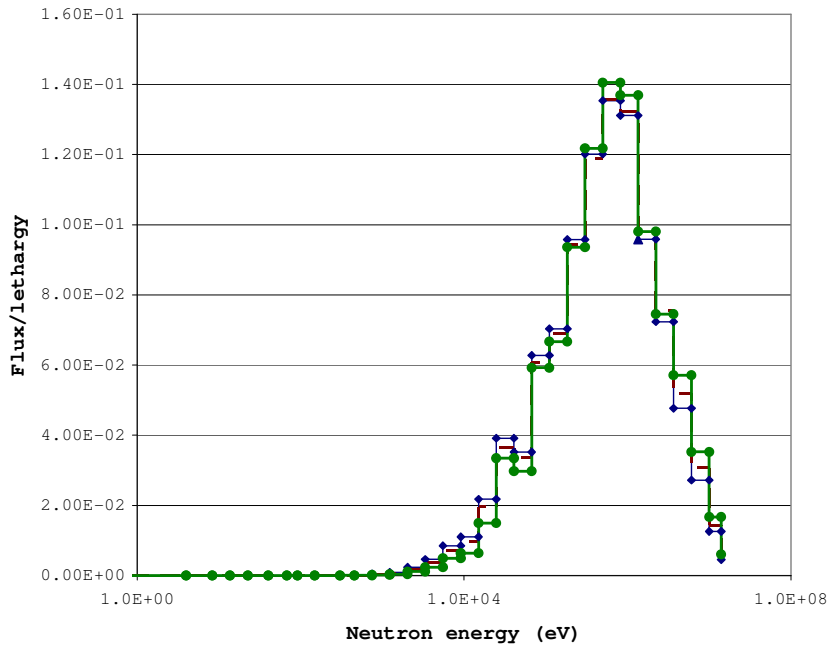


Figure 47. Flux/Lethargy vs. Neutron Energy at the Beginning of Cycle, Time=0 days.

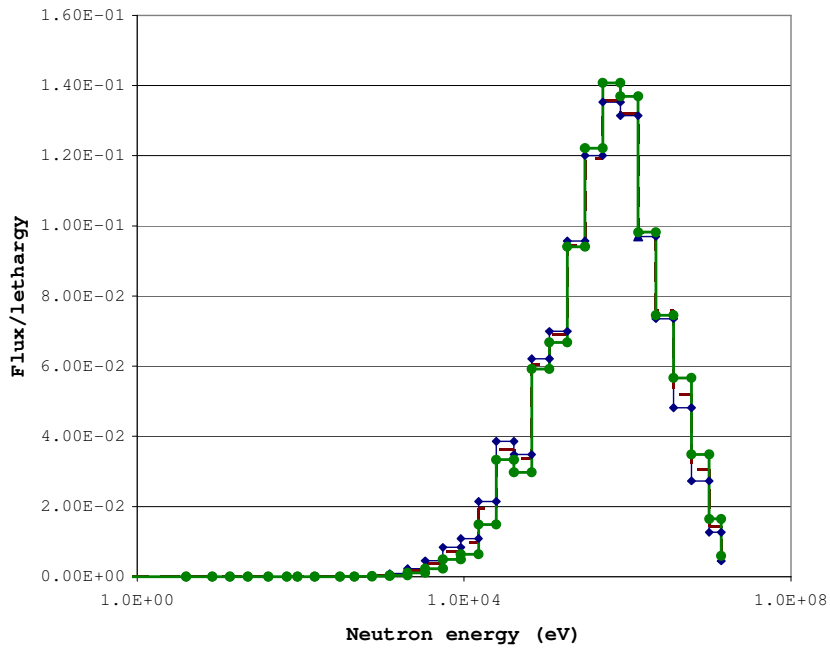


Figure 48. Flux/Lethargy vs. Neutron Energy at the End of Cycle, Time=2100 days.

Table 17. Volume Averaged Neutron Spectra in the Core, 6 Cycles

Energy (eV)	0			300			360		
	Core 1	Core 2	Core 3	Core 1	Core 2	Core 3	Core 1	Core 2	Core 3
1.41E+07	2.16E+11	1.88E+11	1.31E+11	2.16E+11	1.83E+11	1.27E+11	2.16E+11	1.83E+11	1.27E+11
1.00E+07	3.82E+12	3.32E+12	2.28E+12	3.84E+12	3.24E+12	2.22E+12	3.84E+12	3.26E+12	2.23E+12
6.07E+06	1.84E+13	1.59E+13	1.08E+13	1.85E+13	1.55E+13	1.05E+13	1.85E+13	1.56E+13	1.05E+13
3.68E+06	5.01E+13	4.17E+13	2.71E+13	5.03E+13	4.08E+13	2.63E+13	5.03E+13	4.10E+13	2.65E+13
2.23E+06	1.03E+14	8.22E+13	4.79E+13	1.04E+14	8.05E+13	4.67E+13	1.04E+14	8.08E+13	4.69E+13
1.35E+06	1.72E+14	1.35E+14	7.96E+13	1.73E+14	1.32E+14	7.76E+13	1.73E+14	1.32E+14	7.80E+13
8.21E+05	2.85E+14	2.20E+14	1.34E+14	2.85E+14	2.15E+14	1.31E+14	2.85E+14	2.16E+14	1.32E+14
4.98E+05	3.45E+14	2.64E+14	1.61E+14	3.45E+14	2.58E+14	1.58E+14	3.45E+14	2.60E+14	1.58E+14
3.02E+05	3.51E+14	2.66E+14	1.60E+14	3.51E+14	2.60E+14	1.57E+14	3.51E+14	2.61E+14	1.57E+14
1.83E+05	3.15E+14	2.37E+14	1.39E+14	3.15E+14	2.33E+14	1.36E+14	3.15E+14	2.33E+14	1.37E+14
1.11E+05	2.58E+14	1.94E+14	1.10E+14	2.57E+14	1.90E+14	1.08E+14	2.58E+14	1.90E+14	1.08E+14
6.74E+04	2.54E+14	1.87E+14	1.08E+14	2.53E+14	1.83E+14	1.06E+14	2.53E+14	1.84E+14	1.06E+14
4.09E+04	1.56E+14	1.14E+14	5.94E+13	1.55E+14	1.12E+14	5.80E+13	1.55E+14	1.12E+14	5.83E+13
2.48E+04	1.87E+14	1.33E+14	7.23E+13	1.86E+14	1.30E+14	7.06E+13	1.87E+14	1.31E+14	7.09E+13
1.50E+04	1.12E+14	7.72E+13	3.49E+13	1.12E+14	7.56E+13	3.41E+13	1.12E+14	7.59E+13	3.42E+13
9.12E+03	6.12E+13	4.08E+13	1.60E+13	6.08E+13	3.99E+13	1.56E+13	6.09E+13	4.01E+13	1.57E+13
5.53E+03	5.04E+13	3.27E+13	1.32E+13	5.00E+13	3.20E+13	1.29E+13	5.01E+13	3.22E+13	1.30E+13
3.36E+03	2.92E+13	1.83E+13	6.71E+12	2.89E+13	1.79E+13	6.53E+12	2.89E+13	1.80E+13	6.57E+12
2.04E+03	1.60E+13	9.60E+12	3.44E+12	1.58E+13	9.37E+12	3.33E+12	1.59E+13	9.41E+12	3.35E+12
1.23E+03	6.67E+12	3.86E+12	1.29E+12	6.57E+12	3.76E+12	1.25E+12	6.59E+12	3.78E+12	1.25E+12
7.49E+02	3.24E+12	1.86E+12	6.65E+11	3.15E+12	1.79E+12	6.34E+11	3.17E+12	1.81E+12	6.39E+11
4.54E+02	9.22E+11	5.15E+11	2.08E+11	8.91E+11	4.95E+11	1.96E+11	8.96E+11	4.99E+11	1.98E+11
3.04E+02	5.47E+11	2.99E+11	1.68E+11	5.12E+11	2.80E+11	1.53E+11	5.18E+11	2.84E+11	1.55E+11
1.49E+02	8.03E+10	4.33E+10	4.29E+10	7.13E+10	3.90E+10	3.78E+10	7.27E+10	3.97E+10	3.86E+10
9.17E+01	1.90E+10	1.05E+10	1.48E+10	1.53E+10	8.76E+09	1.22E+10	1.59E+10	9.02E+09	1.26E+10
6.79E+01	1.39E+10	7.98E+09	1.47E+10	1.01E+10	6.11E+09	1.13E+10	1.06E+10	6.38E+09	1.18E+10
4.02E+01	4.85E+09	2.88E+09	5.78E+09	3.58E+09	2.24E+09	4.52E+09	3.76E+09	2.34E+09	4.71E+09
2.26E+01	8.80E+08	5.22E+08	7.10E+08	6.53E+08	4.08E+08	5.55E+08	6.85E+08	4.25E+08	5.78E+08
1.37E+01	7.75E+08	4.54E+08	6.92E+08	3.86E+08	2.57E+08	4.00E+08	4.30E+08	2.81E+08	4.36E+08
8.32E+00	1.87E+08	1.09E+08	1.36E+08	1.00E+08	6.55E+07	8.07E+07	1.10E+08	7.09E+07	8.77E+07
3.99E+00	8.70E+08	5.79E+08	1.42E+09	5.62E+08	4.22E+08	1.11E+09	6.01E+08	4.43E+08	1.15E+09
5.41E-01	4.55E+07	2.84E+07	6.20E+07	2.26E+07	1.64E+07	3.93E+07	2.50E+07	1.77E+07	4.20E+07
4.14E-01	7.12E+07	4.26E+07	5.60E+07	1.32E+07	1.05E+07	1.77E+07	1.66E+07	1.28E+07	2.08E+07

2.4.5. Benchmarking Pre-Existing Russian Criticals Data Relevant to Lead-Cooled Reactors

The benchmarking calculations have been performed for a specified reactor core concept. There is no supporting experiment data for the specified core configuration. A number of

LFR-relevant configurations have been studied using critical facilities located at IPPE in Russia. Some of the data has been published in Russian. A brief review of available Russian literature on LFR-relevant criticals data [11-13] was carried out to identify what Russian data might eventually be made available for future international benchmarking exercises. A summary of data from the BFS-77 critical assembly obtained in support of the BREST-OD-300 lead-cooled fast reactor and its comparison to calculations is presented in Tables 17 through 19. The BFS-77 critical assembly was created on the BFS-1 critical facility. Its main purpose was to provide a mockup of the low enrichment zone of the BREST-OD-300 reactor core. The assembly was extensively used to study the spectral characteristics of the active core zone.

Table 18. Criticality Comparison				
BFS	Characteristics	MMK-KENO	MCNP	
		ABBN-93	ENDF/B-6	ABBN/BREST
61-0	Pb+SS+UO ₂	0.9995(5)	1.0009	
61-1	Pb+UO ₂	0.9971(5)	1.0009	
61-2	UO ₂	0.9977(5)	1.0000	
77	UO ₂	1.0016(6)	1.0002(2)	1.0033
87-1	Pb-Bi	0.9979(5)	1.0041	
87-2	Pb	0.9976(5)	1.0061	
95-1	Pb, (Pu-95%+Pu-89%)	1.0003(2)	-	
95-2	Pb, (Pu-95%)	0.9997(2)	-	

Table 19. Theoretical/Experimental data for spectral indexes for BFS-77			
Index	BFS-61	BFS -77	BFS -77
	TRIGEX	TRIGEX	MCNP
C238/F235	1.001 ± 0.024	1.056±0.050	1.013±0.050
F238/F235	0.968 ± 0.030	1.011±0.030	0.985±0.030
F239/F235	1.002 ± 0.015	0.996±0.014	0.995±0.014
F240/F239	1.050 ± 0.020	1.043±0.033	1.103±0.033
²³⁷ FNp /F239	-	1.079±0.042	1.039±0.042
²³⁸ FPu /F239	-	1.056±0.022	1.063±0.022
²⁴¹ FAm /F239	-	0.985±0.039	0.907±0.039
²⁴³ FAm /F239	-	1.15±0.08	1.016±0.080

Table 20. Control Rod Worth, BFS-77			
Rod Type	Experiment β_{eff}	TRIGEX	MCNP
Test zone BREST-300	0.11	0.082	0.091±0.05
Test zone BREST-300	0.10	0.080	0.13±0.05
Driver zone	0.31	0.307	0.36±0.05
Driver zone	0.30	0.276	0.32±0.05
Absorber B ₄ C	1.16	1.16	1.23±0.05
3 rods c B ₄ C	3.22	3.18	3.26±0.05
4 rods c B ₄ C	4.01	3.97	4.15±0.05
Reflector	0.07	0.042	-
Reflector	0.08	0.038	-

2.4.6. Benchmarking Summary

The RBEC-M benchmark problem defined in the IAEA CRP on “Small Reactors without On-site Refueling” was investigated. Analysis of three different reactor operational modes with various edits at the beginning and end of the specified cycles was performed. The results for all three modes of reactor operation were obtained and discussed; i.e., criticality calculation, axial and radial power profiles, neutron spectra, power peaking factors, and k-infinity in the core central zone. The results of the benchmarking calculations were submitted to the IAEA.

2.5. Industrial Health and Safety Aspects of Lead and Lead Industrial Practice

2.5.1. Introduction

The use of lead or lead-bismuth coolant involves consideration of the potential for exposure of personnel to lead due to postulated incidents during construction, initial startup, operation, or decommissioning and decontamination of the plant. Depending upon the incident, the lead may be contained in the form of a solid, liquid, vapor, or aerosol. For example, exposure to lead might be postulated during certain accidents, refueling operations, replacement of components, or leakages (e.g., from the active system for controlling the coolant dissolved oxygen potential or from the coolant purification system). A review has been initiated of the health effects of lead and bismuth, U.S. regulations for protecting workers from lead hazards, as well as examples of industrial and construction practice for working with lead. The review has not considered the effects of radioactivity. Additional regulations to protect against the

effects of radioactivity with lead or lead-bismuth coolant are not addressed here. Initial results of the review are presented below. They demonstrate that regulations and procedures for protecting industrial and construction workers from the health hazards of lead are well established and routinely implemented. The review has not identified any regulations that would be expected to significantly impact the initial startup, operation, or decommissioning and decontamination of a LFR. U.S. regulations for protecting workers from lead hazards or analogous regulations in other nations have not impeded the charging, startup, operation, or modification of experiment loops or facilities utilizing LBE or lead coolants.

2.5.2. Acronyms and Definitions

EPA	Environmental Protection Agency
HUD	Department of Housing and Urban Development
NEA	Negative Exposure Assessment
NIOSH	National Institute for Occupational Safety and Health
OSHA	Occupational Safety and Health Administration
ACGIH	American Conference of Governmental Industrial Hygienists
PEL	Permissible Exposure Limit
REL	Recommended Exposure Limit
TLV	Threshold Limit Value

"Assistant Secretary" means the Assistant Secretary of Labor for Occupational Safety and Health, U.S. Department of Labor, or designee.

"Director" means the Director, National Institute for Occupational Safety and Health (NIOSH), U.S. Department of Health, Education, and Welfare, or designee.

2.5.3. Health Effects of Lead

All lead compounds can be classified as either organic or inorganic. Organic compounds are those which contain carbon. Organic lead has been used in the past in leaded gasoline. The forms of lead known as tetraethyl-lead and tetramethyl-lead were added to motor-vehicle fuels as anti-knock agents. However due to the dangerous health effects and environmental effects, use of lead in gasoline was

successfully phased out between 1974 and 1990, and therefore, exposure to this form has been greatly reduced.

The widespread occurrence of lead in the environment is largely the result of anthropogenic activity, which has occurred since prehistoric times. Lead usage increased progressively with industrialization and rose dramatically with the use of lead-acid batteries and leaded fuel for automobiles in the twentieth century. The predominant use of lead is now in batteries and, to a lesser extent, in construction materials and lead-based chemicals.

Lead exposure may occur in many operations today. It is important to be aware of the toxic effects that lead has on the human body through various routes of entry. It is absorbed into the body primarily through inhalation, ingestion, and/or the skin. The important routes of human exposure from lead-contaminated air, dust, soil, water, and food are through inhalation and ingestion. Recent human exposure has arisen predominantly from the widespread use of leaded gasoline. Also, areas near lead mines and smelters have high environmental concentrations of lead. Occupations in which the highest potential exposure to lead exists include mining, primary and secondary smelting, production of lead-acid batteries, pigment production, construction, and demolition. In spite of the persistence of lead in the environment, exposures have decreased substantially in countries where lead control measures have been implemented over the past 10 to 30 years.

Lead is a toxin and it accumulates in the blood, bones, kidneys, brain, and liver causing a variety of health problems. Children and unborn babies are much more susceptible to the effects of lead poisoning during the time when their bodies go through development stages.

Exposure to lead may be acute or it may be chronic. Symptoms of acute exposure may be headaches, fatigue, abdominal pain, loss of appetite, vomiting, muscular aches and weakness, loss of coordination, sleep disturbances, irritability, convulsions, stupor, and possibly coma. Symptoms of chronic exposure may be insomnia, metallic taste in the mouth, anemia, constipation, headache, muscle and joint pain, neuromuscular dysfunction, liver or kidney damage, possible paralysis and encephalopathy, and reproductive changes in both males and females.

It is important that workers be trained to understand and recognize the symptoms of lead poisoning so that they can receive prompt medical attention. It is also important to be aware that lead poisoning is not always accompanied by symptoms until a significant amount of damage has been done. One way to account for safety is to have regular checkups with a doctor and to do biological monitoring to watch the blood levels of lead in the body. Immediate attention to medical needs will greatly decrease the potential for long term health effects from overexposure.

Lead is devastating to the human body inhibiting oxygen and calcium transport, and altering nerve transmissions in the brain.

Lead is a cardiovascular toxicant. Exposure to chemical substances can cause adverse effects on the cardiovascular heart and blood vessels or hematopoietic blood systems (Cardiovascular or Blood Toxicity). Exposure to cardiovascular toxicants can contribute to a variety of diseases, including elevated blood pressure (hypertension), hardening of the arteries (arteriosclerosis), abnormal heartbeat (cardiac arrhythmia), and decreased blood flow to the heart (coronary ischemia).

Human studies are inconclusive regarding lead exposure and an increased cancer risk. The EPA and the International Agency for Research on Cancer (IARC) have categorized lead and inorganic lead as a B2 classification (probable/possible human carcinogen).

2.5.4. Emergency and First Aid Procedure Recommendations

Inhalation:	Remove from exposure, gargle with fluid to clean throat, wash nose and lips; consult a physician.
Ingestion:	Induce vomiting if individual is conscious, wash nose and lips; give a demulcent, consult a physician.
Skin:	Wash immediately with brush using soap and water, flush with plenty of water; contact physician.
Eyes:	Flush immediately with large amounts of water for at least 15 minutes; consult a physician immediately.

2.5.5. Health Effects of Bismuth

Bismuth is a brittle metal with a pinkish hue and an iridescent oxide tarnish showing many refractive colors from yellow to blue. Among the heavy metals, bismuth is unusual in that its toxicity is much lower than that of its neighbors in the periodic table such as lead, thallium, and antimony. Thus, the use of bismuth in industry is not of significant concern regarding its health effects.

2.5.6. Health Rules and Regulations for Lead

There are several agencies in the United States which concern themselves with the safe practice of operating with lead and using lead in industry. The EPA, OSHA, NIOSH, and ACGIH are concerned with protecting the workers and surrounding environment with respect to operating with lead. Each agency in accordance has developed a set of rules and regulations to be followed.

Partial Sources of Information

The following documents were reviewed:

- 29 CFR 1910.1025 Occupational Safety and Health Standards Toxic and Hazardous Substances

- 29 CFR 1926.26 Safety and Health Regulations for Construction Occupational Health and Environmental Controls
- DHHS (NIOSH) Publication No. 2005-149 NIOSH Pocket Guide to Chemical Hazards
- EPA 40 CFR Part 63 National Emission Standards for Hazardous Air Pollutants for Primary Lead Smelting

The regulations most widely used in operations dealing with lead are 1910.1025 Occupational Safety and Health Standards Toxic and Hazardous Substances.

Some of the more pertinent aspects of this document are:

Viable Levels

- The employer shall assure that no employee is exposed to lead at concentrations greater than fifty micrograms per cubic meter of air ($50 \mu\text{g}/\text{m}^3$) averaged over an 8-hour period.
- If an employee is exposed to lead for more than 8 hours in any work day, the permissible exposure limit, as a time weighted average (TWA) for that day, shall be reduced according to the following formula:

Maximum permissible limit (in $\mu\text{g}/\text{m}^3$) = 400 divided by hours worked in the day.

- When respirators are used to supplement engineering and work practice controls to comply with the PEL and all the requirements of respiratory protection have been met, employee exposure, for the purpose of determining whether the employer has complied with the PEL, may be considered to be at the level provided by the protection factor of the respirator for those periods the respirator is worn. Those periods may be averaged with exposure levels during periods when respirators are not worn to determine the employee's daily TWA exposure.

Exposure monitoring

- Employee exposure is that exposure which would occur if the employee were not using a respirator.
- The employer shall collect full shift (for at least 7 continuous hours) personal samples including at least one sample for each shift for each job classification in each work area.
- Full shift personal samples shall be representative of the monitored employee's regular, daily exposure to lead.

- Initial determination. Each employer who has a workplace or work operation covered by this standard shall determine if any employee may be exposed to lead at or above the action level.

Employee notification

- The employer must, within 15 working days after the receipt of the results of any monitoring performed under this section, notify each affected employee of these results either individually in writing or by posting the results in an appropriate location that is accessible to affected employees.
- Whenever the results indicate that the representative employee exposure, without regard to respirators, exceeds the PEL, the employer shall include in the written notice a statement that the permissible exposure limit was exceeded and a description of the corrective action taken or to be taken to reduce exposure to or below the permissible exposure limit.
- Accuracy of measurement. The employer shall use a method of monitoring and analysis which has an accuracy (to a confidence level of 95%) of not less than plus or minus 20 percent for airborne concentrations of lead equal to or greater than $30 \mu\text{g}/\text{m}^3$.

Methods of compliance

- Where any employee is exposed to lead above the permissible exposure limit for more than 30 days per year, the employer shall implement engineering and work practice controls (including administrative controls) to reduce and maintain employee exposure to lead in accordance with the implementation schedule, except to the extent that the employer can demonstrate that such controls are not feasible. Wherever the engineering and work practice controls which can be instituted are not sufficient to reduce employee exposure to or below the permissible exposure limit, the employer shall nonetheless use them to reduce exposures to the lowest feasible level and shall supplement them by the use of respiratory protection.
- Where any employee is exposed to lead above the permissible exposure limit, but for 30 days or less per year, the employer shall implement engineering controls to reduce exposures to $200 \mu\text{g}/\text{m}^3$, but thereafter may implement any combination of engineering, work practice (including administrative controls), and respiratory controls to reduce and maintain employee exposure to lead to or below $50 \mu\text{g}/\text{m}^3$.

Written plans for these compliance programs shall include at least the following:

- A description of each operation in which lead is emitted; e.g. machinery used, material processed, controls in place, crew size, employee job responsibilities, operating procedures and maintenance practices.
- A description of the specific means that will be employed to achieve compliance, including engineering plans and studies used to determine methods selected for controlling exposure to lead.
- A report of the technology considered in meeting the permissible exposure limit.
- Air monitoring data which documents the source of lead emissions.
- A detailed schedule for implementation of the program, including documentation such as copies of purchase orders for equipment, construction contracts, etc.
- A work practice program.
- An administrative control schedule if applicable.

Other relevant information

- Written programs shall be submitted upon request to the Assistant Secretary and the Director, and shall be available at the worksite for examination and copying by the Assistant Secretary, Director, any affected employee or authorized employee representatives.
- Written programs must be revised and updated at least annually to reflect the current status of the program.

Mechanical ventilation

- When ventilation is used to control exposure, measurements which demonstrate the effectiveness of the system in controlling exposure, such as capture velocity, duct velocity, or static pressure shall be made at least every 3 months. Measurements of the system's effectiveness in controlling exposure shall be made within 5 days of any change in production, process, or control which might result in a change in employee exposure to lead.
- Recirculation of air. If air from exhaust ventilation is recirculated into the workplace, the employer shall assure that:
 - the system has a high efficiency filter with reliable back-up filter;

- controls to monitor the concentration of lead in the return air and to bypass the recirculation system automatically if it fails are installed, operating, and maintained.
- Administrative controls. If administrative controls are used as a means of reducing employees TWA exposure to lead, the employer shall establish and implement a job rotation schedule which includes:
 - Name or identification number of each affected employee;
 - Duration and exposure levels at each job or work station where each affected employee is located; and
 - Any other information which may be useful in assessing the reliability of administrative controls to reduce exposure to lead.

Respiratory Protection

- For employees who use respirators required by this section, the employer must provide respirators.
- The employer must implement a respiratory protection program in accordance with 29 CFR 1910.134

Protective work clothing and equipment

- Provision and use. If an employee is exposed to lead above the PEL, without regard to the use of respirators or where the possibility of skin or eye irritation exists, the employer shall provide at no cost to the employee and assure that the employee uses appropriate protective work clothing and equipment such as, but not limited to:
 - Coveralls or similar full-body work clothing;
 - Gloves, hats, and shoes or disposable shoe coverlets; and
 - Face shields, vented goggles, or other appropriate protective equipment which complies with 1910.133 of this Part.

Cleaning and replacement

- The employer shall provide the protective clothing in a clean and dry condition at least weekly, and daily to employees whose exposure levels without regard to a respirator are over 200 $\mu\text{g}/\text{m}^3$ of lead as an 8-hour TWA.
- The employer shall provide for the cleaning, laundering, or disposal of protective clothing and equipment required.
- The employer shall repair or replace required protective clothing and equipment as needed to maintain their effectiveness.

- The employer shall assure that contaminated protective clothing which is to be cleaned, laundered, or disposed of, is placed in a closed container in the change-room which prevents dispersion of lead outside the container.
- The employer shall inform in writing any person who cleans or launders protective clothing or equipment of the potentially harmful effects of exposure to lead.
- The employer shall assure that the containers of contaminated protective clothing and equipment labeled as follows: CAUTION: CLOTHING CONTAMINATED WITH LEAD. DO NOT REMOVE DUST BY BLOWING OR SHAKING. DISPOSE OF LEAD CONTAMINATED WASH WATER IN ACCORDANCE WITH APPLICABLE LOCAL, STATE, OR FEDERAL REGULATIONS.

Hygiene facilities and practices

- The employer shall assure that in areas where employees are exposed to lead above the PEL, without regard to the use of respirators, food or beverage is not present or consumed, tobacco products are not present or used, and cosmetics are not applied, except in change rooms, lunchrooms, and showers.
- The employer shall provide clean change rooms for employees who work in areas where their airborne exposure to lead is above the PEL, without regard to the use of respirators.
- The employer shall assure that change rooms are equipped with separate storage facilities for protective work clothing and equipment and for street clothes which prevent cross-contamination.
- The employer shall assure that employees who work in areas where their airborne exposure to lead is above the PEL, without regard to the use of respirators, shower at the end of the work shift. The employer shall provide shower facilities in accordance with 1910.141.
- The employer shall assure that employees who are required to shower do not leave the workplace wearing any clothing or equipment worn during the work shift.

Medical surveillance

- The employer shall institute a medical surveillance program for all employees who are or may be exposed above the action level for more than 30 days per year. The employer shall assure that all medical examinations and procedures are performed by or under the supervision of a licensed physician.

Biological monitoring

- Blood lead and ZPP (Zinc protoporphyrin) level sampling and analysis. The employer shall make available biological monitoring in the form of blood sampling and analysis for lead and zinc protoporphyrin levels to each employee on the following schedule:
- At least every 6 months to each employee covered under paragraph (j)(1)(i) of this section;
- At least every two months for each employee whose last blood sampling and analysis indicated a blood lead level at or above 40 µg/100 g of whole blood. This frequency shall continue until two consecutive blood samples and analyses indicate a blood lead level below 40 µg/100 g of whole blood; and
- At least monthly during the removal period of each employee removed from exposure to lead due to an elevated blood lead level.
- Employee notification. Within five working days after the receipt of biological monitoring results, the employer shall notify in writing each employee whose blood lead level exceeds 40 µg/100 g:
- A blood sample and analysis which determines:
 - Blood lead level
 - Hemoglobin and hematocrit determinations, red cell indices, and examination of peripheral smear morphology
 - Zinc protoporphyrin
 - Blood urea nitrogen
 - Serum creatinine
- A routine urinalysis with microscopic examination

Signs

- The employer may use signs required by other statutes, regulations or ordinances in addition to, or in combination with, signs required by this paragraph.
- The employer shall assure that no statement appears on or near any sign required by this paragraph which contradicts or detracts from the meaning of the required sign.
- The employer shall post the following warning signs in each work area where the PEL is exceeded:

WARNING
LEAD WORK AREA
POISON
NO SMOKING OR EATING

- The employer shall assure that signs required by this paragraph are illuminated and cleaned as necessary so that the legend is readily visible.

Recordkeeping

- The employer shall establish and maintain an accurate record of all monitoring required.
- This record shall include:
 - The date(s), number, duration, location and results of each of the samples taken, including a description of the sampling procedure used to determine representative employee exposure where applicable;
 - A description of the sampling and analytical methods used and evidence of their accuracy;
 - The type of respiratory protective devices worn, if any;
 - Name, social security number, and job classification of the employee monitored and of all other employees whose exposure the measurement is intended to represent; and the environmental variables that could affect the measurement of employee exposure.
- The employer shall maintain these monitoring records for at least 40 years or for the duration of employment plus 20 years, whichever is longer.

2.5.7. Lead Health Industrial Practice

Lead is used in a number of operations such as recycling of scrap metal, manufacturing and/or recycling of car batteries, the ceramics industry, soldering, welding, cutting, smelting, refining, and operations using or removing lead based paints. It is quite surprising that the effects of lead have been understood for some time.

Lead, is found to be absorbed through natural environmental exposure. The amounts found on average in the human body are blood lead levels in the range, 0.00 to 0.25 $\mu\text{mol/L}$. However, in a closed area where lead may be in the form of dust or fume, special clothing is required as mentioned in the previous section. When working with molten metal, it is a requirement to provide adequate general and local exhaust ventilation. Chemical resistant protective gloves are required for prolonged or repeated contact. Wearing of safety goggles to prevent any possibility of contact with molten

material is required. It is vital to follow good personal hygiene to avoid inhalation and ingestion: wash hands, face, neck, and arms thoroughly before eating, smoking, or leaving the work site.

Thus, industries handling lead are required to provide certain accommodations in their facilities for their workers. Industries are required to follow the rules and regulations set forth in the previous section. However, the extent of which rules and regulations they follow is decided by the type of work that they are engaged in. It is important to maintain cleanliness by using certain equipment which also is highly dependent on the environment and type of operation the worker shall be dealing with.

In the case where particles of lead may be airborne whether they are in the form of dust or vapor, industry is required to provide proper ventilation and a breathing apparatus such as the one shown in Figure 49.

All clothing after working in a contaminated area should be carefully cleaned and disposed of into specified laundry areas. The utilities for cleansing the lead particles off of work clothing may be simple like the one in Figure 50 or more complex like in Figure 51. This is to be determined by the level and type of lead particles that the workers shall interact with.



Figure 49. Example of Protection Against Inhalation.

Shoe Cleaning Machine

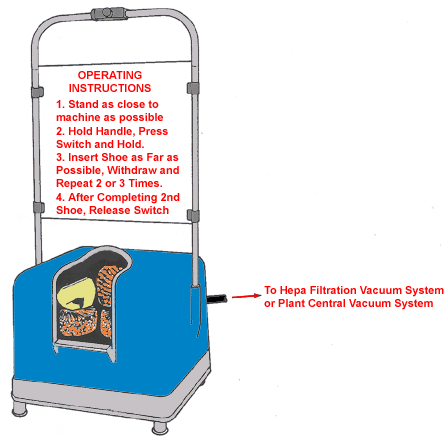


Figure 50. Shoe Cleaning Machine.

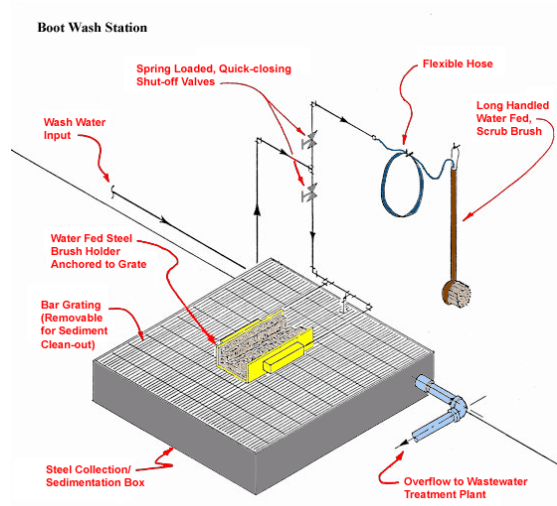


Figure 51. Boot Washing Machine

In lead contaminated areas where the contamination is above the specified PEL there should be signs posted which are clearly visible at the entrance of the structure or at the specified work area. The signs should also be illuminated and cleaned as needed. These work areas are also required to provide a strong enough ventilation system with air filtering equipment to prevent the emission of lead dust into the environment.

2.5.8. Lead Industrial Accident Practice

The word accident pertains to an unforeseen and unexpected situation. The main procedures in case of an industrial accident relate to a wide variety of incidents for which the hazards are rather small.

Personnel working in areas with hazardous lead fumes or dust, given a scenario where the ventilation or air filtering equipment malfunctions, should immediately halt their work, evacuate the area of concern, and call in a proper maintenance crew.

If there is an individual injured during an operation, guidelines should be followed. Most importantly, a medical doctor should be consulted for more intensive examination where blood tests should be taken.

Given a scenario where there is a spill of molten lead or lead dust, personnel should immediately evacuate the area and cease any processes being performed. Precautions to protecting the environment in this case should be to pick up the small pieces carefully using a wet mop or a filtered vacuum. During every accident scenario, respirators should be used, if dust or fumes are present.

2.5.9. Respirator Requirements of 29 CFR 1910.1025 (General Industry Lead Standard)

Airborne Concentration or Condition of Use	Required Respirator
$\leq 0.5 \text{ mg/m}^3$ (milligrams per cubic meter) (10 X PEL)	Half-mask* air-purifying respirator equipped with high-efficiency filters**.
$\leq 2.5 \text{ mg/m}^3$ (50 X PEL)	Full-facepiece air-purifying respirator with high-efficiency filters**.
$\leq 50 \text{ mg/m}^3$ (1000 X PEL)	(1) Any powered air-purifying respirator with high-efficiency filters**; or (2) Half-mask* supplied-air respirator operated in positive-pressure mode.
$\leq 100 \text{ mg/m}^3$ (2000 X PEL)	Supplied-air respirators with full facepiece, hood, helmet, or suit, operated in positive-pressure mode.
$> 100 \text{ mg/m}^3$, unknown concentration, or firefighting	Full-facepiece, self-contained breathing apparatus operated in positive-pressure mode.
<p>* Full facepiece is required if the lead aerosols cause eye or skin irritation at the use concentrations.</p> <p>** A high-efficiency filter means a filter that is at least 99.97% efficient against mono-dispersed particles of $0.3 \mu\text{m}$ (micrometers) in diameter or higher.</p>	

2.5.10. Respirator Requirements of 29 CFR 1926.62 (Construction Lead Standard)

Airborne Concentration or Condition of Use	Required Respirator
$\leq 0.5 \text{ mg/m}^3$ (milligrams per cubic meter)	(1) Half-mask* air-purifying respirator with high-efficiency filters**; or (2) Half-mask* supplied-air respirator operated in demand (negative pressure) mode.
$\leq 1.25 \text{ mg/m}^3$	(1) Loose-fitting hood or helmet powered air-purifying respirator with high-efficiency filters**; or (2) Hood or helmet supplied-air respirator operated in a continuous-flow mode (e.g., Type CE abrasive blasting respirators [see page 360] operated in a continuous-flow mode).
$\leq 2.5 \text{ mg/m}^3$	(1) Full-facepiece air-purifying respirator with high-efficiency filters**; (2) Tight-fitting powered air-purifying respirator with high-efficiency filters**; (3) Full-facepiece supplied-air respirator operated in demand mode; (4) Half-mask* or full-facepiece supplied-air respirator operated in a continuous-flow mode; or (5) Full-facepiece self-contained breathing apparatus operated in demand mode.
$\leq 50 \text{ mg/m}^3$	Half-mask* supplied-air respirator operated in pressure-demand or other positive-pressure mode.
$\leq 100 \text{ mg/m}^3$	Full-facepiece supplied-air respirator operated in pressure-demand or other positive-pressure mode (e.g., Type CE abrasive blasting respirators [see page 360] operated in a continuous-flow mode).
$> 100 \text{ mg/m}^3$, unknown concentration, or firefighting	Full-facepiece self-contained breathing apparatus in pressure-demand or other positive-pressure mode.
<p>* Full facepiece is required if the lead aerosols cause eye or skin irritation at the use concentrations.</p> <p>** A high-efficiency filter means a filter that is at least 99.97% efficient against mono-dispersed particles of $0.3 \mu\text{m}$ (micrometers) in diameter or higher.</p>	

2.5.11. Supplementary Exposure Limits

NIOSH considers “Lead” to mean metallic lead, lead oxides, and lead salts (including organic salts such as lead soaps but excluding lead arsenate). The NIOSH REL for lead (10-hour TWA) is 0.050 mg/m^3 ; air concentrations should be maintained so that worker blood lead remains less than $0.060 \text{ mg Pb/100 g}$ of whole blood.

OSHA considers “Lead” to mean metallic lead, all inorganic lead compounds (lead oxides and lead salts), and a class of organic compounds called soaps; all other lead compounds are excluded from this definition. The OSHA PEL (8-hour TWA) is 0.050 mg/m³; other OSHA requirements can be found in 29 CFR 1910.1025. The OSHA PEL (8 hour-TWA) for lead in “non-ferrous foundries with less than 20 employees” is 0.075 mg/m³.

2.5.12. Partial List of Websites

http://www.osha.gov/pls/oshaweb/owadisp.show_document?p_table=STANDARDS&p_id=10031

http://www.osha.gov/pls/oshaweb/owadisp.show_document?p_table=STANDARDS&p_id=10030

<http://www.osha.gov/SLTC/etools/leadsmelter/refiningcasting/casting.html>

<http://www.osha.gov/SLTC/etools/leadsmelter/smelting/blastfurnace.html>

<http://www.leadpoison.net/general/understanding.htm>

<http://www.epa.gov/ttn/atw/hlthef/lead.html>

<http://www.epa.gov/ttn/atw/hlthef/lead.html>

2.6. Argonne National Laboratory International Collaborations

ANL is participating in the following International-Nuclear Energy Research Initiative (INERI) joint collaborations:

2004-003-E, “Lead (Pb) Fast Reactor Engineering and Analysis,” Three-year project with the Joint Research Center of the European Commission, Institute for Energy (JRC/IE), Petten, the Netherlands. The project runs from November 2004 through November 2007;

2005-001-K, “Supercritical Carbon Dioxide Brayton Cycle Energy Conversion,” Three-year project with the Korea Atomic Energy Research Institute (KAERI). The project duration is October 1, 2005 through September 30, 2008.

Jim Sienicki is the U.S. DOE-designated member of the Generation IV International Forum (GIF) Sodium-Cooled Fast Reactor (SFR) System Steering Committee (SSC) Component Design and Balance of Plant Project Management Board (PMB). He participated in meetings of the Component Design and Balance of Plant PMB held at JAEA in O-arai, Japan, February 20 and 21, 2006, and in Reno, Nevada, June 4, 2006. He arranged and hosted the meeting in Reno. Sienicki created a set of ten Task Sheets describing the projects on the U.S. side related to supercritical CO₂ Brayton cycle power

conversion. One set of five Task Sheets covers the interval through 2007 while the other five Task Sheets cover 2008 through 2010. Sienicki thus formulated a five-year plan and estimated budgets for U.S. activities related to supercritical CO₂ Brayton cycle power conversion.. He also reviewed and modified the Project Plan for the Component Design and Balance of Plant (CD & BOP) Project Management Board (PMB) to reflect the new set of U.S. Task Sheets.

2.7. Argonne National Laboratory International Interactions

Jim Sienicki participated in the IAEA Technical Meeting to “Review Experience and Options Relevant for Validation, Testing and Demonstration of Passive Safety Systems for Small and Medium Reactors” held at IAEA Headquarters in Vienna on October 17-21, 2005. Jim Sienicki was elected chairman of the Technical Meeting and served in that capacity. He prepared and delivered a presentation, “Regulatory Issues Relevant to the Validation, Testing and Demonstration of Passive Systems for Advanced Reactors in the United States.” He prepared two contributions to a draft follow-on IAEA TECDOC, “Review of Experience and Options Relevant for Validation, Testing and Demonstration of Passive Safety Systems for SMRs.” Specifically, Sienicki authored Section III-3, ““License-by-test” Approach,” and Section V-4, “PRISM Pre-application Review.”

Jim Sienicki prepared with input from Anton Moisseytsev and Dave Wade a description of the SSTAR and STAR-LM LFRs and the passive safety design features of SSTAR and STAR-LM for a draft IAEA TECDOC on Passive Safety Design Options for Small and Medium Sized Reactors.

Jim Sienicki, Dave Wade, and Anton Moisseytsev participated in the Lead Interest Group Meeting held in conjunction with the LFR System Steering Committee (SSC) Meeting in Reno on June 8. As the Generation IV LFR Co-SIM, Sienicki presented the status, priorities, and plans for LFR work in the U.S. He also attended a portion of the GIF LFR SSC Meeting.

Jim Sienicki participated in the meeting of the OECD NEA Lead Alloy Coolant Advanced Nuclear Energy Systems (LACANES) Working Group chaired by Professor Il Soon Hwang of Seoul National University (SNU) held in Reno on June 8. The Working Group accepted Sienicki’s suggestion that the near-term focus be limited initially to comparison of methodologies for the calculation of natural circulation thermal hydraulics with available data from heavy liquid metal coolant loops such as the HELIOS loop at SNU, and that the subsequent focus be directed towards the need for three-dimensional facilities investigating LFR thermal hydraulics including natural circulation flows and heat transfer.

Luciano Cinotti of Del Fungo Giera Energia and Stefano Monti of ENEA in Italy visited ANL/NE on the afternoon of Thursday, August 3, and morning of Friday, August 4. Luciano is leading the development of the European Lead System (ELSY) 600 MWe Lead-Cooled Fast Reactor. Presentations and discussions involved Jim Sienicki, Dave

Wade, Anton Moiseyev, and Won Sik Yang as well as students, Anna Nikiforova, Pierre Hanania, and Konrad Kulesza. Craig Smith from LLNL also traveled to ANL to participate together with Levent Can, a Turkish graduate student from the Naval Postgraduate School.

Dave Wade participated in a five-day IAEA technical meeting on Small Reactors Without Onsite Refueling in November 2005. The four overview chapters that he had written for a TECDOC on Small Reactors Without Onsite Refueling were reviewed and commented by meeting participants. (In addition, three 35-page detailed descriptions of SSTAR, STAR-LM and STAR-H2 have been prepared for the TECDOC by Jim Sienicki and Dave Wade.) The TECDOC is to be released by the IAEA in October or November of 2006.

The workplans for the first year of a Coordinated Research Project on Small Reactors Without Onsite Refueling were laid out at the meeting. Relevant to LFRs, a Pb-cooled fast reactor neutronics benchmark was planned – see Section 2.4 of this report for the ANL contribution to that benchmark activity.

Dave Wade participated in a three-day IAEA consultancy on Enabling Technologies for Small and Medium Reactors (SMRs) and on Measures to Achieve Economic Competitiveness of SMRs. A TECDOC on the second subject was planned. A section on modeling tools for dynamic market penetration studies has been prepared for the TECDOC by Luc Van Den Duerpel and Dave Wade. A technical meeting in Vienna to address the first subject is scheduled for October 16-20, 2006. Dave Wade will attend; Jim Sienicki's extensive writeups on SSTAR safety philosophy and approach and on recent activities of the U.S. NRC regarding licensing approaches for advanced reactors will be reviewed and commented on by meeting participants.

Dave Wade attended the opening dedication of the School of Nuclear Science and Engineering at Shanghai Jiao Tong University in April 2006. Dialogs with the Dean, Xu Cheng (formerly at the Forschungszentrum Karlsruhe), were directed toward establishing interactions, among which would be participation in an IAEA-sponsored dynamic scenario investigation of the role of Small Reactors Without Onsite Refueling in 21st century nuclear markets.

Jim Sienicki, Anton Moiseyev, and Jim Cahalan met with Seong-O Kim from KAERI who visited ANL on September 19 and 20, 2006. Sienicki and Kim are Principal Investigators for the joint U.S./ROK I-NERI project, 2005-001-K, "Supercritical Carbon Dioxide Brayton Cycle Energy Conversion." On September 20, Sienicki and Kim worked on an initial draft of an Annual Progress Report for the I-NERI project.

J. J. Sienicki and D. C. Wade reviewed the draft report, "Role of Liquid Metals in the Development Programmes of Fast Reactors (Reactors Cooled by Sodium and Lead/Lead-Bismuth)," which was provided to members of the Generation IV LFR Team by Ning Li of LANL. The report was prepared by the Russians (Toshinsky, V. Orlov, Fomitichenko, and others) as part of an IAEA Cooperative Research Project that Ning is involved in.

Following the Workshop on Alternative Energy Conversion Systems and the Meeting of the GIF Scientific Steering Committee Project Management Board for Component Design and Balance of Plant held at JAEA in O-arai, Japan on February 20 and 21, Jim Sienicki met by himself with researchers at JAEA conducting S-CO₂ Brayton Cycle research and development for more detailed presentations and technical discussions as well as an extended visit to the Supercritical CO₂ Cycle Mockup Test Loop, Supercritical Corrosion Apparatus, and Na-CO₂ Reaction Test facilities at JAEA on February 22. He visited the Tokyo Institute of Technology (TIT) on February 23 and 24 where he was provided with more detailed presentations and technical discussions on S-CO₂ Brayton Cycle Energy Conversion for both Sodium-Cooled Fast Reactor and Gas-Cooled Fast Reactor concepts, residential hot water supply using a S-CO₂ heat pump, and a waste heat recovery steam condenser based upon boiling of liquid CO₂. He visited the smaller Supercritical CO₂ Cycle Mockup Test Loop and saw a residential hot water heat supply facility being used to test the performance of an alternative compact heat exchanger. On February 24, Sienicki also toured two factories located in the Tokyo area that have been involved with TIT in the manufacture of compact heat exchangers; one factory chemically etches microchannels into metal alloy plates and the second factory diffusion bonds the plates together using hydraulic presses.

2.8. LFR Co-System Integration Manager Coordination

Jim Sienicki prepared a presentation with input from Craig Smith and Bill Halsey (LLNL) and Ning Li (LANL), and delivered it at the Generation IV Budget Planning Meeting held at DOE Headquarters in Germantown on June 27 and 28, 2006.

2.9. ANL Conference Proceeding Publications and Reports

The following open-literature publications were prepared or published during FY 2006:

- A. Moisseytsev and J. J. Sienicki, "Automatic Control Strategy Development for the Supercritical CO₂ Brayton Cycle for LFR Autonomous Load Following," Paper 6074, Proceedings of the 2006 International Congress on Advances in Nuclear Power Plants (ICAPP 06), Reno, Nevada, June 4-8, 2006.
- A. Moisseytsev and J. J. Sienicki, "Transient Accident Analysis of a Supercritical Carbon Dioxide Brayton Cycle Coupled to an Autonomous Lead-Cooled Fast Reactor," Paper ICONE14-89544, Proceedings of the 14th International Conference on Nuclear Engineering (ICONE 14), Miami, July 17-20, 2006.
- J. J. Sienicki and D. C. Wade, "Nonproliferation Features of the Small Secure Transportable Autonomous Reactor (SSTAR) for Worldwide Sustainable Nuclear Energy Supply," Transactions of the American Nuclear Society, Vol. 93, p. ,

American Nuclear Society 2005 Winter Meeting, Washington DC, November 13-17, 2005.

- A Moiseyev and J. J. Sienicki, “Control of Supercritical CO₂ Brayton Cycle for LFR Autonomous Load Following,” Transactions of the American Nuclear Society, Vol. 93, p. 342, American Nuclear Society 2005 Winter Meeting, Washington, DC, November 13-17, 2005.
- A. Moiseyev and J. J. Sienicki, “Development of a Plant Dynamics Computer Code for Analysis of a Supercritical Carbon Dioxide Brayton Cycle Energy Converter Coupled to a Natural Circulation Lead-Cooled Fast Reactor”, ANL-06/27, July 2006.

3. Los Alamos National Laboratory – Lead Coolant Testing

3.1. Introduction to Lead Coolant Testing

Los Alamos National Laboratory (LANL) carried out a number of tasks and obtained results of significant importance to the development of LBE/Pb coolant technology and materials. In particular, a corrosion database was built (with the assistance of an Idaho National Laboratory (INL) intern, Jana Jensen), and systematic analysis was started of the reported corrosion test data from around the world with the LANL oxidation and corrosion kinetics model, and the oxidation rate constants and long-term corrosion rates were compiled and compared. XPS analysis was carried out of DELTA-tested ODS steels where the protective oxide layers are too thin to be detected in the SEM analysis. Additional nano-indentation analysis of laser peened materials was performed. The analysis of Mo and W coated steels tested in DELTA was completed. Based on last year's DELTA experiment, the effects of oxygen in LBE on heat transfer were analyzed, and a correlation was obtained for the "fouling factor" with the oxygen concentration. The key results are summarized below.

3.2. Modeling System Corrosion Kinetics

With support from the DOE Advanced Fuel Cycle Initiative (AFCI), LANL initiated a sustained effort to establish a system kinetic model of corrosion in oxygen controlled LBE/Pb and has gradually incorporated the key processes and mechanisms of surface oxidation, scale removal by flowing liquid metal, mass transfer, and deposition of corrosion products.

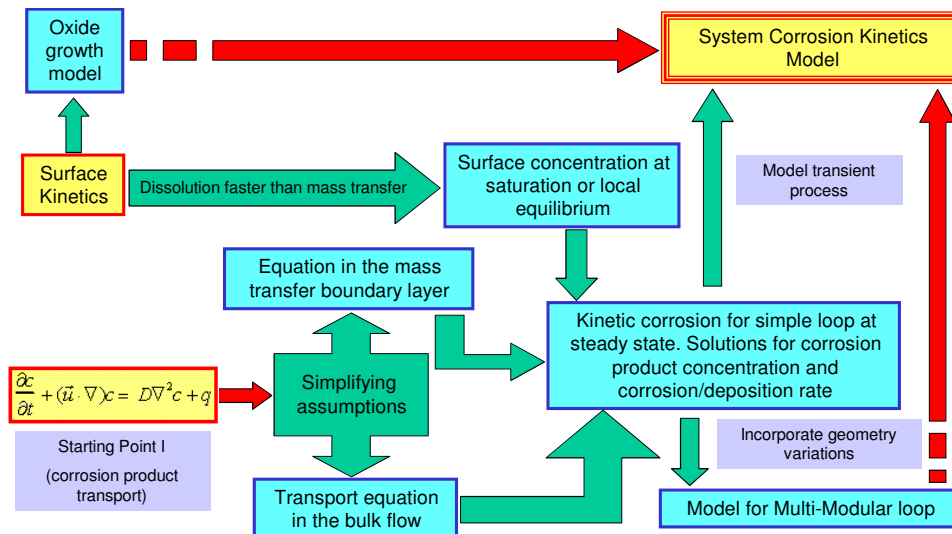


Figure 52. Framework of Modeling System Corrosion Kinetics in Closed Flowing Systems.

This model is more complete in its direct coupling of hydrodynamics to surface reactions, has higher fidelity than the existing local and sectioned models, and has been benchmarked successfully against a number of liquid metal loop experiments. In particular, LANL researchers have clearly identified and modeled the scale removal of oxidized steels in oxygen-controlled lead and lead-bismuth eutectic, and can use the model to extract long-term corrosion rates from measured oxide thickness in short times. The long-term corrosion rates have not been directly measured by most experimental groups, or reported in their analyses. For Generation IV LFR concepts with peak cladding temperatures of ~ 550 °C or higher, however, long-term corrosion rates are critical for long-life core designs.

Generally, high-temperature oxidation with scale removal simultaneously involves both thermodynamics and kinetics. Because of the fast oxidation reaction, the process reaches local thermodynamic equilibrium quickly. Kinetics, such as species diffusion, becomes the most important and dominates. In the temperature range of interest, the kinetics can be described by a parabolic rate constant for oxidation, K_p , and a linear rate constant for scale removal, K_r . The oxide thickness, x , obeys Tedmon's equation:

$$\frac{dx}{dt} = \frac{K_p}{2x} - K_r. \quad (1)$$

The solution for $x(t=0) = 0$ (no pre-oxidation) is:

$$t = -\frac{x}{K_r} - \frac{K_p}{2K_r^2} \ln \left| 1 - \frac{2K_r}{K_p} x \right|. \quad (2)$$

Equation (1) is demarcated by $x < x_f$ for oxide growth and $x > x_f$ for oxide thinning, where

$$x_f = \frac{K_p}{2K_r}. \quad (3)$$

It is clear that x_f is the asymptotic oxide thickness, assuming it is structurally stable (no spalling). The oxide thickness and time can then be scaled as

$$X = \frac{x}{x_f} = \frac{2K_r x}{K_p}, \quad \tau = \frac{t}{t_c} = \frac{2K_r^2 t}{K_p}, \quad (4)$$

where $t_c = K_p / 2K_r^2 = x_f / K_r$ is not the time for achieving the asymptotic thickness. Equation (2) becomes:

$$\tau = -X - \ln |1 - X|. \quad (5)$$

3.3. Sources and Categories of Test Results

Corrosion tests of a wide variety of materials under wide ranging conditions have been carried out in both static (in crucibles) and dynamic (in isothermal or non-isothermal flow loops) LBE/Pb environments. The steels tested include ferritic and martensitic steels

(P22, F82H, STBA28, T91, NF616, ODS-M, Eurofer 97, STBA26, Optifer IVc, EM10, Manet II, 56T5, ODS, EP823, HT9, HCM12A, HCM12, 410ss, T410, 430ss, etc.), and austenitic steels (D9, 14Cr-16Ni-2Mo, 1.4970, 316L, 304L, 1.4984, etc.). The test temperatures range from 300 to 650 °C, times from 100 – 10,000 hours (tests longer than 3000 hrs are mostly in static LBE/Pb). The oxygen concentrations vary from depleted (10^{-12} wt %) to saturated ($\sim 10^{-4}$ wt %). The range covers the oxygen control band that is below the formation of PbO and above the formation of Fe₃O₄, which is temperature dependent. The following is a tally of the test results available as of the fall of 2005 that were collected:

- There are over 22 ferritic/martensitic (F/M) steels (including a number of ODS steels), and 6 austenitic steels tested in stagnant and/or flowing LBE and/or Pb. The test duration ranges from a few hundred hours to up to 10000 hrs (the longer durations are mostly for stagnant testing).
- In stagnant LBE (in crucibles, with or without oxygen control), more than 165 results for F/M steels and over 102 for austenitic steels are available.
- In flowing LBE (in loops, usually with oxygen control), more than 70 results for F/M steels and over 42 for austenitic steels are reported.
- In Pb, 12 results are reported for stagnant testing, while 20 are reported for dynamic (flowing) testing.
- Most groups only analyzed oxide growth based on simple oxidation power laws, and were not able to extract liquid metal corrosion rates. This is complicated by the difficulty in measuring weight changes due to residual LBE/Pb on specimens.

The general conclusions may be drawn as the following:

- For unprotected steels (no coatings), the necessity and efficacy of oxygen control are validated in all tests; i.e., in-situ growth of surface oxide layers on steels in LBE/Pb with sufficient concentration of oxygen significantly reduces corrosion.
- In static tests within the oxygen control band, most martensitic and austenitic steels form oxides that are protective under ~ 550 °C, especially for oxygen concentrations above 10^{-6} wt %.
- In dynamic tests, most of which are in LBE and the oxygen concentrations are in 10^{-6} - 10^{-5} wt % range, the austenitic and martensitic steels formed protective oxides.
- Between 550 and 600 °C, the formation and protectiveness of oxides on martensitic steels are uncertain for durations up to a few hundred hours, but usually fail after that. For austenitic steels, the oxides are thin and not completely protective at ~ 550 °C.

Table 21. Reported Test Conditions and Durations for Steels in LBE and Pb

Steels	Stagnant LBE	Flowing LBE	Stagnant Pb	Flowing Pb
(I) Austenitic: 316L, 304L, D9, 1.4948, 1.4970, 14Cr-16Ni-2Mo	$T = 300\text{-}600^{\circ}\text{C}$, $c_{\text{O}} = 10^{-10}\text{-}c_{\text{O},s}$, $t = 100\text{-}10,000h$	$T = 400\text{-}600^{\circ}\text{C}$, $c_{\text{O}} = 10^{-9}\text{-}10^{-5}$, $t = 133\text{-}10,000h$ (mostly 316L)	$T = 550, 464^{\circ}\text{C}$, $c_{\text{O}} = 8 \times 10^{-6}$, $c_{\text{O},s}$, $t = 1,200,$ $3,000h$ (1.4970, 316L)	$T = 400, 500^{\circ}\text{C}$, $c_{\text{O}} = 3\text{-}4 \times 10^{-5}$, $t = 3,027h$ (1.4948, 1.4970)
(I) Ferritic/Martensitic: T91, HT-9, EP823, F82H, Manet II, EM10, Eurofer 91, Optifer IVc, HCM12, HCM12A, T410, 430, 56T5, STBA26, T22, T122, 9Cr-2WVTa	$T = 300\text{-}650^{\circ}\text{C}$, $c_{\text{O}} = 10^{-12}\text{-}c_{\text{O},s}$, $t = 100\text{-}10,000h$ (mostly T91, HT-9, EP823)	$T = 300\text{-}600^{\circ}\text{C}$, $c_{\text{O}} = 10^{-9}\text{-}10^{-5}$, $t = 133\text{-}10,000h$	$T = 464\text{-}550^{\circ}\text{C}$, $c_{\text{O}} = 8 \times 10^{-6}$, $c_{\text{O},s}$, $t = 1,200\text{-}$ $3,700h$ (Optifer IVc, F82H)	$T = 400, 500^{\circ}\text{C}$, $c_{\text{O}} = 3\text{-}4 \times 10^{-5}$, $t = 3,027h$ (Optifer IVc, EM10)
(I.alt) Al-coating: GESA, pack cementation	$T = 350\text{-}650^{\circ}\text{C}$, $c_{\text{O}} = 10^{-10}\text{-}10^{-4}$, $t = 100\text{-}10000h$	$T = 450\text{-}520^{\circ}\text{C}$, $c_{\text{O}} = 10^{-7}\text{-}10^{-5}$, $t = 133\text{-}400h$		$T = 550^{\circ}\text{C}$, $c_{\text{O}} = 10^{-6}$, $t = 1,500,$ $3,000h$
(I.alt) Surface-treated: shot-peening		$T = 450\text{-}520^{\circ}\text{C}$, $c_{\text{O}} = 10^{-7}\text{-}10^{-5}$, $t = 133\text{-}400h$		
(II) Si modified: 1-5% Si addition in 2-12% Cr alloys, 18Cr-20Ni-5Si	$T = 400\text{-}700^{\circ}\text{C}$, $c_{\text{O}} = c_{\text{O},s}$, $t = 100\text{-}3,000h$	$T = 450\text{-}520^{\circ}\text{C}$, $c_{\text{O}} = 10^{-7}\text{-}10^{-5}$, $t = 133\text{-}400h$		
(II) Oxide Dispersion Strengthened: ODS-M (9Cr-2W), MA957	$T = 500\text{-}650^{\circ}\text{C}$, $c_{\text{O}} = 10^{-6}$, $t = 800\text{-}5,000h$	$T = 550^{\circ}\text{C}$, $c_{\text{O}} = 10^{-7}\text{-}10^{-5}$, $t = 2,000\text{-}$ $10,000h$		

3.4. Results

Analyses were performed based on the LANL kinetics modeling of the oxidation and corrosion of steels in LBE/Pb. Using several data sets with well defined test conditions in loops, long-term corrosion rates were extracted which have not been reported by others (very difficult to measure, especially in the short to medium duration tests), and had not been contained in the analyses conducted or models used. These rates are essential for LFR long-life core designs, and the modeling clarifies a complex process that had not been adequately studied and understood. The LANL analyses characterize the temperature, alloy composition dependence, and loop dependence of the oxidation and corrosion rates.

The analysis of the massively collected data shows great promise of the model-based approach for analyzing the wide-ranging test results reported by groups from around the world. The modeling also reveals the inadequacy of tests performed in static and/or low

flow environments for extracting long-term corrosion rates, and the difficulty in analyzing this class of data (the majority of the reported results).

The results are as follows:

- Compilation of experiment oxidation/corrosion studies and creation a cohesive database,
- Separate analyses of individual steels of loop test data for flowing LBE and Pb to extract oxidation and corrosion rates.

Table 22 shows the resulting parabolic and linear rate constants as well as the asymptotic thickness. Thicknesses versus time are show in dimensional and non-dimensional form in Figures 53 and 54, respectively.

Table 22. Temperature Dependence of K_p , K_r , and x_f .

Temperature	Cr Composition	Material	k_p m ² /s	k_r micron/yr	x_f micron
Fe-Si					
700		Fe-3.82%Si	8.97E-17	235.61	6.00
		Fe-1.24%Si	3.82E-17	108.89	5.53
Martensitic steel	Ni<1%				
470	8.97	EM10	8.67E-17	140.17	9.75
470	8.98	T91	9.84E-17	84.77	18.30
470	8.98	T91	5.84E-17	48.36	19.03
470	9	Batman27	3.64E-17	21.73	26.40
470	9.1	Optifer lvc	8.61E-17	43.09	31.52
470	12	EP823	1.00E-17	2.53	62.27
530	8.67	ODS	1.92E-16	283.67	10.68
530	8.82	NF616	5.70E-17	32.60	27.57
530	10.83	HCM12A	1.46E-16	196.27	11.7
550	2.139	F22	5.54E-16	305.24	28.63
550	12	HT-9	8.07E-17	189.97	6.70
550	12.5	410	1.12E-17	8.81	20.06
Austenitic Steel	Ni>1%				
550	1	1Cr1.5Si-MoV	8.77E-16	78.84	175.42
550	11	Cr11Ni3Mo	6.60E-17	11.33	91.78
550	14	Cr14Ni11Mo	2.30E-17	8.61	42.05
550	15	15Cr11Ni3SiMoNb	2.44E-17	12.78	30.13
550	16.34	316L	2.74E-17	100.49	4.30
650	16.34	316L	1.44E-16	203.09	11.20

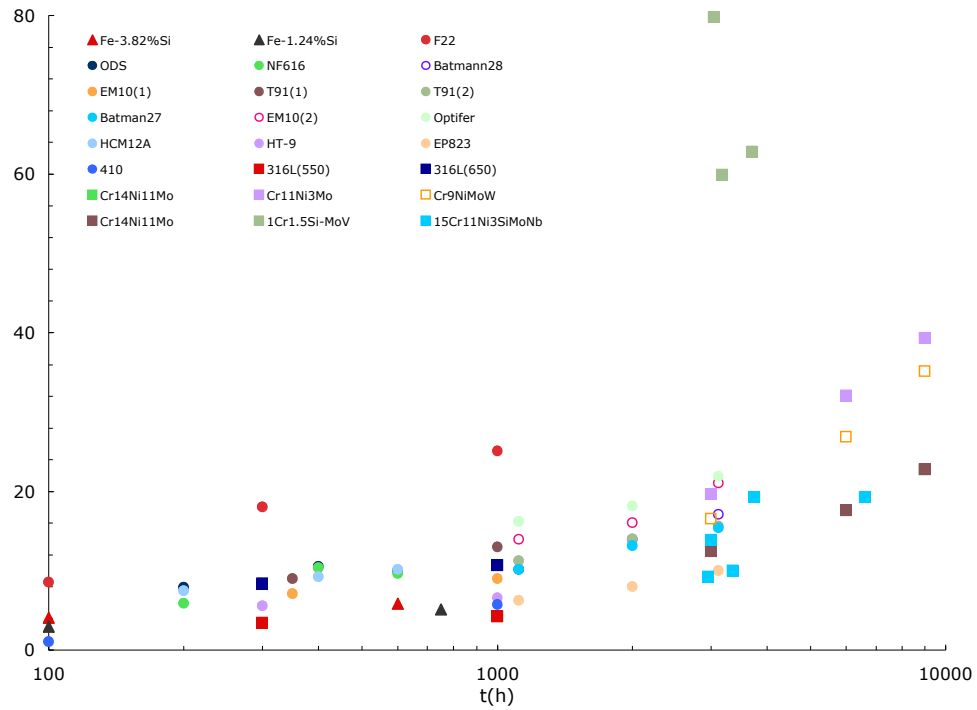


Figure 53. Part of the Reported Oxide Thickness Data for a Number of Steels Tested in Flowing LBE Loops in the Literature. Long-Term Corrosion Rates Cannot be Obtained from These Results Using the Previous Models.

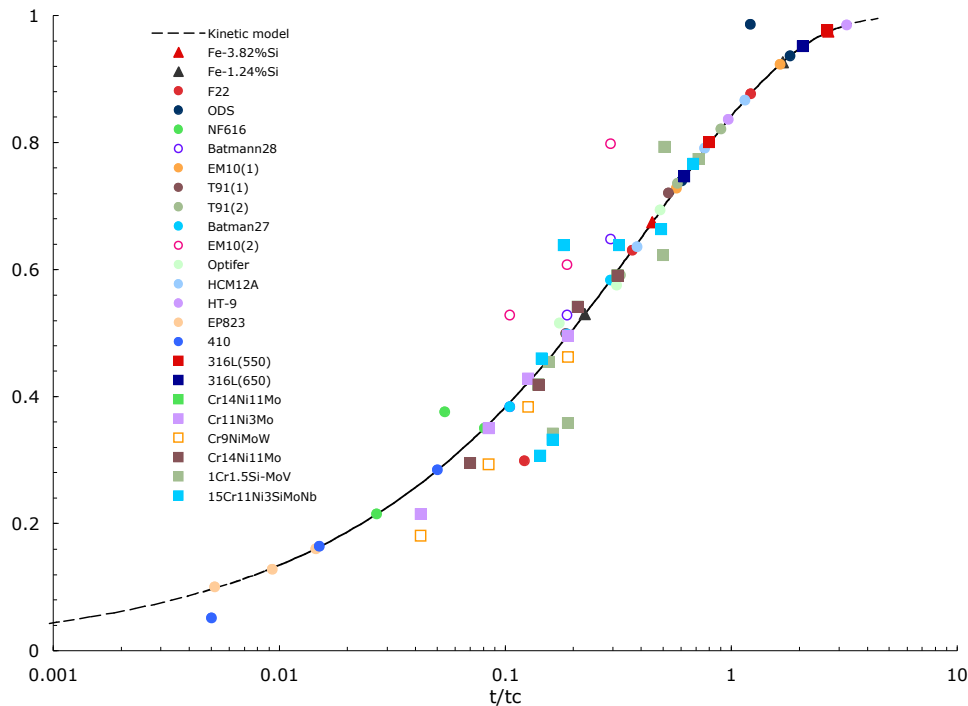


Figure 54. Using the Kinetics Model Developed at LANL and Nonlinear Least Square Fitting, the Majority of the Test Results Can be Collapsed onto One Universal Curve. The Length and Time Scales in This Model Can be Used to Determine the Asymptotic Oxide Thickness and the Long-Term Corrosion Rate of an Individual Steel. There are Still Considerable Scatter and Uncertainties in the Prediction, Highlighting the Need for Longer-Term Tests.

3.5. Analysis of DELTA Tested Al-Rich ODS Steels

Characterization of DELTA-tested Al-rich ODS steel specimens with extremely thin surface oxides (too thin to be detected by SEM analysis) was completed:

The SEM/EDX and XPS measurements on the ODS alloys, 14YWT, 12YWT, MA957, MA956, and PM2000, were finished and calibrated. The results were summarized in a poster presentation at the RENO ANS Meeting and have been submitted to the journal, Acta Materialica. Two major issues are discussed in that paper:

(1) Influence of Al as an alloying element on the corrosion properties. It was found that the material, PM 2000, showed the best corrosion properties so far. Only a 150 - 200 nm thick oxide layer was found on PM2000 while a more than 4 μm thick oxide layer was found at MA956. It seems that the 1 % higher Al content in the PM 2000 results in a much more protective and thinner oxide layer than at the less Al-containing MA956.

Figure 55 presents calibrated XPS results of PM2000 and MA956. The results show the presence of a protective oxide layer to a depth of about 250 nm from the surface

of PM2000 containing 5.5 % Al. The oxide layer prevents significant diffusion of Fe from deeper within the sample. In contrast, with MA956 containing 4.5 % Al, oxygen penetration and Fe diffusion take place to at least 4450 nm (4.45 μm) into the sample. Therefore, it is concluded that a corrosion resistant Al-alloyed material should contain at least 5.5 % Al. This result is comparable to Ni-based alloys where it has been shown that at least 5 % Al is needed in the alloy in order to form a protective Al-oxide layer.

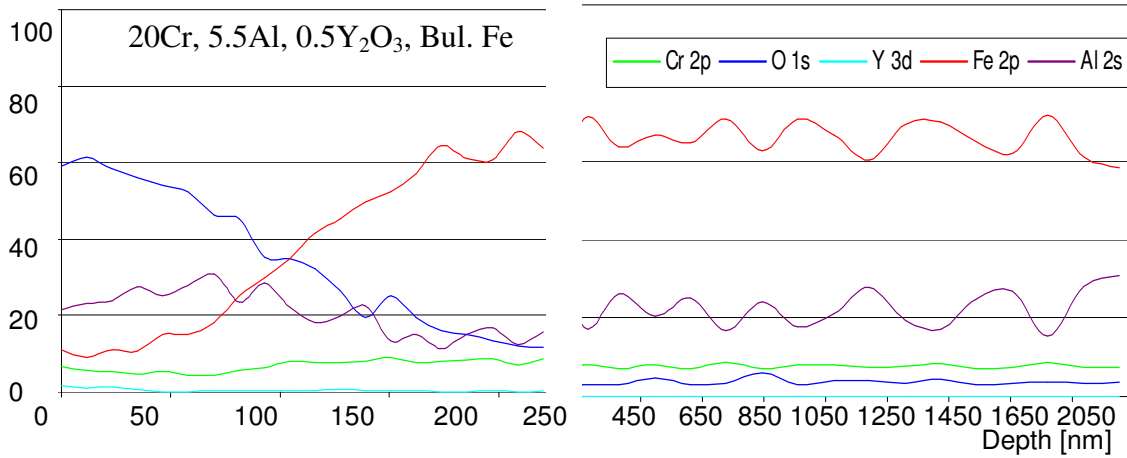


Figure 55. (a) Shallow SDP and Deep SDP (Sputter Depth Profile) of PM2000 using XPS.

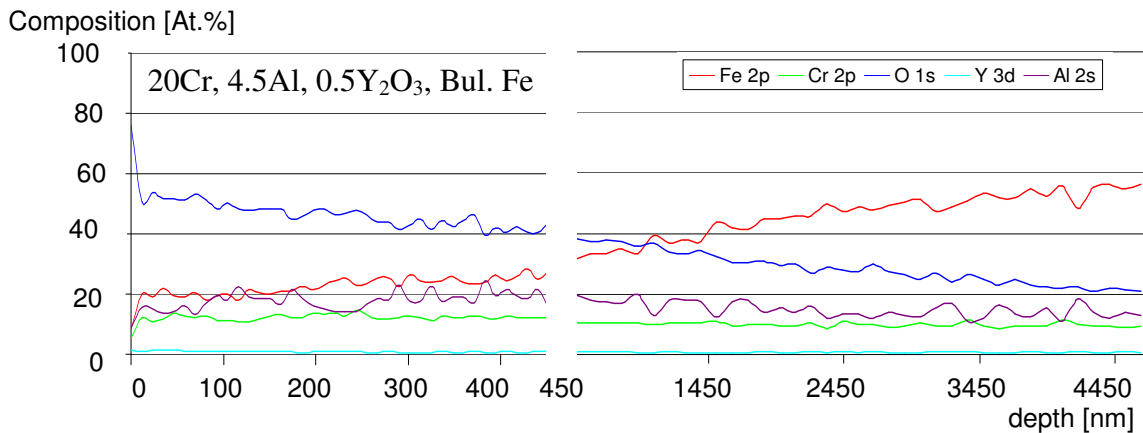


Figure 55. (b) Shallow SDP and Deep SDP (Sputter Depth Profile) of MA956 using XPS.

XPS allows determination of which elements are oxidized and which are in a metallic state. A comparison (Figure 55 for PM2000) between measured oxygen in the layer and the calculated amount of oxygen in the material if the elements are oxidized to Fe_2O_3 , Cr_2O_3 , Y_2O_3 , and Al_2O_3 according to the binding energies shows good agreement.

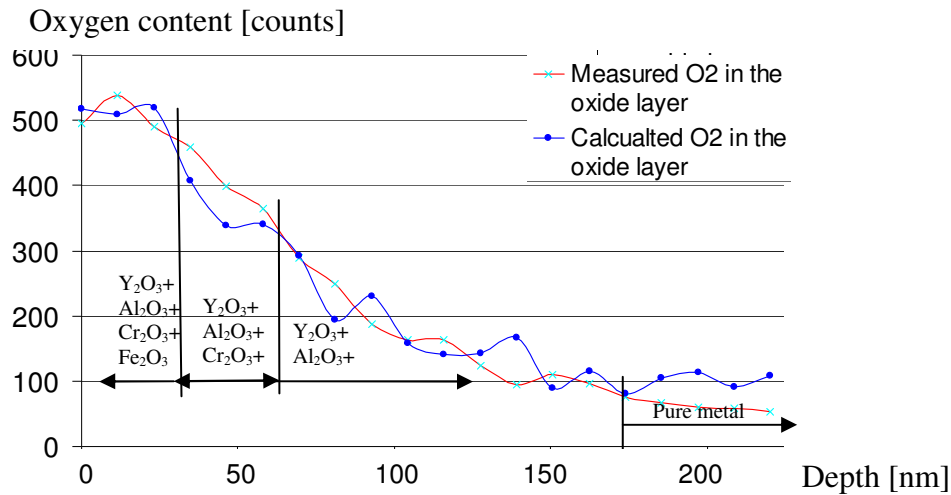


Figure 56. A Comparison Between the Measured Amount of O_2 in the Oxide Layer and a Calculation Based on the Stoichiometric Amount of O_2 in Cr_2O_3 , Fe_2O_3 , Al_2O_3 and Y_2O_3 .

(2) Influence of the grain structure on the corrosion behavior. The materials, MA957 and 14YWT, have almost the exact same compositions. But the grain structures are significantly different. (see Figure 57). It was found that smaller grains (14YWT) lead to a more homogeneous oxidation while larger grains (MA957) lead to grain boundary oxidation. Therefore, to achieve a predictable and controllable oxidation rate smaller grains are needed.

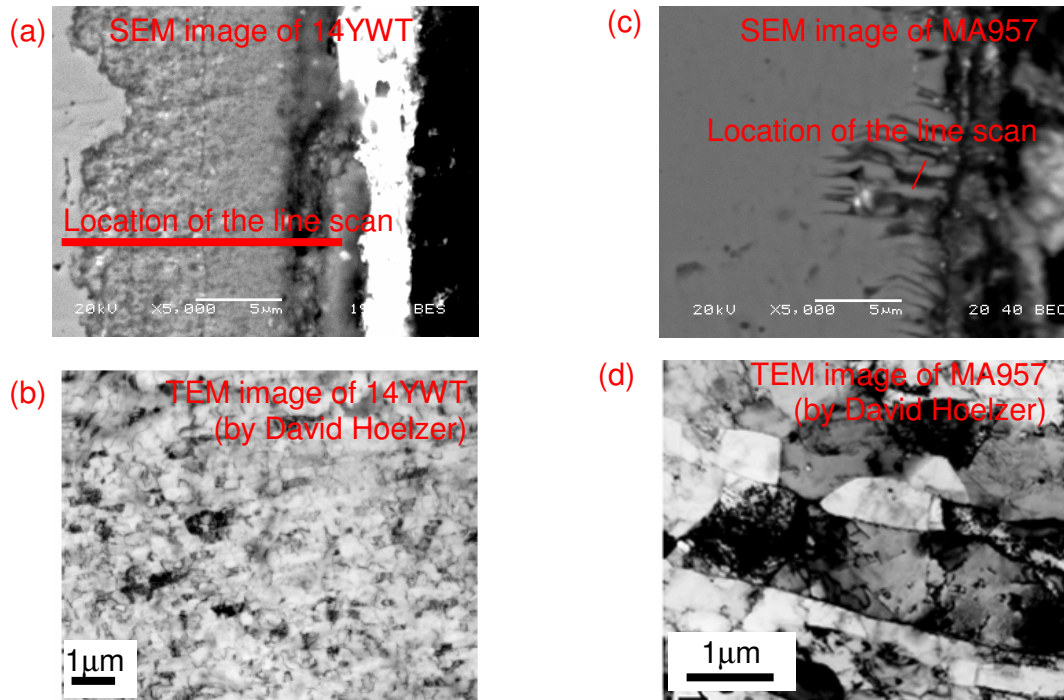


Figure 57. (a) Cross Section of the 14YWT Sample after Exposure to LBE for 600 h at 535 °C. (b) Grain Structure of the Same Material (TEM Image, Un-Exposed). (c) Cross Section of the MA957 Sample after Exposure to LBE for 600 h at 535 °C. (d) Grain Structure of this Material (TEM Image, Un-Exposed).

3.6. Additional Analysis of DELTA Tested Laser-Peened Specimens

SEM/EDX/WDX, nano-indentation measurements were finished on the surface treated specimens tested in DELTA at 535 °C for 600 h, including laser peened, shot peened, and un-peened HT-9, 316L, T91, EP823. Figure 58 shows the results for peened and un-peened HT-9. The results of HT-9 are representative of the behavior of the tested ferritic/martensitic materials. There are no significant differences between laser peened and un-peened samples. This seems to result from the fact that laser peening induces only a stress state and no real structural change. The nano indentation and the micro hardness measurements show that after exposing the samples in LBE, the initial (before exposure to LBE) hardness difference between peened and un-peened disappeared. Therefore, it seems that exposure at 535 °C for 600 h anneals the samples enough to eliminate the influence of laser peening on the samples. The nano-indentation results show that the oxide layer itself is “weaker” (lower E-modulus and hardness than the pure Fe-Cr oxide). This may be caused by the high porosity in the layer itself. The results agree with the literature where it is reported that a thicker oxide layer causes “weaker” mechanical properties due to higher porosity.

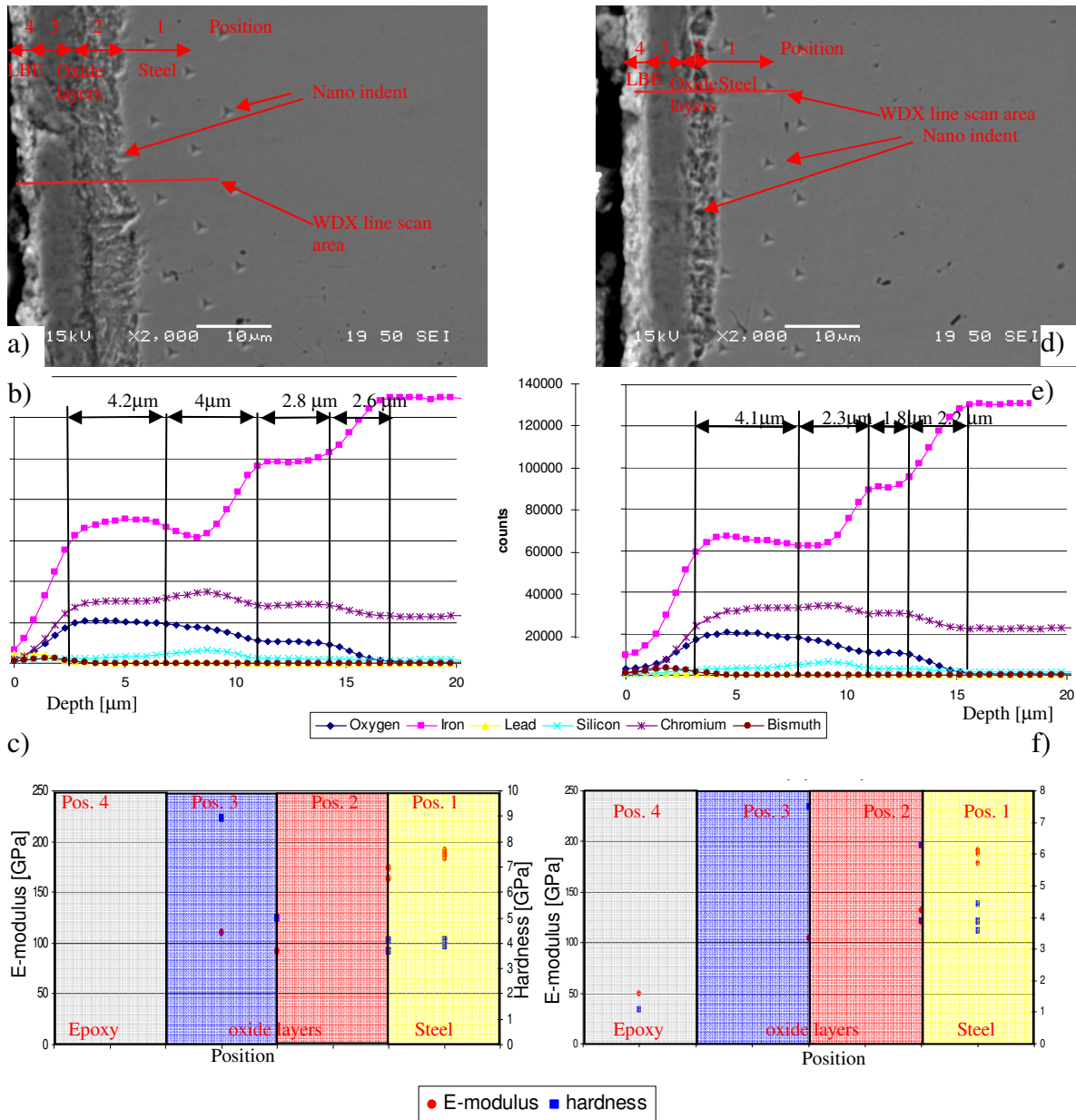


Figure 58. Figures 58a and 58b Present the SEM Image and the Corresponding WDX Line Scan of the As Received HT-9 Material after 600 h Exposure to LBE. Figures 58d and 58e Present the SEM Image and the Corresponding WDX Line Scan of the Laser Peened HT-9 Material after 600 h Exposure to LBE. At both SEM Images, the Nano Indents are Visible. The Area where the Nano Indents were Made (Results are Given in Figures 58c and 58f) are Marked in the SEM Images as Well as the Area where the Line Scans were Made.

Type 316L on the other hand seems to show a slight improvement due to laser peening. Micro hardness measurements show that the compression stress is still in the materials after the experiment. On the laser peening side, less grain boundary oxidation was found.

Therefore, it can be said that the compression stress stays in 316L at these test conditions and improves the oxidation behavior.

3.7. W- and Mo-Coated F/M Steels Tested in DELTA

Four different ferritic/martensitic materials (EP823, MA957, 9Cr, and HT-9) were coated with W and Mo with a Ni binding layer in between. The materials were tested in the DELTA Loop at LANL for 600 h at 535 °C in flowing LBE with 10^{-6} wt % oxygen concentration. The LBE flow velocity was 2 m/sec. After exposure, each sample was cut in cross section and polished. The last polishing step was a 1 μ m diamond polish. The cross sections were analyzed using SEM and EDX. In the following, these results are presented for each tested specimen.

3.7.1. W-Coated EP823

Figure 59 presents a summary of SEM images. It shows that a 10 to 20 μ m wide gap filled with epoxy was found between the substrate (EP823) and the coating (W). The EDX map shows that Cr and oxygen enrichment in this gap is found. This indicates a formation of a chrome-iron oxide at the interface between W layer and EP823 substrate. The LBE-facing surface of W showed some cracking. Since the starting condition is not known, it is difficult to determine if these cracks are due to the LBE exposure.

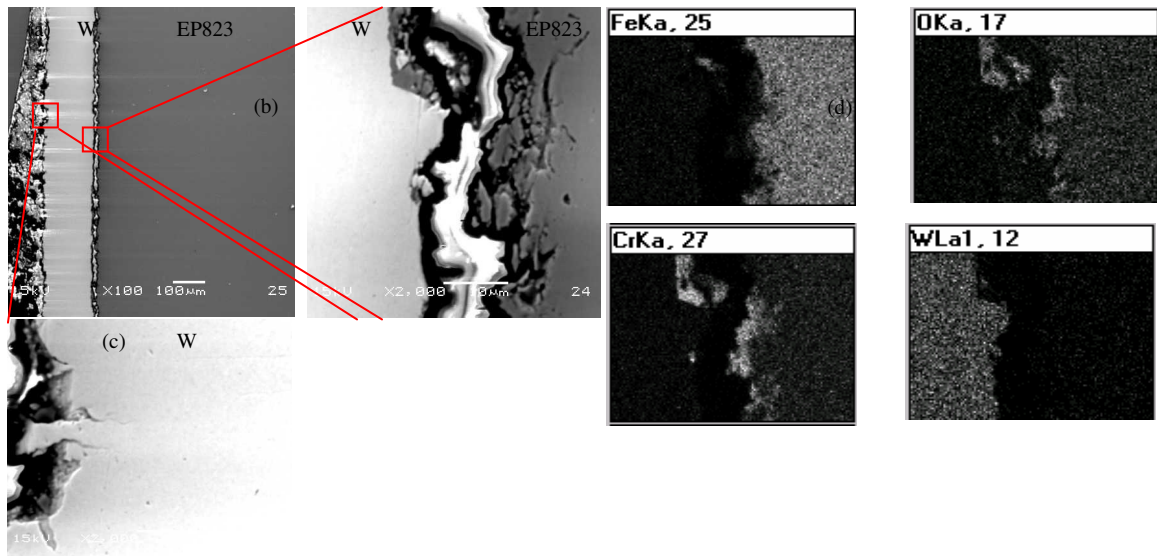


Figure 59. W Coated EP823. a) 100x SEM Image. b) 2000x SEM Image Between Layer and Substrate. c) 2000x W Layer Surface Image. d) SEM/EDX Results Taken at Location b).

3.7.2. Mo-Coated EP823

The Mo coating on EP823 seems to adhere better to the substrate than the W coating. The appearance of the substrate and the layer after corrosion testing is shown in Figure 60. It shows that an almost continuous Cr-enriched oxide layer was formed between the Mo coating and the substrate. No traces of Ni were found. In Figure 60b, it can be seen that cracking occurred just underneath the oxide in the substrate. It is assumed that the substrate surface before coating was flat. After the testing, it can be seen that the interface between the coating and substrate shows some buckling, particularly where the cracks occur. This leads to the assumption that stresses due to the different thermal expansion coefficients (W 4.2-4.6 $\mu\text{m/mK}$, Mo 4.8-5.5 $\mu\text{m/mK}$, ferritic stainless steels 10-12 $\mu\text{m/mK}$) lead to this buckling and eventually to delaminating and cracking.

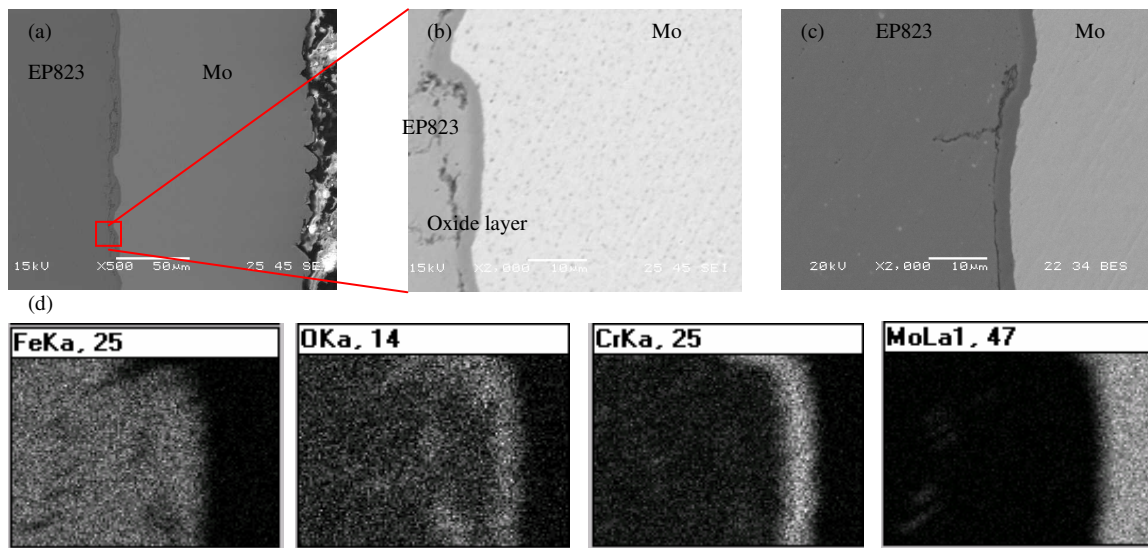


Figure 60. Mo coated EP823. a) 500x SEM Image of the Mo/Substrate Interface. b) 2000x SEM Image of the Mo/Substrate Interface. c) 2000x SEM Image of the Mo/Substrate Interface at a Different Location. d) 5000x SEM/EDX Results of Location in Image b) Showing the Cr and O Enrichment in the Interface.

3.7.3. W-Coated HT-9

The SEM results obtained after the LBE experiment are shown in Figure 61. It was found that the coating stayed on the substrate. Similar to EP823, a Cr- and oxygen-enriched layer was found on the interface. Also, interesting surface features on the substrate were found as shown in Figure 61b. So far, it is not clear how these were formed. The W surface facing LBE showed no significant corrosion attack and only cracking was found.

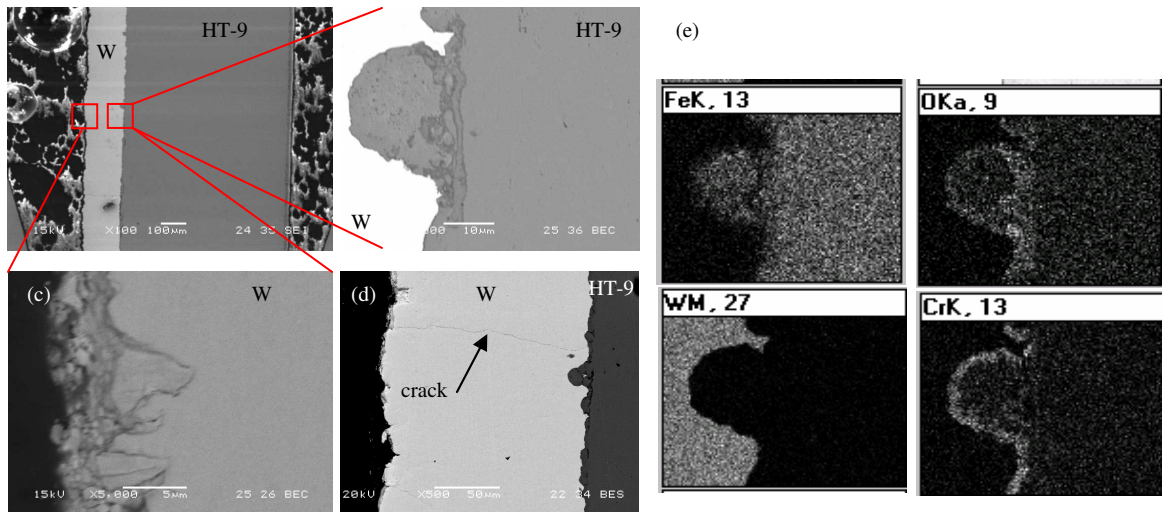


Figure 61. W-Coated HT9. a) 100x SEM Image. b) 2000x SEM Image of the Interface Features Marked in a). c) LBE-Facing Surface of the W Coating. d) A Crack in W Coating. e) SEM/EDX Results of the Area in b).

3.7.4. Mo-Coated HT-9

Figure 62 presents the SEM and EDX results of this sample after the experiment. It is shown that the Mo layer stayed on the substrate. At the interface between the substrate and coating, a Cr-and O-enriched layer was found. In Figure 62b, it can be seen that the cracks start to develop underneath the oxide layer. The Mo surface image (Figure 62c) shows a rough surface that might come from dissolution attack. However, not knowing how flat the original surface (before exposure) was, it is difficult to determine.

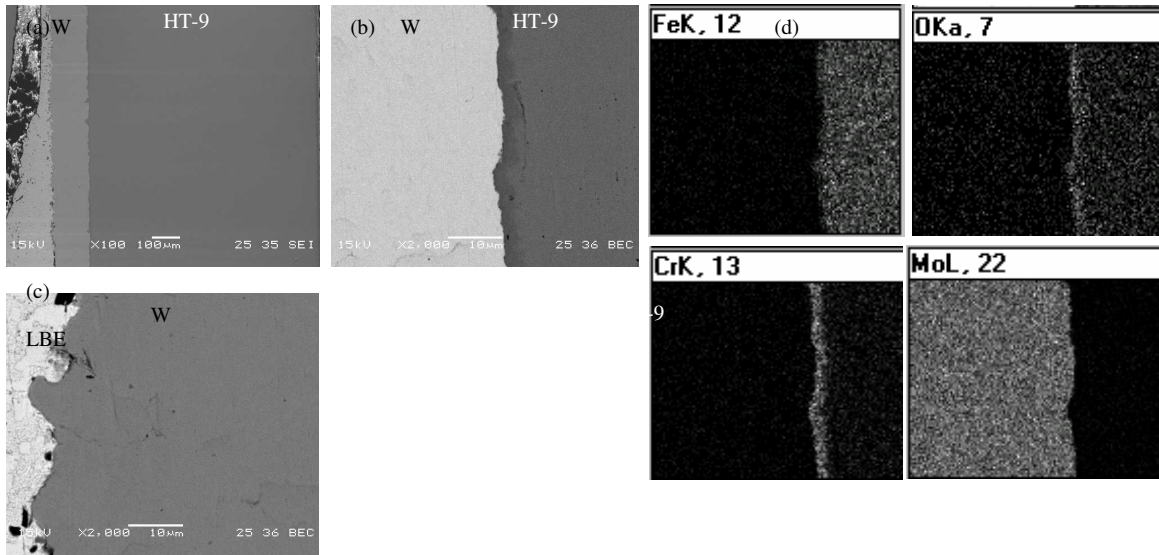


Figure 62. HT-9 Mo-Coated. a) 100x SEM Image. b) 2000x SEM Image of the Interface Features Marked in a). c) 2000x LBE-Facing Surface of the Mo Coating. d) SEM/EDX Results of the Area in b).

3.7.5. W-coated 9Cr

This sample showed separation between the coating and substrate (Figure 63). Also, cracks in the W coating were found. The surface of the coating is not flat so dissolution of W or oxidation of the W and loss of the oxidized W could have happened. However, the original thickness of the coating is not known; therefore, it is difficult to determine whether the W was attacked. At the interface between the substrate and W coating, Cr and O enrichment was found.

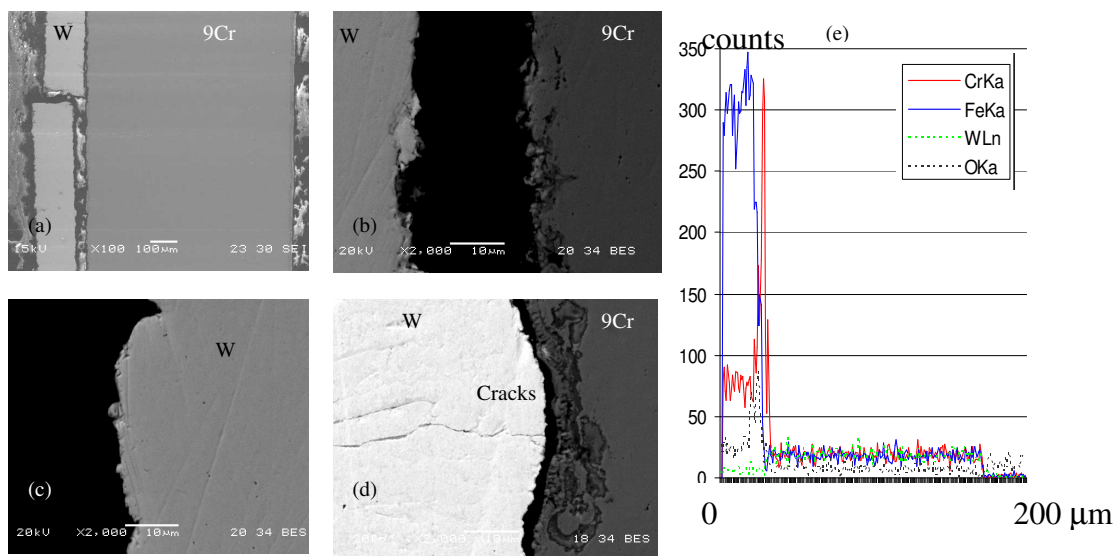


Figure 63. W-Coated 9Cr. a) 100x SEM Image. b) 2000x SEM Image of the Interface. c) 2000x SEM Image of the LBE-Facing Side of the W Layer. d) 2000x SEM Image of the W Layer. Cracks are Visible. e) SEM/EDX Analysis of the Layer Substrate

3.7.6. Mo-Coated 9Cr

Similar to the W-coated sample, the Mo coating was separated from the substrate. The gap in between was filled with epoxy during sample preparation. The LBE-facing surface of the Mo was rough which indicates a loss of material. The interface between the substrate and the Mo coating again showed a clear O and Cr enrichment.

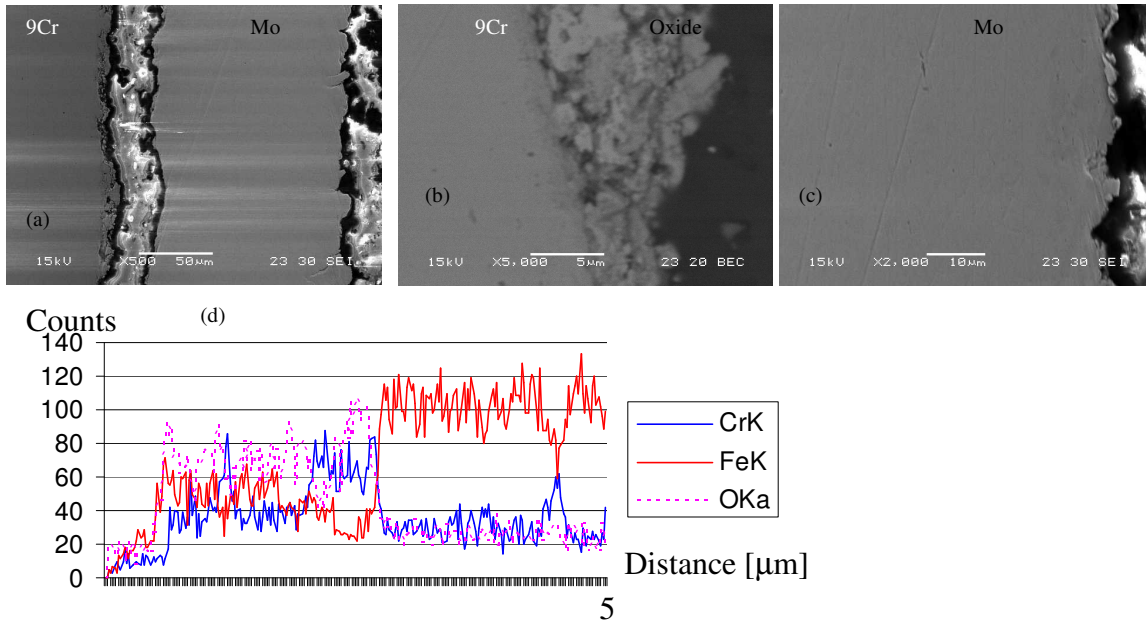


Figure 64. Mo-Coated 9Cr. a) 500x SEM Image. b) 5000x SEM Image of the Interface. c) 2000x SEM Image of the LBE-Facing Side of the Mo Layer. d) SEM/EDX Analysis of the Layer Substrate Interface.

3.7.7. W-Coated MA957

For this sample, the W coating is still attached to the substrate but cracking in the W layer was also found. The outside of the W layer is very rough, so it might have experienced corrosion (oxidation) and dissolution attacks. The steel right underneath the W layer is Cr- and O-enriched and shows cracking. This might be the first sign of de-bonding of the layer from the substrate.

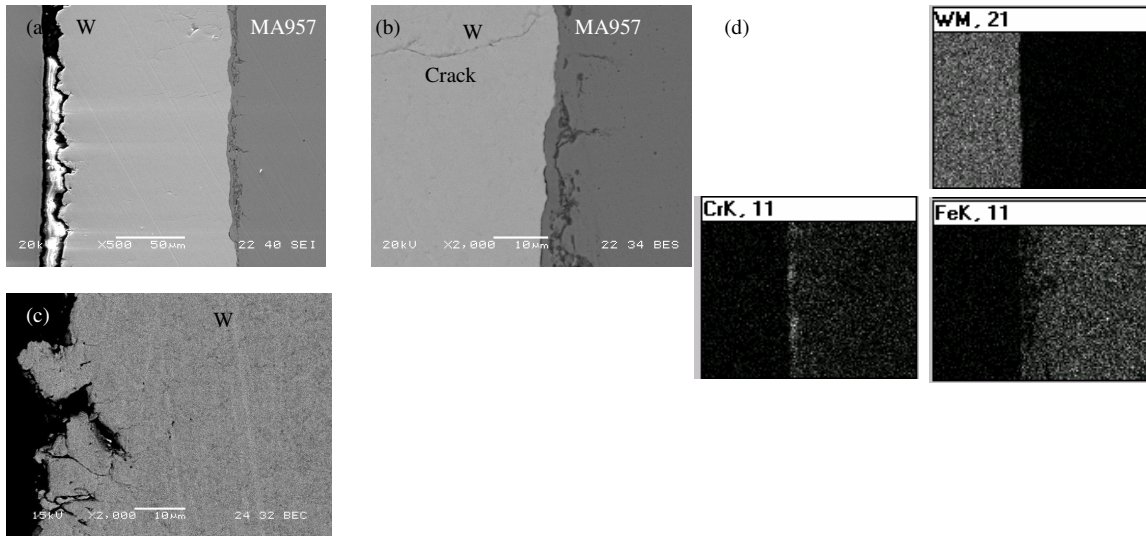


Figure 65. W-Coated MA957. a) 500x SEM Image. b) 2000x SEM Image the Interface is Shown. c) 2000 x SEM Image the W Surface is Shown. d) SEM/EDX Element Maps of the Interface Between the Coating and Substrate.

3.7.8. Mo-Coated MA957

The Mo-coated sample showed a similar behavior with the previous samples. The Mo layer might show dissolution attack while the steel underneath the layer is oxidized. Figure 66c shows a line scan where the oxidized steel can be seen underneath the Mo layer.

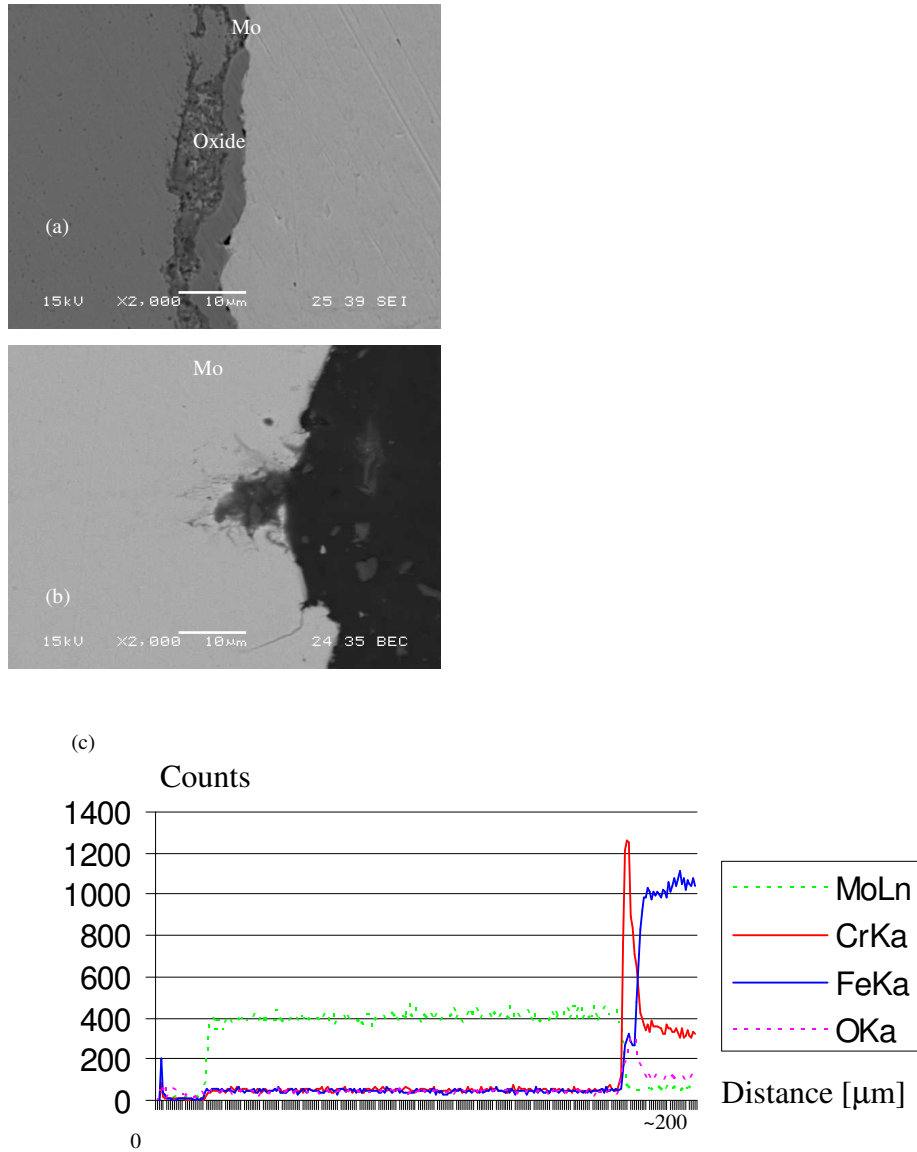


Figure 66. MA957 Mo-Coated. a) 2000x SEM Image of the Interface. b) 2000x SEM Images of the Mo Surface. c) SEM/EDX Line Scan Across the Mo Layer. Cr and O Enrichment Can be Seen.

3.8. Effects of Oxygen on Heat Transfer Due to Fouling

The effects of oxygen on fouling behavior were analyzed. The relationship between the fouling factor and oxygen concentration is characterized with a power-law correlation (Figure 67). A paper has been written and submitted to the Journal of Nuclear Materials.

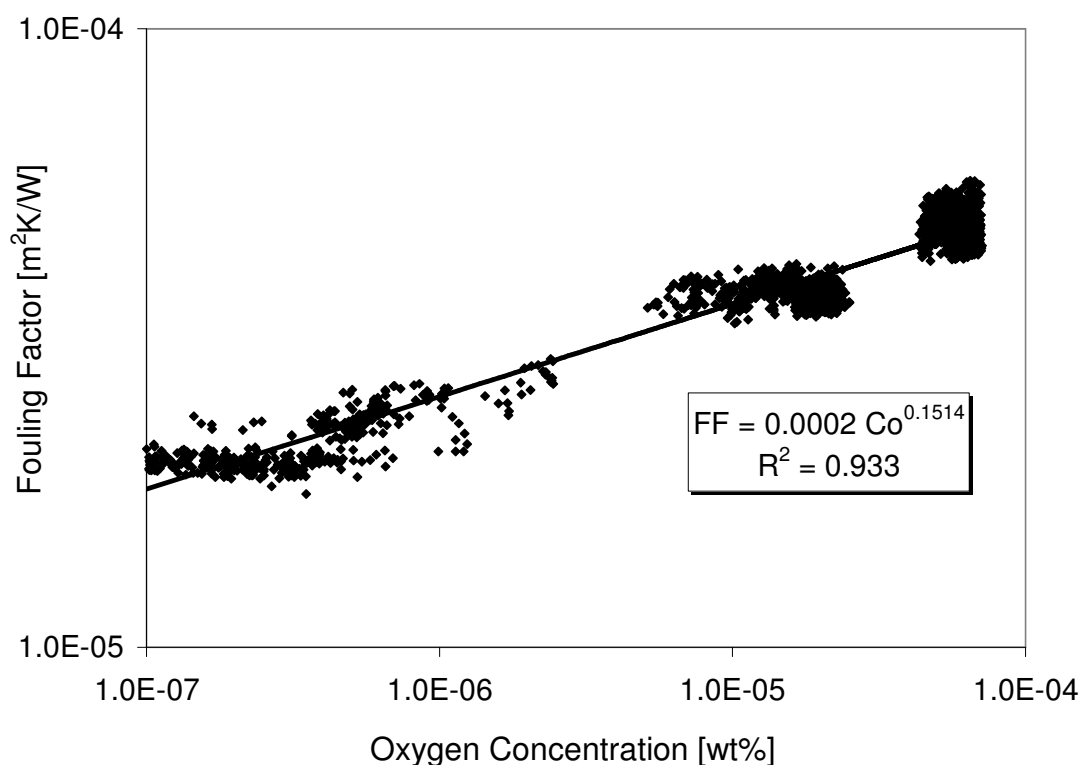


Figure 67. Fouling Factor versus Oxygen Concentration.

3.9. Preparation of Materials for DELTA Testing

Preparation of materials (see table below) for upcoming DELTA testing was initiated. The specimens will be partially coated with alumina (Al_2O_3) so that one can make a direct measurement of corrosion rather than only measuring oxide thickness.

Table 23. Partial List of Materials and Conditions to be Included in the Next DELTA Test

Material	Condition	Material	Condition
HT-9	As recived (Timken)	SMAT 316L	Surface deformed 316L
HT-9	HTP nano crystal	SMAT 420SS	Surface manipulated 420SS
HT-9	New heat	420 SS	As received
T91	As received (Timken)	MA956	As received
T91	New heat	Ma956 welding	welding
T91	HTP nano crystal	PM2000	As received
14Cr single crystal	Spherical shaped single crystal	Aluchrome Y wire	Welding rod
		Crofer 22 APU	As received

4. Lawrence Livermore National Laboratory

This section provides an update on analyses and activities conducted at LLNL supporting LFR development during FY 2006. The work is discussed below in five topic areas:

- LFR System Design Support
- International Cooperation
- University Partnership
- LFR Materials Evaluations
- Early Technology Demonstration

Much of this work is documented elsewhere, and is only summarized in this report, with reference to the full documentation. The work completed by the University of California under the direction of Dr. Ehud Greenspan has been published in the open literature and in addition to providing unique insights into performance of SSTAR-type reactors has provided confirmatory results to work done at ANL. The work on an early technology demonstration was reported in UCRL-MI-220282, “Options for an Early Technology Demonstrator.” A detailed summary of the materials research is provided here with references made to published work.

4.1. LFR System Design Support Activities

LLNL provides LFR R&D planning and project control as Co-System Integrator. In addition, with support from UC Berkeley via subcontract, LLNL conducts LFR System Design support activities in a number of areas.

4.1.1. General LFR Planning, Reporting, and Interface

LLNL staff prepared and reported LLNL work packages and products, and reviewed and approved other LFR work packages and products, and represented the LFR at GEN-IV Semi-Annual meetings.

The description of LFR research and development needs as described in Appendix 4 of the Generation IV Nuclear Energy Systems Ten-Year Plan was updated in February 2006. This included revised near-term budgets and a revised schedule to prepare for a future fast-spectrum reactor technology selection [14].

4.1.2. Generation IV System Support

As the Global Nuclear Energy Partnership (GNEP) developed during the past year, LLNL conducted a brief assessment of potential roles for the LFR in the context of the SSTAR. In summary, SSTAR represents a current GEN-IV R&D program that maps precisely into multiple GNEP missions:

- GNEP uses a sodium cooled fast spectrum actinide burner reactor.
 - SSTAR provides a somewhat different option for actinide management - the long life SSTAR “stores” the actinides securely in an operating power

- reactor for 20-30 years then returns it to the supplier when the core is reprocessed.
 - The SSTAR nuclear technology also serves as a backup to the sodium-cooled ABR.
- GNEP includes a small secure reactor for use in developing nations.
 - This is precisely the mission for which SSTAR is designed.
 - The LFR team has led consideration of the ‘user-supplier’ paradigm.
- SSTAR provides coordination with Japan on small modular reactors and Europe on Pb reactor technology, with potential for Russian Federation cooperation.
 - Long-standing cooperation agreements with CRIEPI/Toshiba (4S reactor).
 - Recent cooperation agreement with EU-ELSY R&D program.
 - Potential for cooperation with Russian Federation (SBVR-75/100 and BREST reactors) when desired.

The long core life SSTAR is designed to be fueled with the actinide mixture obtained from recycle of LWR spent fuel, and thus directly addresses the waste minimization objectives of the GNEP advanced fuel cycle. The SSTAR was specifically conceived for the developing world and the small and remote markets that GNEP wishes to engage with the GNEP Reactors for International Deployment program. The SSTAR paradigm of providing nuclear energy without any need for the user to have any fuel cycle technology is reflected in the GNEP user-supplier and reliable fuel services concepts.

4.2. International Cooperation

International cooperation is of great potential value to the LFR R&D program. Sharing of information and coordination of research can permit more rapid progress while optimizing resources utilization. LLNL performs coordination both through the Generation IV International Forum (GIF) and through bilateral cooperation, particularly with the Japanese small modular fast reactor programs.

4.2.1. Generation IV International Forum (GIF) LFR SSC

Good progress was made during the year in preparing the LFR system planning documents in the Gen-IV International Forum (GIF).

Following the first formal meeting of the GIF-LFR-System Steering Committee (SSC) hosted by LLNL in Monterey, CA earlier in 2005, the second meeting took place in Seoul, Republic of Korea, during the period, August 31 through September 2, 2005, hosted at Seoul National University. In attendance were committee members from the US, Euratom, Japan, Korea, and a representative of the GIF Secretariat. Results of the meeting include:

- The GIF web site (operated by OECD-NEA) and the associated LFR page were introduced as a communication and collaboration resource to the committee.

- The committee was briefed on an upcoming proposed effort within the Euratom 6th framework to develop a European LFR system identified as ELSY. Members of the SSC were invited to join in the proposed effort.
- The current draft of the R&D plan was distributed and discussed; actions to advance its completion were identified and scheduled. Sections on current R&D programs are 75 % complete. Sections on coordinated R&D plans are in the initial stage of formulation.
- An overall concept for the needed research in the R&D plan was discussed and a high-level schedule was drafted.

Following the September, 2005 GIF-LFR-SSC meeting, further information on several foreign LFR concepts and R&D programs were provided to the US LFR team. These included:

- BORIS (Battery Optimized Reactor Integral System) – a small (10MWe) Pb cooled long-core-life concept from Seoul National University in South Korea
- PEACER (Proliferation-resistant Environment-friendly Accident-tolerant Continuable-Energy Economical Reactor) – a mid-size (300-500 MWe) LBE-cooled actinide burning concept from Seoul National University in South Korea
- ELSY (European Lead-cooled SYstem) – a new 6th Framework proposal for a Pb-cooled reactor R&D program. The US has been invited to participate with the 6th Framework ELSY project, and this possibility is being investigated.

LLNL staff participated in a special working meeting of the GIF-LFR-SSC at OECD-NEA in Paris on November 9 to 11, 2005 to work on the draft LFR R&D Plan. Progress was made on the plan, and a review draft may be available by January. US input is in good shape for the review draft, and US staff are helping coordinate international input.

Another full meeting of the GIF LFR System Steering Committee was held in Florence, Italy during the week of April 10. The meeting consisted of update reports from each member, introductory discussions with the Committee's new member from Japan, and working sessions on the LFR-SSC R&D Draft Plan.

On July 17 and 18, 2006, a working meeting was held by the GIF LFR Steering Committee at NEA in Paris. The committee reviewed and developed comments on the GIF Quality Management System, prepared a draft of the LFR System Arrangement (based on the GIF Template); and assembled a set of responses to the GIF Experts Group's comments on the initial draft LFR System Research Plan (SRP). In addition, the committee began its re-draft of the SRP.

4.2.2. Heavy Metal-Cooled Reactor Technology Meeting

Meetings of the Lead Alloy Nuclear Energy Systems Interest Group and of the GIF LFR-SSC were held in conjunction with the ANS Annual Meeting in Reno NV on June 8 and 9, 2006. These meetings were well attended and brought together researchers interested

in Pb and LBE coolant technology from foreign and domestic laboratories, universities, and industry to discuss future cooperation opportunities. The discussions led to establishing a proposal for an I-NERI program with the Koreans and Japanese. New initiatives in Europe (the ELSY program) and the Russian Federation (SVBR-75/100) were announced.

4.2.3. Cooperation with ELSY

LLNL has maintained continuing contact with the EU program to design a lead-cooled reactor system (ELSY) that can compete economically with alternative power reactors. This effort is directed toward developing a design in sufficient detail to establish a cost estimate that would support a decision on construction in 2008. The design parameter selections for this reactor have been driven by the objective of early demonstration of an economically attractive system. This has led to selection of temperatures that are compatible with readily available materials for the coolant boundary and fuel cladding. If this project proceeds to construction, it will be an important point of contact and continued cooperation for the GIF.

4.2.4. Small Modular Fast Reactor Coordination with CRIEPI

LLNL has ongoing cooperation with the Japan Central Research Institute of the Electric Power Industry (CRIEPI). Dr. Akio Minato from CRIEPI has been the point of contact for this cooperative effort. He has returned to Japan following his year long assignment as a participating guest at LLNL. During his residence at LLNL, three reports were completed [15, 16, 17] that addressed topics of interest to small sodium- and heavy liquid metal-cooled fast reactors. Reference [17] developed a plan for post- irradiation examination of structural materials irradiated in FFTF in an effort to establish an I-NERI program with co-funding from Japan and the US.

LLNL continues to monitor the proposal for Toshiba to provide a small modular fast reactor (4S – sodium cooled) to the town of Galena, Alaska as a demonstration of long core life fast reactor use in remote areas. There is sufficient technology overlap between the sodium-cooled and lead-cooled small transportable long-core-life reactors for this connection to be of mutual benefit.

4.3. University Partnership: UC-Berkeley

The University of California, Berkeley (UCB) has continued to support the Gen IV LLNL LFR program with analysis of core and fuel cycle design alternatives that may improve the safety, economics, and proliferation resistance of a LFR. These analyses have been completed within the context of the Encapsulated Nuclear Heat Source (ENHS) reactor but may also have applicability to small LFR designs that are cooled by natural circulation. The results of this work have been reported in papers published in the open literature including the following:

- Y. Nishi, N. Ueda, I. Kinoshita and E. Greenspan, “Computational Analysis of the Thermal-Hydraulic Characteristics of the Encapsulated Nuclear Heat Source,” *Nuclear Technology*, 152, 324-338, December 2005.
- T. Okawa and E. Greenspan, “Effect of Fuel Type on the Attainable Power of the Encapsulated Nuclear Heat Source Reactor,” *Proc. of ICAPP ‘06*, Reno, NV, June 4-7, 2006.
- M. Milosevic, E. Greenspan and J. Vujic, “Uncertainties in Monte Carlo Analysis of Innovative Lead-Cooled Fast Reactors,” *PHYSOR 2006*, Vancouver, BC, Canada, September, 10 - 14, 2006.
- E. Greenspan and the ENHS Design Team, “Innovations in the ENHS Reactor Design and Fuel Cycle,” 2nd Int. Symp. on Innovative Nuclear Energy Systems, Yokohama, Japan, 26 - 30 Nov., 2006.
- A. Susplugas and E. Greenspan, “ENHS Reactor Power Level Enhancement Possibilities,” *ibid.*
- L. Monti, E. Greenspan, M. Sumini, M. Fratoni and F. Rocchi, “Multi-Recycling in the ENHS,” *ibid.*
- M. Fratoni, L. Kim, S. Mattafirri, R. Petroski and E. Greenspan, “Preliminary Feasibility Study of the Heat-Pipe ENHS Reactor,” *ibid.*
- E. Greenspan, S. G. Hong, L. Monti, T. Okawa, M. Sumini and A. Susplugas, “Encapsulated Nuclear Heat Source Reactors for Energy Security,” 15th Pacific Basin Nuclear Conference, Sydney, Australia, October 15-20, 2006.
- T. Okawa and E. Greenspan, “Feasibility of Negative Void Reactivity Feedback in the Encapsulated Nuclear Heat Source Reactor,” to be published in *Nuclear Technology*.
- L. Monti, E. Greenspan, M. Sumini, M. Fratoni, F. Rocchi, and M. Frignani, “Effect of Multi-recycling on the Encapsulated Nuclear Heat Source Core Design,” to be published in *Nuclear Science and Engineering*.

4.4. LLNL Materials Evaluations

4.4.1. Material Modeling

A significant effort is being devoted to investigating radiation-induced microstructural changes in Fe-Cr steels. Chromium-based ferritic/martensitic (F/M) steels are of interest

for use as core component materials in liquid metal-cooled fast reactors. Controlling the formation of precipitated phases and irradiation defects in these systems is essential for the development of radiation resistant materials for advanced nuclear reactors. A better understanding of the mechanisms involved in phase transformation at the nanometer scale is needed to derive a correlation with chemical composition or microstructural parameters. Computational materials modeling is helping to bridge the gap between theory and experiment.

Mechanical property changes in Fe-Cr steels (swelling, embrittlement induced by neutron irradiation) depend on chromium concentration. Experiments in Fe-Cr alloys have shown order at low Cr concentration, and phase separation at high Cr content. In the case of a Cr-rich material such as HT9, experiments show that a significant contribution to the yield stress increase comes from the precipitation of the α' phase [18]. The quantity of precipitated α' phase increases with the Cr content, the neutron irradiation dose, and as the irradiation temperature is reduced. Atomistic studies are of relevance for these complex alloys, with changes in the order versus segregation tendency at ~ 10 at. % Cr, and precipitation of α' phase affecting alloys with 12 at. % Cr. In the computer simulation studies, the effects of Cr concentration on defect evolution, segregation behavior, and second phase precipitation in the early stages of damage in both single crystal and polycrystalline Fe-Cr systems are investigated and results of computer simulations results of irradiated Fe-Cr systems are compared with those of pure iron [19].

Modeling binary Fe-Cr alloys provides further fundamental understanding on the Cr concentration dependence of mechanical properties induced by neutron irradiation. The LLNL research focus is in the generation of new classical potentials for computer simulation studies of concentrated Fe-Cr binary alloys that correctly incorporate all of the available thermodynamic data for the system and its defect properties. Formation of α' precipitates in Fe-Cr is modeled with a thermodynamic approach that captures the unusual behavior of the system as the negative heat of formation, the tendency to deplete solute contents at grain boundaries, and the significant critical radius for nucleation, resulting from a complex magnetic origin of its energetics [20].

Modeling the behavior of Fe-Cr alloys under irradiation is a challenge due to the complex nature originated in its magnetic structure. Recent ab-initio results from Klaver et. al. (Private Communication 2006) show how magnetic frustration effects account for the change in sign of the formation energy of the alloy, which in turn is at the basis of the change from ordering to segregation tendency observed at low Cr composition. The Fe-Cr interatomic potentials that have been developed for the LLNL computer simulations follow a general formalism that accounts for this change of sign [21]. Moreover, using the LLNL thermodynamic package, one is able to predict the new location of the miscibility gap in the ferromagnetic phase of this alloy. These tools together with the recently developed massive parallel Monte Carlo code in the transmutation ensemble with displacements allow one to follow nucleation and growth processes involved in α' precipitation.

Spectacular advances in computational materials science are providing a complete new vision of the radiation damage problem in Fe-Cr systems. Computer modeling has placed within reach the long term goal of incorporating basic physical understanding to the development of new radiation resistant materials. By investigating early stages of radiation damage, one unveils the role played by different components of the radiation damage problem and uses these properties to advantage to formulate the condition a material has to fulfill to be radiation resistant. The final goal is to adopt a Multi-Scale Materials Modeling (MMM) methodology and merge atomistic and meso-scale levels together to analyze effects of precipitation hardening in terms of a parameter free model of crystal plasticity [22]. Leadership class simulations are furthering investigation and bringing LLNL a step closer to “real experiment” simulation and to the development of an integrated platform for modeling radiation damage in nuclear materials. New simulation methods will be proposed that will extract the path to the continuum and thermal-mechanical Finite Elements Methods (FEM). With these results in hand, it will be possible to formulate constitutive models of radiation damage that can be incorporated into the computer codes used in the engineering design process.

Experiment data on the effects of irradiation on new materials is often scarce and covers a limited range of temperatures and doses. It is often difficult to elaborate trend lines and extrapolations outside of the indicated small ranges of doses. A question that can be asked is whether it is possible to develop engineering-scale material strength models for irradiated alloys.

Multi-scale modeling of materials is emerging as a promising tool to predict materials behavior. Within the LLNL LDRD, "Critical Issues on Materials for Gen-IV Reactors," it is intended to develop methods largely sought by the scientific community that contribute some of the pieces that shall be needed to realize MMM development. LLNL has here unique tools for studying point defect interaction using the full potential of LLNL's massively parallel super-computing resources. Use is made of atomistic-information as input to the meso-scale, and coupling the meso-scale Dislocation Dynamics methodology to Quasi-continuum and other multi-scale methods to produce an "Integrated Modeling Platform" that connects to polycrystal plasticity studies. This is the forefront of the mechanical properties field.

A deeper understanding is being sought of the variables that control changes in the microstructure. One needs to control these variables if one wants to develop radiation resistant materials. Fe-Cr is the perfect example of the way in which atomistic modeling of radiation damage is helping to gain an understanding of materials behavior under irradiation. These are complex alloys, with changes in the order versus segregation tendency at ~ 10 at % Cr, and precipitation of the alpha prime phase affecting alloys with 12 at. % Cr. To study Fe-Cr alloys with compositions of interest for the nuclear industry, a powerful approach has been developed that generalizes many-body classical potentials by incorporating their complex formation energy curves. One can then derive free energies and compute the thermodynamics of the system (melting temperatures, entropy, and the equilibrium phase diagram) and use of the full potential of LLNL's massively

parallel super-computing resources to study point defect interaction and precipitation on 10^6 atom scale.

Fe-Cr alloys are considered for use as structural materials (cladding, fuel assembly ducts, in-core structural components) in LFR concepts. Structural components, fuel cladding, and reflector materials are expected to undergo significant degradation under the high temperature and high neutron-flux over the reactor life time. Defect formation and migration determine the microstructural evolution of the alloy under irradiation. Radiation-enhanced diffusion and radiation-induced precipitation are among the mechanisms that lead to changes in their microstructure. Macroscopic damage effects, such as swelling and α' -precipitation, are in part controlled by the energetics of defects and by thermodynamic forces that drive the system through these phase transformations.

Fe-Cr is a complex system with a tendency to Cr ordering below ~ 10 % Cr and to Cr clustering above it, which corresponds to a change of sign in the Fe-Cr mixing enthalpy (see Figure 68).

The red solid line in the Δh plot shows the results of ab-initio calculations recently reported by Olsson et al. [23]. The dotted line corresponds to the CALPHAD database [24]. Note that even if the maximum occurs at about the same Cr concentration (~ 50 % Cr), there is still a discrepancy in the height. Ab-initio results at Cr ~ 0.5 are greater and don't reproduce those of CALPHAD. The reason for this discrepancy is yet to be explained but is not relevant to this discussion. At low Cr concentration, Cr atoms tend to be distributed as far as possible from each other giving rise to the formation of stoichiometric ordered phases represented by this negative mixing enthalpy. As the Cr concentration increases the mixing enthalpy becomes positive. In this region the alloy has a tendency to cluster which gives rise to the formation of the Cr-rich α' phase.

The complex behavior of the alloy at low Cr concentration has an impact in the phase diagram; it implies that the solubility limit at low temperatures is larger than expected (see Figure 69). This is extremely important because this is the area of interest for nuclear applications, see star indicating temperatures below the Curie temperature, $T_C = 1043$ K (770°C) and Cr concentrations below 0.15 at %. Note that the standard Fe-Cr phase diagram exhibits a large miscibility gap, which closes above T_C .

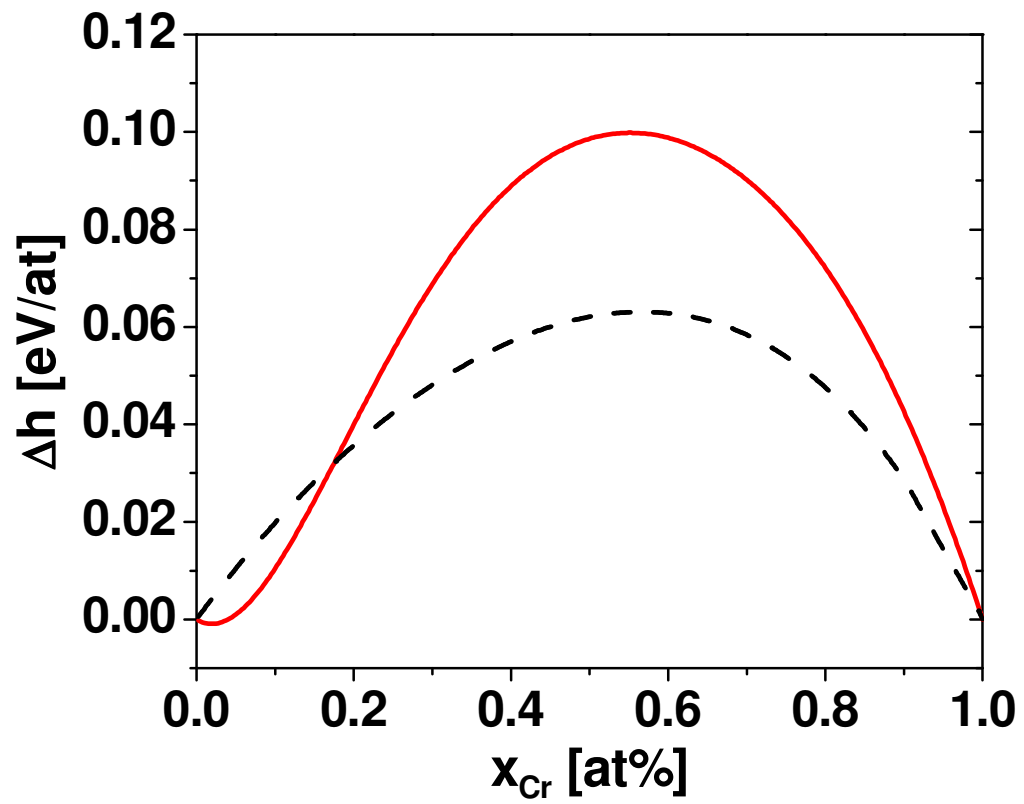
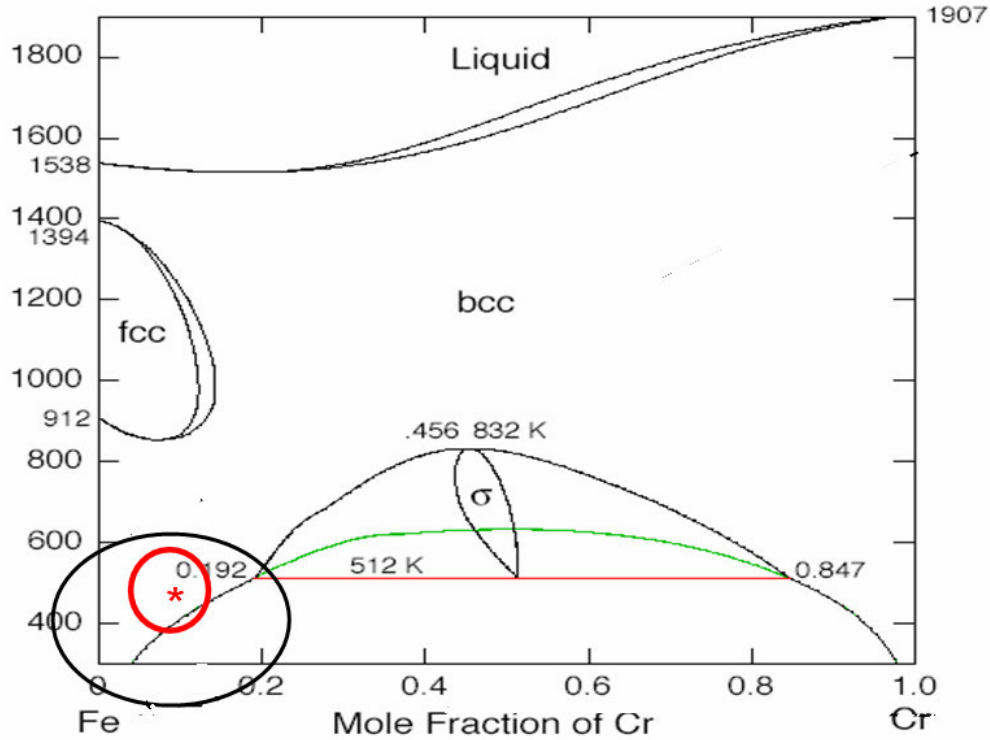


Figure 68. Fe-Cr Mixing Enthalpy a) Red Line from Ab-Initio Calculations b) Dotted Line from CALPHAD Database.



Area of interest for
nuclear applications

Figure 69. CALPHAD Phase Diagram for Fe-Cr.

Precipitation was observed and reported in [25 and 26]. Experiment work done on short-range order SRO measurements by Mirabeau [27] is relevant to the analysis of the mixing enthalpy in the Fe-rich region. Recently, results of neutron irradiations were reported by Mathon [28] which seem to confirm the larger solubility limit at low Cr concentrations.

The powerful approach developed by Caro et. al. [29] incorporates ab-initio calculations and experiment results to correctly describe the thermodynamics of the system. Following the embedded-atom methodology, the energy of the system is obtained as a sum of two terms: the embedded function, $F(\rho)$, where $\rho(r_{ij})$ is the electronic density and r_{ij} is the distance between atoms, i and j, and the pair potential, $V_{\alpha,\beta}$. The method makes use of a function, $h(x)$, which accounts for changes in the mixing enthalpy as a function of Cr concentration. $h(x)$ is obtained using a Redlich-Kister expansion of the heat of solution following the CALPHAD methodology; see the expression below:

$$E = \sum_i^N \left[F \left(\sum_{j \neq i} \rho_{\alpha}(r_{ij}) \right) + 1/2 \sum_{j \neq i} V(x, r_{ij}) \right]$$

$$V(x, r) = h(x) v_{AB}(r)$$

$h(x)$ is obtained using a

Redlich - Kister expansion of the heat of solution (CALPHAD methodology)

The thermodynamic package developed in 2005 [30] allows one to derive free energy curves and from them obtain the new phase diagram (see Figure 70). Experiment data points correspond to irradiations (red triangles) and measurements in thermal equilibrium (blue circles).

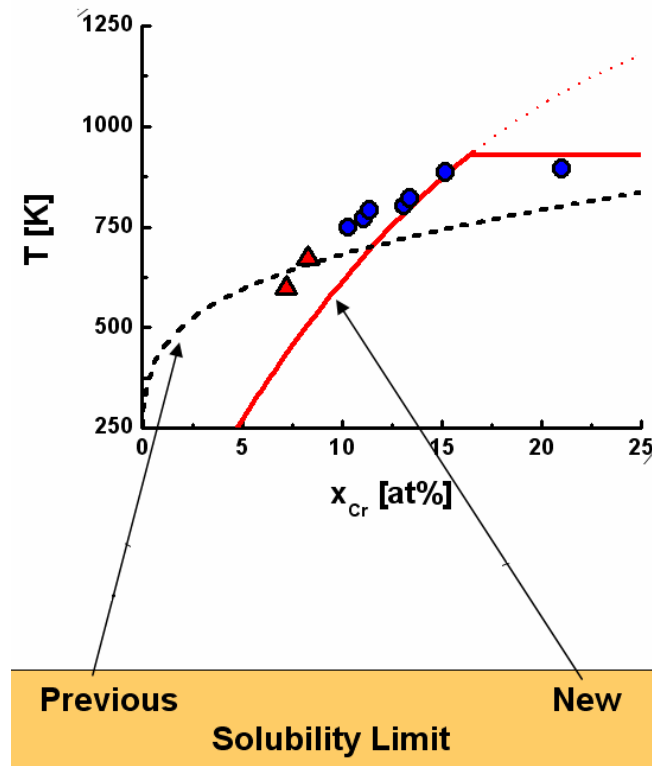


Figure 70. New Phase Diagram (Solid Red Line) as Compared to the Standard Phase Diagram from CALPHAD (Black Dashed Curve).

This new description of the Fe-Cr system in the classic approximation was applied to evaluate the energetics of point defect configurations. The formation of vacancies and self and mixed interstitials in the $\langle 110 \rangle$ and $\langle 111 \rangle$ directions was investigated with

Molecular Dynamics (MD) using the interatomic potential of Mendelev [31] for Fe and that of Wallenius [32] for Cr. Details on formation energies of vacancies are reported in [33]. The formation energies of only two configurations of self-interstitial atom defects are shown here. These results are obtained for both pure elements and for the binary alloy as a function of Cr concentration.

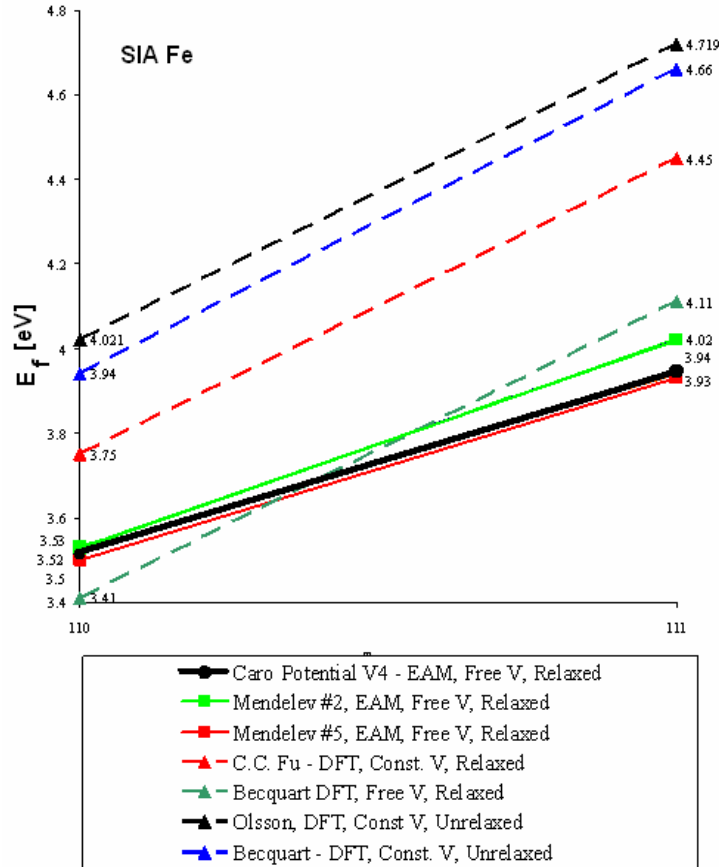


Figure 71. Formation Eenergy of <110> and <111> Self-Interstitial Atoms in Pure Fe.

Note that the stability of <110> relative to <111> interstitials in pure Fe was investigated during many years; the reason being that in non-magnetic bcc metals (like V, Nb, Ta), the <111> SIA formation energies have the lowest values, and only Fe has an “anomalous” trend due to magnetism. Also the formation energy of the <110> SIA in W, Mo and even Cr is higher than that of the corresponding <111> SIA. Fe behaves in an “anomalous” way: the <110> SIA has lower formation energy than the <111>. This fact was recently revealed by ab-initio calculations. Ab-initio formation energies of self-interstitial atoms reported in the literature (dashed lines in Figure 71) are compared to our MD results (solid black line in the same figure). Different ab-initio results are obtained depending on the number of atoms and the method but they all show the same trend. Clearly, our EAM calculations and those of Mendelev reflect this tendency.

Ab-initio results for Cr show that the difference between the formation energy of both SIA $\langle 110 \rangle$ and $\langle 111 \rangle$ is smaller than in Fe (see Figure 72). Our results (black solid line) obtained with Version 4 of the Cr interatomic potential seem to be in good agreement with ab-initio data. Version 4 of the Cr potential was developed using parameters reported by Olsson and Wallenius in [32] which give better results than those from an older version also shown in Figure 72 (magenta solid line).

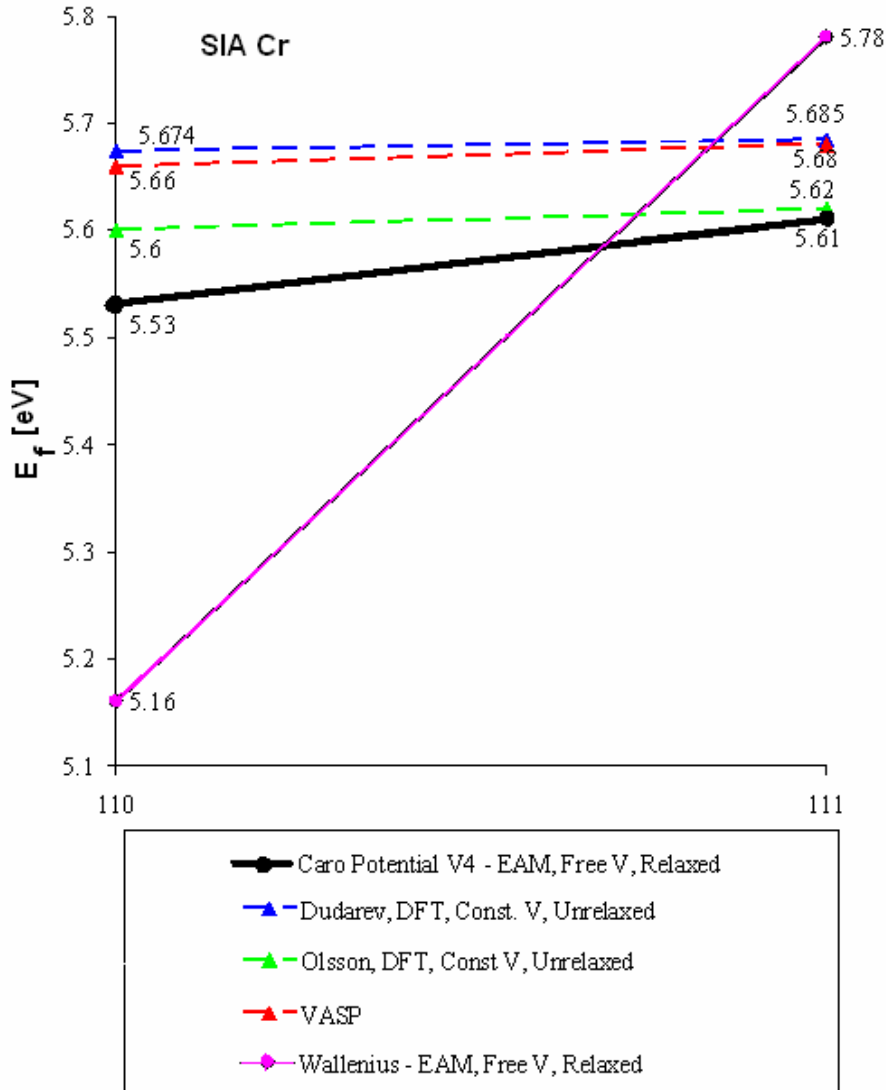


Figure 72. Formation Energy of $\langle 110 \rangle$ and $\langle 111 \rangle$ Self-Interstitial Atoms in Pure Cr.

The new approach is fundamental to obtaining the formation energy of point defects as a function of Cr concentration (see Figure 73). Short Monte Carlo (MC) runs at high temperature ($T \sim 500$ K) were carried out for each Cr concentration. At each MC step

during this run, the energy was evaluated. The mean energy was calculated and the sample with energy corresponding to the mean energy was selected as the reference case. This sample was then quenched to $T = 0$ K, and the reference energy determined. Starting from the reference sample, thousands of new samples were generated with interstitials located at each and every site of the lattice. The energy corresponding to each sample at $T = 0$ K was calculated using MD. The energy values were fit to a Gaussian. The error bars that are shown in Figure 73 are associated to the full-width-at-half-maximum (FWHM) of that Gaussian. The formation energy, E_f , is given by

$$E_f = E_{\text{sample with 1025 atoms}} - 1025 (E_{\text{sample with 1024 atoms}}/1024)$$

As said before, $\langle 110 \rangle$ SIA in pure Fe has lower formation energy than the $\langle 111 \rangle$. This leads to the presence of a second Gaussian in the $\langle 110 \rangle$ case, indicating the presence of two kinds of interstitials in the relaxed configuration. This implies that several of the initial $\langle 111 \rangle$ SIA converted into $\langle 110 \rangle$; this last configuration being that of minimum energy.

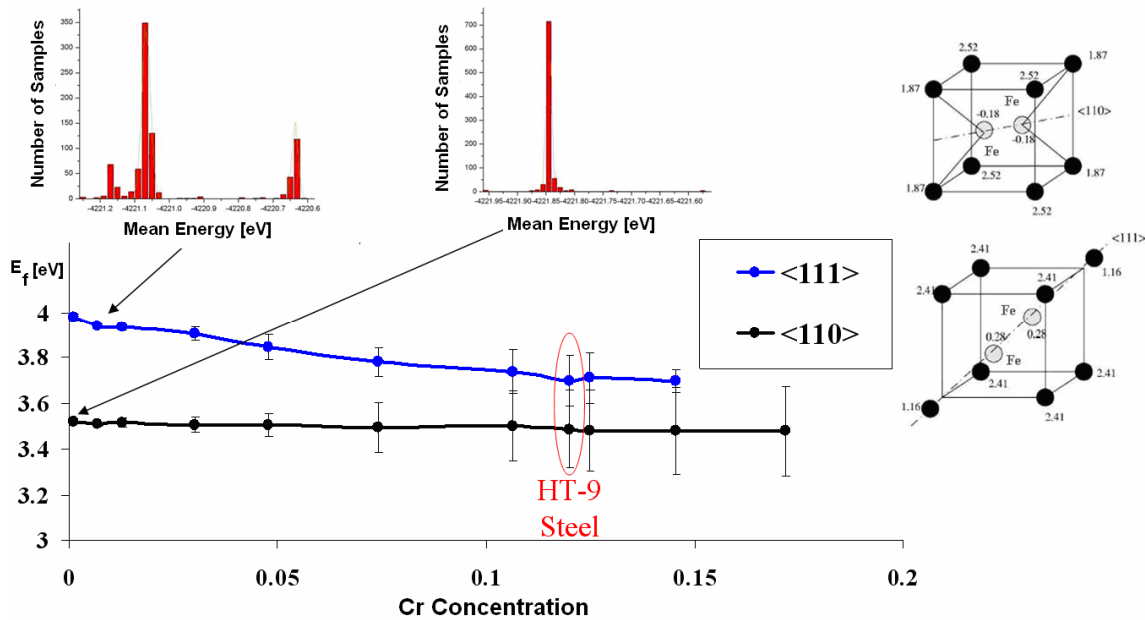


Figure 73. $\langle 110 \rangle$ and $\langle 111 \rangle$ Self-Interstitial Formation Energy as a Function of Cr Concentration.

Similar evaluations were done for mixed interstitials in Fe and Cr. This validation of static properties of defects is to be continued by studies of their dynamic evolution. One of the computer tools to be used for this is MCCASK. MCCASK is a hybrid Monte Carlo-Molecular Dynamics code developed by A. Caro and B. Sadigh in 2005. MCCASK code performs sequences of MC events and MD time steps. In this way, the

equilibrium concentrations in the alloy are obtained, enabling precipitation and defect studies on 10^6 atom scale. This provides a unique tool for studying point defect interaction using the full potential of LLNL's massively parallel super-computing resources. In Figure 74, the process of homogeneous Cr precipitation is simulated in a 20 at. % Cr sample.

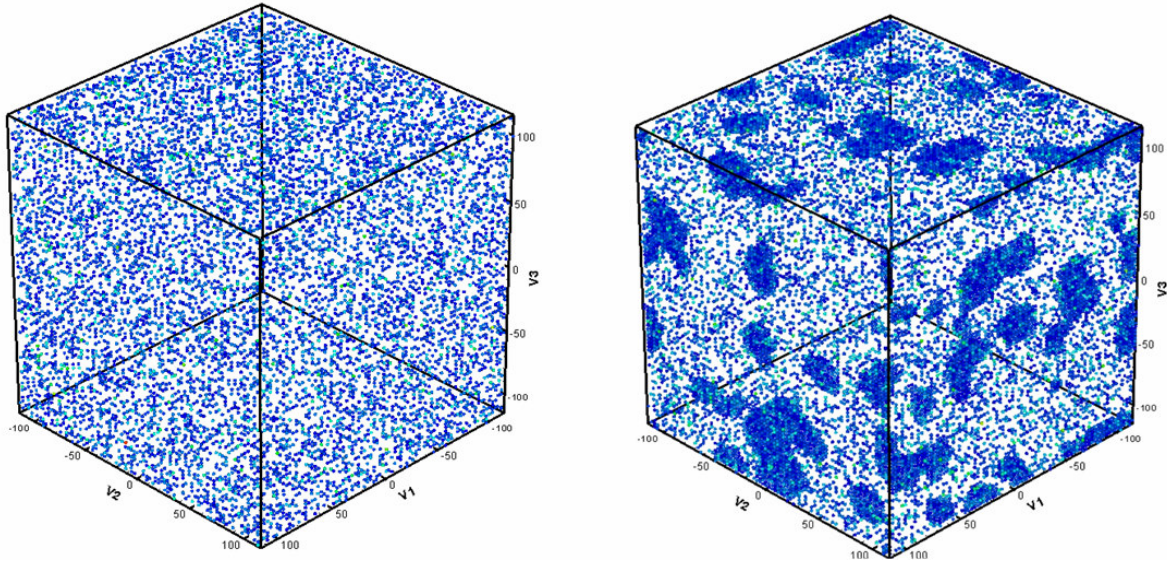


Figure 74. Homogeneous Precipitation in a Fe-Cr Sample (xCr ~ 20 at %).

4.4.2. Laser Peening

Laser-peening technology is emerging as a promising technique to enhance corrosion-resistance of materials that must withstand high operating temperatures and high fast fluxes during a large number of years. The laser peening (LP) treatment generates a compressive stress state potentially altering the metal-oxide bonds on the surface (see Figure 75).

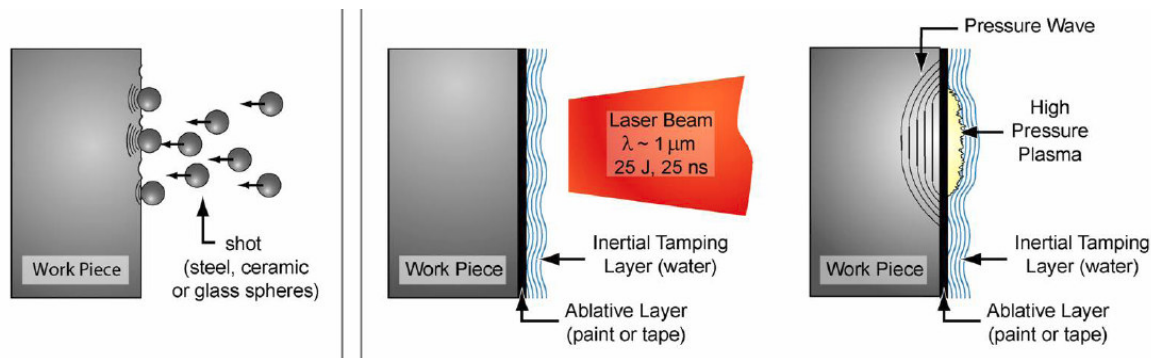


Figure 75. Shot Peening and Laser Peening Process (LP) Description. a) The Sample is Protected by an Ablative Layer and an Inertial Tamping Layer b) Laser Pulse Forms High Pressure Plasma on the Surface. The Shock Wave Travels Through the Depth and Plastically Deforms It in Its Wake. [34].

The laser beam is pulsed upon the metallic surface. The high rate of deformation during laser peening produces a layer of plastically deformed materials that is significantly deeper than that produced by other techniques. The potential of this advanced surface treatment to retard the corrosion of LFR structural materials was investigated.

The primary objective of this study [35] was to analyze the potential benefit of laser peening (LP) for fuel claddings in LBE environments. Ferritic-martensitic (F/M) steels have been considered as possible candidate materials that could perform suitably under conditions of high dose (150 dpa), and temperatures of ~500 to 600 °C while exposed to flowing molten lead or lead-bismuth containing dissolved oxygen.

Coupons of F/M steels, HT9, T91, EP823, and the austenitic stainless steel, 316 L, were laser peened before participating in several experiments. The samples were peened on both sides to half height level (see Figure 76) using laser treatment parameters. These specimens were treated with two layers of LP with each layer providing 100 % surface coverage and a 50 % overlap in both horizontal and vertical directions. Laser peening parameters for sixteen coupons (316L, HT9, T91, and EP823) are 8GW/cm² irradiance, 18 ns pulse width, and 2 layers of treatment (8-18-2).



Figure 76. T91, HT-9, 316 L, and EP-823 Samples after Laser Peening.

4.4.3. Thermal Treatment Experiments

Some spare T91 samples underwent a thermal treatment in an oven at 520 °C. Five 1-mm thick T91 samples were tested for thermal relaxation (see Table 24).

Table 24. T91 Test Matrix for X-ray Diffraction (XRD) Measurements

Type	Laser Peening (8-18-2)	Heat Treatment (520 °C)
CASE 0	None	None
CASE 1	LP	1 week
CASE 2	LP	2 weeks
CASE 3	LP	None
CASE 4	None	2 weeks

Residual stress (RS) relaxation measurements using X-ray diffraction (XRD) were done after one week and two weeks of heating. RS relaxation results corresponding to the five

T91 coupons tested are presented in Figures 77 and 78. Two data points were obtained from each coupon at three different depths (surface, 0.25 mm, 0.5 mm). Results indicate that the F/M samples do not retain the residual stress after two weeks of heat treatment. XRD measurements show large errors in small levels of residual stress (RS), and are difficult to interpret.

All the laser peened samples were first laser peened and then underwent thermal treatment. Further studies should consider laser peening the sample after the thermal treatment is applied.

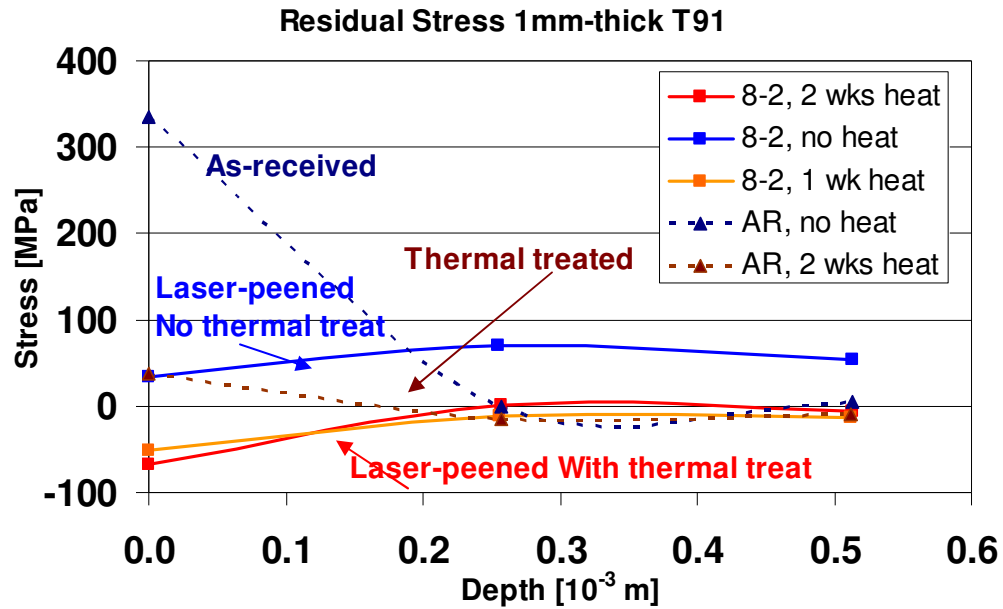


Figure 77. Residual-Stress versus Depth for Laser Peened (LP).

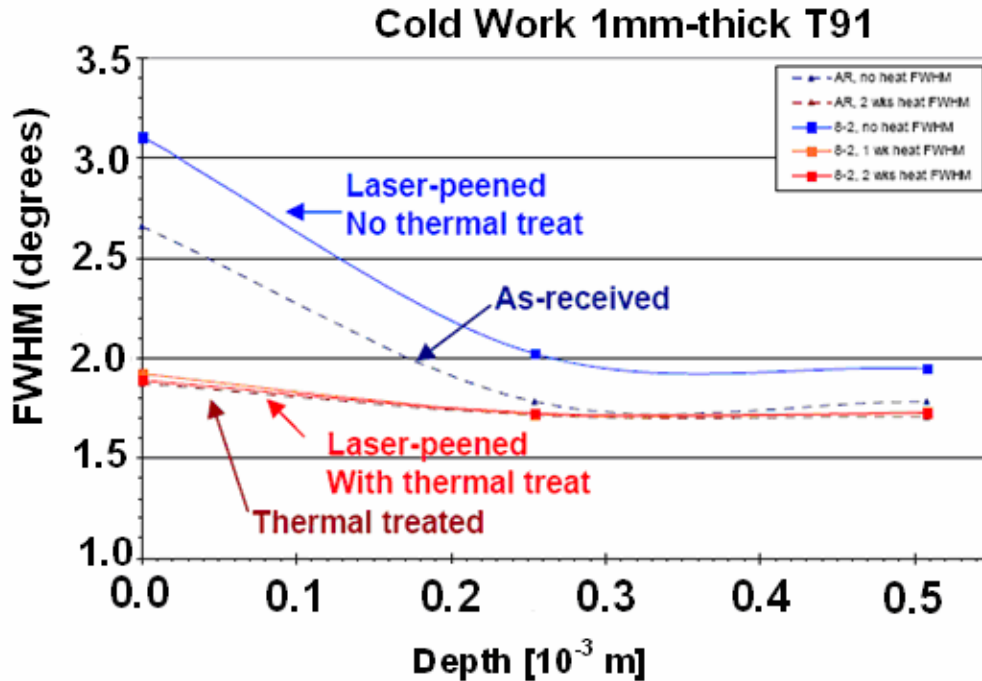


Figure 78. Cold-Work Measured in Terms of Full-Width-Half-Maximum (FWHM) for Laser Peened (LP) and Un-Peened T91 Steel Samples with and without Thermal Treatment.

4.4.4. Residual Stress Measurements using the Slitting Method

The residual stress in the bulk of the coupons was measured using the slitting method. See Table 25 for the coupons measured using the slitting method.

Due to the difficulty in obtaining sufficient material, EP823 and T91 coupons were not included in the slitting residual stress measurements. Thicker coupons of 3 mm were measured in 316L to more accurately determine the reduction in residual stress due to the heating process.

Laser peening parameters for the 1 mm coupons (316L and HT9) are $8\text{GW}/\text{cm}^2$ irradiance, 18 ns pulse width, and two layers of treatment (8-18-2). Both sides of each coupon were treated. The 316L 3 mm thick coupons were treated with a slightly higher irradiance ($10\text{GW}/\text{cm}^2$) to induce more residual stress.

Table 25. Experiment Parameters for Residual Stress Coupons

SN	Mat'l	t (mm)	Laser-peening Treatment Irradiance - # layers	Heat (1wk)
2-LH-HT9	HT9	1	LP 8-2	500 C
1-HH-HT9	HT9	1	LP 8-2	600 C
3-NH-HT9	HT9	1	LP 8-2	none
4-NH-HT9	HT9	1	None	none
2-LH-316L	316L	1	LP 8-2	500 C
1-HH-316L	316L	1	LP 8-2	600 C
3-NH-316L	316L	1	LP 8-2	none
4-NH-316L	316L	1	None	none
5-NH-316L	316L	3	LP 6-2	none
4-NH-316L	316L	3	LP 8-2	none
3-NH-316L	316L	3	LP 10-2	none
1-LH-316L	316L	3	LP 10-2	500 C
2-HH-316L	316L	3	LP 10-2	600 C

The residual stress data in Figure 79 seems to show two trends. First, the laser peened coupon with no heat treatment (blue) shows a tensile stress at the surface. The tensile peak at the coupon surface is different than expected as these coupons were all cut using a wire EDM and then polished to remove the recast layer. Regardless, the stress seems to relax in the laser peened samples during both heat treatments (orange and red). Second, reducing the laser treatment intensity seems to generate more residual stress. The highest level of residual compressive stress is obtained with the 6 GW/cm² treatment (pink), leading the authors to believe that the 1 mm coupons may have been laser peened “too hard.”

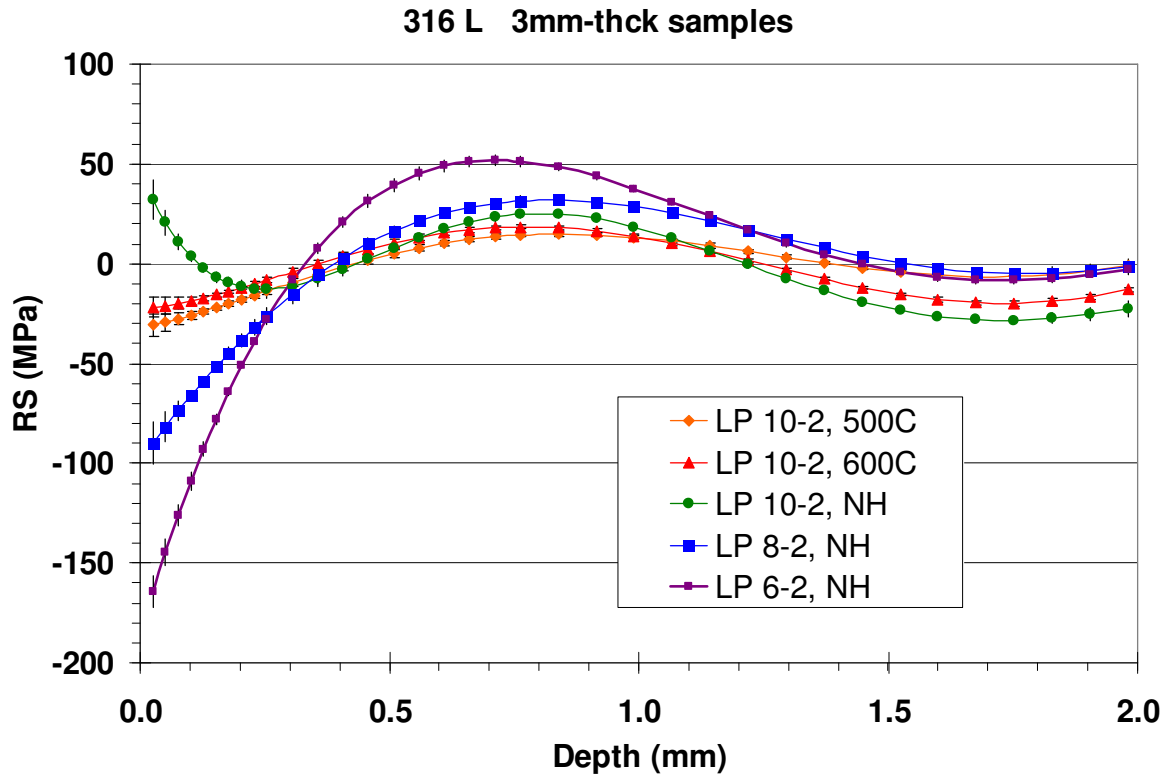


Figure 79. Residual Stress Measurements for 3 mm Thick 316 L Coupons.

Further studies of thermal exposure effects are needed to quantify the magnitude and rate of thermal relaxation of the layer of compression induced by laser peening. It is also desired to extrapolate that to higher temperatures (800 °C)

The 1 mm data results are unclear. There seems to be an unexpected amount of residual stress remaining in HT-9 samples from the machining process. These coupons were wire EDM cut from plate material and then polished by hand to remove the EDM recast layer. This process had been expected to induce the least amount of residual stress in the coupons; however, the data we obtained seems to suggest otherwise.

4.4.5. EDS in Samples Participating in Corrosion Tests

Eight LP samples (316L, HT-9, T-91, and EP-823) that participated in a corrosion test in the DELTA loop at LANL were sliced in two. One-half of the sample was sent back to LLNL for further RS measurements using the slitting method. These samples had been immersed for 400 and 600 h in flowing lead-bismuth eutectic (LBE) at 535 °C.

EDS maps of the laser peened region for the 316 L coupon are compared in Figures 80 and 81 with those corresponding to the unpeened case. The figure suggests that laser peening prevents LBE penetration in 316 L.

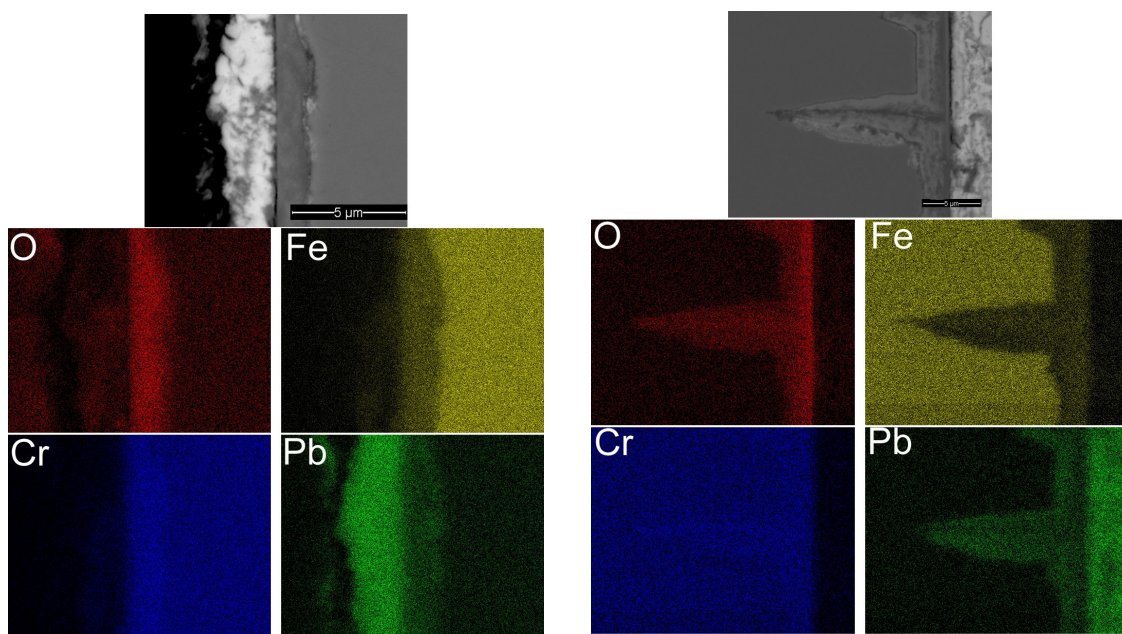


Figure 80. Micrographs for 316 L Samples: a) Peened and b) Unpeened. Corresponding EDS Maps for Oxygen, Iron, Chromium and Lead Content in the Sample.

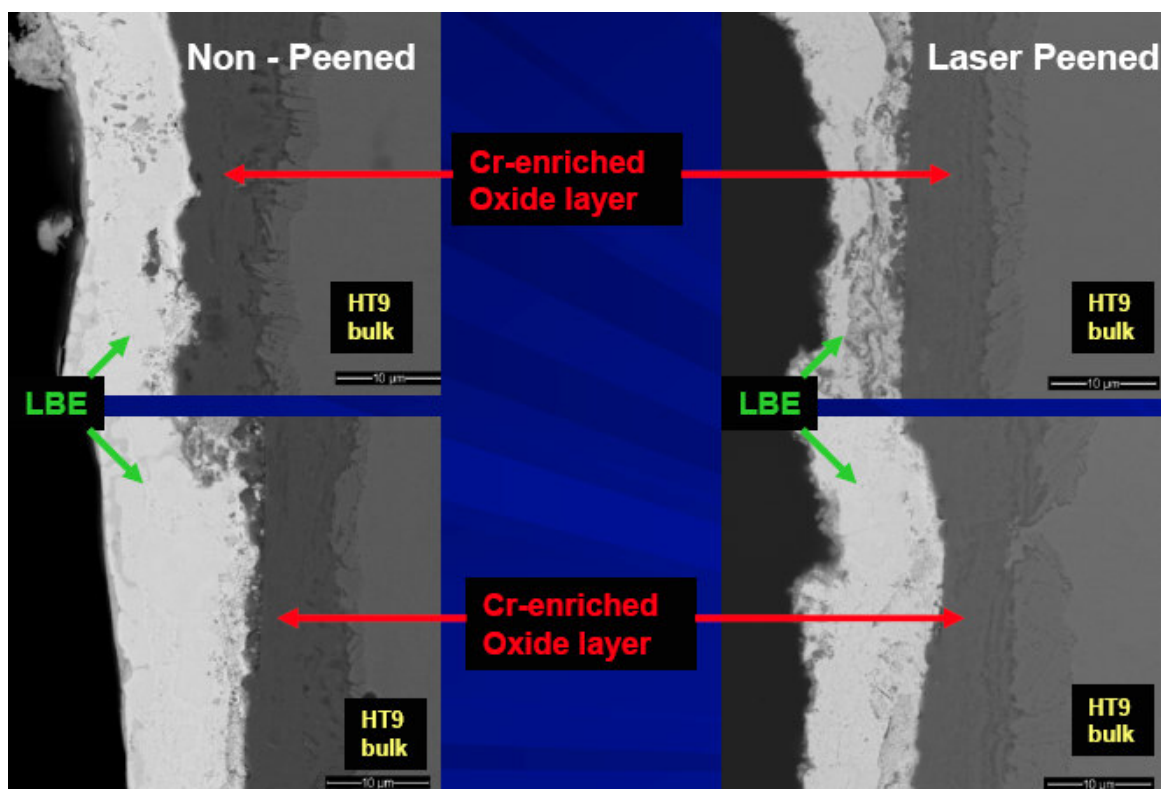


Figure 81. HT-9 Micrographs: a) Non-Peened and b) Peened Samples.

Micrographs for HT-9 non-peened and laser peened samples are shown in Figure 81. A white region corresponding to a lead-bismuth deposit covers the Cr-enriched oxide layer that lies facing the bulk of the sample (to the left of the picture). Laser peened and non-peened regions show the same chromium-oxide thicknesses. The oxide layer in the peened sample shows a smoothness that is not apparent in the non-peened case. No LBE penetration is observed after 600 h exposure to LBE at 535 °C. No significant difference was found when comparing HT-9 and T-91 micrographs.

There is great interest to have more laser peened specimens for future irradiation testing. There is a need to optimize the laser parameters until the highest level of compressive stress is obtained. Also, further thermal effects studies on RS relaxation should be done to differentiate behaviors that are not visible now due to the lack of experiment data. Differences between lead and lead-bismuth environments, and also exploring higher temperatures (800 °C) should be investigated for the case of laser peened surfaces. The effects of high doses of irradiation (~ 200 dpa) as are typical of the cladding surface remain to be determined. LANL has sent a first set of LP T91, HT9, and 316 L samples and is participating in the STIP V irradiation campaign of the spallation neutron source at the Paul Scherrer Institute (PSI), Switzerland.

5. Acknowledgements

The authors are indebted to Dr. Rob M. Versluis, U.S. DOE Program Manager, for his continued support and guidance. The authors are also grateful to Dr. Cliff Fineman, U.S. DOE, Idaho, for his comprehensive review of the report and many helpful comments.

6. References

1. D. C. Wade, R. D. Doctor, J. J. Sienicki, D. T. Matonis, R. S. Faibish, and A. V. Moiseyev, "STAR-H2: A Long Refueling Interval Battery Reactor for Hydrogen and Water Supply to Cities of Developing Countries," 5th International Conference on Nuclear Option in Countries with Small and Medium Electric Grids, Dubrovnik, Croatia, May 16-20, 2004.
2. D. Wade, "The STAR Concept A Hierarchal Hub Spoke Nuclear Architecture Based on Long Refueling Interval Battery Reactors and Regional Fuel Cycle Centers," Innovative Small and Medium Sized Reactors: Design Features, Safety Approaches and R&D Trends, Final Report of a Technical Meeting Held in Vienna, 7-11 June 2004, IAEA-TECDOC-1451, Annex II, International Atomic Energy Agency (2005).
3. N. Li, "Lead-Alloy Coolant Technology and Materials – Technology Readiness Level Evaluation," The 2nd COE-INES International Symposium on Innovative Nuclear Energy Systems, INES-2, Yokohama, Japan, November 26-30, 2006.
4. J. Y. Lim and R. G. Ballinger, "Alloy Development for Lead-Cooled Reactor Service," MIT-Tokyo Tech Symposium on Innovative Nuclear Energy Systems,

- Massachusetts Institute of Technology, Cambridge, Massachusetts, November 2-4, 2005.
5. K. E. Nichols and R. L. Fuller, "Review of Turbomachinery for a Supercritical CO₂ Power Cycle," Barber-Nichols Inc., September 7, 2005.
 6. A. Moiseyev and J. J. Sienicki, "Control System Options and Strategies for Supercritical CO₂ Cycles," Deliverable Report, WBS No. 1.10.03, August 1, 2005.
 7. H. Henryson II, B. J. Toppel, and C. G. Stenberg, "MC2-2: A Code to Calculate Fast Neutron Spectra and Multigroup Cross Sections," ANL-8144, Argonne National Laboratory (1976).
 8. R. E. Alcouffe, F. W. Brinkley, D. R. Marr, and R. D. O'Dell, "User's Guide for TWODANT: A Code Package for Two-Dimensional, Diffusion-Accelerated, Neutral-Particle Transport," LA-10049-M, Los Alamos National Laboratory (1990).
 9. B. J. Toppel, "A User's Guide to the REBUS-3 Fuel Cycle Analysis Capability," ANL-83-2, Argonne National Laboratory Report (1983).
 10. R. P. Hosteny, "The ARC System Fuel Cycle Analysis Capability, REBUS-2," ANL-7721, Argonne National Laboratory Report (1978).
 11. I. P. Matveenko, V. V. Orlov et. al., "Experimental and Calculational Investigations of Neutron-Physical Characteristics of BREST-OD-300 Reactor," Russian Forum for Science and Technology FAST NEUTRON REACTORS, The Second International Conference on Heavy Liquid Metal Coolants in Nuclear Technologies (HLMC-2003), Obninsk, Russia, December 8-12, 2003 (in Russian).
 12. I. P. Matveenko, A. M. Tsiboulya, G. N. Mantourov et. al., "Experimental Investigations of BREST-OD-300 Reactor Characteristics at BFS Facility," Working materials for IAEA-AG-1076, IWG-FR/104, Vienna, Austria, pp. 204-239 (2001).
 13. A. M. Tsiboulya, I. P. Matveenko et. al., "Benchmark Experiments for Validation of Neutron Data for Pb, Bi and Minor Actinides," Russian Forum for Science and Technology FAST NEUTRON REACTORS, The Second International Conference on Heavy Liquid Metal Coolants in Nuclear Technologies (HLMC-2003), Obninsk, Russia, December 8-12, 2003 (in Russian).
 14. "Appendix 4 - Lead-Cooled Fast Reactor, FY-06 Update to GEN-IV 10-Year Plan," UCRL-MI-219342, Lawrence Livermore National Laboratory, Livermore, CA, February 28, 2006.

15. UCRL-TR-216546, "Business Opportunities for Small Reactors-A Collaborative Study by CRIEPI and LLNL," Akio Minato, CRIEPI; Neil W. Brown, LLNL, August 2005.
16. UCRL-TR-2170931, "Small Liquid Metal Cooled Safety Study," A. Minato, N. Ueda, D. Wade, E. Greenspan, N. Brown, November 14, 2005.
17. UCRL-TR-216098 (Controlled Distribution), "Post-Irradiation Examination Program for FFTF and CIS Irradiated F/M Materials," Neil W. Brown, Magdalena Caro, William G. Halsey, Mychailo B. Toloczko, Frank A. Garner, March 2005.
18. M. H. Mathon, Y. de Carlan, G. Geoffroy, X. Averty, A. Alamo, C.H. de Novion, "A SANS investigation of the irradiation-enhanced α - α' phases separation in 7–12 Cr martensitic steels," *Journal of Nucl. Mater.* 312 (2003) 236–248.
19. S. G. Srivilliputhur, C. Tomchik, A. Caro, M. I. Baskes, M. Caro, S. Maloy and J. Stubbins, "Atomistic simulations of radiation-induced defect processes and segregation in Fe-Cr systems," to be presented at the 2007 TMS annual Meeting, February 25- March 1, 2007, Orlando, Florida, USA (private communication July 24, 2006).
20. A. Caro, and M. Caro, "Heterogeneous precipitation in FeCr alloys," submitted to American Nuclear Society ANS MC + SNA 2007, April 15-19, 2007, Monterey, CA, USA (private communication, September 25, 2006).
21. A. Caro, E. M. Lopasso, M. Caro, B. Sadigh, D. A. Crowson, S. G. Srivilliputhur, "Modeling radiation damage in FeCr alloys," to be presented at the MRS 2006 Fall Meeting, Symp. JJ: Structural and Refractory Materials for Fusion and Fission Technologies, November 27-December 1, 2006, Boston, MA, USA (private communication July 31, 2006).
22. M. Caro, J. Marian, J. Knap, E. Martinez, M. Victoria, W. G. Halsey, LLNL-LDRD "Critical Issues on Materials for Generation-IV Reactors," 3 year project started October 2005.
23. P. Olsson, I. A. Abrikosov, L. Vitos, and J. Wallenius, Jr. *Nuc. Mat.* 321, 84 (2003).
24. Computer Coupling of Phase Diagrams and Thermochemistry, www.calphad.org, See also: N. Saunders, A.P. Miodownik, CALPHAD, Calculation of Phase Diagrams: a Comprehensive Guide, Pergamon, New York, 1998.
25. V. A. Shabashov, A. L. Nikolaev, A. G. Mukoseev, V. V. Sagaradze, and N. P. Filippova, *Bulletin of the Russian Academy of Sciences* 65, 1094 (2001).

26. V. V. Sagaradze, I. I. Kositsyna, V. L. Arbuzov, V. A. Shabashov, and Y. I. Filippov, *The Physics of Metals and Metallography* 92, 508 (2001).
27. I. Mirebeau, M. Hennion, and G. Parette, *Phys. Rev. Lett.* 53, 687 (1984).
28. M. H. Mathon, Y. de Carlan, G. Geoffroy, X. Averty, A. Alamo and C. H. de Novion, *J. Nucl. Mater.* **312**, 236-248 (2003).
29. A. Caro, D. A. Crowson, and M. Caro, *Phys. Rev. Lett.* 95, 075702 (2005).
30. A. Caro, M. Caro, E.M. Lopasso, P.E.A. Turchi, D. Farkas, "Thermodynamics of Fe–Cu alloys as described by a classic potential," *J. of Nucl. Mater.* 349 (2006) 317–326.
31. "Development of new interatomic potentials appropriate for crystalline and liquid iron," *Phil. Mag.*, Vol. 83 (2003) 3977.
32. P. Olsson, J. Wallenius, C. Domain, K. Nordlung, and L. Malerba, "Two band model of alpha-prime phase formation in Fe-Cr," *Physical Review B (Condensed Matter and Materials Physics)*, vol.72, no.21, 1 Dec. 2005, pp. 214119-1-6.
33. H. Dogo, "Point Defect Properties in Iron-Chromium Alloys," HD Naval Postgraduate School Master's Thesis. Mentors M. Caro, A. Caro, Thesis Advisor C. Smith, Second Reader X. Maruyama, (August 06).
34. M. R. Hill, A. T. DeWald, A. G. Demma, L. A. Hackel, H.L. Chen, C. B. Dane, R. C. Specht, F. B. Harris, "Laser Peening Technology," *Advanced Materials and Processes*, August 2003, Volume 161, No 8, www.asminternational.org/AMP.
35. M. Caro, T. Zalesky, P. Hosemann, B. S. El-Dasher, W. G. Halsey, B. Stuart, "Thermal Effects on Thin Laser-Peened Ferritic-Martensitic Samples," to be published as a LLNL UCRL (2006).